Run-Up Distance From Deflagration to Detonation In Fast Flames

by

Mohamed Saifelislam Abelgadir Ahmed

Thesis submitted to the
Faculty of Graduate and Postdoctoral Studies
In partial fulfillment of the requirements
For the M.A.Sc. degree in
Mechanical Engineering

Ottawa-Carleton Institute for Mechanical and Aerospace Engineering
Faculty of Graduate and Post-doctoral Studies
University of Ottawa

© Mohamed Saifelislam Abelgadir Ahmed, Ottawa, Canada, 2016

Abstract

In the process of deflagration-to-detonation transition (DDT) in reactive gases, the flame typically accelerates first to the choked flame condition (known as a Chapman-Jouguet deflagration), where it propagates at the sound speed with respect to the product gases. Subsequently, the choked flame may transit to a detonation. In the present study, the transition length from choked flames to detonations was measured experimentally in laboratory-scale experiments in methane, ethane, ethylene, acetylene, and propane with oxygen as oxidizer. The choked flames were first generated following the quenching of an incident detonation after its interaction with cylindrical obstacles with two different blockage ratios, 75% and 90%. Comparison with a recently proposed model confirms that these are Chapman-Jouguet deflagrations. The subsequent acceleration was monitored via large-scale time-resolved shadowgraphy. The mechanism of transition was found to be through the amplification of transverse waves and hot spot ignition from local Mach reflections. The transition length was found to correlate very well with the mixture's sensitivity to temperature and pressure fluctuations. These fluctuations could be connected to a unique parameter (χ), introduced by Radulescu. The parameter is the product of the non-dimensional activation energy (E_a/RT) and the ratio of chemical induction to reaction time (t_i/t_r). Mixtures with a higher χ were found to be more prompt to hot spot ignition and amplification of the fast flame into detonations. The run-up distance for unstable mixtures was found to be much shorter than anticipated from a model neglecting the fluctuations in a 1-D framework. The run-up distance was also correlated to the detonation cell size λ, yielding $L_{DDT} \simeq 7 - 50\lambda$, with the proportionality coefficient depending on χ and the obstacle blockage ratio. Finally, a unique correlation for the run-up distance is proposed, yielding $L_{DDT} \simeq 3000ct_r$, where c is the sound speed in the shocked non-reacted gas, valid for large χ.

Acknowledgements

First, I would like to give my special thanks and appreciations to my advisor Dr. Matei Ioan Radulescu, for giving me the chance to be part of his research team, and guiding me through all the difficulties that I faced. His mentoring, advice and guidance were essential for my improvement, and his exemplary dedication in the field of science and engineering set the bar high for us who worked with him.

I would also like to thank all who helped me during my master study. Special thanks to all the Detonation and Reactive Dynamics laboratory team, for their help and continual support in all the aspects of my research.

Gratitudes are also conveyed to the Machine-shop crew, who helped me in manufacturing my research hardware parts.

Last but not least, I would like to give my appreciation to Shell and the Natural Sciences and Engineering Research Council of Canada (NSERC) for their financial support toward this research.

Dedication

To my father Saif.

To my mother Najwa.

To my sisters, Malaz, Mehad, Maaza, Menan and Montaha.

Thank you.

All the Love.

Table of Contents

List of Tables viii

List of Figures x

1 Introduction 1

1.1 Problem Definition 1

1.2 Background and State-of-the-Art 2

1.3 Current Study 15

2 Review of Relevant Theoretical Concepts 17

2.1 Chapman-Jouguet Theory 17

2.2 Deflagrations as Gasdynamic Discontinuities 22

2.2.1 CJ Deflagrations in Tubes with a Closed End Wall 22

2.2.2 Gasdynamic Model for the Current Problem 24

2.3 Ignition Time Scales Behind a Leading Shock 25

2.4 χ Parameter 28

3 Experimental Setup 29

3.1 Physical Apparatus 29

3.2 Obstacle Configurations 30

3.3 Flow Visualization 31
3.4 Experimental Procedure 34
3.5 Uncertainty of Velocity Measurements 35

4 Experimental Results **36**

4.1 Methane 36
4.1.1 Methane with 75% Blockage Ratio 36
4.1.2 Methane with 90% Blockage Ratio 40
4.2 Propane 43
4.2.1 Propane with 75% Blockage Ratio 43
4.2.2 Propane with 90% Blockage Ratio 46
4.3 Ethane 48
4.3.1 Ethane with 75% Blockage Ratio 48
4.3.2 Ethane with 90% Blockage Ratio 50
4.4 Ethylene 59
4.4.1 Ethylene with 75% Blockage Ratio 59
4.4.2 Ethylene with 90% Blockage Ratio 61
4.5 Acetylene Diluted with 75% Argon 64
4.5.1 Acetylene-Argon with 75% Blockage Ratio 64
4.5.2 Acetylene-Argon with 90% Blockage Ratio 66

5 Discussion **69**

5.1 CJ Deflagrations and Required Turbulence Intensity 69
5.2 DDT Length Correlations 71
5.2.1 Correlations with the Detonation Cell Size λ 71
5.2.2 Correlation with the Ignition Delay and 1D DDT Characteristic Length 77

6 Conclusion **86**

6.1 Contributions to the State of Knowledge 86

6.2 Future Work 87

APPENDICES **88**

A 75% Blockage Ratio Experiments **89**

A.1 Methane 89

A.2 Ethane 99

A.3 Ethylene 105

A.4 Acetylene 110

A.5 Propane 118

B 90% Blockage Ratio Experiments **124**

B.1 Methane 124

B.2 Ethane 130

B.3 Ethylene 134

B.4 Acetylene 139

B.5 Propane 147

C Full List of Experiments **153**

C.1 75 % Blockage ratio experiments 153

C.2 90 % Blockage ratio experiments 158

References **162**

List of Tables

3.1 The parameters used in the 75% and 90% blockage ratio configurations, as seen in Figure 3.2. 30

5.1 Calculated laminar flame speeds s_L at 75% blockage ratio and 90% blockage ratio behind the leading shock. 70

5.2 Inferred mean turbulent flame speed and burning rate enhancement s_T/s_L in the current experiments. 71

5.3 Cell size and pressure correlations for methane, propane, ethane, ethylene, acetylene-argon as a function of λ [m] $= \alpha$ $[p_0$[kPa]$]^{-\beta}$ 73

5.4 L_{1-D} and pressure correlations for methane, propane, ethane, ethylene, acetylene as a function of L_{1-D} [m] $= \theta$ $[p_0$[kPa]$]^{-\phi}$ 81

C.1 A full list of experiments conducted for the 75% blockage ratio experiments 154

C.2 Continuation of table C.1 155

C.3 Continuation of table C.2 156

C.4 Continuation of table C.3 156

C.5 Continuation of table C.4 157

C.6 Continuation of table C.5 157

C.7 A full list of experiments conducted for the 90% blockage ratio experiments 158

C.8 Continuation of table C.7 159

C.9 Continuation of table C.8 160

C.10 Continuation of table C.9 161

C.11 Continuation of table C.10 161

List of Figures

1.1 Two Schlieren images of fast flames and detonation wave in CH_4+$2O_2$ at p_0=17.9 kPa and 10 kPa respectively. Image (a) from [30] and image (b) from [35]. 2

1.2 A figure showing the set of obstacles used by Maley and Bhattacharjee. All the experiments shown are for methane-oxygen. a) Experiment done by [4] with half cylinder configuration. b) Experiment done by [30] with single cylinder configuration. c) Experiment done by [30] with five cylinders configuration. 6

1.3 Overlayed shadowgraph images of fast flames in methane oxygen at p_0=10.3 kPa. Adopted from [30]. 7

1.4 a) Irregular Mach reflections in fast flames for CH_4+$2O_2$ at p_0=10.3 kPa. From [4]. b) CH_4+$2O_2$ detonation structure at p_0=3.4 kPa. From [36] . . . 8

1.5 Two sequential schlieren images of an experiment conducted at p_0=10.5 kPa in methane-oxygen. The images shows the hot spot ignition and the re-initiation event behind the Mach stem. 9

1.6 Schlieren images of an experiment conducted in methane-oxygen mixture at p_0= 10.1 kPa, showing the forward vortex process. Adopted from [4] . . . 9

1.7 Shadowgraph records of a methane-oxygen experiment showing hot spot ignition behind the Mach stem, p_0= 8.5 kPa. From [30]. 11

1.8 A comparison of reflection behavior between (a) hydrogen-oxygen at p_0=11.0 kPa, and (b) methane-oxygen at p_0=8.3 kPa, from [30]. 12

1.9 Comparison of fast flames in (a) unstable and (b) stable mixtures adopted from [20]. (a) The structure of a C_3H_8+$5O_2$ fast metastable combustion wave generated downstream of a perforated plate, p_0=4.0 kPa. (b) The structure of a high-speed deflagration that fails to transit back to a detonation, $2C_2H_2$+$5O_2$+70%Ar, p_0=12.0 kPa. The distances are normalized by the channel width. 13

1.10 Comparison between stable and unstable detonation cellular structures. The schlieren photographs are on the left, and sample of soot foils to the right. (a) irregular structure in C3H8-5O2-9N2, p_0=20 kPa. Detonation propagated from left to right and foils were mounted downstream of the window section of the narrow channel. (b) regular cellular structure in $2H_2$-O_2-7Ar, p_0=20 kPa. The figures are from [1]. 14

1.11 A schematic diagram showing a cellular detonation wave passing through a cylindrical obstacles to form de-coupled shock-flame complex 15

2.1 A sketch depicting a control volume over a combustion wave in a frame of reference attached to the wave. 18

2.2 Domains of detonation and deflagration solutions in the pv plane 19

2.3 A sketch showing the tangency of CJ solution for deflagration and detonation. From [25] 21

2.4 Schematic of the one dimensional deflagration model. 23

2.5 An x t diagram, showing the gas dynamic model used for predicting CJ deflagration and inert shock speeds. From [37]. 25

2.6 A sketch showing the states from Figure 2.5, and the location of the shocks. 26

2.7 Predicted transmitted shock speed for the reactive case assuming a CJ deflagration or inert shock as a function of the obstacle blockage ratio for $p_0 = 7.2$ kPa. From [37]. 27

2.8 A schematic showing the ignition delay and reaction time scales behind a leading shock. 28

3.1 Schematic of shock tube apparatus. Adapted from [30]. 29

3.2 Schematic of the obstacle configuration and the dimensions of the viewing section, with the length of the viewing section: a, the hight of the viewing section: b, the location of the obstacles from the left corner of the viewing section: c, the diameter of the obstacles d, the gap between the first obstacle and the top walls: e, the gap between the obstacles f. 31

3.3 Top-view illustration of the retro-reflective shadowgraph system [12]. . . . 32

3.4 Top-view picture of the optical components in the shadowgraphy system [12]. 33

4.1 Selected Shadowgraph images illustrating the re-initiation of detonation in CH_4+$2O_2$, p_0=10.3 kPa. Recorded at 23.76 μs interframe, 1 μs exposure, 42049 fps. The full record can be found in A.1, A.2, and A.3 37

4.2 Enlarged frames from Figure 4.1. 38

4.3 Selected Shadowgraph images illustrating the propagation of fast flames in CH_4+$2O_2$, p_0=8.2 kPa. Recorded at 23.76 μs interframe, 1 μs exposure, 42049 fps. The full record can be found in A.4, A.5, and A.6 39

4.4 Selected Shadowgraph images illustrating the propagation of fast flames in CH_4+$2O_2$, p_0=8.2 kPa. Recorded at 23.76 μs interframe, 1 μs exposure, 42049 fps. The full record can be found in A.4, A.5, and A.6 40

4.5 Selected Shadowgraph images illustrating the propagation of fast flames in CH_4+$2O_2$, p_0=3.4 kPa. Recorded at 23.76 μs interframe, 1 μs exposure, 42049 fps. The full record can be found in A.7, A.8, and A.9 41

4.6 Selected Shadowgraph images illustrating the propagation of fast flames in CH_4+$2O_2$, p_0=3.4 kPa. Recorded at 23.76 μs interframe, 1 μs exposure, 42049 fps. The full record can be found in A.7, A.8, and A.9 42

4.7 Velocity profiles for the test conducted for CH_4+$2O_2$, using the 75% blockage ratio configuration. 43

4.8 Shadowgraph images illustrating the re-initiation of detonation after interacting with obstacles in CH_4+$2O_2$, p_0 = 14.5 KPa. Recorded at 23.53 μs interframe, 0.7 μs exposure, 42496 fps. 44

4.9 Shadowgraph images illustrating the re-initiation of detonation after interacting with obstacles in CH_4+$2O_2$, p_0=14.5 KPa. Recorded at 23.53 μs interframe, 0.7 μs exposure, 42496 fps. The full record can be found in Fig B.1, B.2 and B.3. 45

4.10 Shadowgraph images illustrating the failure of detonation after interacting with obstacles in CH_4+$2O_2$, p_0=12.4 KPa. Recorded at 23.53 μs interframe, 0.7 μs exposure, 42496 fps. The full record can be found in B.4, B.5, B.6, and B.7 46

4.11 Velocity profiles for the test conducted for CH_4+$2O_2$, using the 90% blockage ratio configuration. 47

4.12 Shadowgraph images illustrating the re-initiation of detonation after interacting with obstacles in C_3H_8+$5O_2$, p_0=4.1 kPa. Recorded at 23.53 μs interframe, 1.0 μs exposure, 42492 fps. The full record can be found in Fig A.29, A.30, and A.31. 48

4.13 Shadowgraph images illustrating the propagation of fast flames after interacting with obstacles in C_3H_8+$5O_2$, p_0=2.0 kPa. Recorded at 23.53 μs interframe, 1.0 μs exposure, 42492 fps. The full record can be found in Fig A.32, A.33, and A.34 49

4.14 Velocity profiles for the test conducted for C_3H_8+$5O_2$, using the 75% blockage ratio configuration. 50

4.15 Shadowgraph images illustrating the re-initiation of detonation after interacting with obstacles in C_3H_8+$5O_2$, p_0=7.5 kPa. Recorded at 23.53 μs interframe, 0.8 μs exposure, 42496 fps. The full record can be found in Fig B.36, B.37, B.38 51

4.16 Shadowgraph images illustrating the failure of detonation after interacting with obstacles in C_3H_8+$5O_2$, p_0= 4.1 kPa. Recorded at 23.53 μs interframe, 0.8 μs exposure, 42496 fps. The full record can be found in Figure B.31, B.32, B.33, B.34, B.35. 52

4.17 Velocity profiles for the test conducted for C_3H_8+$5O_2$, using the 90% blockage ratio configuration. 53

4.18 Shadowgraph images illustrating the re-initiation of detonation after interacting with obstacles in $2C_2H_6$+$7O_2$, p_0= 4.1 kPa. Recorded at 23.53 μs interframe, 0.7 μs exposure, 42496 fps. The full record can be found in Fig A.10, A.11, and A.12 53

4.19 Shadowgraph images illustrating the re-initiation of detonation after interacting with obstacles in $2C_2H_6$+$7O_2$, p_0 = 4.1 kPa. Recorded at 23.53 μs interframe, 0.7 μs exposure, 42496 fps. The full record can be found in Fig A.10, A.11, and A.12 54

4.20 Shadowgraph images illustrating the failure of detonation after interacting with obstacles in $2C_2H_6$+$7O_2$, p_0 = 2.7 kPa. Recorded at 23.53 μs interframe, 0.7 μs exposure, 42496 fps. The full record can be found in Fig A.13, A.14, and A.15 55

4.21 Velocity profiles for the test conducted for $2C_2H_6$+$7O_2$, using the 75% blockage ratio configuration. 55

4.22 Shadowgraph images illustrating the re-initiation of detonation after interacting with obstacles in $2C_2H_6$+$7O_2$, p_0 = 9.6 kPa. Recorded at 23.53 μs interframe, 0.7 μs exposure, 42496 fps. The full record can be found in Fig B.8, B.9 and B.10 56

4.23 Shadowgraph images illustrating the failure of detonation after interacting with obstacles in $2C_2H_6$+$7O_2$, p_0 = 8.2 KPa. Recorded at 23.53 μs interframe, 0.7 μs exposure, 42496 fps. The full record can be found in Fig B.11, B.12, B.13, and B.14 57

4.24 Velocity profiles for the test conducted for $2C_2H_6+7O_2$, using the 90% blockage ratio configuration. 58

4.25 Shadowgraph images illustrating the re-initiation of detonation after interacting with obstacles in $C_2H_4+3O_2$, p_0 = 6.2 kPa. Recorded at 23.53 μs interframe, 0.8 μs exposure, 42496 fps. The full record can be found in Fig A.16, and A.17 59

4.26 Shadowgraph images illustrating the failure of detonation after interacting with obstacles in $C_2H_4+3O_2$, p_0=3.4 kPa. Recorded at 23.53 μs interframe, 0.8 μs exposure, 42496 fps. The full record can be found in Fig A.18, A.19, and A.20 60

4.27 Velocity profiles for the tests conducted for $C_2H_4+3O_2$, using the 75% blockage ratio configuration. 61

4.28 Shadowgraph images illustrating the re-initiation of detonation after interacting with obstacles in $C_2H_4+3O_2$, p_0 = 8.2 kPa. Recorded at 23.53 μs interframe, 0.8 μs exposure, 42496 fps. The full record can be found in Fig B.15, B.16, and B.17 62

4.29 Shadowgraph images illustrating the failure of detonation after interacting with obstacles in $C_2H_4+3O_2$, $p_0 = 6.2$ kPa. Recorded at 23.53 μs interframe, 0.8 μs exposure, 42496 fps. The full record can be found in Fig B.18, B.19, B.20, and B.21 63

4.30 Velocity profiles for the tests conducted for $C_2H_4+3O_2$, using the 90% blockage ratio configuration. 63

4.31 Shadowgraph images illustrating the re-initiation of detonation after interacting with obstacles in $2C_2H_2+5O_2+21Ar$, p_0=11 kPa. Recorded at 23.53 μs interframe, 0.8 μs exposure, 42496 fps. The full record can be found in Fig A.21, A.22, and A.23 64

4.32 Shadowgraph images illustrating the failure of detonation after interacting with obstacles in $2C_2H_2+5O_2+21Ar$, p_0 = 9.6 kPa. Recorded at 23.53 μs interframe, 0.8 μs exposure, 42496 fps. The full record can be found in Fig A.24, A.25, A.26, A.27, and A.28 65

4.33 Velocity profiles for the tests conducted for $2C_2H_2+5O_2+21Ar$, using the 75% blockage ratio configuration. 66

4.34 Shadowgraph images illustrating the failure of detonation after interacting with obstacles in $2C_2H_2+5O_2+21Ar$, p_0 = 18 KPa. Recorded at 23.53 μs interframe, 0.8 μs exposure, 42496 fps. The full record can be found in Fig B.26, B.27, B.28, B.29, and B.30 67

4.35 Velocity profiles for the tests conducted for $2C_2H_2+5O_2+21Ar$, using the 90% blockage ratio configuration. 68

5.1 The relation between the initial pressure and detonation cell size for the relevant tests conducted. 72

5.2 Correlation between the run-up distance to detonation L_{DDT} and detonation cell size λ, at 75%. 74

5.3 Correlation between the run-up distance to detonation L_{DDT} and detonation cell size λ, at 90% blockage ratio obstacles configurations. 75

5.4 The correlation between (L_{DDT}/λ) and χ 76

5.5 A space time diagram illustrating the L_{1-D} distance 78

5.6 The correlation between the initial pressure p_0 and the characteristic length L_{1-D}. 80

5.7 The correlation between the run up distance from deflagration to detonation (L_{DDT}) distance and L_{1-D}. 82

5.8 The correlation between (L_{DDT}/L_{1-D}) and χ 84

5.9 The variation of L_{DDT}/ct_r with χ 85

A.1 The full record of the Shadowgraph images illustrating the re-initiation of detonation after interacting with obstacles in CH_4+$2O_2$, p_0=10.3 KPa. Recorded at 23.76 μs interframe, 1 μs exposure, 42049 fps 90

A.2 The full record of the Shadowgraph images illustrating the re-initiation of detonation after interacting with obstacles in CH_4+$2O_2$, p_0=10.3 KPa. Recorded at 23.76 μs interframe, 1 μs exposure, 42049 fps 91

A.3 The full record of the Shadowgraph images illustrating the re-initiation of detonation after interacting with obstacles in CH_4+$2O_2$, p_0=10.3 kPa (1.5 psi). Recorded at 23.76 μs interframe, 1 μs exposure, 42049 fps 92

A.4 The full record of the Shadowgraph images illustrating the re-initiation of detonation after interacting with obstacles in CH_4+$2O_2$, p_0=8.2 kPa (1.2 psi). Recorded at 23.76 μs interframe, 1 μs exposure, 42049 fps 93

A.5 The full record of the Shadowgraph images illustrating the re-initiation of detonation after interacting with obstacles in CH_4+$2O_2$, p_0=8.2 kPa (1.2 psi). Recorded at 23.76 μs interframe, 1 μs exposure, 42049 fps 94

A.6 The full record of the Shadowgraph images illustrating the re-initiation of detonation after interacting with obstacles in CH_4+$2O_2$, p_0=8.2 kPa (1.2 psi). Recorded at 23.76 μs interframe, 1 μs exposure, 42049 fps 95

A.7 The full record of the Shadowgraph images illustrating the re-initiation of detonation after interacting with obstacles in CH_4+$2O_2$, p_0=3.4 kPa (0.5 psi). Recorded at 23.76 μs interframe, 1 μs exposure, 42049 fps 96

A.8 The full record of the Shadowgraph images illustrating the re-initiation of detonation after interacting with obstacles in CH_4+$2O_2$, p_0=3.4 kPa (0.5 psi). Recorded at 23.76 μs interframe, 1 μs exposure, 42049 fps 97

A.9 The full record of the Shadowgraph images illustrating the re-initiation of detonation after interacting with obstacles in CH_4+$2O_2$, p_0=3.4 kPa (0.5 psi). Recorded at 23.76 μs interframe, 1 μs exposure, 42049 fps. 98

A.10 The full record of the Shadowgraph images illustrating the re-initiation of detonation after interacting with obstacles in $2C_2H_6+7O_2$, p_0= 4.1 kPa(0.6 psi). Recorded at 23.53 μs interframe, 0.7 μs exposure, 42496 fps. 99

A.11 The full record of the Shadowgraph images illustrating the re-initiation of detonation after interacting with obstacles in $2C_2H_6+7O_2$, p_0= 4.1 kPa(0.6 psi). Recorded at 23.53 μs interframe, 0.7 μs exposure, 42496 fps. 100

A.12 The full record of the Shadowgraph images illustrating the re-initiation of detonation after interacting with obstacles in $2C_2H_6+7O_2$, p_0= 4.1 kPa(0.6 psi). Recorded at 23.53 μs interframe, 0.7 μs exposure, 42496 fps. 101

A.13 The full record of the Shadowgraph images illustrating the failure of detonation after interacting with obstacles in $2C_2H_6+7O_2$, p_0=2.7 kPa(0.4 psi). Recorded at 23.53 μs interframe, 0.7 μs exposure, 42496 fps. 102

A.14 The full record of the Shadowgraph images illustrating the failure of detonation after interacting with obstacles in $2C_2H_6+7O_2$, p_0=2.7 kPa(0.4 psi). Recorded at 23.53 μs interframe, 0.7 μs exposure, 42496 fps. 103

A.15 The full record of the Shadowgraph images illustrating the failure of detonation after interacting with obstacles in $2C_2H_6+7O_2$, p_0=2.7 kPa(0.4 psi). Recorded at 23.53 μs interframe, 0.7 μs exposure, 42496 fps. 104

A.16 The full record of the Shadowgraph images illustrating the re-initiation of detonation after interacting with obstacles in $C_2H_4+3O_2$, p_0=6.2 kPa (0.9 psi). Recorded at 23.53 μs interframe, 0.8 μs exposure, 42496 fps. 105

A.17 The full record of the Shadowgraph images illustrating the re-initiation of detonation after interacting with obstacles in $C_2H_4+3O_2$, p_0=6.2 kPa (0.9 psi). Recorded at 23.53 μs interframe, 0.8 μs exposure, 42496 fps. 106

A.18 The full record of the Shadowgraph images illustrating the failure of detonation after interacting with obstacles in $C_2H_4+3O_2$, p_0=3.4 kPa (0.5 psi). Recorded at 23.53 μs interframe, 0.8 μs exposure, 42496 fps. 107

A.19 The full record of the Shadowgraph images illustrating the failure of detonation after interacting with obstacles in C_2H_4+3O_2, p_0=3.4 kPa (0.5 psi). Recorded at 23.53 μs interframe, 0.8 μs exposure, 42496 fps. 108

A.20 The full record of the Shadowgraph images illustrating the failure of detonation after interacting with obstacles in C_2H_4+3O_2, p_0=3.4 kPa (0.5 psi). Recorded at 23.53 μs interframe, 0.8 μs exposure, 42496 fps. 109

A.21 The full record of the Shadowgraph images illustrating the re-initiation of detonation after interacting with obstacles in 2C_2H_2+5O_2+21Ar, p_0=11.0 kPa (1.6 psi). Recorded at 23.53 μs interframe, 0.8 μs exposure, 42496 fps. 110

A.22 The full record of the Shadowgraph images illustrating the re-initiation of detonation after interacting with obstacles in 2C_2H_2+5O_2+21Ar, p_0=11.0 kPa (1.6 psi). Recorded at 23.53 μs interframe, 0.8 μs exposure, 42496 fps. 111

A.23 The full record of the Shadowgraph images illustrating the re-initiation of detonation after interacting with obstacles in 2C_2H_2+5O_2+21Ar, p_0=11.0 kPa (1.6 psi). Recorded at 23.53 μs interframe, 0.8 μs exposure, 42496 fps. 112

A.24 Shadowgraph images illustrating the failure of detonation after interacting with obstacles in 2C_2H_2+5O_2+21Ar, p_0=9.6 kPa (1.4 psi). Recorded at 23.53 μs interframe, 0.8 μs exposure, 42496 fps. 113

A.25 Shadowgraph images illustrating the failure of detonation after interacting with obstacles in 2C_2H_2+5O_2+21Ar, p_0=9.6 kPa (1.4 psi). Recorded at 23.53 μs interframe, 0.8 μs exposure, 42496 fps. 114

A.26 Shadowgraph images illustrating the failure of detonation after interacting with obstacles in 2C_2H_2+5O_2+21Ar, p_0=9.6 kPa (1.4 psi). Recorded at 23.53 μs interframe, 0.8 μs exposure, 42496 fps. 115

A.27 Shadowgraph images illustrating the failure of detonation after interacting with obstacles in 2C_2H_2+5O_2+21Ar, p_0=9.6 kPa (1.4 psi). Recorded at 23.53 μs interframe, 0.8 μs exposure, 42496 fps. 116

A.28 Shadowgraph images illustrating the failure of detonation after interacting with obstacles in $2C_2H_2+5O_2+21Ar$, p_0=9.6 kPa (1.4 psi). Recorded at 23.53 μs interframe, 0.8 μs exposure, 42496 fps. 117

A.29 The full record of the Shadowgraph images illustrating the re-initiation of detonation after interacting with obstacles in $C_3H_8+5O_2$, p_0=4.1 kPa(0.6 psi). Recorded at 23.53 μs interframe, 1.0 μs exposure, 42492 fps. 118

A.30 The full record of the Shadowgraph images illustrating the re-initiation of detonation after interacting with obstacles in $C_3H_8+5O_2$, p_0=4.1 kPa(0.6 psi). Recorded at 23.53 μs interframe, 1.0 μs exposure, 42492 fps. 119

A.31 The full record of the Shadowgraph images illustrating the re-initiation of detonation after interacting with obstacles in $C_3H_8+5O_2$, p_0=4.1 kPa(0.6 psi). Recorded at 23.53 μs interframe, 1.0 μs exposure, 42492 fps. 120

A.32 The full record of the Shadowgraph images illustrating the propagation of fast flames after interacting with obstacles in $C_3H_8+5O_2$, p_0=2.0 kPa(0.3 psi). Recorded at 23.53 μs interframe, 1.0 μs exposure, 42492 fps. 121

A.33 The full record of the Shadowgraph images illustrating the propagation of fast flames after interacting with obstacles in $C_3H_8+5O_2$, p_0=2.0 kPa(0.3 psi). Recorded at 23.53 μs interframe, 1.0 μs exposure, 42492 fps. 122

A.34 The full record of the Shadowgraph images illustrating the propagation of fast flames after interacting with obstacles in $C_3H_8+5O_2$, p_0=2.0 kPa(0.3 psi). Recorded at 23.53 μs interframe, 1.0 μs exposure, 42492 fps. 123

B.1 The full record of the Shadowgraph images illustrating the re-initiation of detonation after interacting with obstacles in CH_4+2O_2, p_0=14.5 KPa. Recorded at 23.53 μs interframe, 0.7 μs exposure, 42496 fps 125

B.2 The full record of the Shadowgraph images illustrating the re-initiation of detonation after interacting with obstacles in CH_4+2O_2, p_0=14.5 KPa. Recorded at 23.53 μs interframe, 0.7 μs exposure, 42496 fps 126

B.3 The full record of the Shadowgraph images illustrating the re-initiation of detonation after interacting with obstacles in CH_4+2O_2, p_0=14.5 KPa. Recorded at 23.53 μs interframe, 0.7 μs exposure, 42496 fps 126

B.4 The full record of the Shadowgraph images illustrating the failure of detonation after interacting with obstacles in CH_4+2O_2, p_0=12.4 KPa. Recorded at 23.53 μs interframe, 0.7 μs exposure, 42496 fps 127

B.5 The full record of the Shadowgraph images illustrating the failure of detonation after interacting with obstacles in CH_4+2O_2, p_0=12.4 KPa. Recorded at 23.53 μs interframe, 0.7 μs exposure, 42496 fps 128

B.6 The full record of the Shadowgraph images illustrating the failure of detonation after interacting with obstacles in CH_4+2O_2, p_0=12.4 KPa. Recorded at 23.53 μs interframee, 0.7 μs exposure, 42496 fps 129

B.7 The full record of the Shadowgraph images illustrating the failure of detonation after interacting with obstacles in CH_4+2O_2, p_0=12.4 KPa. Recorded at 23.53 μs interframe, 0.7 μs exposure, 42496 fps 129

B.8 The full record of the Shadowgraph images illustrating the re-initiation of detonation after interacting with obstacles in $2C_2H_6+7O_2$, p_0=9.6 KPa. Recorded at 23.53 μs interframe, 0.7 μs exposure, 42496 fps. 130

B.9 The full record of the Shadowgraph images illustrating the re-initiation of detonation after interacting with obstacles in $2C_2H_6+7O_2$, p_0=9.6 KPa. Recorded at 23.53 μs interframe, 0.7 μs exposure, 42496 fps. 131

B.10 The full record of the Shadowgraph images illustrating the re-initiation of detonation after interacting with obstacles in $2C_2H_6+7O_2$, p_0=9.6 KPa. Recorded at 23.53 μs interframe, 0.7 μs exposure, 42496 fps. 131

B.11 The full record of the Shadowgraph images illustrating the failure of detonation after interacting with obstacles in $2C_2H_6+7O_2$, p_0=8.2 KPa. Recorded at 23.53 μs interframe, 0.7 μs exposure, 42496 fps. 132

B.12 The full record of the Shadowgraph images illustrating the failure of detonation after interacting with obstacles in $2C_2H_6+7O_2$, p_0=8.2 KPa. Recorded at 23.53 μs interframe, 0.7 μs exposure, 42496 fps. 132

B.13 The full record of the Shadowgraph images illustrating the failure of detonation after interacting with obstacles in $2C_2H_6+7O_2$, p_0=8.2 KPa. Recorded at 23.53 μs interframe, 0.7 μs exposure, 42496 fps. 133

B.14 The full record of the Shadowgraph images illustrating the failure of detonation after interacting with obstacles in $2C_2H_6+7O_2$, p_0=8.2 KPa. Recorded at 23.53 μs interframe, 0.7 μs exposure, 42496 fps. 133

B.15 The full record of the Shadowgraph images illustrating the re-initiation of detonation after interacting with obstacles in $C_2H_4+3O_2$, p_0=8.2 KPa. Recorded at 23.53 μs interframe, 0.8 μs exposure, 42496 fps. 134

B.16 The full record of the Shadowgraph images illustrating the re-initiation of detonation after interacting with obstacles in $C_2H_4+3O_2$, p_0=8.2 KPa. Recorded at 23.53 μs interframe, 0.8 μs exposure, 42496 fps. 135

B.17 The full record of the Shadowgraph images illustrating the re-initiation of detonation after interacting with obstacles in $C_2H_4+3O_2$, p_0=8.2 KPa. Recorded at 23.53 μs interframe, 0.8 μs exposure, 42496 fps. 135

B.18 The full record of the Shadowgraph images illustrating the failure of detonation after interacting with obstacles in $C_2H_4+3O_2$, p_0=6.2 KPa. Recorded at 23.53 μs interframe, 0.8 μs exposure, 42496 fps. 136

B.19 The full record of the Shadowgraph images illustrating the failure of detonation after interacting with obstacles in $C_2H_4+3O_2$, p_0=6.2 KPa. Recorded at 23.53 μs interframe, 0.8 μs exposure, 42496 fps. 136

B.20 The full record of the Shadowgraph images illustrating the failure of detonation after interacting with obstacles in $C_2H_4+3O_2$, p_0=6.2 KPa. Recorded at 23.53 μs interframe, 0.8 μs exposure, 42496 fps. 137

B.21 The full record of the Shadowgraph images illustrating the failure of detonation after interacting with obstacles in C_2H_4+$3O_2$, p_0=6.2 KPa. Recorded at 23.53 μs interframe, 0.8 μs exposure, 42496 fps. 138

B.22 The full record of the Shadowgraph images illustrating the failure of detonation after interacting with obstacles in $2C_2H_2$+$5O_2$+21Ar, p_0=11.0 KPa. Recorded at 23.53 μs interframe, 0.8 μs exposure, 42496 fps. 139

B.23 The full record of the Shadowgraph images illustrating the failure of detonation after interacting with obstacles in $2C_2H_2$+$5O_2$+21Ar, p_0=11.0 KPa. Recorded at 23.53 μs interframe, 0.8 μs exposure, 42496 fps. 140

B.24 The full record of the Shadowgraph images illustrating the failure of detonation after interacting with obstacles in $2C_2H_2$+$5O_2$+21Ar, p_0=11.0 KPa. Recorded at 23.53 μs interframe, 0.8 μs exposure, 42496 fps. 140

B.25 The full record of the Shadowgraph images illustrating the failure of detonation after interacting with obstacles in $2C_2H_2$+$5O_2$+21Ar, p_0=11.0 KPa. Recorded at 23.53 μs interframe, 0.8 μs exposure, 42496 fps. 141

B.26 The full record of the Shadowgraph images illustrating the failure of detonation after interacting with obstacles in $2C_2H_2$+$5O_2$+21Ar, p_0=17.9 KPa. Recorded at 23.53 μs interframe, 0.8 μs exposure, 42496 fps. 142

B.27 The full record of the Shadowgraph images illustrating the failure of detonation after interacting with obstacles in $2C_2H_2$+$5O_2$+21Ar, p_0=17.9 KPa. Recorded at 23.53 μs interframe, 0.8 μs exposure, 42496 fps. 143

B.28 The full record of the Shadowgraph images illustrating the failure of detonation after interacting with obstacles in $2C_2H_2$+$5O_2$+21Ar, p_0=17.9 KPa. Recorded at 23.53 μs interframe, 0.8 μs exposure, 42496 fps. 144

B.29 The full record of the Shadowgraph images illustrating the failure of detonation after interacting with obstacles in $2C_2H_2$+$5O_2$+21Ar, p_0=17.9 KPa. Recorded at 23.53 μs interframe, 0.8 μs exposure, 42496 fps. 145

B.30 The full record of the Shadowgraph images illustrating the failure of detonation after interacting with obstacles in $2C_2H_2+5O_2+21Ar$, p_0=17.9 KPa. Recorded at 23.53 μs interframe, 0.8 μs exposure, 42496 fps. 146

B.31 The full record of the Shadowgraph images illustrating the failure of detonation after interacting with obstacles in $C_3H_8+5O_2$, p_0=4.1 KPa. Recorded at 23.53 μs interframe, 0.8 μs exposure, 42496 fps. 147

B.32 The full record of the Shadowgraph images illustrating the failure of detonation after interacting with obstacles in $C_3H_8+5O_2$, p_0=4.1 KPa. Recorded at 23.53 μs interframe, 0.8 μs exposure, 42496 fps. 148

B.33 The full record of the Shadowgraph images illustrating the failure of detonation after interacting with obstacles in $C_3H_8+5O_2$, p_0=4.1 KPa. Recorded at 23.53 μs interframe, 0.8 μs exposure, 42496 fps. 149

B.34 The full record of the Shadowgraph images illustrating the failure of detonation after interacting with obstacles in $C_3H_8+5O_2$, p_0=4.1 KPa. Recorded at 23.53 μs interframe, 0.8 μs exposure, 42496 fps. 150

B.35 The full record of the Shadowgraph images illustrating the failure of detonation after interacting with obstacles in $C_3H_8+5O_2$, p_0=4.1 KPa. Recorded at 23.53 μs interframe, 0.8 μs exposure, 42496 fps. 150

B.36 The full record of the Shadowgraph images illustrating the re-initiation of detonation after interacting with obstacles in $C_3H_8+5O_2$, p_0=7.5 KPa. Recorded at 23.53 μs interframe, 0.8 μs exposure, 42496 fps. 151

B.37 The full record of the Shadowgraph images illustrating the re-initiation of detonation after interacting with obstacles in $C_3H_8+5O_2$, p_0=7.5 KPa. Recorded at 23.53 μs interframe, 0.8 μs exposure, 42496 fps. 152

B.38 The full record of the Shadowgraph images illustrating the re-initiation of detonation after interacting with obstacles in $C_3H_8+5O_2$, p_0=7.5 KPa. Recorded at 23.53 μs interframe, 0.8 μs exposure, 42496 fps. 152

Chapter 1

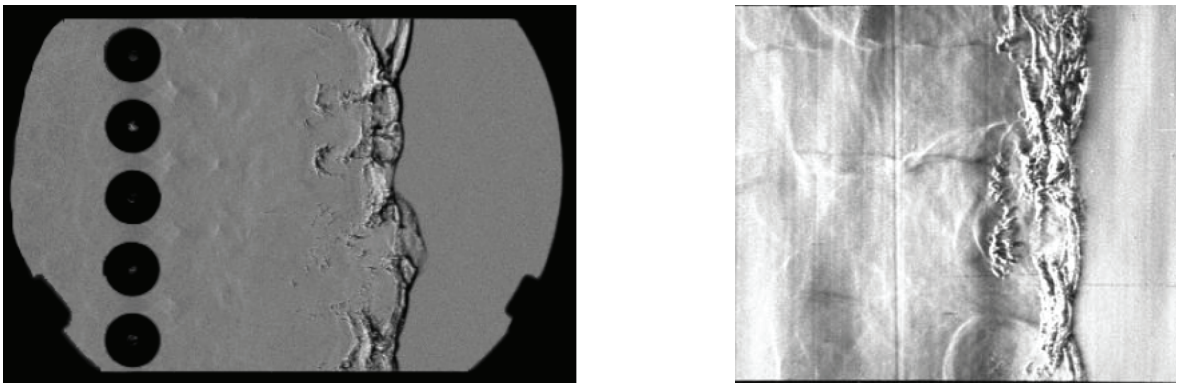
Introduction

1.1 Problem Definition

The study of deflagration to detonation transition (DDT) plays an important role in many areas, such as explosion safety [2], pulse detonation engines [41], and the design of flame arresters [5]. Despite its importance, the quantitative prediction of DDT in reactive gases is one of the major unsolved problems in combustion and detonation theory. It is difficult because of the complex and fast interactions among the different contributing coupled processes, such as turbulence, reactive gas dynamics and chemical kinetics.

In DDT, there is a final transition stage, in which flames coupled closely with a leading shock propagate for several tube diameters before they transit to detonation. These flames, known as fast flames or choked flames, look very similar to Chapman Jouguet (CJ) detonations; however, they propagate with velocities between those expected for CJ deflagrations, and CJ detonations [7, 30, 37]. Figure 1.1 shows how fast flames are similar to detonation waves, with both having a complex shock-flame structure punctuated by auto-ignition spots. Quantitatively, the mechanisms that control the acceleration of fast flames into CJ detonation are not clear.

This work focuses on clarifying the propagating, and accelerating mechanism(s) of these fast flames in the context of DDT and proposing correlations for the so-called run-



a) Fast Flames b) Detonation Wave

Figure 1.1: Two Schlieren images of fast flames and detonation wave in CH_4+$2O_2$ at p_0=17.9 kPa and 10 kPa respectively. Image (a) from [30] and image (b) from [35].

up-distance, or DDT length in several light hydrocarbon mixtures (methane, acetylene, ethylene, ethane and propane).

1.2 Background and State-of-the-Art

There are two types of combustion waves: detonations and deflagrations. Detonations propagate at supersonic speeds relative to the unburned gases ahead of them, with velocities of the order of a few kilometres per second. These are compression waves, with both the pressure and the density increasing across the wave. Since the detonation wave travels at supersonic speed, the unburned gases ahead of the wave are undisturbed and remain in their initial condition. The propagation mechanism of detonations is based on auto-ignition. A shock, coupled closely to the reaction zone, compresses the gases and heats them up to a higher temperature, until they start to ignite. The expansion of these burned gases, resulting from the chemical energy release, drives the shock-flame complex as a unit at detonation velocity in a self-supported manner[25].

Deflagrations, on the other hand, are subsonic combustion waves, relative to the unburned gases ahead of them, with typical velocities on the order of metres per second. They

are expansion combustion waves, meaning that both pressure and density drop across the wave. Since they are subsonic, they can perturb the state of unburned gases ahead of them. Compression waves may be ahead of the flame's front due to the expansion of the burned gases in non-stationary situations, such as DDT. The propagation mechanism of deflagrations is based on heat and mass diffusion [25].

The deflagration to detonation transition, or DDT, is the abrupt transition from a deflagration combustion mode to a detonation combustion mode. DDT consists of two stages. The initial stage describes the flame acceleration starting from a weak ignition source until the flame reaches a maximum critical speed. At this stage, it is believed that the flame is a Chapman-Jouguet deflagration, propagating at sonic speed relative to the burned gases. The second part of the DDT process is the subsequent acceleration of these fast flames into detonations.

Several reviews of the first stage of the DDT process were reported in the past for DDT in both smooth and obstructed geometries [9, 27, 45, 26, 51]. In summary, in a smooth tube for example, if we allowed the mixture to ignite at the closed end of the tube, using a weak ignition source, a flame kernel will emerge. At first, the flame front will have a hemispherical shape, and the expansion of the combustion products will send pressure waves and set the unburned gases ahead of the flame into motion in the direction of the flame propagation. At the centre of the tube, the initially hemispherical laminar flame will start to wrinkle due to various instabilities, such as the Landau-Darrieus [11, 23] instability and the thermal diffusional instability.

The flow of the unburned gases ahead of the flames then interacts with the walls, creating a boundary shear layer. The interaction of flames with that boundary layer results in a significant increase in burning rates near the walls. The overall result is a distorted flame front with larger surface area. The increase of the flame surface area leads to an increase in the burning rates and flame velocity. As a result, a feedback loop will be generated with a larger displacement of the burned products, more velocity gradients, and more stretching and folding of the flame.

At the same time, the pressure waves generated by the expansion of the combustion

products will pre-compress the fresh mixture ahead of the flames, increasing their temperature, leading to further increase in burning rates and flame velocity.

Turbulence causes the flames to corrugate more, which also leads eventually to higher burning rates and flame velocity. The accelerating turbulent flames will send more compression waves ahead of them. At some point, these compression waves will coalesce and form a shock wave. The shock wave compresses the gases and increases their temperature and pressure even further. The flames keep accelerating until they reach a critical value.

As pointed out by Taylor and Tankin [47, 9, 10], the deflagration critical speed corresponds to the condition that the flow behind the deflagration combustion wave is sonic in the burned products. Higher speeds do not allow steady state solutions. That speed marks the beginning of the last stage of deflagration to detonation transition, so-called fast-flames, or choking regime; where a deflagration wave and shock complex propagates quasi-steady at approximately half CJ velocity in a closed end tube [7, 20, 6]. This regime is poorly understood, sometimes even called "strange wave" [48]. This stage has been observed to propagate many tube diameters before the transition to detonation, and despite the importance of that regime, the propagating mechanism remains unclear [20].

At present, it is difficult to predict accurately whether or not DDT can occur in a reactive mixture for given initial and boundary conditions [6]. However, qualitatively, the mechanisms of transition are reasonably well understood. We can describe all the elementary processes involved [9, 27, 33]. This qualitative understanding has been acquired largely from photographic observations of the transition phenomenon, mainly from the early work conducted by Oppenheim et al.[50, 49]. Despite that, the sequence of events that clearly show which mechanisms are responsible for increasing the burning rate and subsequently causing re-initiation into a detonation are not clear [4].

In the past, many studies were conducted in an attempt to find the ruling mechanisms responsible for fast flame acceleration and transition into detonation. Some of the most recent are the work done by Maley and Bhattacharjee [30, 4, 3, 29]. They produced these flames in the lab by allowing a CJ detonation wave to quench after interacting with different sets of obstacles. They adapted this method from previous studies conducted

by Chao, and Grondin and Lee [6, 20]. Figure 1.2 shows an example of the experiments they performed with different obstacle configurations. In all three obstacle configurations they used, a CJ detonation wave - propagating from left to right - was allowed to diffract around the obstacles, and subsequently produce fast flames. These fast flames were then monitored using shadowgraph and Schlieren visualization systems. The setup by Maley and Bhattacharjee allowed them to obtain these fast flames without relying on slow flame acceleration.

After diffracting around the obstacles, fast flames develop irregular Mach reflections. As seen in Fig. 1.3, the structure of these Mach reflections consist of three shocks: Incident shock, Transverse shock, and Mach shock or Mach stem. These shocks meet at a point called a "triple point". Following the path of that triple point, we can see how they collide with the top and bottom wall, generating a new sequence of Mach reflections. The new Mach stems (seen in the top and the bottom) propagate toward each other, with one incident shock in the middle. Finally, the triple points intersect again, generating another sequence of Mach reflections. As seen in the enlarged section below, a slip line is observed. The slip line separates gases shocked by the Mach stem and those shocked by the incident and transverse shock. Along the contact surface, the pressure and the flow direction are equal.

The high-resolution Schlieren images obtained by Bhattacharjee [4] in methane-oxygen showed that the structure of the irregular Mach reflections in these fast flames looks very similar to the structure of a single mode unstable detonation [36]. As we can see in Figure 1.4, the picture to the left shows an experiment done by [4] for fast flame in methane-oxygen at $p_0 = 10.3$ kPa, while the picture to the right shows an experiment done by Radulescu et al.[36] in the same mixture but for a single mode detonation at $p_0 = 3.4$ kPa. The structures of both fast flames and single mode detonation look similar.

Bhattacharjee observed auto-ignition events behind the Mach stem, which is the hottest portion of the triple shock structure [25]. These occurred after the collision of two triple points with each other, or a triple point with the top or the bottom wall. He referred to these events as hot spot ignition. Bhattacharjee believed that this discrete hot spot ignition

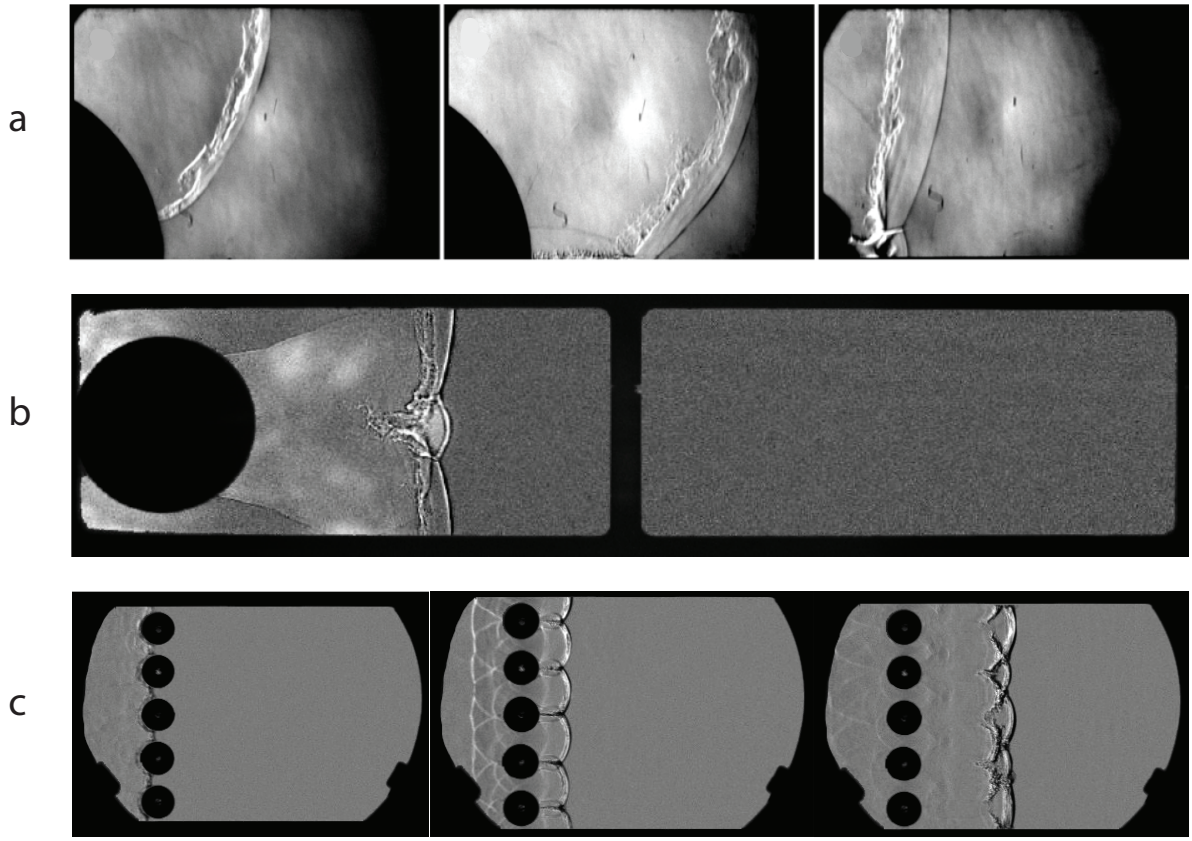


Figure 1.2: A figure showing the set of obstacles used by Maley and Bhattacharjee. All the experiments shown are for methane-oxygen. a) Experiment done by [4] with half cylinder configuration. b) Experiment done by [30] with single cylinder configuration. c) Experiment done by [30] with five cylinders configuration.

cause the flame-shock complex to accelerate and subsequently transit to detonation. Figure 1.5 shows two sequential Schlieren frames of an experiment done by Bhattacharjee. In the first frame, we observe how the triple point impinges on the bottom wall. The second frame shows the re-initiation event behind the Mach stem.

In other tests conducted by Bhattacharjee, he observed the extension of the slip line of the triple point structure to curl up into a vortex that mixes unburned gases, shocked by the incident and the transverse shocks, with burned gases behind the Mach stem. In the presence of a reflective surface (a wall or a line of symmetry for example), the flow along the contact surface intersects with the wall and forces the flow back toward the Mach stem,

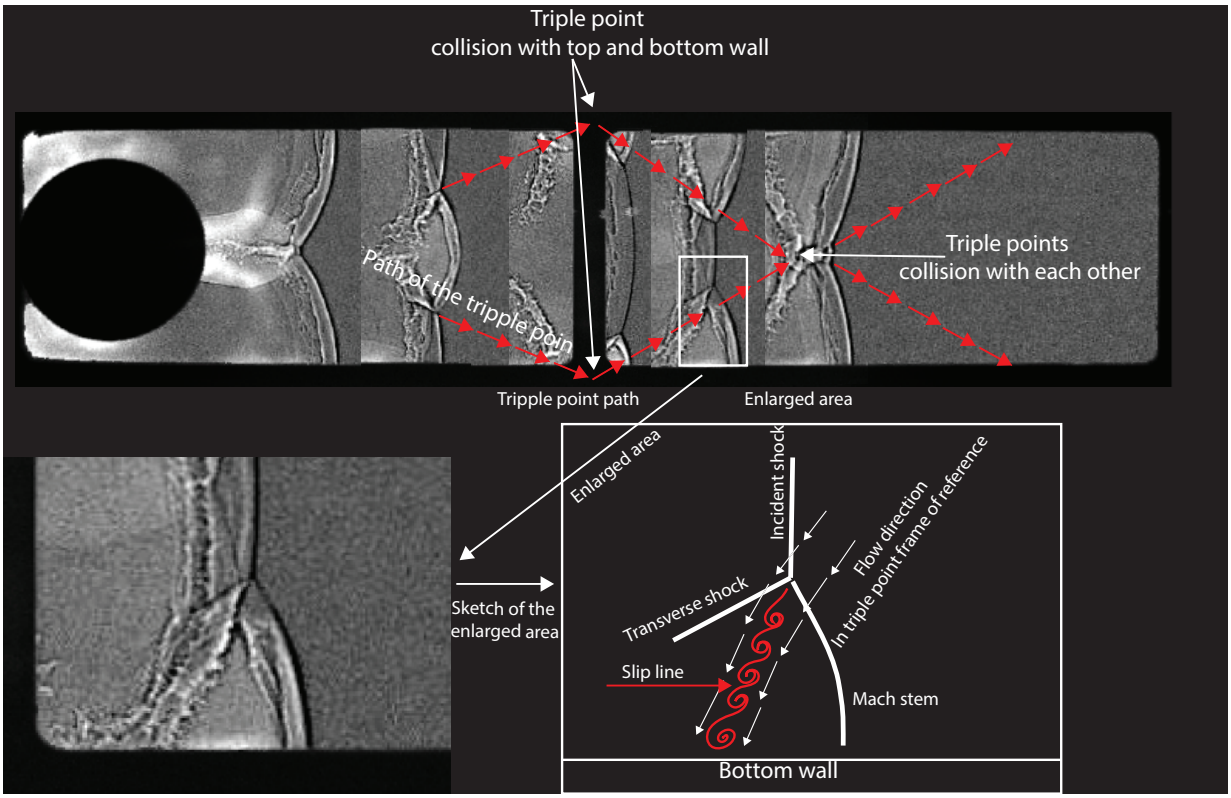


Figure 1.3: Overlayed shadowgraph images of fast flames in methane oxygen at p_0=10.3 kPa. Adopted from [30].

forming a large rolled-up vortex that mixes hot combustion products behind the Mach stem with the unburned gases. The mixing causes an increase and acceleration of reaction rates and potentially triggers DDT [28]. Figure 1.6 shows an example of the scenario that Bhattacharjee observed. In the figure, three sequential frames show the growth of that vortex with time. The enlarged section in the second frame shows how the flow along the contact surface would intersect with the bottom wall and subsequently generate the vortex.

Bhattacharjee's experiments were numerically modelled by Lau-Chapdelaine [24], to find the mechanism for DDT in irregular Mach reflections. Lau-Chapdelaine's numerical results agreed with the experiments done by Bhattacharjee. He concluded that autoignition caused by the shock compression, seen behind the Mach stem, increases the velocity of the shock-flame complex and causes re-initiation into detonation.

Experiments conducted by Maley in single cylinder configurations for methane-oxygen

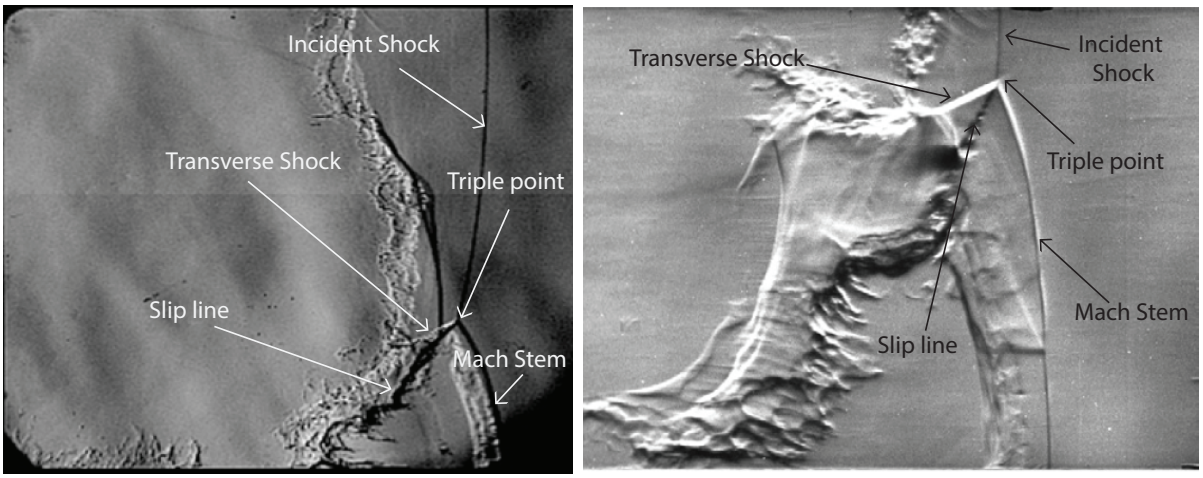


Figure 1.4: a) Irregular Mach reflections in fast flames for CH_4+$2O_2$ at p_0=10.3 kPa. From [4]. b) CH_4+$2O_2$ detonation structure at p_0=3.4 kPa. From [36]

showed the same results. The sequential frames seen in Figure 1.7 show the periodic generation of these Mach stems after each collision, as seen in frame 3 and 5. In frame 4 and 6, it can be seen that the flames are closely coupled behind the Mach stems, meaning that the induction length is short. This gives an indication that the Mach stem is stronger than the incident and transverse shocks.

Maley further observed, when testing fuels with different thermochemical properties (hydrogen-oxygen and methane-oxygen), that hydrogen and methane showed different behaviour of Mach reflections. As seen in Figure 1.8, the fundamental difference between these two mixtures, is the roll-up of the slip line in the forward jet. Hydrogen-oxygen (as seen in picture a) has a slip line that does not appear to produce a predominant forward jet. On the other hand, methane-oxygen (as seen in picture b) shows a slip line which displays a prominent forward jet causing what appears to be two re-circulation zones behind the Mach stem. His other results showed that, in hydrogen-oxygen, a limited number of hot spot and Mach reflections are generated (mostly near the obstacle field), and they fail to recreate additional Mach reflections and hot spots in the far field. The methane-oxygen showed a continuous generation of hot spots, in the near field and the far field. Maley suggested that the low specific heat ratio (γ) in methane-oxygen was the main reason

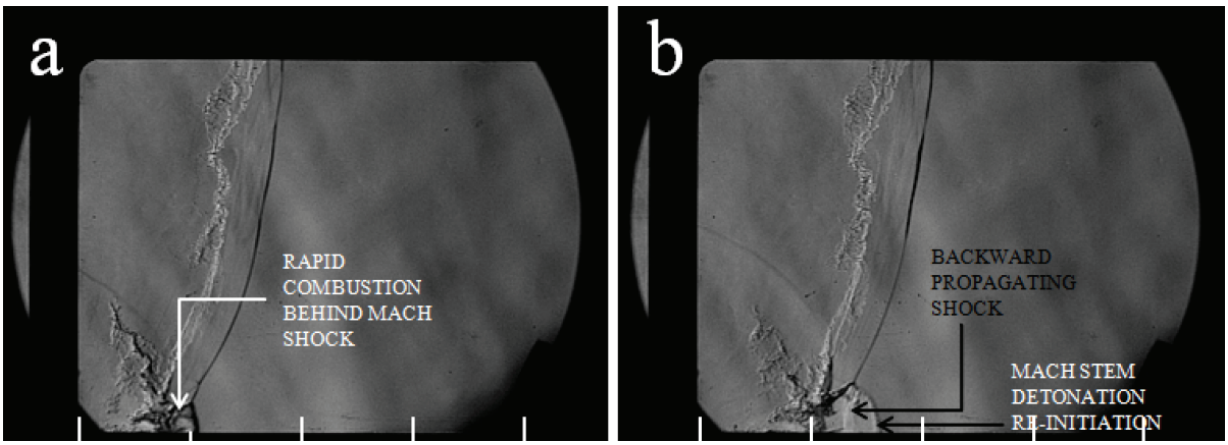


Figure 1.5: Two sequential schlieren images of an experiment conducted at p_0=10.5 kPa in methane-oxygen. The images shows the hot spot ignition and the re-initiation event behind the Mach stem.

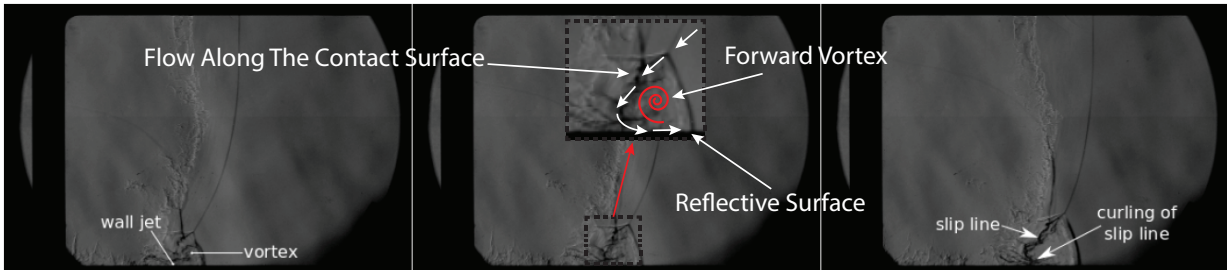


Figure 1.6: Schlieren images of an experiment conducted in methane-oxygen mixture at p_0= 10.1 kPa, showing the forward vortex process. Adopted from [4]

for the predominant forward jets. His results pointed that the specific heat ratio of the hydrogen-oxygen mixture ($\gamma = 1.36$) is higher than that of the methane-oxygen mixture ($\gamma = 1.22$).

Other studies conducted by Chao[6] and Grondin and Lee [20] pointed that in unstable mixtures, where the reaction rates are very sensitive to temperature fluctuations, the initial perturbations generated after the interaction with the obstacles (perforated plate in their case) were maintained downstream. In stable mixtures, these perturbations could not be sustained, and the high-speed deflagrations decayed to sub-critical velocities, with a flat shock leading in front of a trailing flame. Figure 1.9 shows an example of a stable and unstable mixture after they get diffracted over a perforated plate. The experiment

performed with unstable gas on the left (propane-oxygen), showed a chaotic shock-flame complex, that was maintained to the end of the channel. The stable gas on the right (acetylene-oxygen diluted with argon) showed how the initial perturbations generated by the plate were not maintained, with the flames seen decoupling from the front shock as they propagated toward the end of the channel.

Unstable mixtures are mixtures with irregular detonation cell size. Stable mixtures are mixtures with fine and regular detonation cell size. Figure 1.10 shows an example of both cases. On the top, the schlieren picture to the left demonstrated how unstable mixtures have a chaotic shock-flame complex. The soot foil imprint to the right showed how they have irregular cell patterns. Conversely, the stable mixture on the bottom showed a fine shock-flame complex with regular cell pattern, as seen in the soot foil imprint.

Kuznetsov et. al. [22] also showed that the critical conditions for DDT were strongly influenced by the regularity of the detonation cellular structure. Their results concluded that systems with highly regular detonation structures are less capable of undergoing DDT when compared to irregular ones with the same values of detonation cell size. In summary, there are strong indications that DDT is favoured in mixtures with more sensitive chemical kinetic rates to temperature fluctuations.

Recently, Radulescu et al.[39], proposed a non-dimensional parameter to characterize the propensity for hot spot ignition and the regularity of detonations in reactive mixtures, given by

$$\chi = \frac{E_a}{RT}\frac{t_{ig}}{t_r} \tag{1.1}$$

where Ea/RT is the reduced activation energy, t_{ig} is the ignition delay time and t_r is the reaction time. This parameter was suggested to control fast flame's acceleration in 1-D, detonation stability, and the propensity for hot spot formation in the presence of temperature fluctuations [38, 39, 46].

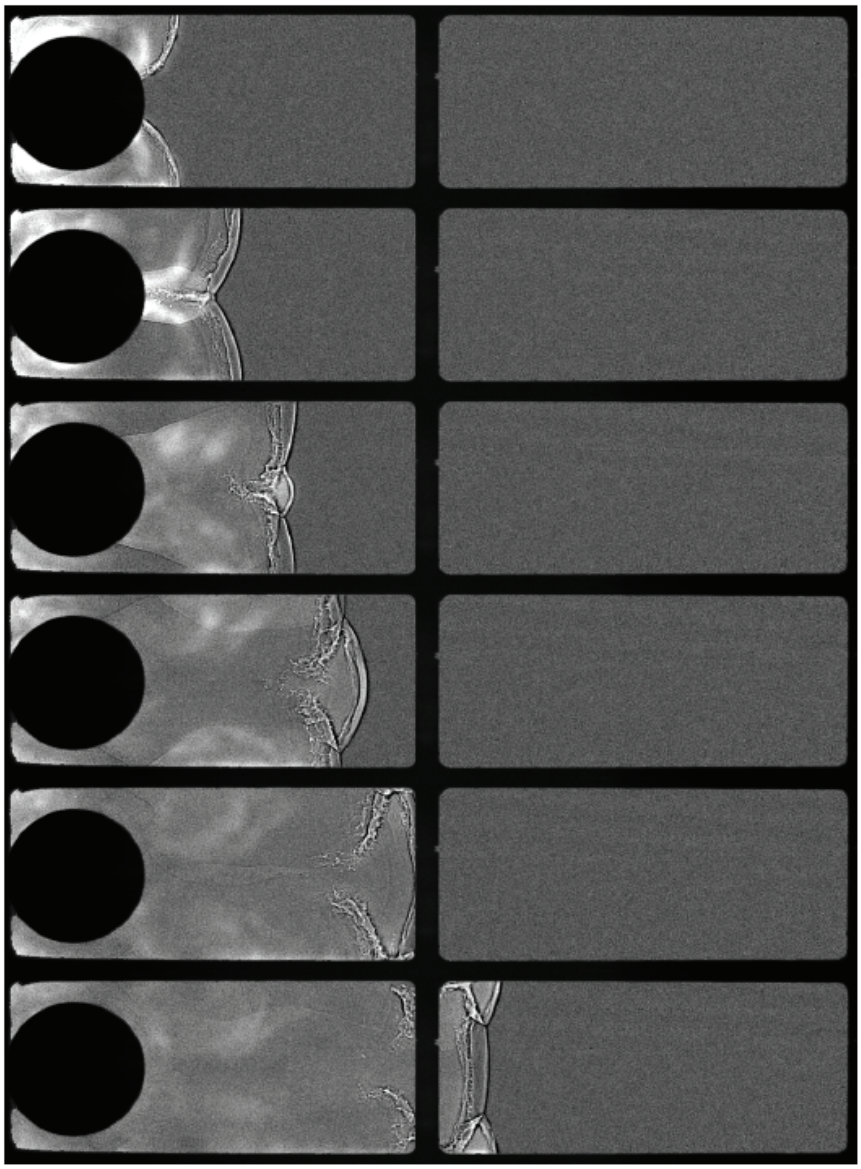


Figure 1.7: Shadowgraph records of a methane-oxygen experiment showing hot spot ignition behind the Mach stem, p_0= 8.5 kPa. From [30].

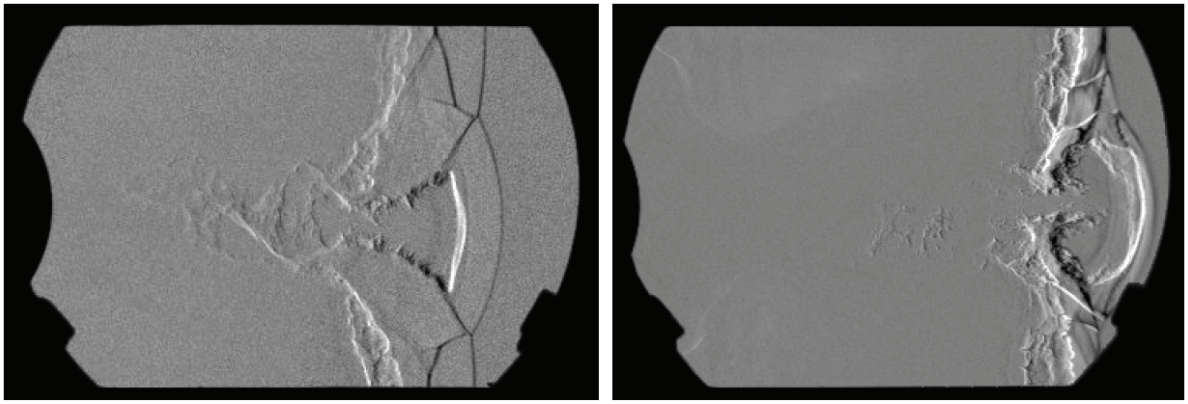


Figure 1.8: A comparison of reflection behavior between (a) hydrogen-oxygen at p_0=11.0 kPa, and (b) methane-oxygen at p_0=8.3 kPa, from [30].

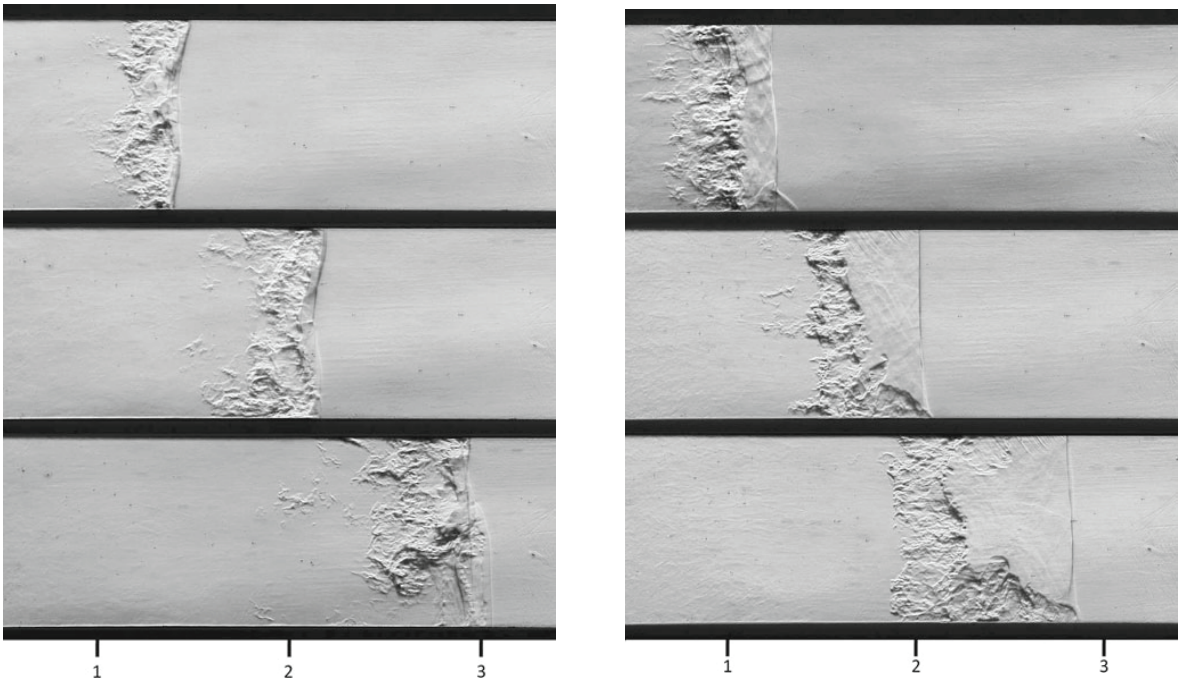


Figure 1.9: Comparison of fast flames in (a) unstable and (b) stable mixtures adopted from [20]. (a) The structure of a C_3H_8+$5O_2$ fast metastable combustion wave generated downstream of a perforated plate, p_0=4.0 kPa. (b) The structure of a high-speed deflagration that fails to transit back to a detonation, $2C_2H_2$+$5O_2$+70%Ar, p_0=12.0 kPa. The distances are normalized by the channel width.

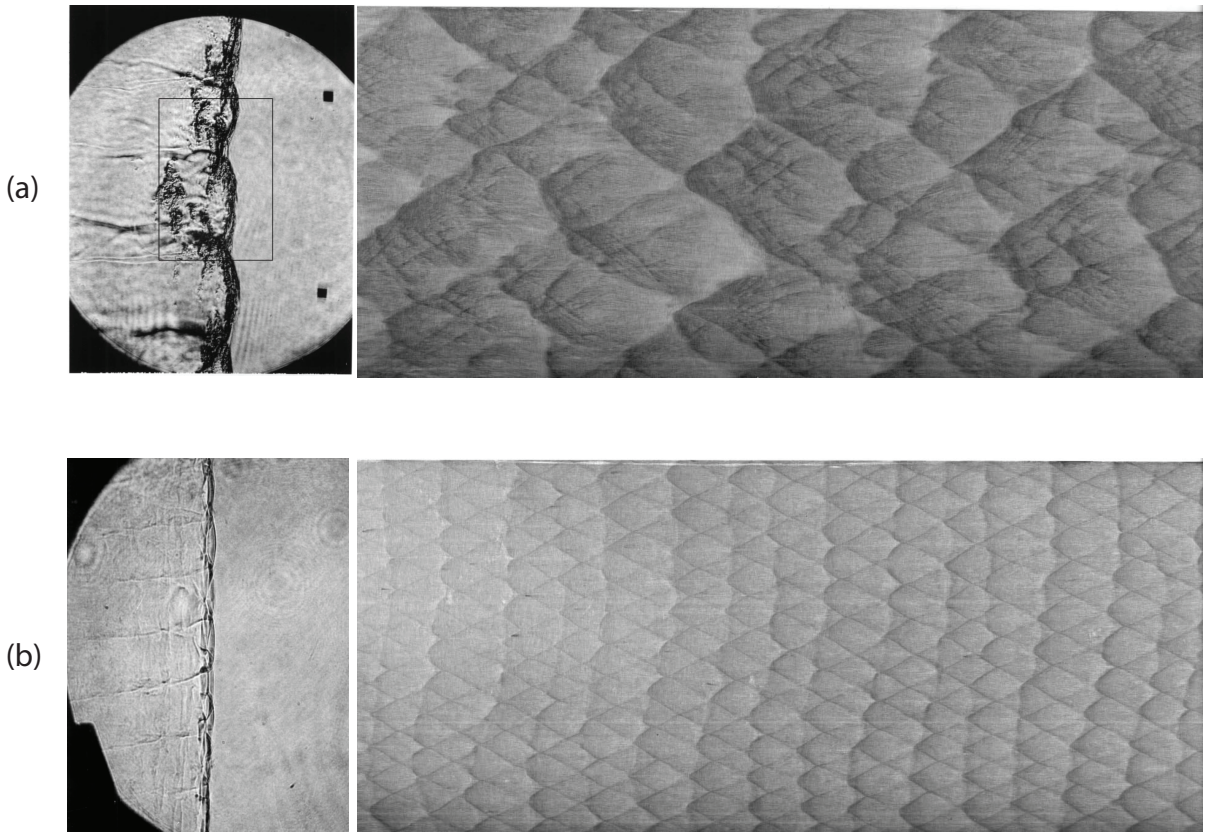


Figure 1.10: Comparison between stable and unstable detonation cellular structures. The schlieren photographs are on the left, and sample of soot foils to the right. (a) irregular structure in C3H8-5O2-9N2, p_0=20 kPa. Detonation propagated from left to right and foils were mounted downstream of the window section of the narrow channel. (b) regular cellular structure in $2H_2$-O_2-7Ar, p_0=20 kPa. The figures are from [1].

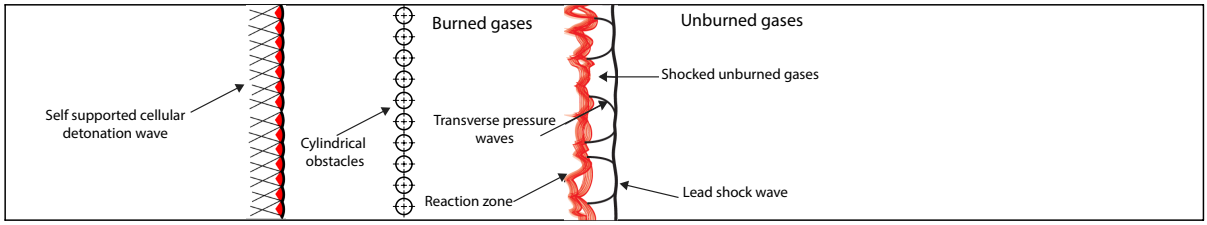


Figure 1.11: A schematic diagram showing a cellular detonation wave passing through a cylindrical obstacles to form de-coupled shock-flame complex

1.3 Current Study

The current study extends the previous work done by Maley [30] and Bhattacharjee [4], and focuses on quantifying DDT by measuring the run-up distance to detonation in mixtures with different thermo-chemical properties. This will be done in order to generate a correlation between the run-up distance and other characteristic length scales representative of the mixture sensitivity, such as the detonation cell size, and the chemical induction and reaction length scales obtained from chemical kinetic calculations. The same technique of creating high-speed deflagrations as previous work was adopted [6, 30, 20, 4], whereby an incident detonation impinging on a series of obstacles gives rise to a fast flame, which subsequently accelerates to a detonation.

The experiments were conducted for mixtures with different thermo-chemical properties, namely methane, ethane, ethylene, propane and acetylene diluted with 75% argon, with oxygen as oxidizer. The use of mixtures with different thermochemical properties will enable us to correlate the run-up distance and verify whether the χ parameter controls the propensity for DDT, as suggested previously by Radulescu.

The present thesis is organized as follows. Chapter 2 presents a brief summary of the necessary theoretical concepts for the non-specialist. Chapter 3 presents the experimental setup and the procedure used for conducting the tests. Chapter 4 reports the results of the experiments. This is followed by a general discussion of the results in Chapter 5, and the generation of various correlations of the experimental data. The conclusion of the thesis is in Chapter 6, where a brief summary of the main findings is reported and recommendations

are made for further research.

Chapter 2

Review of Relevant Theoretical Concepts

2.1 Chapman-Jouguet Theory

Chapman-Jouguet theory is a quantitative theory that predicts the detonation and deflagration velocity in a given mixture from thermodynamic arguments. The theory was formulated by Chapman (1889) and Jouguet (1904–1905). The theory is widely known and available in most combustion textbooks [25].

The theory does not consider the structure of the reaction wave. Instead, the conservation laws are applied for a control volume traveling with the wave, which is essentially assumed to be a discontinuity. Figure 2.1 illustrates the analysis. If subscript (0) denotes the fresh mixture and subscript (1) denotes the burned gases, then the conservation of mass and momentum yield, respectively,

$$\rho_0 u_0 = \rho_1 u_1 \tag{2.1}$$

and

$$p_0 + \rho_0 u^2 = p_1 + \rho_1 u^2 \tag{2.2}$$

If we separate the enthalpy into sensible and formation enthalpy, the conservation of energy

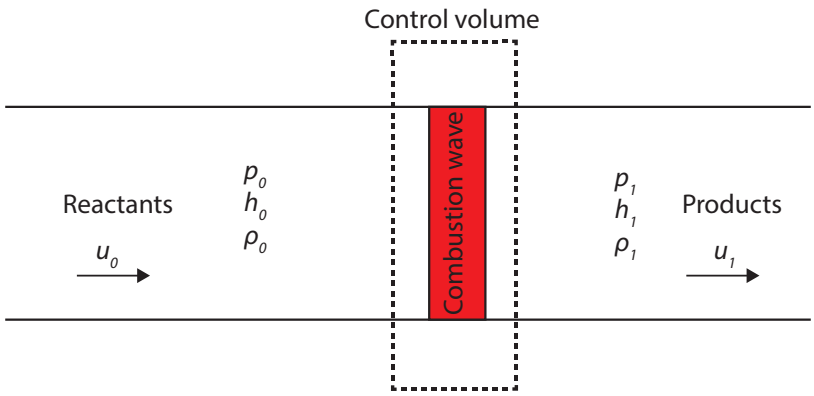


Figure 2.1: A sketch depicting a control volume over a combustion wave in a frame of reference attached to the wave.

can be written as:

$$h_{s0} + q + \frac{1}{2}u_0^2 = h_{s1} + \frac{1}{2}u_1^2 \tag{2.3}$$

where (q) is the difference between the enthalpy of formation for reactants and products.

Although the theory can be applied for any multi-component reactive system in chemical equilibrium with arbitrary equation of state, the main results can be illustrated for a perfect gas

$$p = \rho R_s T \tag{2.4}$$

and having constant specific heats, such that

$$h = c_p T = \frac{\gamma}{\gamma - 1}\frac{p}{\rho} \tag{2.5}$$

where γ is the ratio of specific heats. If the initial states (p_0, ρ_0, h_0) are specified, we have four equations (2.1), (2.2), (2.3), (2.5) and five unknowns (p_1, ρ_1, h_1, u_0, u_1). An additional equation is required to close the set of the equations, which is the so-called sonic criterion or Chapman-Jouguet condition, which requires that the flow in the products be sonic:

$$u_1 = c_1 \tag{2.6}$$

as described below.

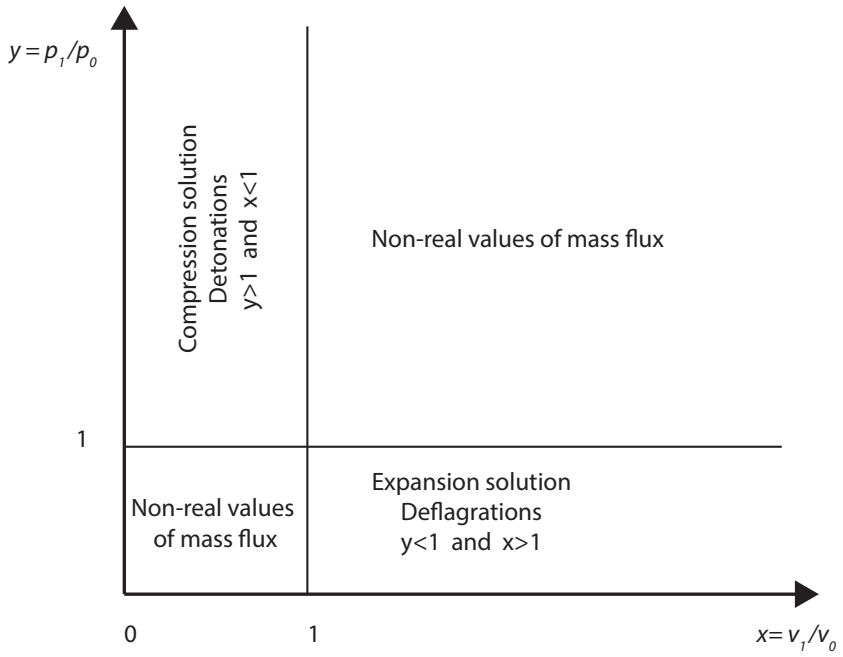


Figure 2.2: Domains of detonation and deflagration solutions in the pv plane

From equations (2.1) and (2.2) we can obtain the mass flux per unit area, which has the following form:

$$\frac{p_1 - p_0}{v_0 - v_1} = \rho_0^2 u_0^2 = \rho_1^2 u_1^2 = \dot{m}^2 \tag{2.7}$$

where $v = 1/\rho$ is the specific volume and $\dot{m} = \rho u$ is the mass flux per unit area. In order for the mass flux $\dot{m}$ to be real, we will have two possible solutions. A compression wave requires that

$$v_0 > v_1$$

$$p_1 > p_0$$

while an expansion wave requires

$$v_0 < v_1$$

$$p_1 < p_0$$

If we let $y = p_1/p_0$ and $x = v_1/v_0$, we can represent the possible solutions in a $p - v$ (or $y - x$) diagram as seen in Figure 2.2.

Now we can write (2.7) as the following:

$$\dot{m} = \sqrt{\frac{(y-1)}{(1-x)}\frac{p_0}{v_0}} \tag{2.8}$$

From the definition of the speed of sound in the upstream flow $c_0^2 = \gamma_0 \frac{p_0}{\rho_0}$, and the Mach number $M_0 = u_0/c_0$, equation (2.8) takes the form:

$$y = (1 + \gamma_0 M_0^2) - (\gamma_0 M_0^2))x \tag{2.9}$$

The above equation (2.9) is known as the Rayleigh line equation, and it is the thermodynamic path along which the initial state proceeds to the final state, across the combustion wave.

By eliminating the velocities using equation (2.7), the energy equation (2.3) could be re-written as the following :

$$h_1 - (h_0 + q) = \frac{1}{2}(p_1 - p_0)(v_0 - v_1) \tag{2.10}$$

The above equation is called the Hugoniot curve equation. The Hugoniot curve represents all the possible solutions for the downstream state of a combustion wave, for a given upstream state. The transition from reactant to products must follow the Rayleigh line from the initial state to the final state, where it intersects with the Hugoniot curve. Several possible solutions (for the compression and the expansion case) could be found, but for the CJ solution, the Hugoniot curve and the Rayleigh line will be tangent in two points, giving the CJ points for detonation and deflagration. Figure 2.3 shows how the Rayleigh line is tangent at one point on the upper branch of the Hugoniot curve, and another point in the lower branch of the Hugoniot curve. The first upper branch point is called CJ detonation, and it is the minimum speed possible for detonation solutions. The lower point is referred to as a CJ deflagration, and it is the maximum velocity possible for deflagrations. These tangent points also correspond to the condition of sonic flow relative to the wave, known as the CJ conditions.

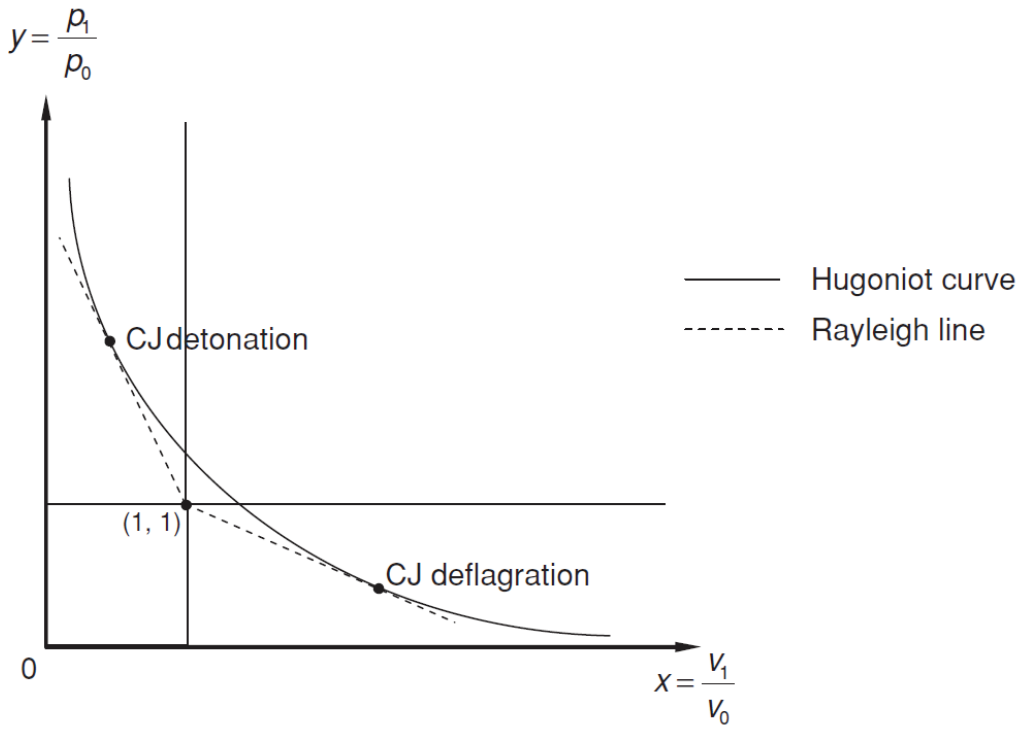


Figure 2.3: A sketch showing the tangency of CJ solution for deflagration and detonation. From [25]

2.2 Deflagrations as Gasdynamic Discontinuities

2.2.1 CJ Deflagrations in Tubes with a Closed End Wall

Solutions on the lower deflagration branch of the Hugoniot curve have not received as much attention as those on the upper detonation branch, due to the conception that they lack a practical reason to consider them. Deflagration wave speeds are governed by mass and heat diffusion rates, yielding propagation speeds of laminar flames two orders of magnitude lower than predicted for CJ deflagrations. However, as discussed in the introduction, experimental evidence suggests that CJ deflagrations are possible provided that sufficiently intense turbulence is present. In order to account for the experimental observations of fast flame propagation, Chue et al.[8] suggested a gasdynamic model where the fast flame consists of two discontinuities: a shock followed by a de-coupled CJ deflagration. This treatment was consistent with the experimental observations of Dupre et al.[17], that these fast flames consisted of a leading shock followed by a reaction zone.

Figure 2.4 illustrates the model of Chue et al. The figure shows three regions: the upstream region, shocked gases region, and burned gases region. In the upstream region, the gas is stationary so the initial velocity (u_0) in the laboratory frame vanishes. The velocity behind the flame in the lab frame (u_1) also vanishes in order to satisfy the end tube boundary condition. Since the deflagration propagates at the sound speed with respect to the burned gas, it is assumed to be a CJ deflagration. Figure 2.4 shows an $x-t$ diagram for the model. If we consider the initial velocity (u_0) of the reactants to be zero, then the displacement effect of the deflagration reaction zone is equivalent to that of a piston generating a shock wave ahead of the reaction front. The particle velocity (u_*) behind the shock is such that the expansion across the reaction zone gives zero particle velocity (u_1) behind it to match the closed wall boundary condition.

If we consider the reaction zone as a CJ deflagration, then the sonic condition behind the deflagration provides an extra equation for closing the set of conservation equations across the deflagration. The precursor shock strength is then determined to satisfy the conservation equations across the shock and the reaction front.

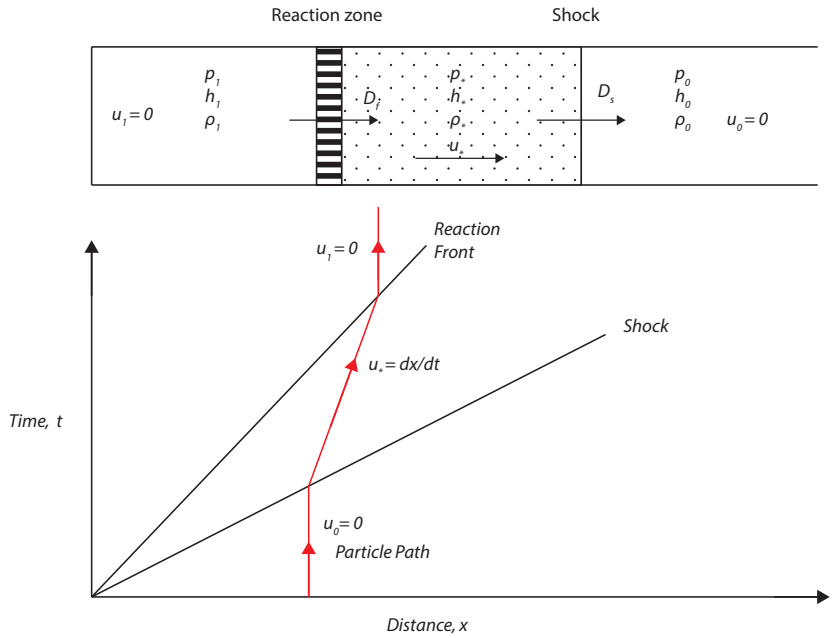


Figure 2.4: Schematic of the one dimensional deflagration model.

The analytical solution obtained by Chue et al. predicts that the shock and flame discontinuities propagate at slightly different speeds in the lab frame, close to one-half the propagation velocity of a CJ detonation in the same fresh mixture. The model was found in general good agreement with experiment.

2.2.2 Gasdynamic Model for the Current Problem

A similar gasdynamic model was recently proposed by Radulescu et al.[37] for the problem considered in the present thesis. The main modification to the theory of Chue et al. is the matching of the double discontinuity fast flame with the flow across the row of cylinders, since the deflagration is supported by this flow. Figures 2.5 and 2.6 illustrate this gasdynamic model. In Figure 2.6, an incident detonation wave (I) is interacting with the obstacles. The state of the unburned reactive mixture before that shock is the initial condition, referred to as state (0). The state after the detonation is denoted as state (1). Subsequent to the interaction, two shocks are assumed to rise, a reflected shock (R) (propagating to the left), and a transmitted shock (T) (propagating to the right). The state of gases behind these two shocks are defined as state (2) and (6) respectively. As time progresses, the burned products expand as they pass over the obstacles as in a converging-diverging nozzle. Thus state (3) is the state of these gas products expanding isentropically across the obstacles. Results obtained from a similar experimental setup conducted by Maley, as seen in Figure 1.2, showed that the expansion of the products across the obstacles is accompanied by a series of shock diamonds. These shocks are modeled as an auxiliary shock (A). Finally, the mixing layer separating the gases initially on the left and on the right of the cylindrical obstacles is modeled as a contact surface. The fast flame is modeled by a lead shock (T) and flame (F) following the treatment of Chue et al. described above. The matching of the product expansion problem and fast flame problem is at the contact surface (C) separating states (4) and (5), where pressure and flow velocity are matched. To simplify the calculations, constant specific heat ratios γ are assumed for the non-reacted and reacted gases respectively. The flow from state (2) to state (3) is assumed to be isentropic nozzle flow, and the various shocks obey the usual shock jump relations. The jump conditions across the flame obey the usual Hugoniot jump conditions using equations (2.10) and (2.9) for CJ deflagration solution. Figure 2.7 shows the prediction of the model for the speed of the transmitted shock as a function of the blockage ratio. The curve labeled "inert" corresponds to the assumption of no heat release across the flame, i.e., quenched reactions. The model predicts a significant drop in the

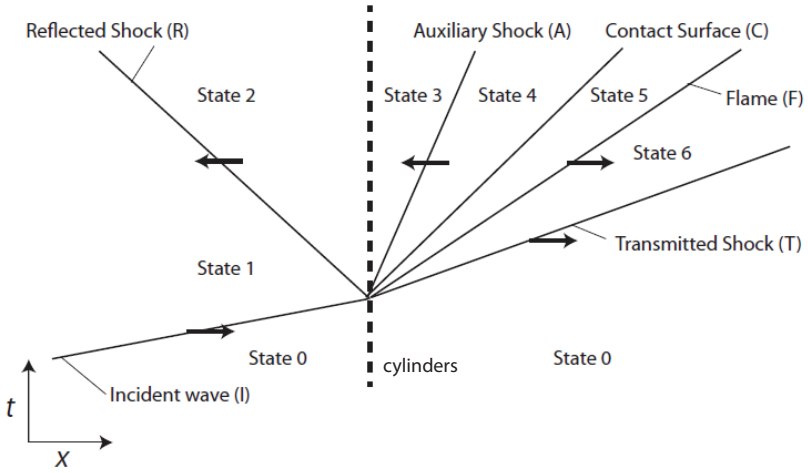


Figure 2.5: An x t diagram, showing the gas dynamic model used for predicting CJ deflagration and inert shock speeds. From [37].

transmitted shock-fast flame complex speed with increasing blockage ratio, which is due primarily to a drop of the speed of the contact surface.

2.3 Ignition Time Scales Behind a Leading Shock

In general, if we consider an ignition process via shock compression, the lead shock will first heat the reactants to sufficiently high temperatures. This is followed by an induction zone where active radicals are generated. When sufficient concentrations of radicals are produced, the reaction zone starts, converting reactants into products, with the heat release characterized by a rise in the temperature. The induction zone is almost thermally neutral, with the thermodynamic state of the shock-heated mixture remaining nearly constant. For this reason, the assumption of either constant volume or constant pressure can be made to calculate the ignition time history.

In order to obtain the time scale of the induction and reaction zone, let us consider the above example, of a shock passing through a reactive mixture. As seen in Figure 2.8, the ignition delay time (t_{ig}) will be the time to maximum change of temperature, $(dT/dt)_{max}$, while, the time of energy deposition (t_r), or reaction time is $((\frac{1}{T})(\frac{dT}{dt})_{max})^{-1}$. One can find these variables by using the CEA NASA [19] package to find the post-shock conditions

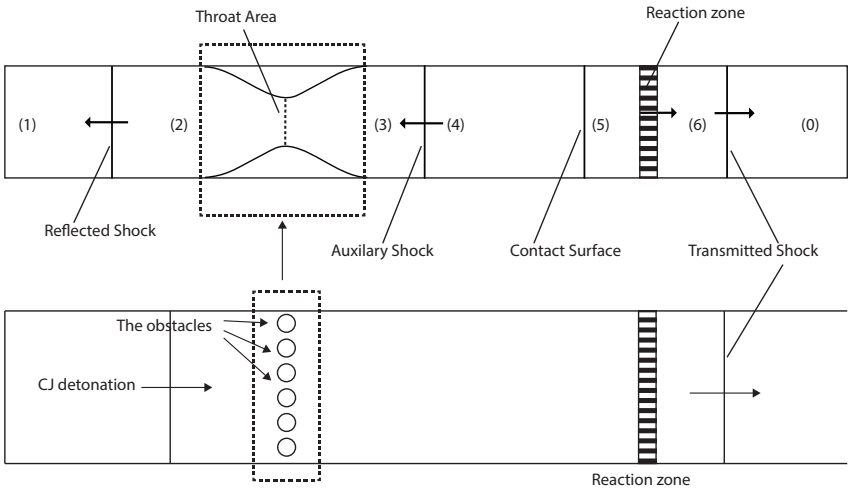


Figure 2.6: A sketch showing the states from Figure 2.5, and the location of the shocks.

(Von-Neumann conditions) given a particular shock speed, and then use the results in CANTERA [18], by conducting constant volume homogeneous reactor calculations.

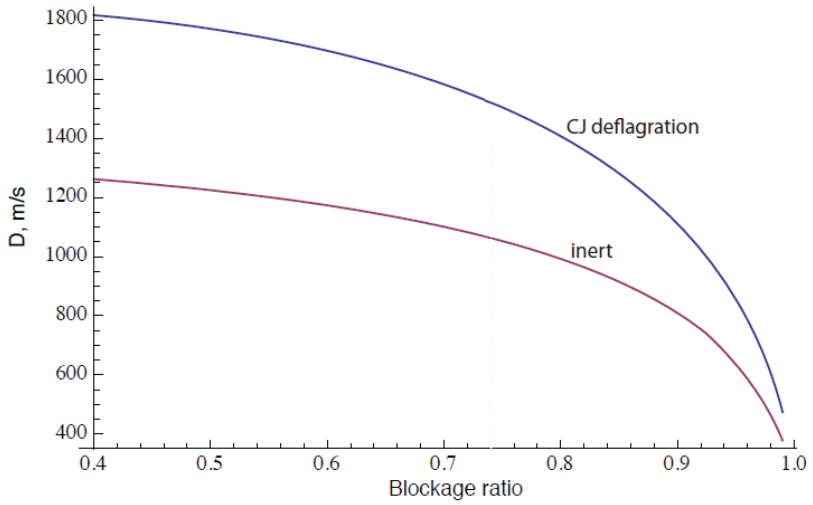


Figure 2.7: Predicted transmitted shock speed for the reactive case assuming a CJ deflagration or inert shock as a function of the obstacle blockage ratio for $p_0 = 7.2$ kPa. From [37].

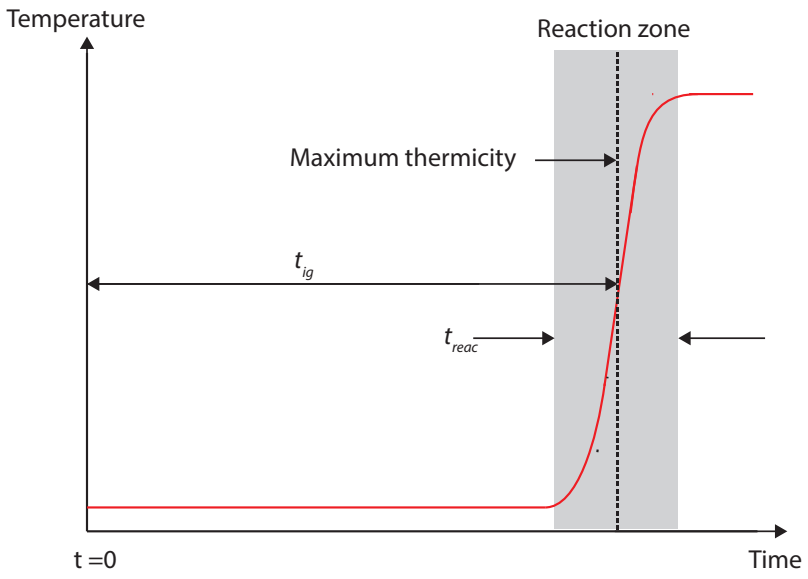


Figure 2.8: A schematic showing the ignition delay and reaction time scales behind a leading shock.

2.4 χ Parameter

As discussed in the introduction, the χ parameter was proposed as an indicator of the propensity for hot spot formation in a reactive mixture, and is further used in the present thesis for generating correlations for the DDT length. This parameter was calculated at the thermodynamic state behind the incident shock. The velocity of the deflagration precursor incident shock was estimated using the self-similar gas dynamic model, explained in section 2.2.2. The ignition delay time (t_{ig}), and reaction time (t_r) were calculated as previously explained in section 2.3. As for the activation energy, it is known that the ignition delay time (t_{ig}) usually follows an Arrhenius law of the form ($t_{ig} \sim exp(\frac{E_a}{RT})$)[25]. One can calculate the activation energy by perturbing the temperature (T) by a small value (we used 5% temperature perturbation in our calculations) and determine the change in ignition delay (t_{ig}) to get $\frac{E_a}{R}$.

Chapter 3

Experimental Setup

This chapter provides the details of the experimental setup and procedure for conducting the experiments.

3.1 Physical Apparatus

All the experiments were conducted in a thin rectangular channel, 3.4-m-long , 203-mm tall, and 19-mm-wide, as described by Maley et al. [30], and shown schematically in Figure 3.1. The first 70 cm of the channel was equipped with wire mesh obstacles to ensure that the detonation was properly initiated (see [4] for more details). The last meter of the channel was equipped with glass windows, allowing for visualization of the flow.

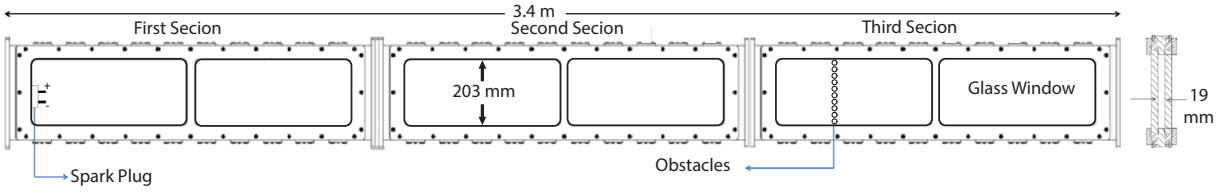


Figure 3.1: Schematic of shock tube apparatus. Adapted from [30].

Table 3.1: The parameters used in the 75% and 90% blockage ratio configurations, as seen in Figure 3.2.

Parameters	**75% Blockage Ratio Configuration**	**90% Blockage Ratio Configuration**
a	1.13 m	1.13 m
b	0.0203 m	0.0203 m
c	0.376 m	0.1 m
d	0.0153 m	0.0153 m
e	0.0025 m	0.0084 m
f	0.005 m	0.00167 m
Number of obstacles	10	12

3.2 Obstacle Configurations

A row of cylindrical obstacles made of aluminum, with 15.3 mm diameter, were placed at the entrance of the last section of the channel of the shock-tube to establish fast-flames downstream. Two configurations were used. The first configuration consisted of 10 cylinders with a ($f = 0.005$ m) gap between each cylinder, corresponding to 75% blockage ratio (BR). Figure 3.2 and Table 3.1 provides the set-up and the dimensions used. The obstacles were placed at ($c = 0.0376$ m) distance from the left corner of the viewing section.

The second configuration consisted of 12 cylinders with a ($f = 0.00167$ m) gap between each cylinder, corresponding to 90% blockage ratio (BR). Figure 3.2 and table 3.1 illustrates the set-up and the dimensions used. The obstacles were placed closer to the corner of the viewing section, at a distance ($c = 0.1$ m), to allow for a wider viewing area of the fast flame's dynamics.

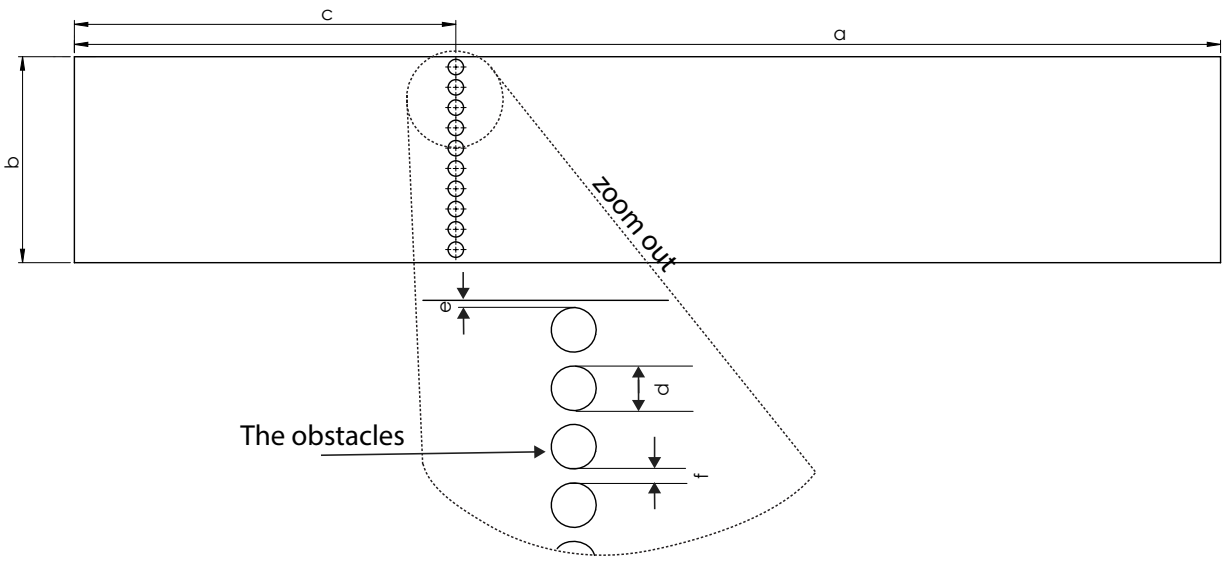


Figure 3.2: Schematic of the obstacle configuration and the dimensions of the viewing section, with the length of the viewing section: a, the hight of the viewing section: b, the location of the obstacles from the left corner of the viewing section: c, the diameter of the obstacles d, the gap between the first obstacle and the top walls: e, the gap between the obstacles f.

3.3 Flow Visualization

The optical system used was a large-scale Edgerton shadowgraph system [21]. An illustration of the system setup can be seen in Figure 3.3. A 2-m by 2-m retro-reflective screen was placed at (x/y=0.5) to obtain the clearest images. The light exiting from the arc lamp was condensed to a 3-5 mm point using a 50 mm glass lens. This point was focused onto a 10 mm diameter cylindrical rod mirror cut at a 45 angle which was glued to a clear lens. The condensed light was then projected by the mirror onto the experimental field. The light casts a shadow of the experimental field on the retro-reflective screen at the back. The camera then records the casted shadows from that screen. Figure 3.4 shows how they are set up.

The light source was manufactured by Newport and used a 1600 W Xenon lamp. The video camera used was a high-speed Phantom v1210 made by Vision Research. The camera

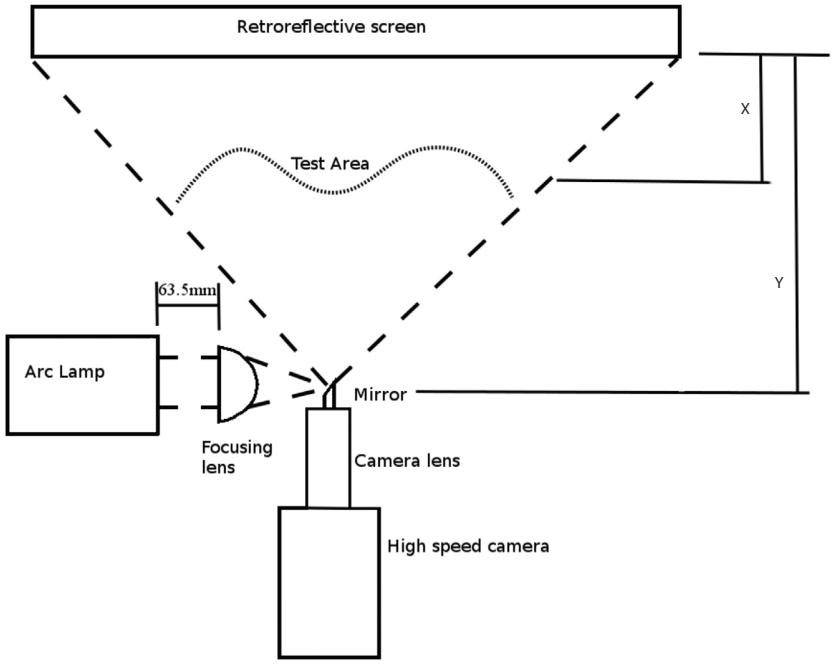


Figure 3.3: Top-view illustration of the retro-reflective shadowgraph system [12].

recorded high speed videos at 42,049 fps (interframe time of 23.8 μsec), using 1152 x 256 pixels resolution, corresponding to a spatial resolution of approximately 1 mm.

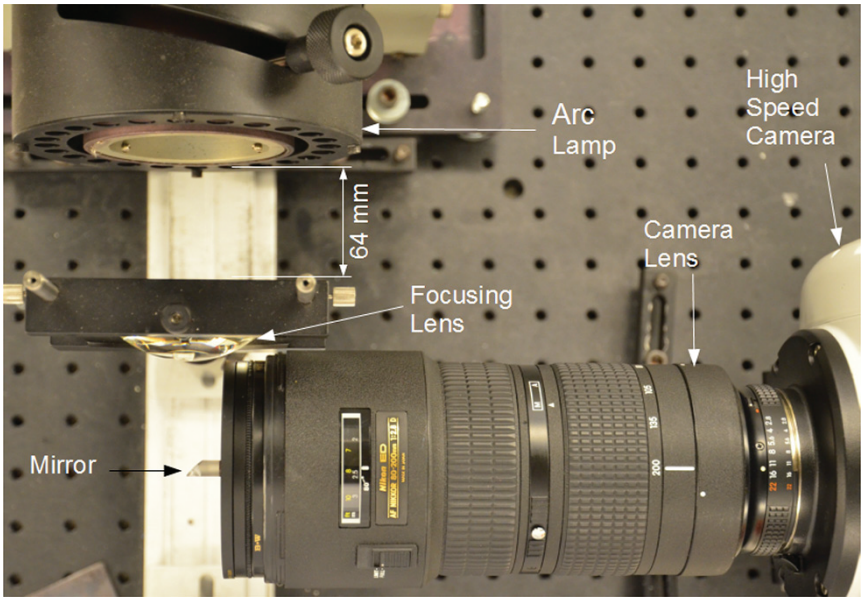


Figure 3.4: Top-view picture of the optical components in the shadowgraphy system [12].

3.4 Experimental Procedure

The mixtures studied were stoichiometric methane, propane, ethane, ethylene, and acetylene with oxygen. The acetylene mixture was diluted with 75% argon per mole, and offered a mixture with a much lower propensity for hot spot formation, as indicated by its low value of χ, as described in Chapter 1.

The gases were mixed in a separate vessel by the method of partial pressures and left to mix for a minimum of 24 hours before an experiment. Varying the initial pressure p_0 of the test mixture permitted us to control the reactivity of the mixture.

For each experiment conducted, the channel was evacuated to below 80 Pa absolute pressure, before filling it with the test mixture, up to the desired pressure. The mixture was then ignited using a high voltage igniter (HVI) that discharges 1000 J within 2 μs from a spark plug mounted at the corner of the first channel. Information about the HVI system was discussed in details elsewhere [30, 4].

In some cases the initial pressure of the mixture was too low to initiate a detonation with the igniter. For these tests, a driver was used to initiate the detonation wave instead. Before the start of each test, a diaphragm was installed between section one and section two of the shock tube, to separate the driver mixture from the test mixture. Afterward, section one was carefully filled with the driver mixture, up to a sufficient pressure. Careful considerations were taken in order not to damage the diaphragm before the test. Section two and three were filled with the desired test gas using the second gas port, up to the desired pressure intended for the test. The detonation wave initiated at the driver section, propagated and ruptured the diaphragm and initiated a detonation at the test gas section. In our case, we used $C_2H_4+2O_2$ and $2C_2H_6+7O_2$ as driver mixtures. Appendix C shows the full list of experiments and drivers used.

3.5 Uncertainty of Velocity Measurements

To calculate the uncertainty of the velocity measurements from the high-speed shadowgraph videos, a standard error propagation method was used. The uncertainty of velocity measurements (δV) was calculated using the uncertainty in time and the uncertainty in distance.

The time uncertainty in our setup was defined as the exposure time of the high-speed camera (t_{exp}) over the time difference between two sequential frames (inter-frame time of the video) (Δt). These values were obtained for each video from the camera setup and recorded for each experiment.

The distance uncertainty was the uncertainty of the shock location, which is limited by the spatial resolution of the camera (x_{pix}). These values were obtained by placing a known distance (a metallic strip with a known length) in the channel, and measure that length of that strip using the camera, in pixels units. The pixels were then converted to SI units from the length of the placed metallic strip.

The uncertainty in the velocity is then calculated from the above uncertainties from

$$\delta V = V((\frac{t_{exp}}{\Delta t})^2 + (\frac{x_{pix}}{\Delta x})^2)^{1/2} \tag{3.1}$$

Chapter 4

Experimental Results

In this chapter, the results of the experiments conducted at 75% and 90% blockage ratio configuration are reported. Five sections detailing the results of the reactive mixtures were addressed: methane-oxygen, ethane-oxygen, ethylene-oxygen, acetylene-oxygen diluted with 75% argon. For each section, selected frames obtained from the videos obtained with the shadowgraph system are shown. These images gave an insight of the flame-shock dynamics before and after interacting with the obstacles. The full set of frames for the selected tests are reported in Appendix A and B. Additional graphs show the history of lead shock velocity for all the tests performed.

4.1 Methane

4.1.1 Methane with 75% Blockage Ratio

Figure 4.1 shows shadowgraph images of a typical test, here in stoichiometric methane-oxygen at p_0= 10.3 kPa initial pressure. Frame 5 shows a propagating CJ detonation wave coming from the left to the right. Frame 8 shows the interaction of the CJ detonation wave with the obstacles. A complex of shock waves are reflected from the obstacles and transmitted across, as seen in frame 9. The enlarged frames in Figure 4.2 show how these transmitted shocks look very similar to the shocks obtained by Maley in five obstacles

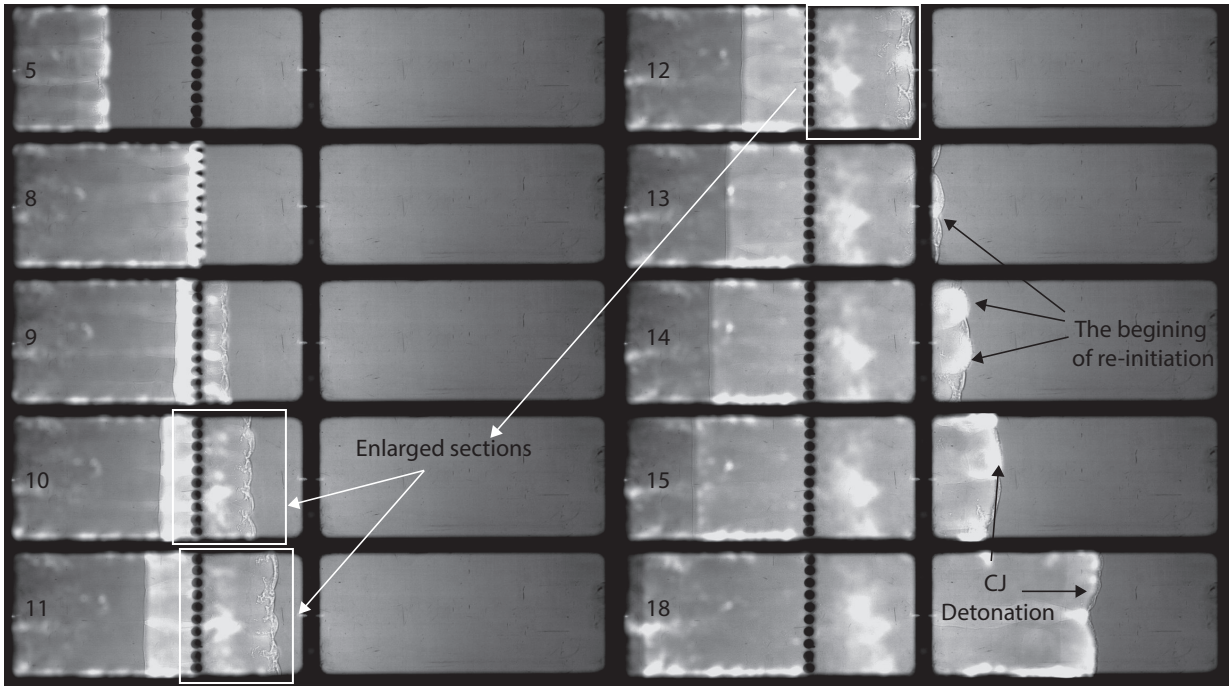


Figure 4.1: Selected Shadowgraph images illustrating the re-initiation of detonation in CH_4+2O_2, p_0=10.3 kPa. Recorded at 23.76 μs interframe, 1 μs exposure, 42049 fps. The full record can be found in A.1, A.2, and A.3

experiments, as discussed in the introduction [30, 29]. Frames 10, 11, and 12 from Figure 4.2 show distinct re-ignition regions behind the lead shock, as described by Maley et al. [30, 29]. These frames also show how the lead shock and the flames organize into a corrugated shock-flame complex. In Figure 4.1, frames number 13, 14, 15 and 18 show various hotspot ignition points with high luminosity. These hotspots cause a re-initiation to detonation that engulfs the whole front.

Figures 4.3 and 4.4 show the results of a test conducted at a lower initial pressure of p_0= 8.2 kPa. Frames 4 to 10 display the same sequence of events as the previous test, with a detonation wave propagating from the left to the right and diffracting around the obstacles. By frame 16, the shock-shock reflections, seen in the previous frames, re-organize themselves into two Mach reflections. In the same frame, an ignition event occurred near the bottom wall. This re-ignition event causes the growth of a new Mach stem, as seen in frame 17 bottom side. Later frames, specifically 19, 20 and 21, show the propagation

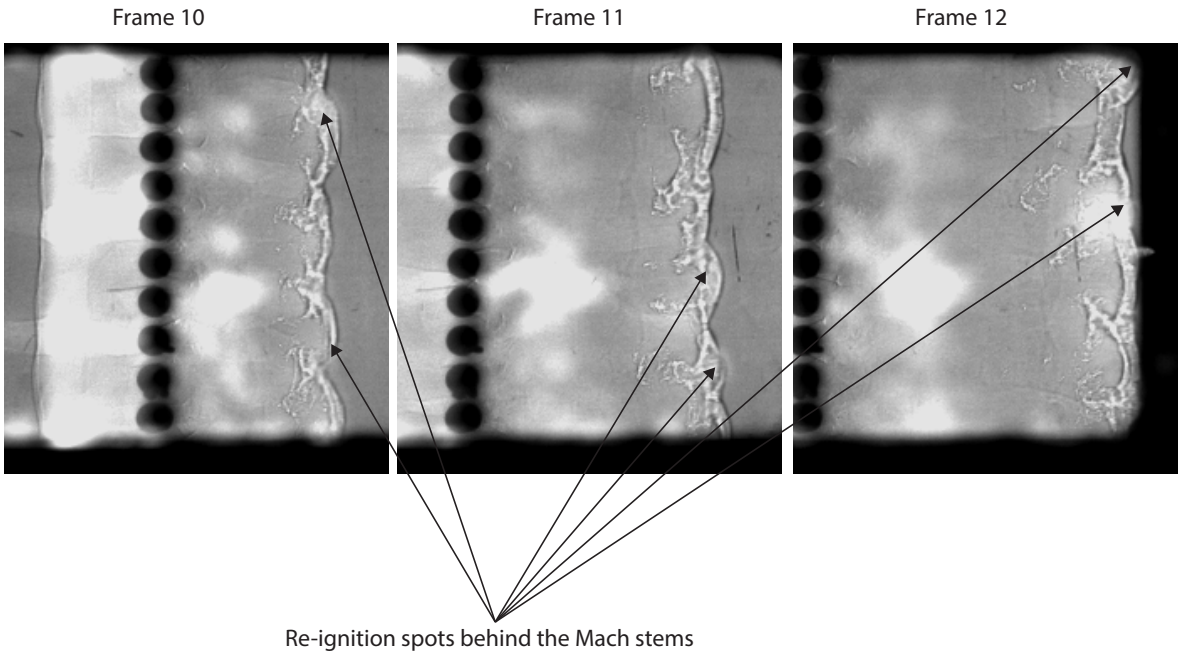


Figure 4.2: Enlarged frames from Figure 4.1.

of two Mach stems toward each other. Frames 22 to 24 show an ignition region generated behind the Mach stem caused by the burning of an un-reacted pocket of gas. That event causes the flame-shock to accelerate toward the right, but no re-initiation into a detonation is observed. As the wave reaches the end of the channel, the shock and the flames are seen closely coupled.

Lowering the initial pressure further to p_0= 3.4 kPa, the sensitivity of the mixture is reduced. Figure 4.5, shows the same propagation sequence of events for all frames from 6 to 15, with the detonation wave propagating from the left to the right and diffracting around the obstacles, and the subsequent generation of the corrugated shock-flame complex. Later frames show the flame-shock complex organizing into one Mach reflection, and an incident shock, as seen in frames 16 to 21. In frames 18 to 20, it can be seen that the induction zone is thicker behind the incident shock when compared to the induction zone behind the Mach stem.

Figure 4.7 shows the evolution of the lead shock speeds, recorded for all the tests performed in methane-oxygen mixtures, at initial pressures between p_0= 3.4 kPa to 11 kPa. For each test, the position of the lead shock was registered at five equally spaced

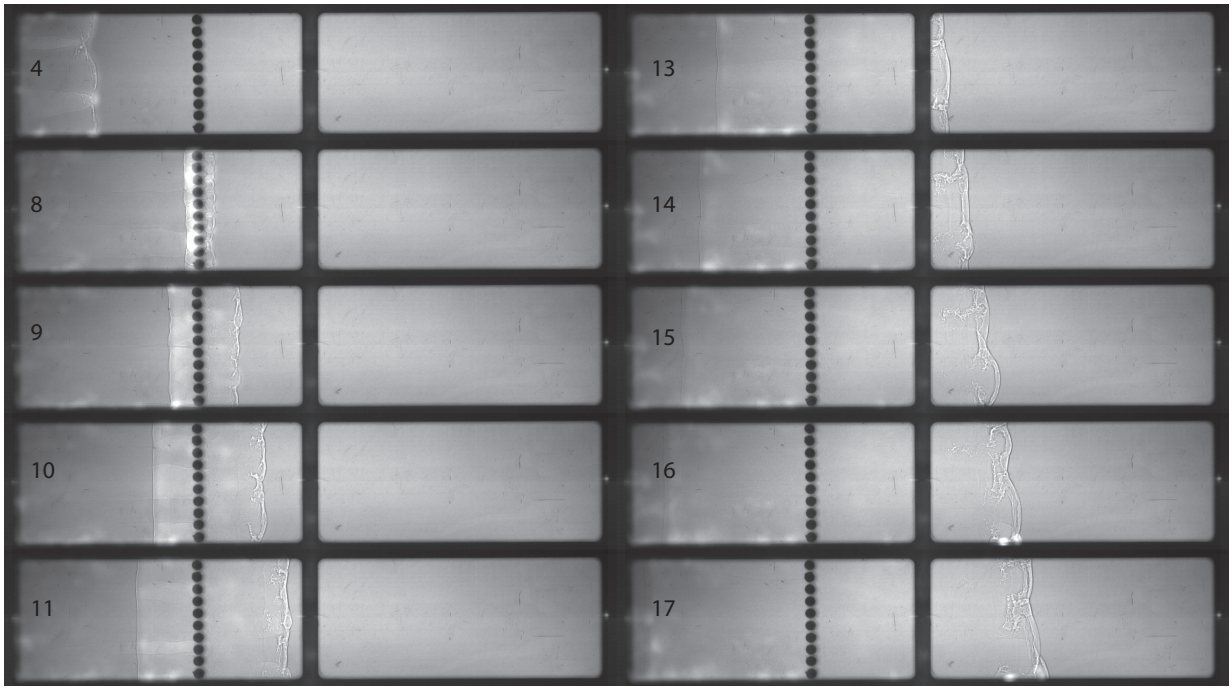


Figure 4.3: Selected Shadowgraph images illustrating the propagation of fast flames in CH_4+$2O_2$, p_0=8.2 kPa. Recorded at 23.76 μs interframe, 1 μs exposure, 42049 fps. The full record can be found in A.4, A.5, and A.6

locations along the shock, then averaged to obtain the mean position of the shock. The speed reported is thus an average value. The predicted CJ deflagration shock speeds and the inert shock speeds were obtained from the gas-dynamic model and evaluated for the highest and lowest pressure reported for each set of experiments. After the interaction with the obstacles, the shock-flame complex propagates at approximately 65% of the CJ detonation speed (1490-1510 m/s), in good agreement with the calculated CJ deflagration speed. For high initial pressure tests (9 kPa - 11 kPa), the fast flames subsequently accelerate to a detonation. It is interesting to notice that even for tests conducted at lower initial pressures (3.4 kPa - 8.2 kPa), the flame-shock complex maintained their speed above/equal to the theoretical CJ deflagration speed of 1600 m/s. The distance traveled by the fast flames from the obstacles to where they reach DDT is labeled L_{DDT}. That distance was the shortest for the tests conducted at 10.3 kPa and 11 kPa and was 0.3 m from the obstacles. The results from Figure 4.7, and the above images for the tests conducted at p_0= 10.3 kPa, 8.2 kPa, and 3.4 kPa, show how reducing the initial pressures

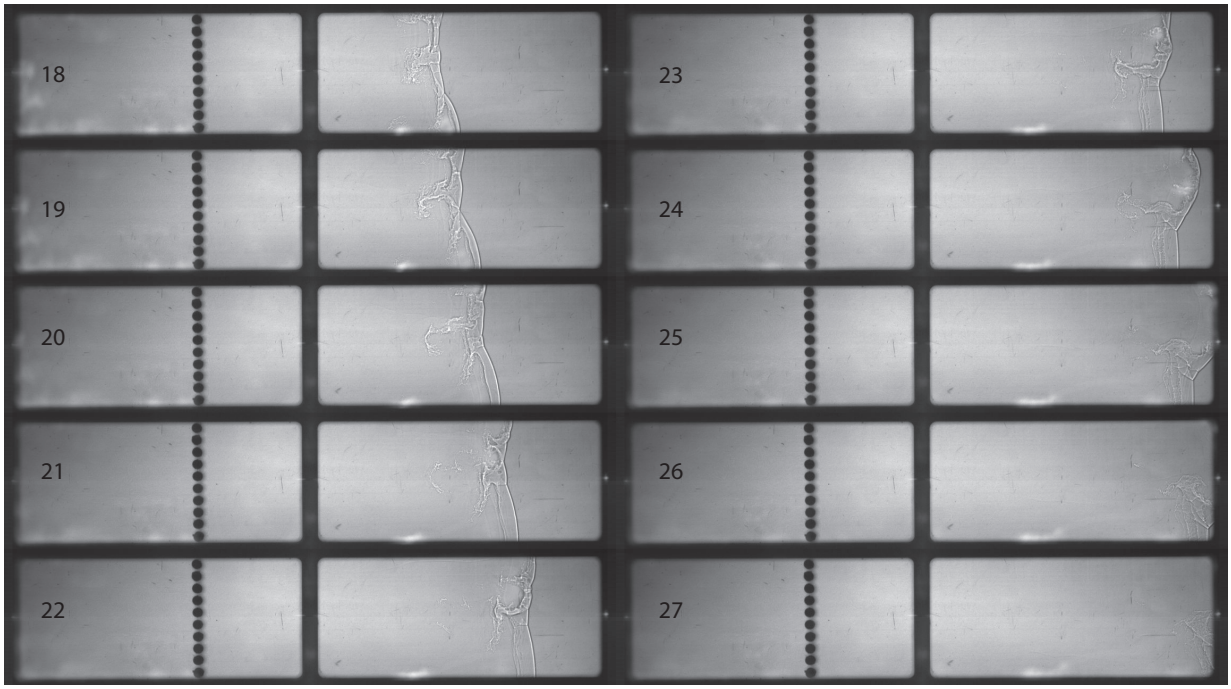


Figure 4.4: Selected Shadowgraph images illustrating the propagation of fast flames in CH_4+$2O_2$, p_0=8.2 kPa. Recorded at 23.76 μs interframe, 1 μs exposure, 42049 fps. The full record can be found in A.4, A.5, and A.6

resulted in a longer L_{DDT} distance. The speed evolution for the test conducted at 10.3 kPa shows how rapidly the flame-shock complex jumped to the CJ detonation speed regime, caused by the hot spot ignitions shown earlier. On the other hand, it can be seen for the test conducted at 8.2 kPa and 3.4 kPa, that the acceleration toward the CJ detonation regime is less rapid and gradual.

4.1.2 Methane with 90% Blockage Ratio

Figures 4.8 and 4.9 show the results obtained at an initial pressure of $p_0 = 14.5$ kPa for 90% blockage ratio. The images of frames 1 to 10 show the same events of a CJ detonation wave diffracting around the obstacles, followed by the subsequent generation of fast flames. These flames have a corrugated flame-shock complex with hotspots seen initiated from the shock-shock reflections. A hotspot ignition, seen after the collision of two Mach stems in frames 11 and 12, causes the re-emergence of a new Mach stem, with

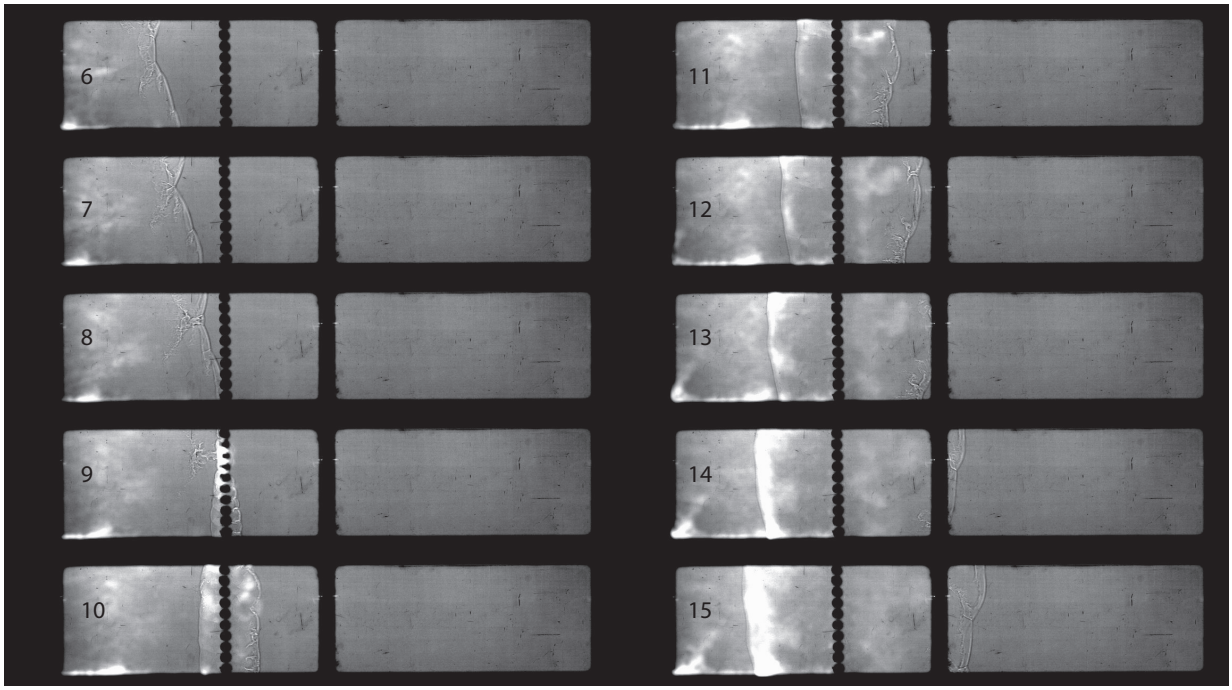


Figure 4.5: Selected Shadowgraph images illustrating the propagation of fast flames in CH_4+$2O_2$, p_0=3.4 kPa. Recorded at 23.76 μs interframe, 1 μs exposure, 42049 fps. The full record can be found in A.7, A.8, and A.9

the flames closely coupled to the front shock. The new Mach stem, seen in Frame 13, moves toward the bottom wall and impinges, causing re-initiation of detonation. The detonation wave engulfs the whole field in the subsequent frames from 14 to 18. The velocity profile for this test, seen in Figure 4.11 shows the jump in velocity caused by the hot spots seen in frames 12 and 13, causing the shock-flame complex to accelerate towards the CJ detonation regime.

Figure 4.10 shows the results of the test conducted at lower initial pressure, $p_0 = 12.4$ kPa. The later frames, 21 to 25, show that the shock-flame complex re-organizes itself into a Mach stem and an incident shock. Frames 26 to 30 show the shock impinging from the top wall, and creating a new Mach stem with the flame coupled closely to the shock. The lower sensitivity affects the rate of re-creating Mach reflections and hotspots, far away from the obstacles. This result could be confirmed by looking at velocity profile for this test from Figure 4.11. We can see that the propagating velocity is lower than the previous

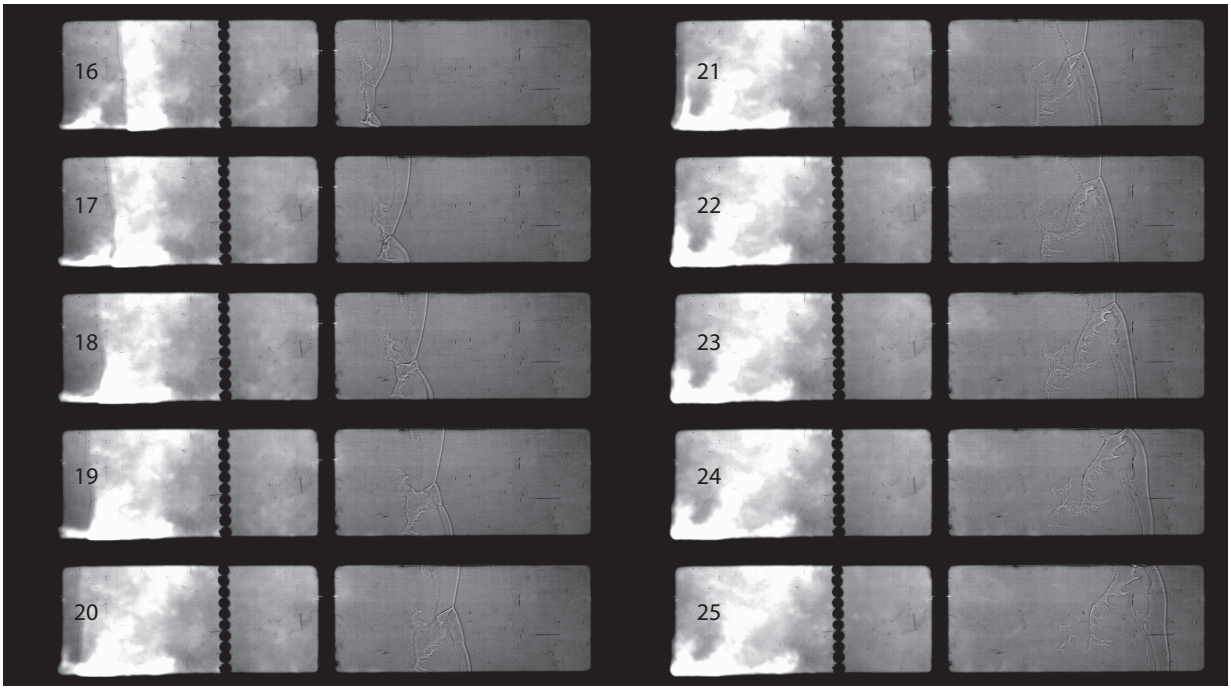


Figure 4.6: Selected Shadowgraph images illustrating the propagation of fast flames in CH_4+$2O_2$, p_0=3.4 kPa. Recorded at 23.76 μs interframe, 1 μs exposure, 42049 fps. The full record can be found in A.7, A.8, and A.9

test conducted at higher initial pressure, and the acceleration is more gradual.

The velocity profiles for all the tests conducted in methane for the 90% blockage ratio configuration for pressures between 10.3 kPa to 15.8 kPa are reported in Figure 4.11. After interacting with the obstacles, the transmitted shocks are found to propagate with speeds between 1200-1400 m/s, which are 55 to 65 % of CJ detonations. The higher blockage ratio resulted in a weaker transmitted shock. This can be observed by a velocity deficit of 30 % lower than the tests conducted at 75% blockage ratio. For tests conducted at high initial pressure (high sensitivity), the flame-shock complex propagated for approximately 0.45 m from the obstacles before they transited into detonations. This corresponds to the tests with initial pressures of 14.5 kPa and 15.1 kPa. As for lower sensitivity, the waves are seen propagating below the predicted CJ deflagration lines, until the end of the channel. The shortest L_{DDT} is 0.55 m, which is longer than the critical run-up distance for 75% blockage ratio. For tests conducted between 11.7 kPa and 15.1 kPa, the effect of the mixture's

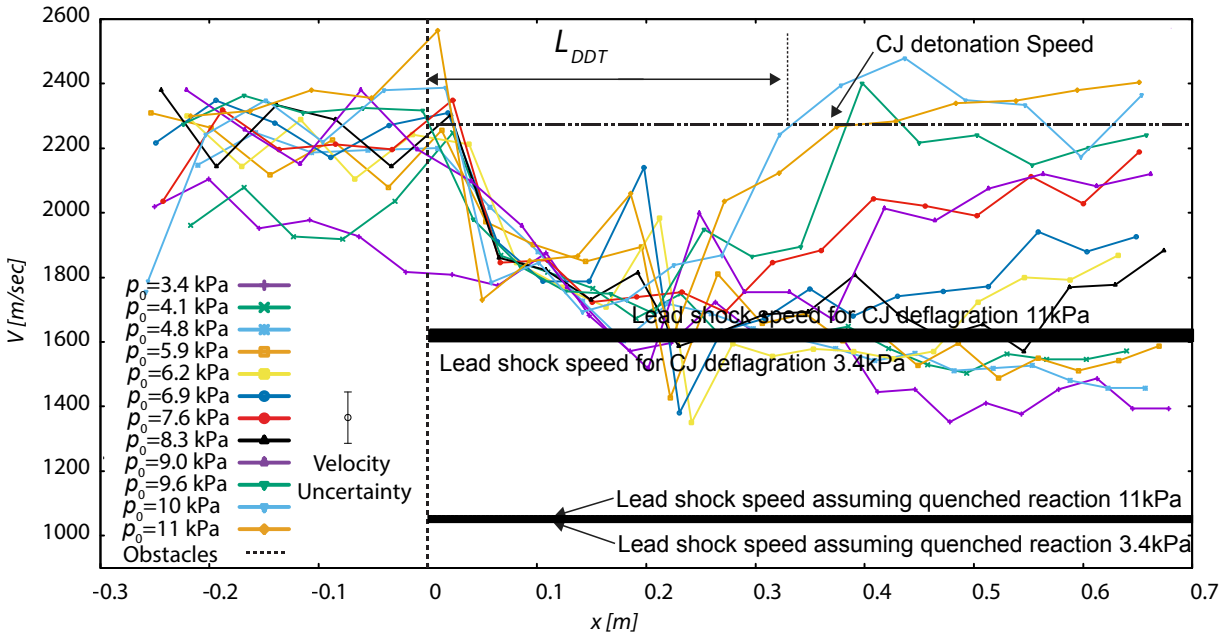


Figure 4.7: Velocity profiles for the test conducted for CH_4+$2O_2$, using the 75% blockage ratio configuration.

sensitivity is clear, as the test conducted at higher pressures have shorter L_{DDT} distance when compared to the test conducted on lower pressures, with a discrepancy seen in the test conducted at 15.8 kPa.

4.2 Propane

4.2.1 Propane with 75% Blockage Ratio

Figure 4.12 shows the results of a test conducted for propane with 75% blockage ratio, and initial pressure of p_0= 4.1 kPa. In this test, from frame 8 we can see the CJ detonation wave interacting with the obstacles. Frame 9 shows the resulting transmitted shock with the distinguished key-stone structures. The interaction of these shock reflections initiate several hotspot ignition points, as observed in frame 10 (the reader can zoom in for more clearer observation). The hotspots cause the flame-shock complex to corrugate, as seen in frame 11 and 12. One of the hotspots in the middle of the channel appeared after the

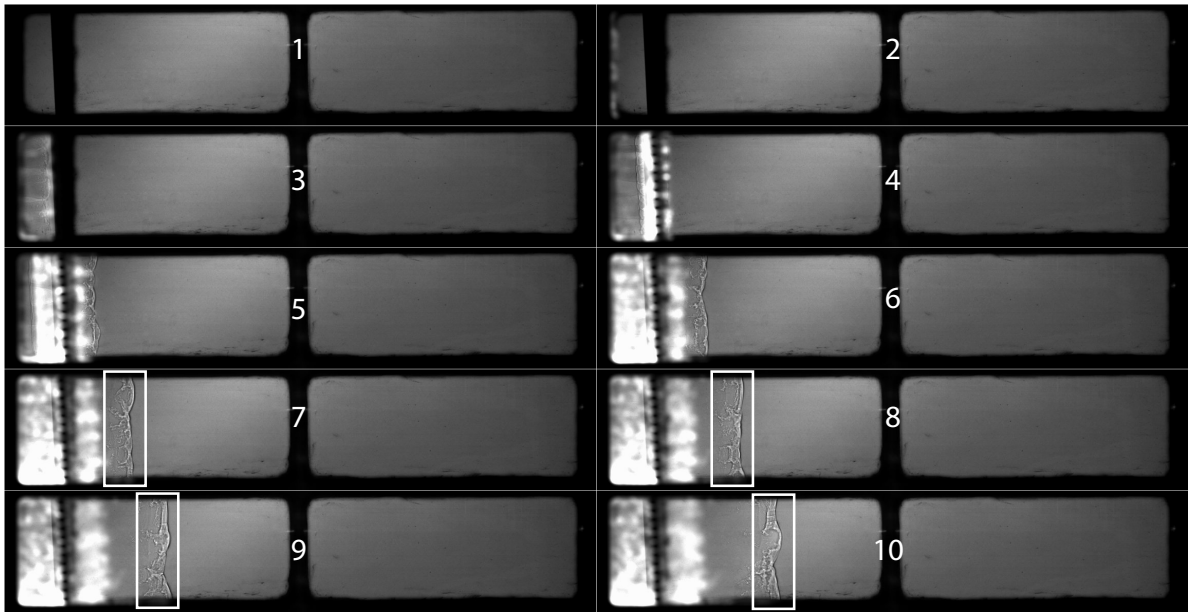


Figure 4.8: Shadowgraph images illustrating the re-initiation of detonation after interacting with obstacles in CH_4+$2O_2$, p_0 = 14.5 KPa. Recorded at 23.53 μs interframe, 0.7 μs exposure, 42496 fps.

collision of two Mach stems as seen in Frame 14, generates a small explosion that causes the complex to accelerate and transit into detonation. The speed histories for this test seen in Figure 4.14, can confirm the acceleration of the flame-shock complex caused by these hot spots, as the line velocity increases and reaches the CJ detonation speed.

Figure 4.13 shows the test conducted at lower initial pressure p_0 = 2.0 kPa. The images from frames 5 to 12 show the same events as the previous test performed at p_0=4.1 kPa. Frame 15 shows how the lead shock and the flames started to decouple, and the gap between them kept increasing until the end of the channel by frame 30. In frame 30, the shock appears to be flat with no corrugation. This result is different from methane tests, as the methane showed corrugation even at lower initial pressure tests. From the speed evolution for this test, seen in Figure 4.14, we can observe the drop of velocity toward the CJ deflagration line, because of the absence of hot spots.

Figure 4.14 shows the history of the velocity profiles for propane at 75% blockage ratio

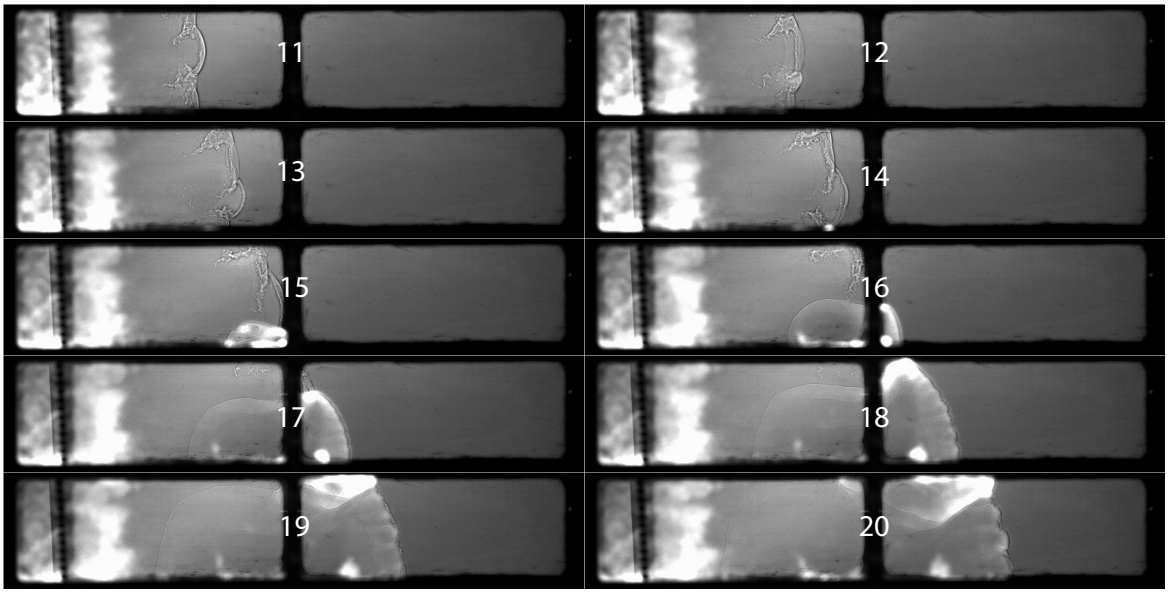


Figure 4.9: Shadowgraph images illustrating the re-initiation of detonation after interacting with obstacles in CH_4+$2O_2$, p_0=14.5 KPa. Recorded at 23.53 μs interframe, 0.7 μs exposure, 42496 fps. The full record can be found in Fig B.1, B.2 and B.3.

configuration. After interacting with the obstacles, we can observe that the propagating velocity dropped to 1500-1600 m/s, which is 65 % of CJ detonation velocity. For tests conducted at high initial pressures, 3.8 kPa to 5.5 kPa, they attenuated for about 0.15 m from the obstacles before they start to accelerate to CJ detonation speeds. The shortest distance to DDT is 0.3 m from the obstacles, corresponding to the test conducted at 5.5 kPa. For the lower initial pressure tests, 2 kPa to 3.4 kPa, they dropped further and attenuated at speeds between 1100 m/s to 1300 m/s, below the calculated CJ deflagration speed.

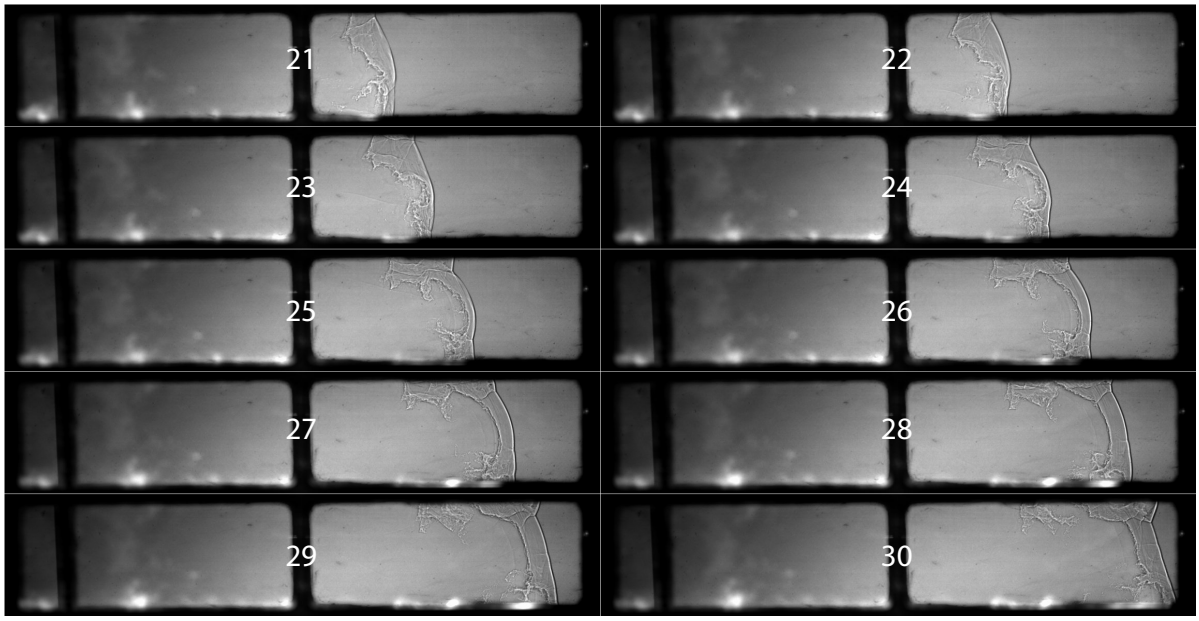


Figure 4.10: Shadowgraph images illustrating the failure of detonation after interacting with obstacles in CH_4+$2O_2$, p_0=12.4 KPa. Recorded at 23.53 μs interframe, 0.7 μs exposure, 42496 fps. The full record can be found in B.4, B.5, B.6, and B.7

4.2.2 Propane with 90% Blockage Ratio

Figure 4.15 shows the results of a test conducted for propane at 7.5 kPa and 90% blockage ratio. We can observe that the same events are seen in the higher blockage ratio configuration. One of the triple points seen in frames 11 and 12 collides with the bottom wall and cause an initiation to detonation. Frames 13 to 20 confirmed the DDT event. The velocity profile for this test, in Figure 4.17, shows how the complex accelerated into detonation because of the triple point collision seen in frame 12.

Lowering the initial pressure of the mixture causes the flames to decouple from the incident shock. Figure 4.16 shows the results for a test conducted at an initial pressure p_0 = 4.1 kPa. Later frames, 21 to 30 show that the incident shock kept propagating with a flat laminar front and no corrugation, with the absence of any hot spot ignitions. The flames are seen trailing behind the shock until the end of the channel. This result is confirmed by the decaying velocity profile in Figure 4.17 below CJ deflagration speed.

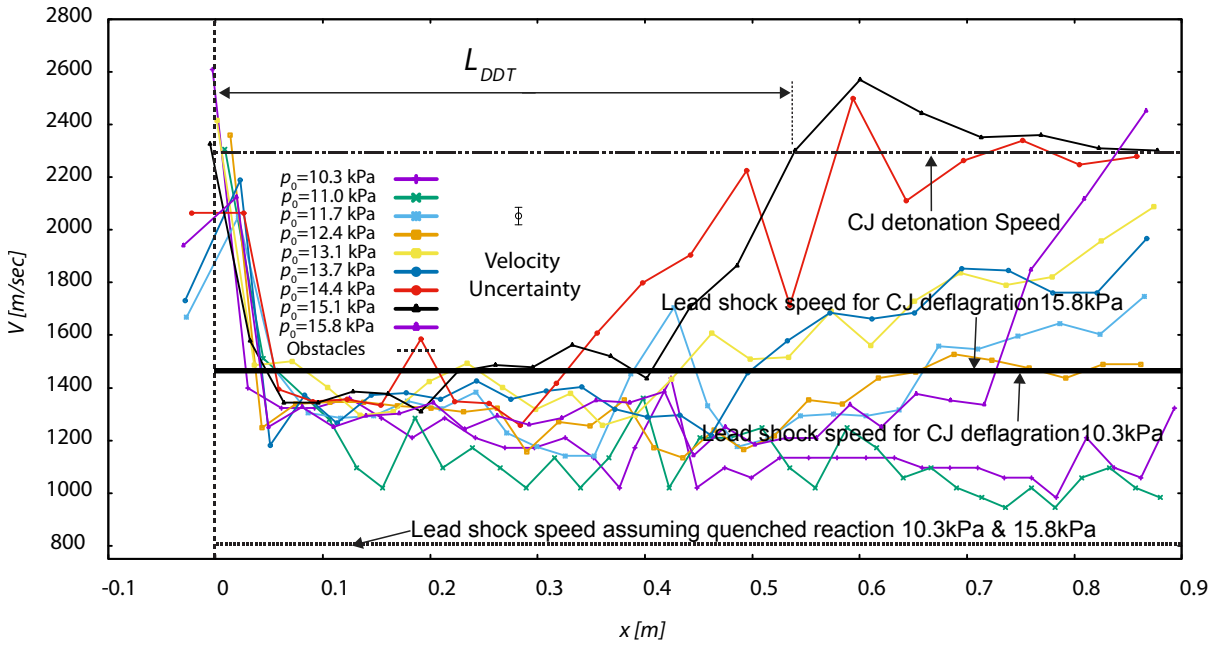


Figure 4.11: Velocity profiles for the test conducted for CH_4+$2O_2$, using the 90% blockage ratio configuration.

Figure 4.17 shows the velocity histories for propane at 90% blockage ratio, and pressures between 4.1 kPa to 7.6 kPa. The shortest distance to detonation (L_{DDT}) is 0.4 m from the obstacles, corresponding to the test conducted at the highest initial pressure, p_0 = 7.6 kPa. In all the test, a velocity deficit is seen after the interaction with the obstacles, with a speed around 1100 m/s (0.5 CJ detonation speed), 20% below the CJ deflagration lines. For tests conducted at high initial pressures, p_0 = 6.9 kPa to 7.6 kPa, the flame-shock complex accelerates into detonation after 0.1m from the obstacles. For lower initial pressures tests, the initiation to detonation took longer distances, corresponding to the test conducted at p_0 = 6.2 kPa. Lowering the initial pressure further, 4.1 kPa to 5.9 kPa, causes the flame-shock complex to attenuate between CJ deflagration and inert cases lines (900-1100 m/s). There are no cases seen to propagate below 900 m/s.

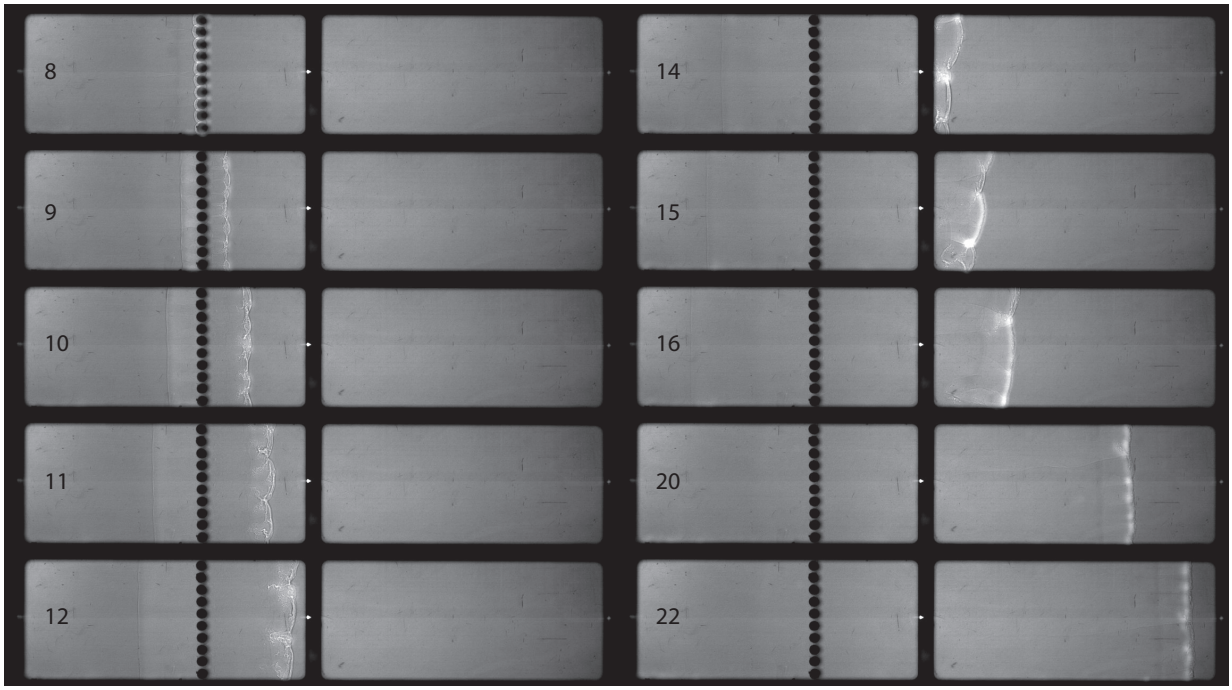


Figure 4.12: Shadowgraph images illustrating the re-initiation of detonation after interacting with obstacles in C_3H_8+5O_2, p_0=4.1 kPa. Recorded at 23.53 μs interframe, 1.0 μs exposure, 42492 fps. The full record can be found in Fig A.29, A.30, and A.31.

4.3 Ethane

4.3.1 Ethane with 75% Blockage Ratio

The shadowgraph images from Figures 4.18 and 4.19 obtained for ethane tests at an initial pressure p_0 = 4.1 kPa, and 75% blockage ratio, show some similarities between ethane, and the previous mixtures at the same conditions, namely methane and propane. Frame 7 shows the attenuation of the CJ detonation wave. Frame 8 shows the interaction with the obstacles. Frame 9, 10 and 11 show the keystone structures of the shock-shock reflections, generated after the obstacles, followed by the rise of hotspots ignition points. Frames 12, 14 and 15 show how the flame-shock complex corrugates, with flames starting to reorganize into fewer and larger modes. Frames 16 to 20 show these flames as they attenuate with what appears to be two Mach reflections and one incident shock in the middle. Frame 21 shows how these two Mach stems meet in the middle and initiate a detonation. The

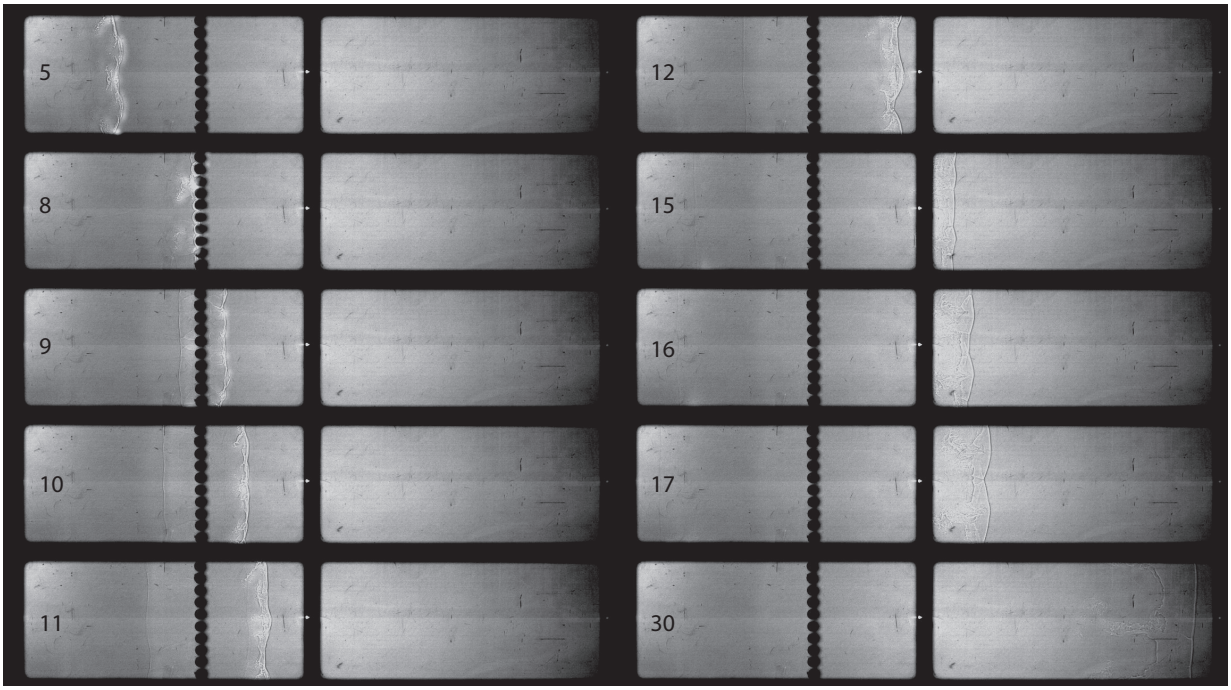


Figure 4.13: Shadowgraph images illustrating the propagation of fast flames after interacting with obstacles in C_3H_8+$5O_2$, p_0=2.0 kPa. Recorded at 23.53 μs interframe, 1.0 μs exposure, 42492 fps. The full record can be found in Fig A.32, A.33, and A.34

rest of the frames show the propagation of detonation wave to the end of the channel. The velocity profile for this test, seen in Figure 4.21, shows how the shock-flame complex accelerates into detonation because of the hot spot seen in frame 21.

Figure 4.20 shows the results of a test conducted at a lower initial pressure of $p_0 = 2.7$ kPa. The same events as the previous test are seen in all frames from 7 to 12. In frame 15, as the flame-shock complex attenuate further from the obstacles, the flames are starting to decouple from the shock. Later frames, 16 up to 30, show the front shock decoupling from the flames, up to the end of the channel. The effect of lowering the initial pressure can be observed by the decaying velocity profile from Figure 4.21. The velocity line is seen propagating below CJ deflagration velocity.

Figure 4.21 shows the velocity histories for ethane at 75% blockage ratio. The shortest L_{DDT} is 0.35 m from the obstacles, corresponding to the test conducted at the highest initial pressure, $p_0 = 6.2$ kPa. After interacting with the obstacles, for high initial pres-

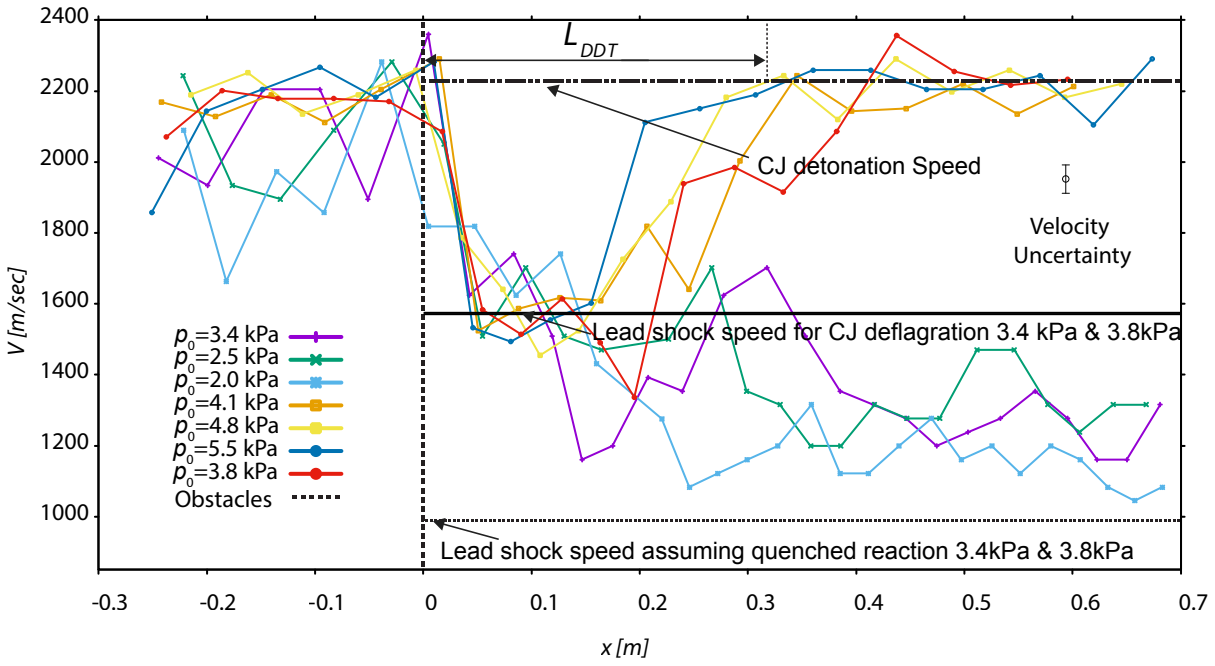


Figure 4.14: Velocity profiles for the test conducted for C_3H_8+$5O_2$, using the 75% blockage ratio configuration.

sure tests, 4.8 kPa to 6.2 kPa, the complex of flames and shocks are seen propagating for 0.25 m, with speeds between 1500-1600 m/sec (0.65 CJ detonation speed), before they start to accelerate toward detonation. Lowering the initial pressure causes the initiation of detonation to take longer distance, corresponding to the test conducted at $p_0 = 4.8$ kPa. Lowering the pressure further, 2.4 kPa to 4.1 kPa, causes the flame-shock complex to attenuate between CJ deflagration and inert cases lines (1100-1500 m/s). There is no case seen to propagate below 1100 m/s.

4.3.2 Ethane with 90% Blockage Ratio

Figure 4.22 shows the results of the test conducted at initial pressure $p_0 = 9.6$ kPa, and 90% blockage ratio in the ethane mixture. Frames 11 to 15 show the attenuation of fast flames far away from the obstacles. It can be observed that they re-organize themselves into two modes. Frames 16 to 19 show the collision of two Mach stems at the center that

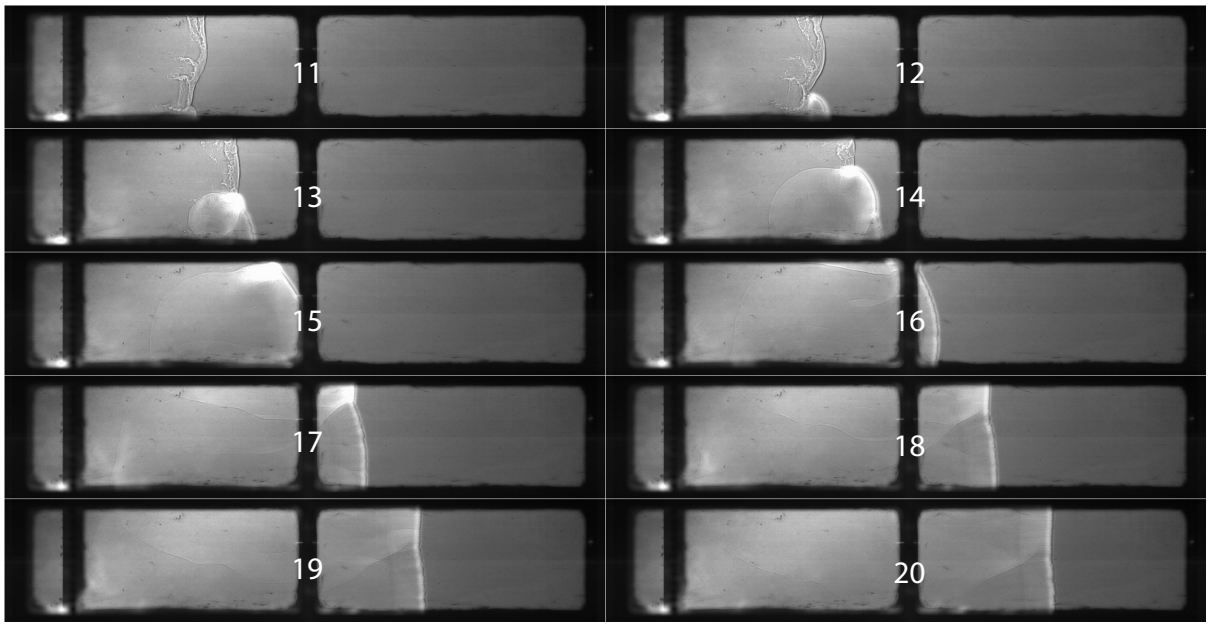


Figure 4.15: Shadowgraph images illustrating the re-initiation of detonation after interacting with obstacles in C_3H_8+$5O_2$, p_0=7.5 kPa. Recorded at 23.53 μs interframe, 0.8 μs exposure, 42496 fps. The full record can be found in Fig B.36, B.37, B.38

causes detonation to initiate. The velocity profile for this test in Figure 4.24 shows the acceleration event that caused the re-ignition spot seen in frames 19.

Figure 4.23 shows the results of the test conducted at initial pressure $p_0 = 8.2$ kPa. Later frames 31 to 40 show the decoupling of the front shock from the flames, as they propagate toward the end of the channel. The velocity profile from Figure 4.24, shows how the flame-shock complex did not accelerate, and was seen propagating very close to CJ deflagration speed.

In Figure 4.24, the shortest L_{DDT} is 0.25 m from the obstacles, corresponding to the test conducted at the highest initial pressure of $p_0 = 11$ kPa. After interacting with the obstacles, the flames are seen propagating for 0.2 m, with speeds between 1000-1100 m/s (0.48 CJ detonation speed), and below the predicted CJ deflagration lines. For tests conducted at high initial pressures, 9.6 kPa to 11 kPa, they are seen accelerating and transiting to detonation right after the obstacles field, corresponding to a distance of 0.1 m from the obstacles. Lowering the initial pressure causes the initiation of detonation to take a

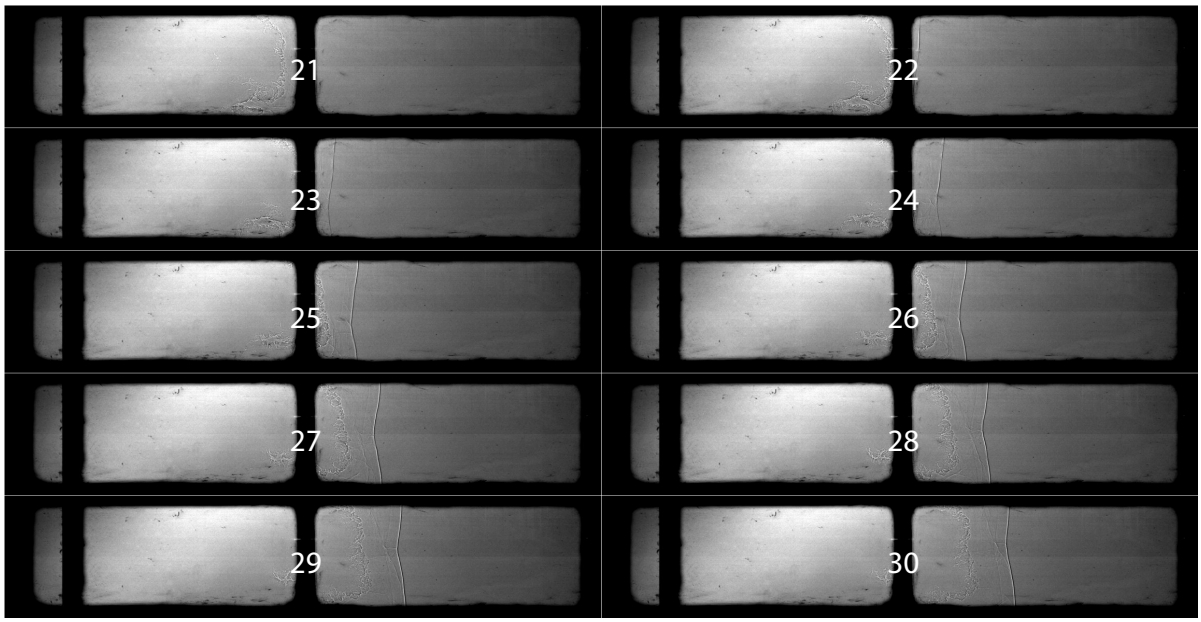


Figure 4.16: Shadowgraph images illustrating the failure of detonation after interacting with obstacles in C_3H_8+$5O_2$, p_0= 4.1 kPa. Recorded at 23.53 μs interframe, 0.8 μs exposure, 42496 fps. The full record can be found in Figure B.31, B.32, B.33, B.34, B.35.

longer distance, corresponding to the test conducted at $p_0 = 9.0$ kPa. Lowering the initial pressure further causes the flame shock complex to attenuate between the CJ deflagration and the inert cases lines (800-1100 m/s). There is no case seen to propagate below 800 m/s.

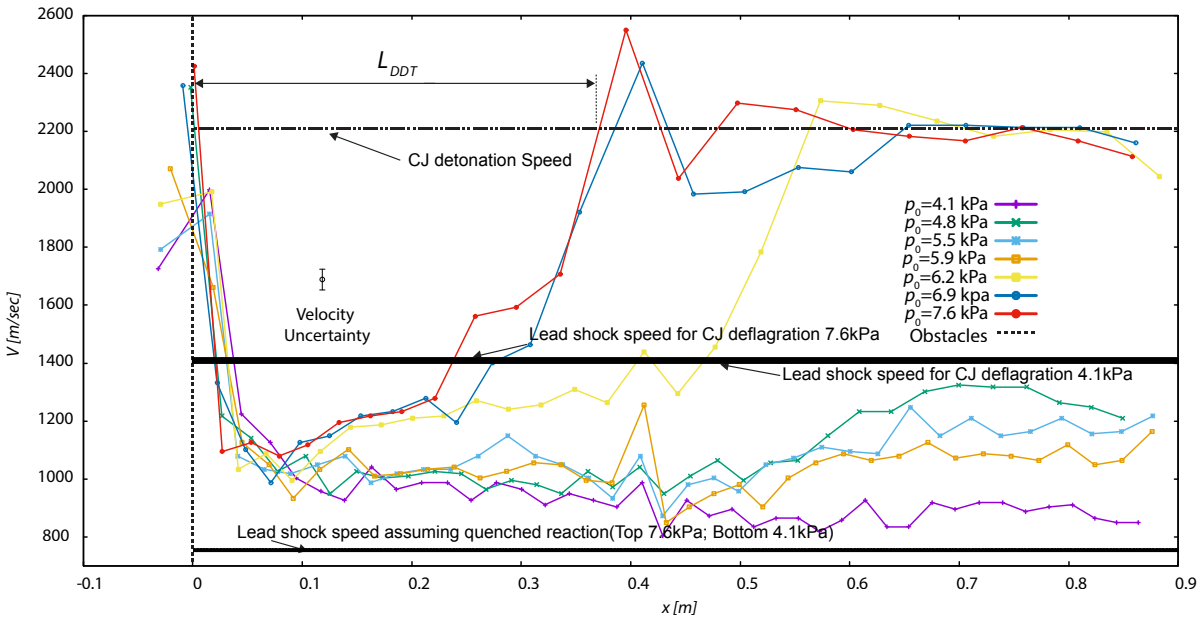


Figure 4.17: Velocity profiles for the test conducted for C_3H_8+$5O_2$, using the 90% blockage ratio configuration.

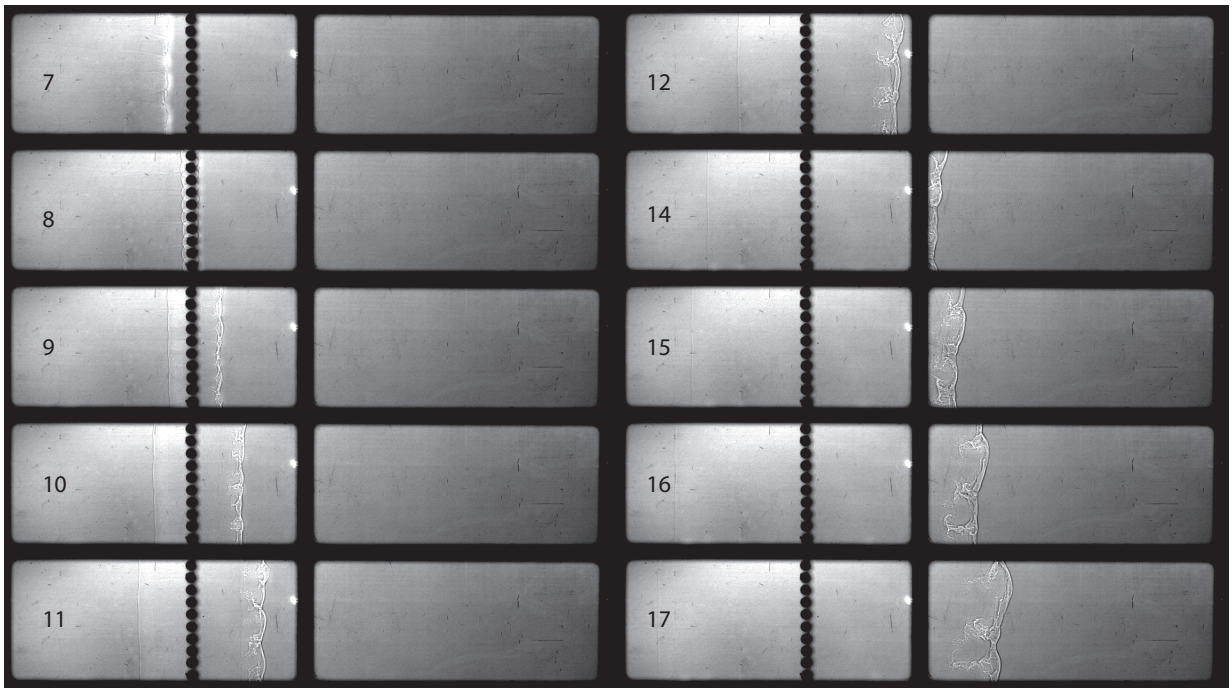


Figure 4.18: Shadowgraph images illustrating the re-initiation of detonation after interacting with obstacles in $2C_2H_6$+$7O_2$, p_0= 4.1 kPa. Recorded at 23.53 μs interframe, 0.7 μs exposure, 42496 fps. The full record can be found in Fig A.10, A.11, and A.12

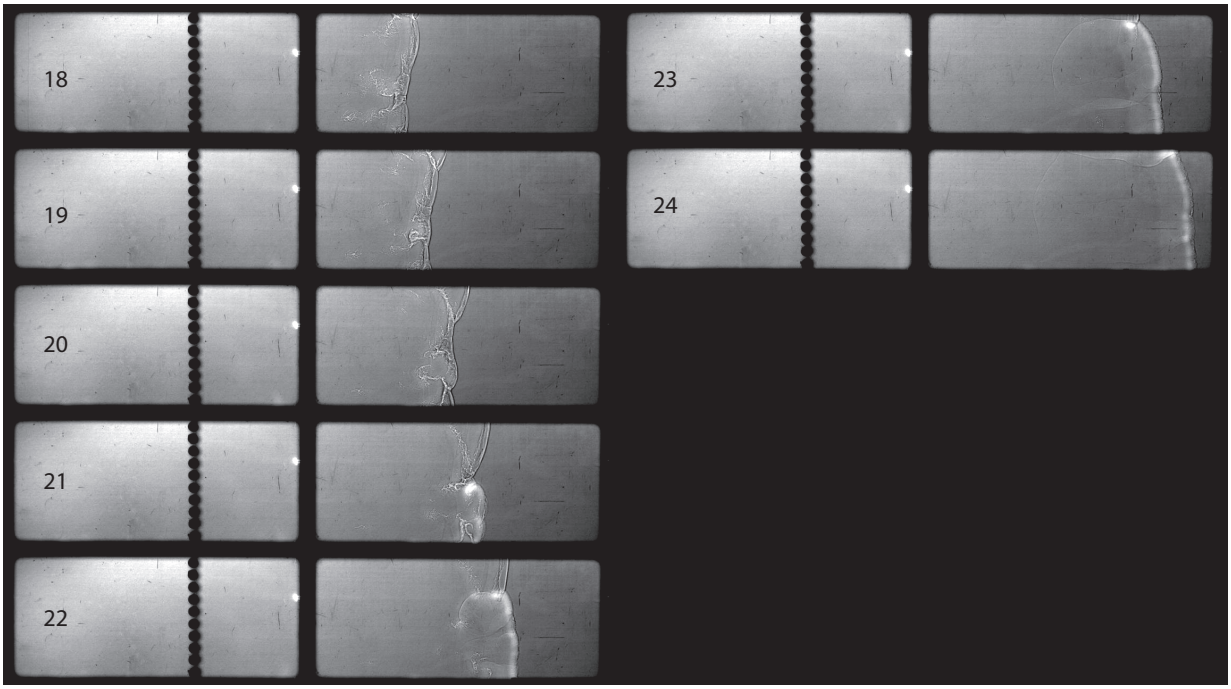


Figure 4.19: Shadowgraph images illustrating the re-initiation of detonation after interacting with obstacles in $2C_2H_6+7O_2$, $p_0 = 4.1$ kPa. Recorded at 23.53 μs interframe, 0.7 μs exposure, 42496 fps. The full record can be found in Fig A.10, A.11, and A.12

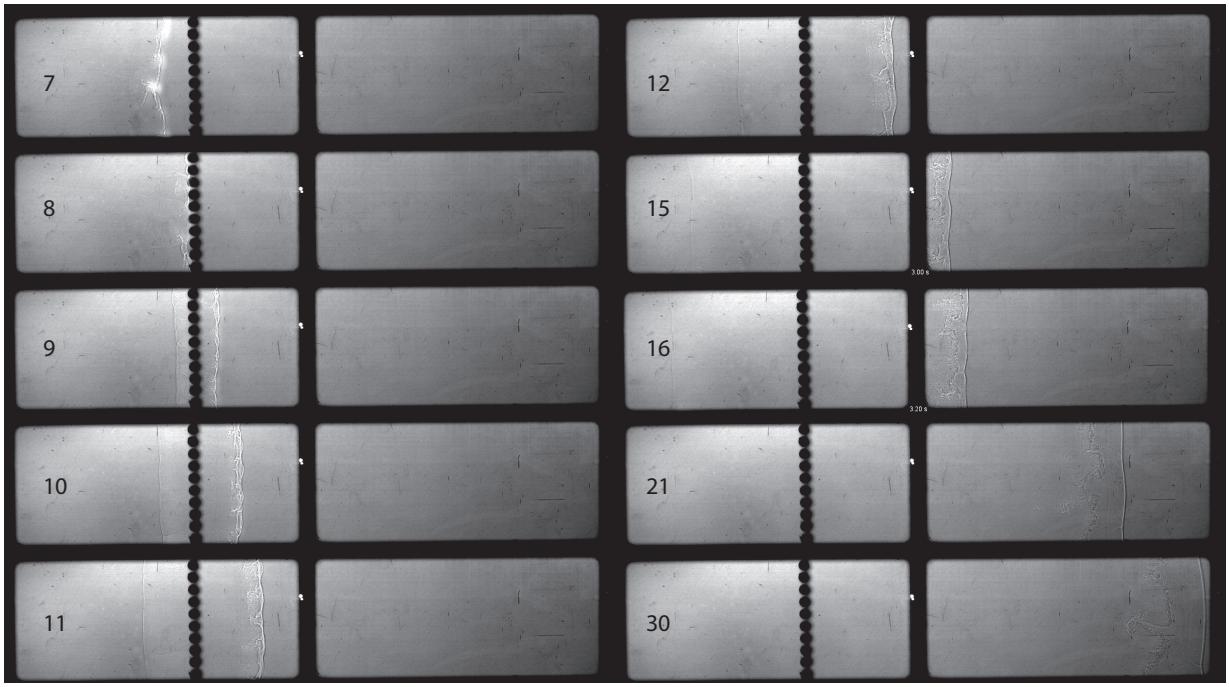


Figure 4.20: Shadowgraph images illustrating the failure of detonation after interacting with obstacles in $2C_2H_6+7O_2$, $p_0 = 2.7$ kPa. Recorded at 23.53 μs interframe, 0.7 μs exposure, 42496 fps. The full record can be found in Fig A.13, A.14, and A.15

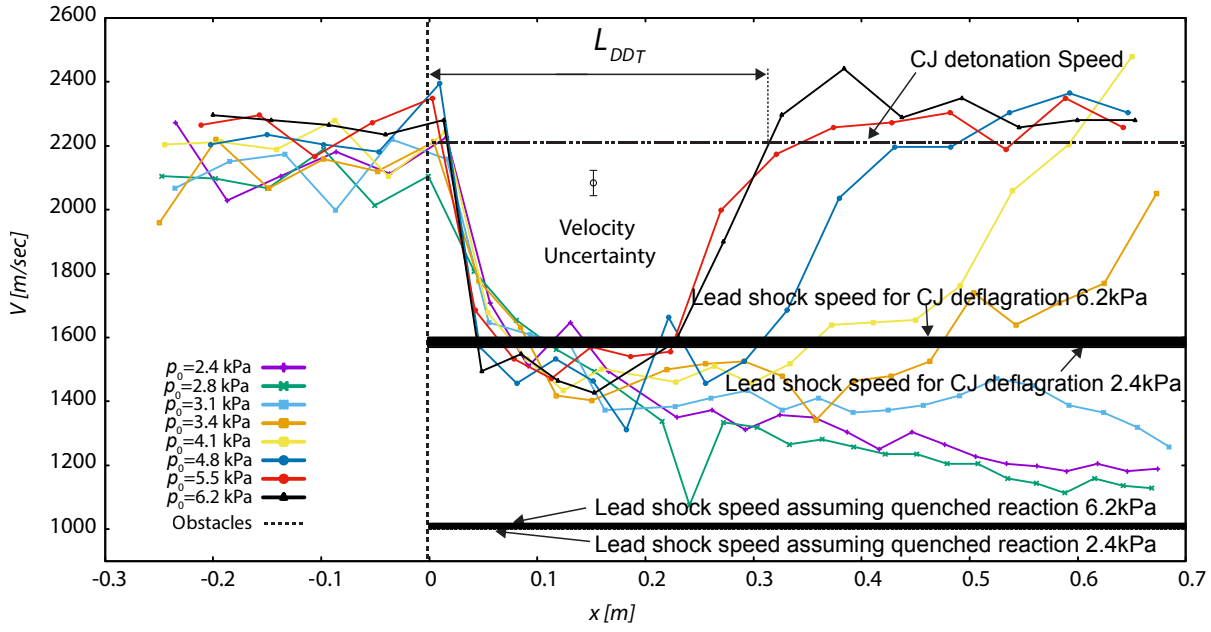


Figure 4.21: Velocity profiles for the test conducted for $2C_2H_6+7O_2$, using the 75% blockage ratio configuration.

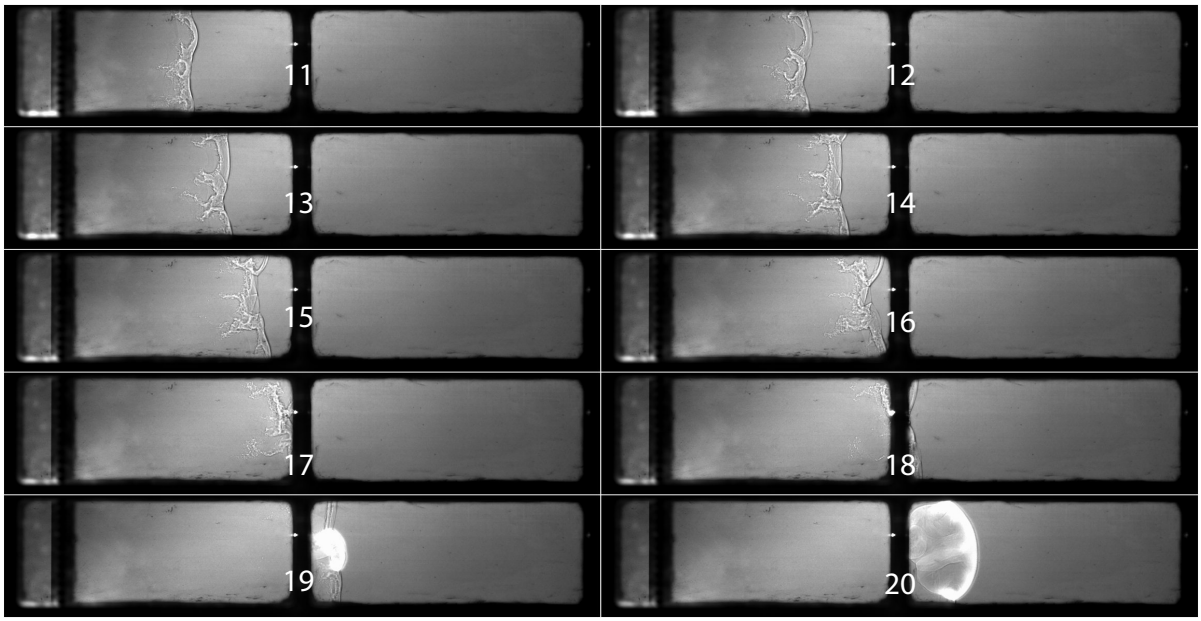


Figure 4.22: Shadowgraph images illustrating the re-initiation of detonation after interacting with obstacles in $2C_2H_6+7O_2$, $p_0 = 9.6$ kPa. Recorded at 23.53 μs interframe, 0.7 μs exposure, 42496 fps. The full record can be found in Fig B.8, B.9 and B.10

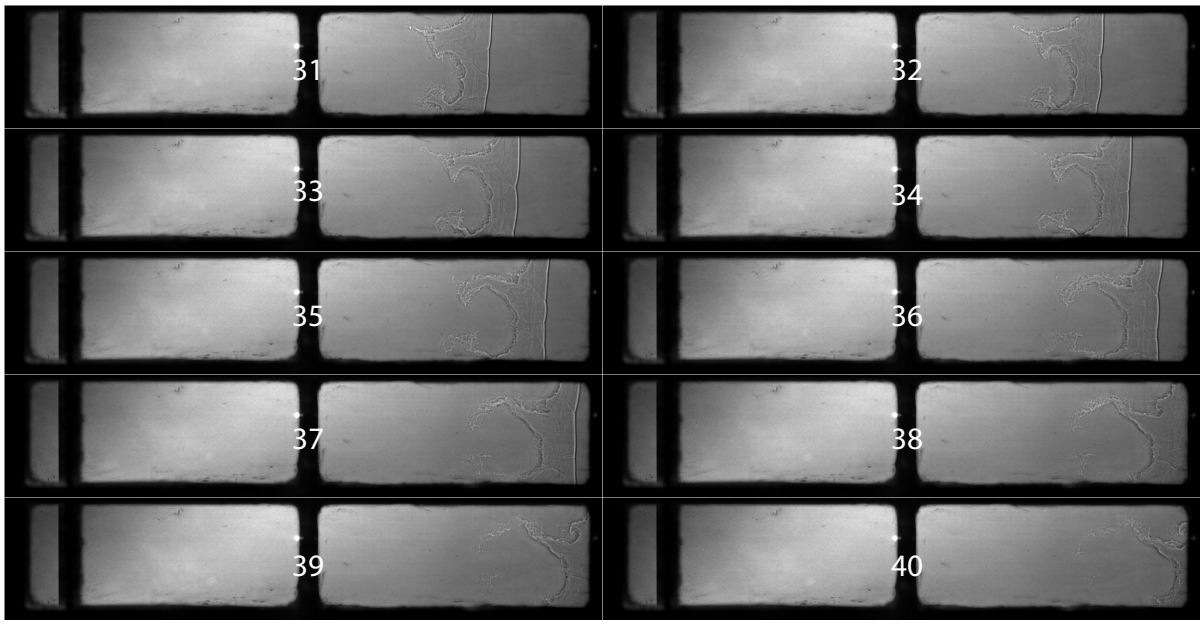


Figure 4.23: Shadowgraph images illustrating the failure of detonation after interacting with obstacles in $2C_2H_6+7O_2$, $p_0 = 8.2$ KPa. Recorded at 23.53 μs interframe, 0.7 μs exposure, 42496 fps. The full record can be found in Fig B.11, B.12, B.13, and B.14

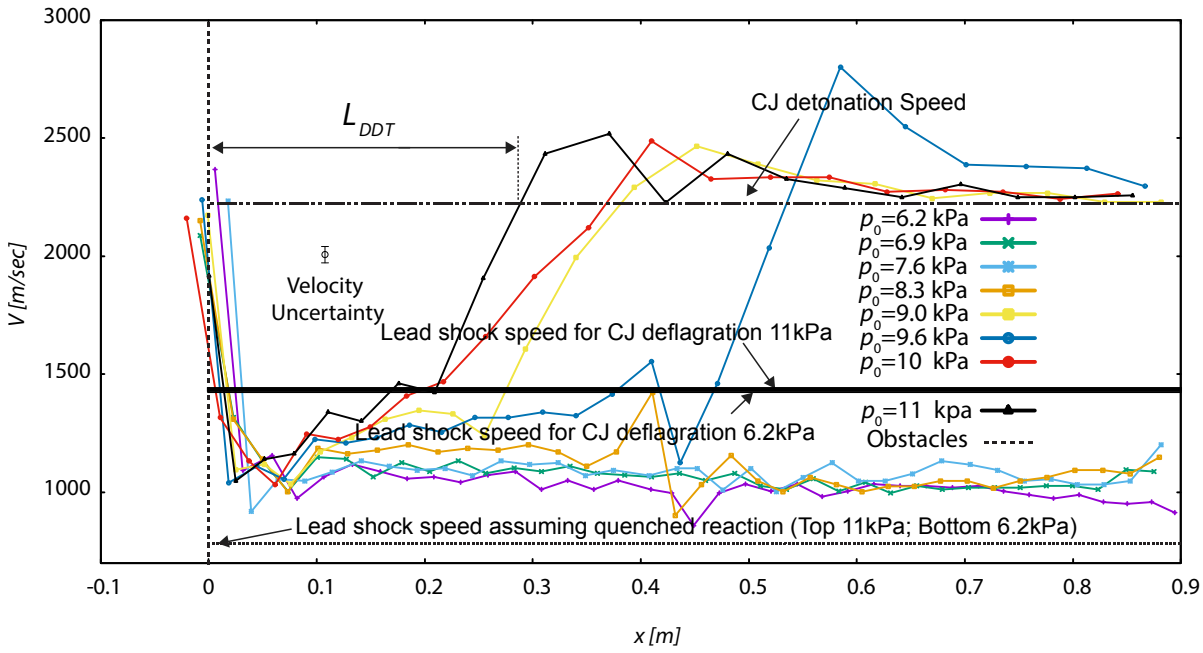


Figure 4.24: Velocity profiles for the test conducted for $2C_2H_6+7O_2$, using the 90% blockage ratio configuration.

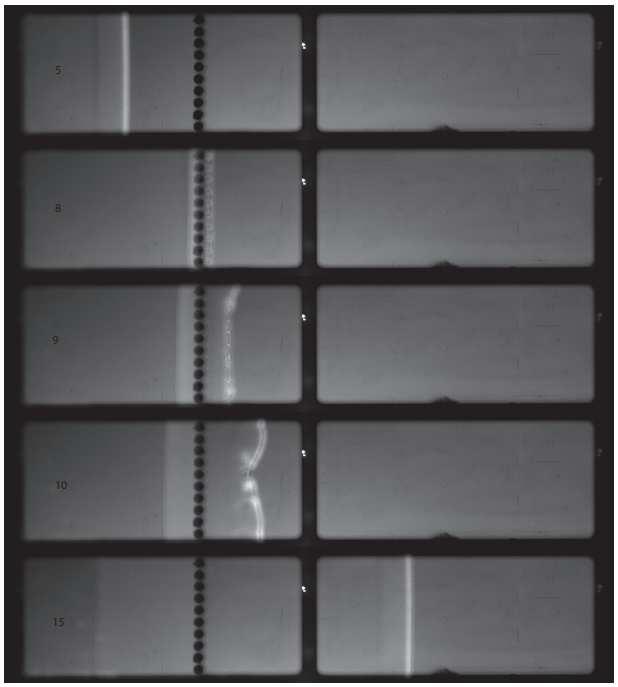


Figure 4.25: Shadowgraph images illustrating the re-initiation of detonation after interacting with obstacles in C_2H_4+$3O_2$, $p_0 = 6.2$ kPa. Recorded at 23.53 μs interframe, 0.8 μs exposure, 42496 fps. The full record can be found in Fig A.16, and A.17

4.4 Ethylene

4.4.1 Ethylene with 75% Blockage Ratio

For ethylene, we started seeing the transition to detonation closer to the obstacles field, as seen here in Figure 4.25. The test here is conducted at an initial pressure of $p_0 = 6.2$ kPa. Frame 5 shows the propagation of the CJ detonation wave from left to right. Frame 6 shows the diffraction of the wave around the obstacles. A series of shocks are seen after the obstacles. Frame 9 shows high luminosity at the top and the bottom from one of these shock-shock reflections. Frame 10 shows their transition into detonation. Frame 15 confirms their attenuation as a detonation wave until the end of the channel. The velocity profile line from Figure 4.27 shows how the flame-shock complex accelerates rapidly to detonation after 0.05 m from the obstacles.

Figure 4.26 shows the results of the test conducted at lower initial pressure, $p_0 = 3.4$

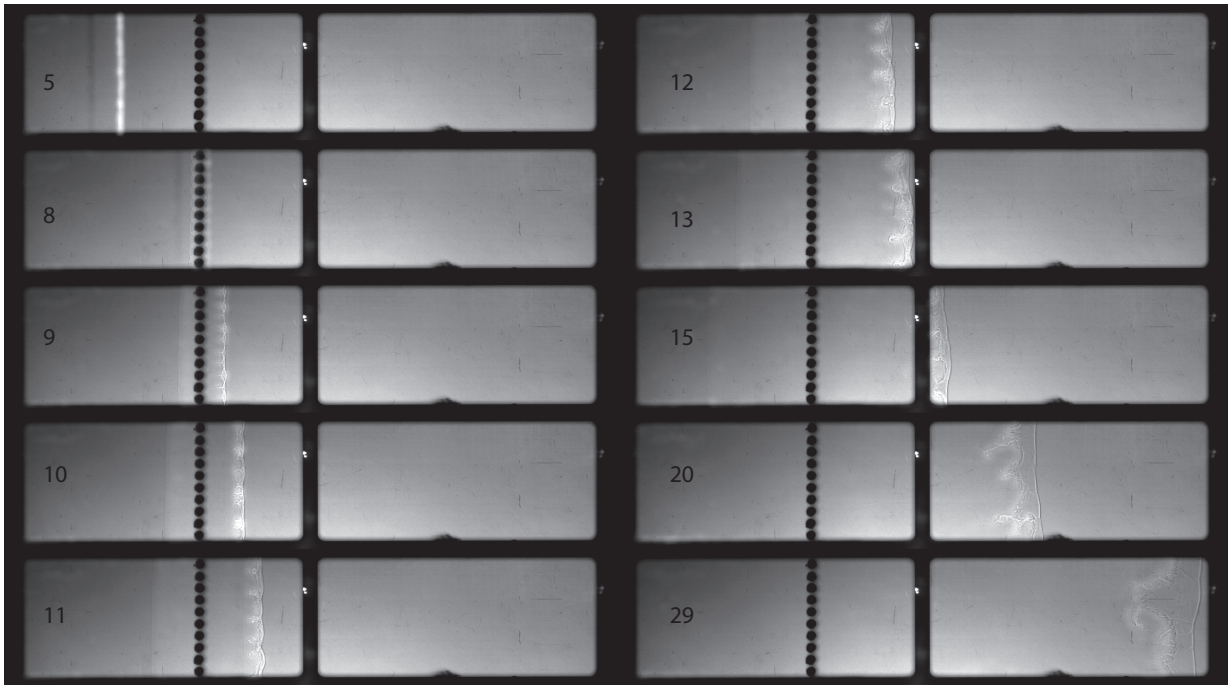


Figure 4.26: Shadowgraph images illustrating the failure of detonation after interacting with obstacles in C_2H_4+3O_2, p_0=3.4 kPa. Recorded at 23.53 μs interframe, 0.8 μs exposure, 42496 fps. The full record can be found in Fig A.18, A.19, and A.20

kPa. Frames 5 to 11 show the same events as the previous test. Frames 12 to 29 show the decoupling of the front shock from the flames. The velocity profile for this test from Figure 4.27 shows how they start to attenuate close to CJ deflagration speed, and then drop below that velocity by the end of the channel.

In Figure 4.27, the shortest L_{DDT} is 0.15 m from the obstacles, corresponding to the test conducted at the highest initial pressure, p_0 = 6.9 kPa. After interacting with the obstacles, the flame speeds are seen dropping to 1500 m/s (65% CJ detonation). For tests conducted at high initial pressures, they are seen propagating for 0.05 m only, before they accelerate and transit to detonation. Lowering the initial pressure causes the initiation of detonation to take a longer distance, corresponding to the test conducted at 4.8 kPa and 5.5 kPa. Lowering the initial pressure further, causes the flame-shock complex to attenuate between the CJ deflagration and the inert cases lines (1000-1500 m/s). There is no case seen propagating below 1000 m/s.

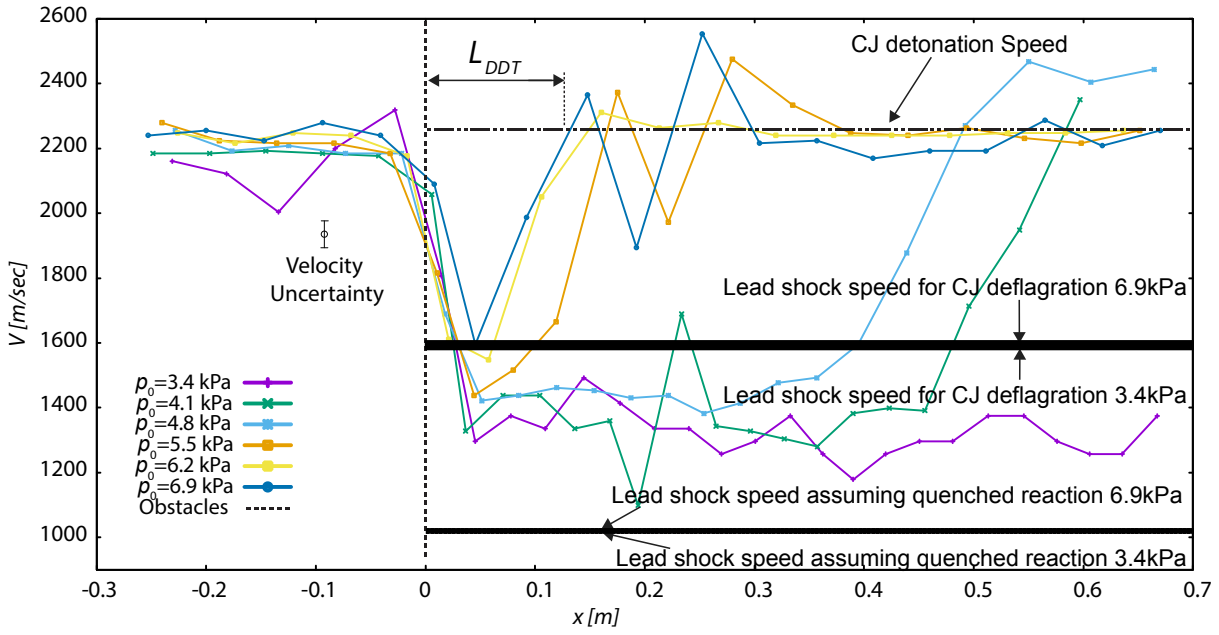


Figure 4.27: Velocity profiles for the tests conducted for C_2H_4+3O_2, using the 75% blockage ratio configuration.

4.4.2 Ethylene with 90% Blockage Ratio

Figure 4.28 shows the results of the test conducted at initial pressure $p_0 = 8.2$ kPa, and 90% blockage ratio. Frames from 11 to 12 show the attenuation of fast flames far away from the obstacles. Frame 13 shows the collision of two Mach stems at the lower part of the channel. That collision causes the re-initiation to detonation, as seen in frames 15 to 20. The velocity profile for this test, seen in Figure 4.30 shows how these flames attenuate for less than 0.05 m from the obstacles before the re-initiation event took place, accelerating the flames rapidly to detonation speeds.

Figure 4.29 shows the results for a lower initial pressure of $p_0 = 6.2$ kPa. Frames 21 to 30 show the decoupling of the front shock from the flames. Despite the decoupled flame-shock complex, it can bee seen in frame 27 that the flames start to roll up toward the front of the shock. By frame 30, it appears to be that this roll up cases the flames to

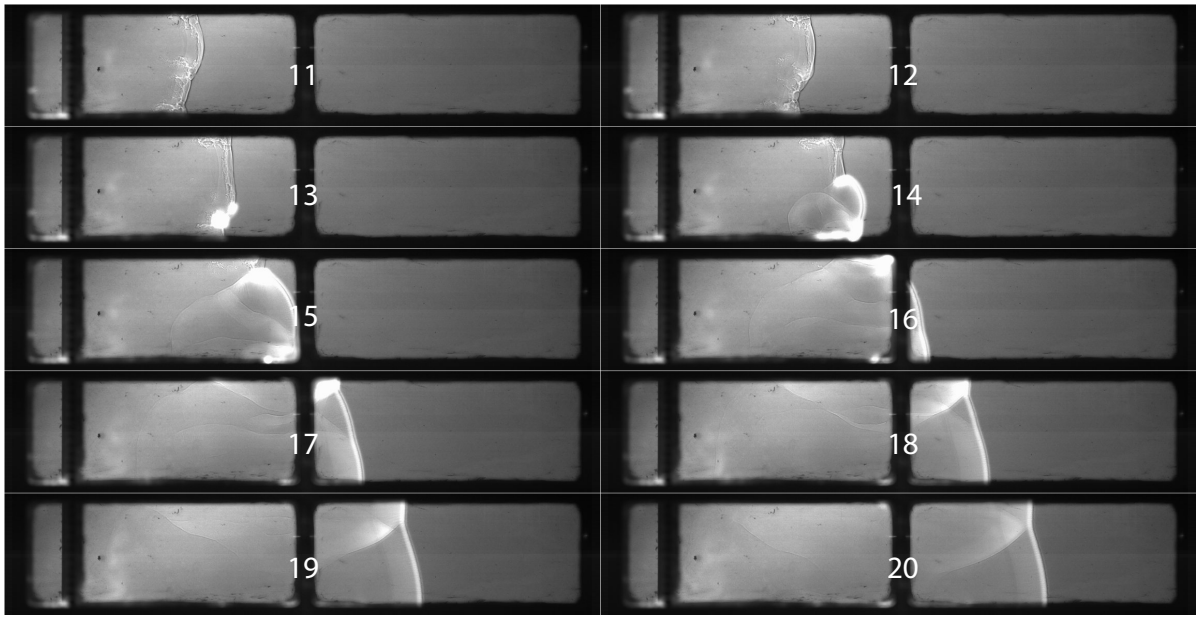


Figure 4.28: Shadowgraph images illustrating the re-initiation of detonation after interacting with obstacles in C_2H_4+3O_2, p_0 = 8.2 kPa. Recorded at 23.53 μs interframe, 0.8 μs exposure, 42496 fps. The full record can be found in Fig B.15, B.16, and B.17

catch up with the front shock again. The velocity profile seen in Figure 4.30, confirms the decoupling of the flames from the shocks, as they propagate close to CJ deflagration line.

In Figure 4.30, the shortest L_{DDT} was 0.25 m from the obstacles, corresponding to the test conducted at the highest initial pressure, p_0 = 9 kPa. After interacting with the obstacles, the flame-shock speeds dropped to 1100 m/s (50% CJ detonation), and below the CJ deflagration lines. For high-pressure cases, they are seen propagating for 0.15 m only, before they accelerate and transit to detonation. Lowering the pressure causes the initiation of detonation to take longer distance, corresponding to the test conducted at 7.6 kPa and 8.2 kPa. Lowering the pressure further causes the flame-shock complex to attenuate between CJ deflagration and inert cases lines (800-1100 m/s). By the end of the channel, they are observed to attenuate closer to the inert speed line.

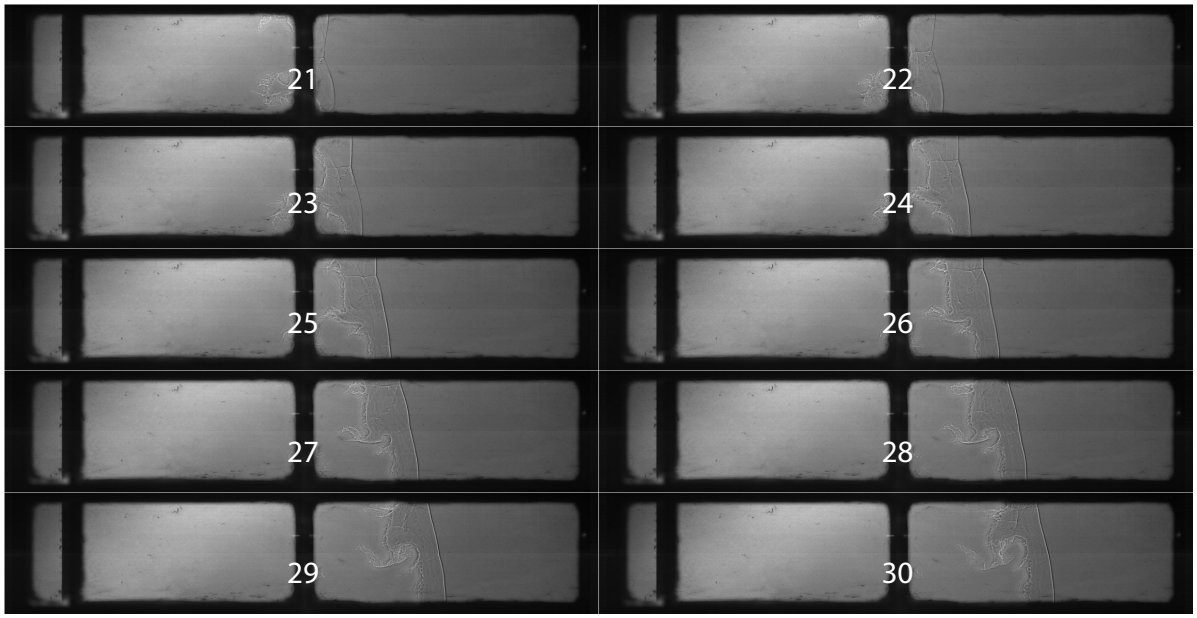


Figure 4.29: Shadowgraph images illustrating the failure of detonation after interacting with obstacles in C_2H_4+3O_2, p_0 = 6.2 kPa. Recorded at 23.53 μs interframe, 0.8 μs exposure, 42496 fps. The full record can be found in Fig B.18, B.19, B.20, and B.21

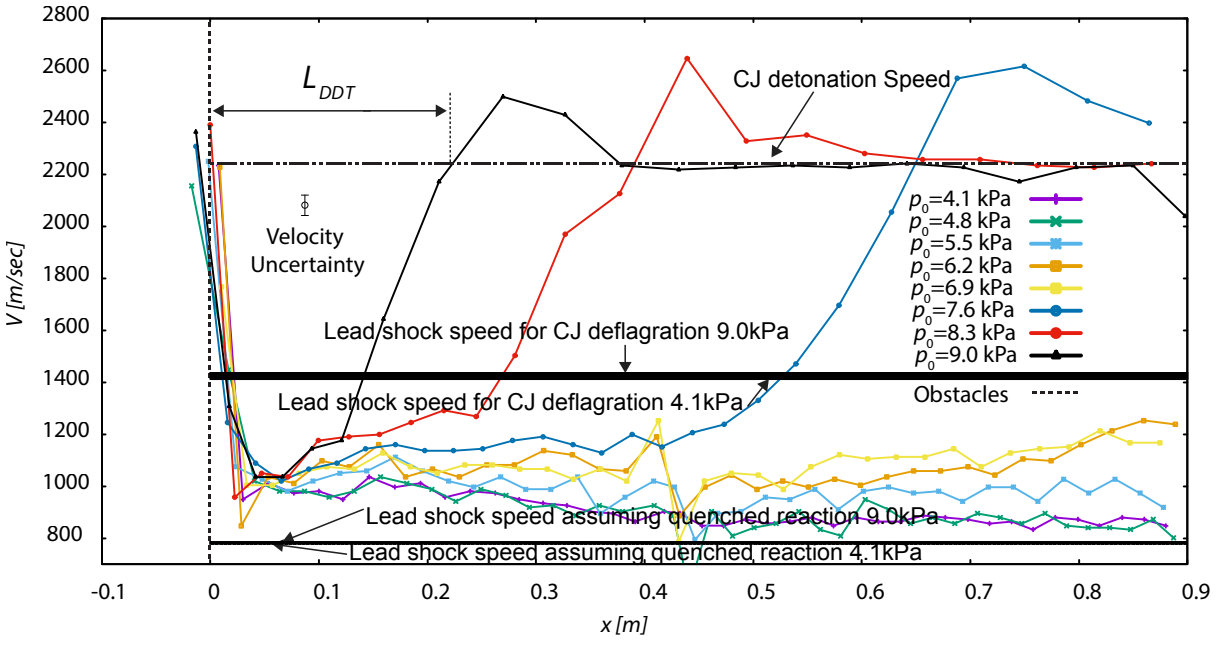


Figure 4.30: Velocity profiles for the tests conducted for C_2H_4+3O_2, using the 90% blockage ratio configuration.

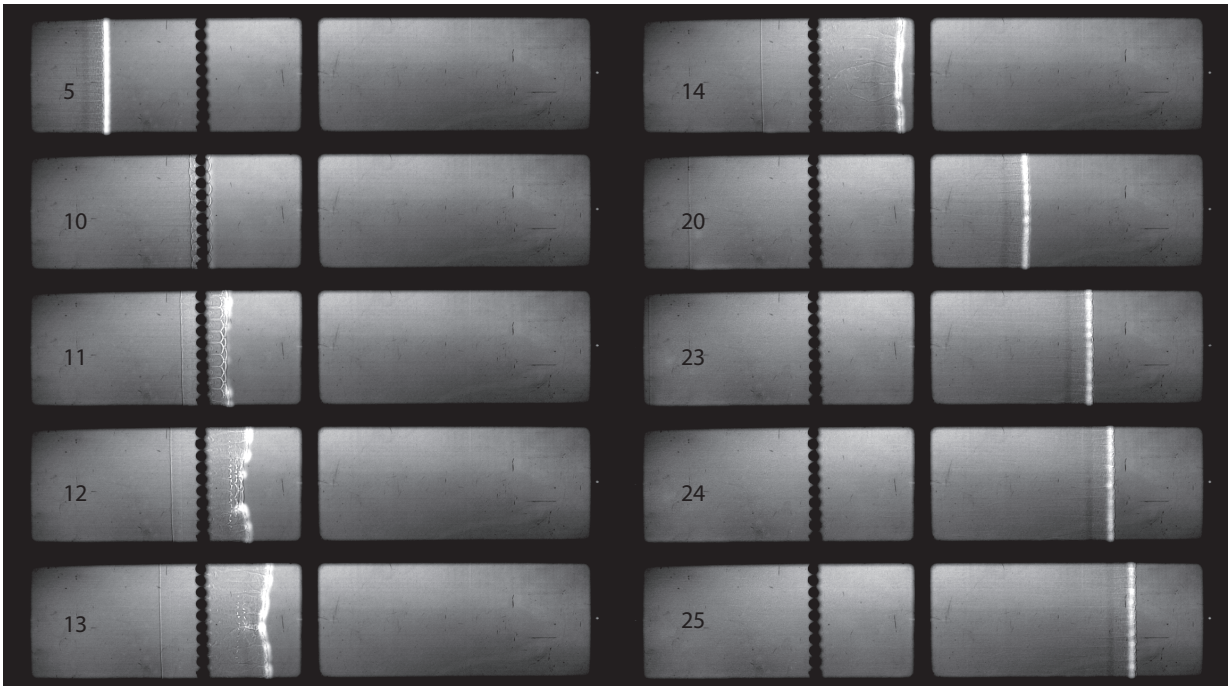


Figure 4.31: Shadowgraph images illustrating the re-initiation of detonation after interacting with obstacles in $2C_2H_2+5O_2+21Ar$, p_0=11 kPa. Recorded at 23.53 μs interframe, 0.8 μs exposure, 42496 fps. The full record can be found in Fig A.21, A.22, and A.23

4.5 Acetylene Diluted with 75% Argon

4.5.1 Acetylene-Argon with 75% Blockage Ratio

In Figure 4.31, the test is conducted at an initial pressure of $p_0 = 11$ kPa, and shows that acetylene adopted the same sequence of events as the previous mixtures, up to the point where they formed the shock-shock reflections in frame 11. Later frames, 12 to 25, show the initiation of detonation from one of the reflections generated after the obstacles. The velocity profile seen in Figure 4.33, shows how they transit almost immediately to CJ detonation after the interaction with the obstacles.

In Figure 4.32, test is conducted at initial pressure of $p_0 = 9.7$ kPa. Frames 14 to 15 show the shock front decoupling from the flame front, and the gap between them kept increasing until the end of the channel. There is no corrugated flame-shock complex generated, as in methane, propane or ethane cases. The velocity profile for this test seen in Figure 4.33,

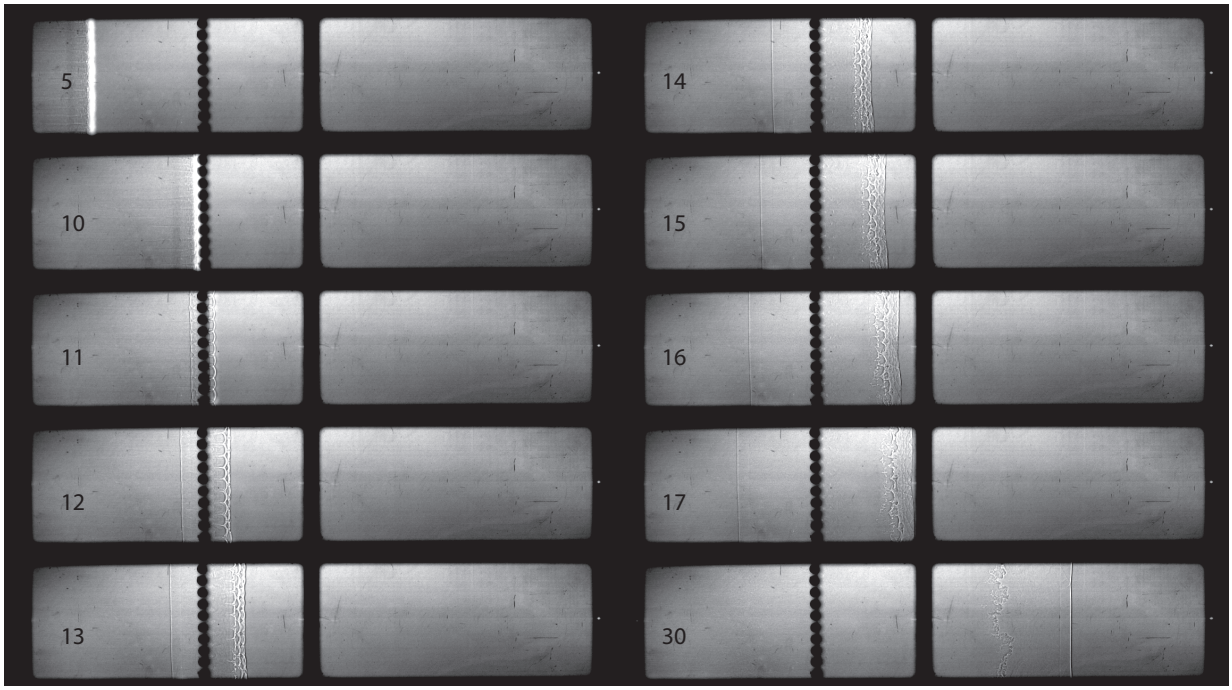


Figure 4.32: Shadowgraph images illustrating the failure of detonation after interacting with obstacles in $2C_2H_2+5O_2+21Ar$, $p_0 = 9.6$ kPa. Recorded at 23.53 μs interframe, 0.8 μs exposure, 42496 fps. The full record can be found in Fig A.24, A.25, A.26, A.27, and A.28

shows the rapid decay to velocities below CJ deflagration toward the inert case.

Figure 4.33, shows the results of the tests conducted in acetylene-argon for initial pressures ranging between 9.7 kPa and 11 kPa. The critical L_{DDT} is 0.15 m, corresponding to the test conducted at $p_0 = 11$ kPa. For all the tests conducted, after the interaction with the obstacles, the flame-shock complex speeds dropped to speeds of 1100 m/s, below teh predicted CJ deflagration lines. They kept propagating for only 0.025 m from the obstacles. They transit almost immediately into CJ detonation speed, except for the test conducted at $p_0 = 9.6$ kPa, in that test, the speed dropped rapidly to 800 m/s, which is close to the prediction made assuming the lead shock is not supported by the flame's energy release.

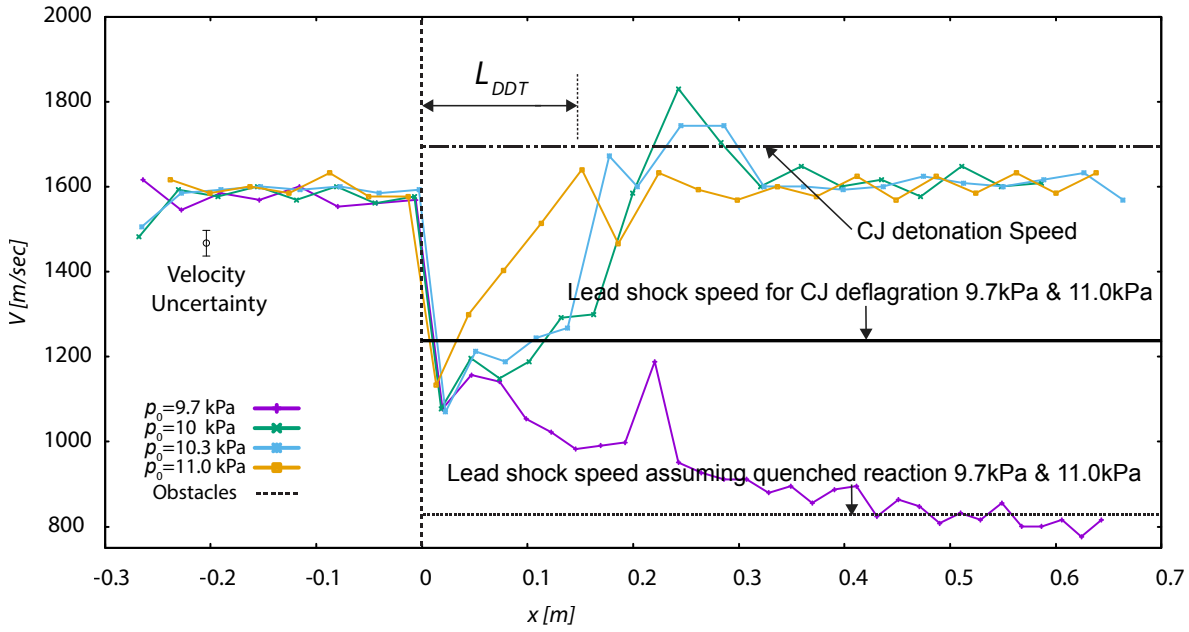


Figure 4.33: Velocity profiles for the tests conducted for $2C_2H_2+5O_2+21Ar$, using the 75% blockage ratio configuration.

4.5.2 Acetylene-Argon with 90% Blockage Ratio

Figure 4.34 shows the test conducted at an initial pressure of $p_0 = 18$ kPa. Frames 21 to 30 show the shock front decoupling from the flame front, and the gap between them kept increasing until the end of the channel. There is no corrugated flame-shock complex generated. The velocity profile for this test seen in Figure 4.35, shows the decay of the velocity of the front shock toward inert case velocities.

Figure 4.35 shows the results of the tests conducted in acetylene-argon for initial pressures ranging between 11 kPa and 18 kPa, for 90% blockage ratio. We can observe that there is no DDT for any of the tests conducted. After the interaction with the obstacles, they dropped to speeds of 900 m/s, which is below the predicted CJ deflagration lines, and propagated for only 0.025 m from the obstacles, before they dropped to lower velocities of 600 m/s. That speed corresponded to the speed predicted when the flame energy release does not support the lead shock.

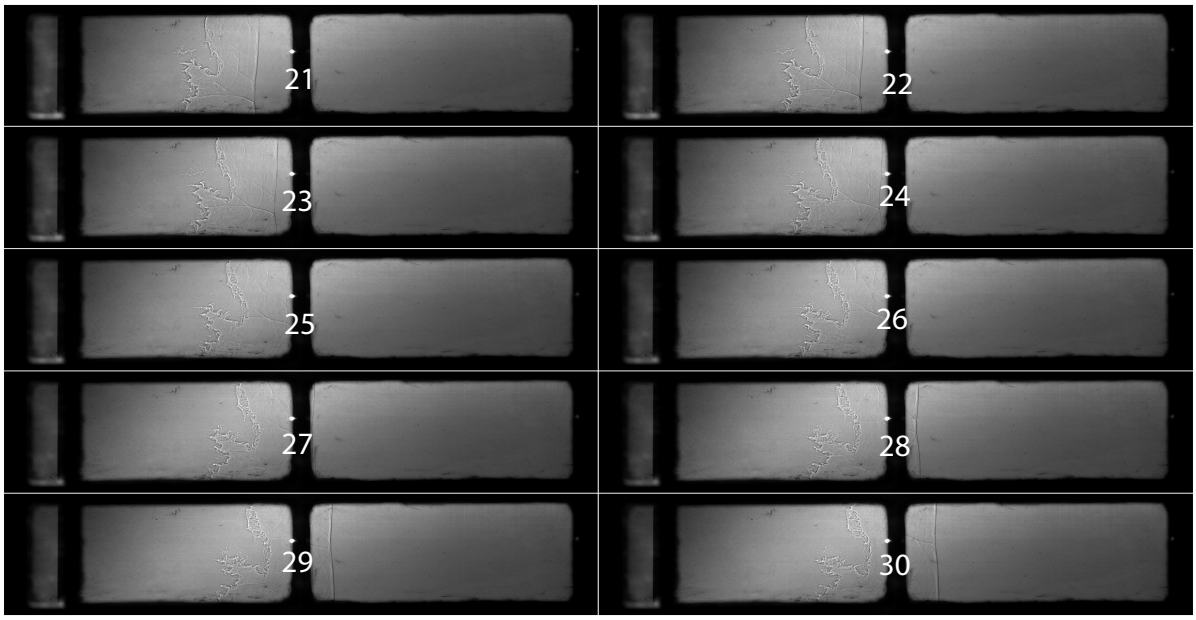


Figure 4.34: Shadowgraph images illustrating the failure of detonation after interacting with obstacles in $2C_2H_2+5O_2+21Ar$, $p_0 = 18$ KPa. Recorded at 23.53 μs interframe, 0.8 μs exposure, 42496 fps. The full record can be found in Fig B.26, B.27, B.28, B.29, and B.30

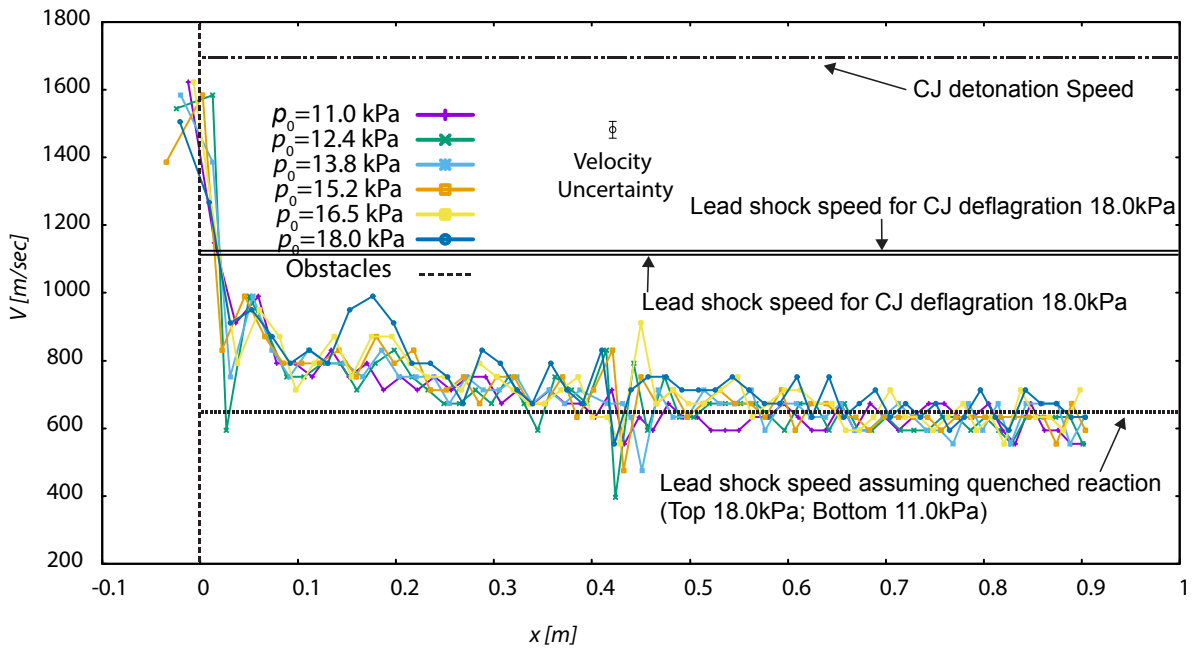


Figure 4.35: Velocity profiles for the tests conducted for $2C_2H_2+5O_2+21Ar$, using the 90% blockage ratio configuration.

Chapter 5

Discussion

5.1 CJ Deflagrations and Required Turbulence Intensity

The results of Chapter 4 indicate that the average speed of the transmitted lead shock predicted by the gas dynamic model of Radulescu et al. [37] is in very good agreement with experiments for all the mixtures studied. Furthermore, it reproduces well the effect of the blockage ratio. To the best of this author's knowledge, this finding is the first unambiguous validation of the CJ deflagration assumption, making it one of the main findings of the present work: that the fast flames do not propagate at half CJ, as anticipated by Chao [6], but they are a direct consequence of the support of the product expansion across the obstacles, which is controlled by the blockage ratio.

The good agreement between model and experiment signifies that the model predictions can also be further used to infer further properties of the high-speed flames. Given the required speed of high-speed flame with respect to the shocked gas, this speed can be compared with the laminar flame speed to further characterize these high-speed deflagrations.

From turbulent combustion theory, the turbulent flame speed s_T is related to the lam-

inar flame speed s_L by [34].

$$\frac{s_T}{s_L} \simeq \frac{v_{rms}^{'}}{s_L} \tag{5.1}$$

where $v_{rms}^{'}$ is the root-mean-square of turbulent fluctuation speed, commonly known as the intensity of turbulence. The laminar flame speeds were provided by Maxwell from separate calculations using an unsteady code [31], taking the post-shock state as initial conditions. The turbulent flame speeds were calculated using the self-similar gasdynamic model from [37]. The summary of the results are reported in Table 5.1 and 5.2. The results show that the obtained values of the laminar flame speeds were two orders of magnitude larger than the usual laminar flame speeds in ambient conditions. This is due to the fact that these flames were estimated in post-shock conditions, with high temperatures, up to 1000 K.. A general estimate of the turbulence intensity required to form these fast flames can thus be established. The results from the tables show that the turbulence intensity required for fast flame speeds are $\frac{s_T}{s_L} \simeq \frac{v_{rms}^{'}}{s_L} \simeq 12 - 30$.

Table 5.1: Calculated laminar flame speeds s_L at 75% blockage ratio and 90% blockage ratio behind the leading shock.

Composition	Mechanism	s_L (m/s)	
		75% Br	90% Br
CH_4+$2O_2$	GRI30 mechanism [44]	14.8	9.2
C_3H_8+$5O_2$	Sandiego mechanism [52]	14.5	8.8
$2C_2H_6$+$7O_2$	Sandiego mechanism [52]	15.8	9.4
C_2H_4+$3O_2$	Sandiego mechanism [52]	25.5	14.8
$2C_2H_2$+$5O_2$+21Ar	Wang mechanism [32]	16.9	6.9

Table 5.2: Inferred mean turbulent flame speed and burning rate enhancement s_T/s_L in the current experiments.

Composition	s_T(m/s)		(s_T/s_L)	
	75% Br	90% Br	75% Br	90% Br
CH_4+2O_2	334.5	208	22.6	23.6
C_3H_8+5O_2	273.4	170.9	18.8	19.4
2C_2H_6+7O_2	293.4	183.1	18.5	19.4
C_2H_4+3O_2	308.6	191.3	12.1	12.9
2C_2H_2+5O_2+21Ar	324.6	201*	19.2	29.1*

*: No fast flames were observed.

5.2 DDT Length Correlations

5.2.1 Correlations with the Detonation Cell Size λ

The detonation cell size λ is usually used as a characteristic length scale measuring the sensitivity of a given mixture to detonation [25]. We thus attempted a correlation between the measured DDT run-up-distance and the cell size of each respective mixture.

Figure 5.1 shows the variation of the cell size with the initial pressure (p_0), obtained from Shepherd's Detonation Database [43], and interpolated at the desired initial pressure (p_0) conducted for each test. From the figure we can see that, for all the mixtures tested, higher pressure values corresponded to smaller cell size. Table 5.3 summarizes the parameters of the power-law fits used to describe the literature data for cell sizes, displayed in Figure 5.1.

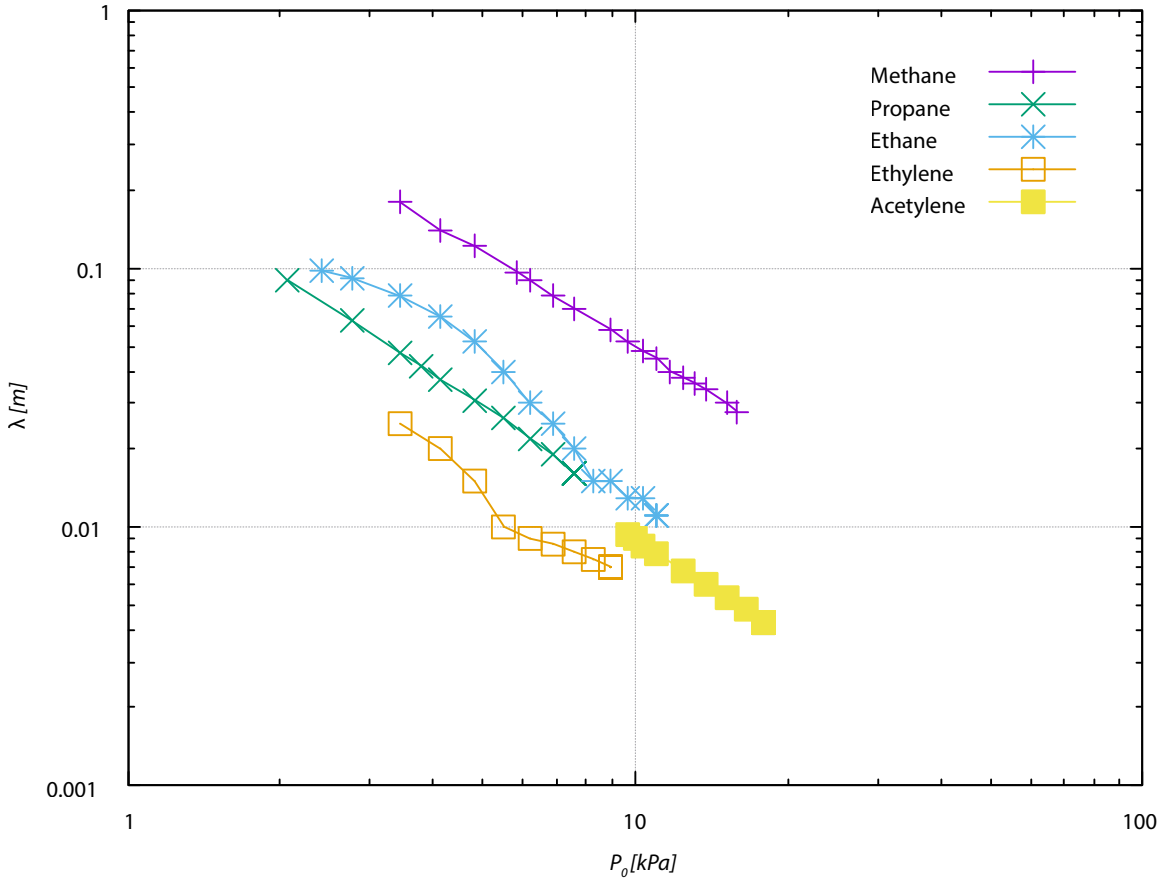


Figure 5.1: The relation between the initial pressure and detonation cell size for the relevant tests conducted.

In our work, we took the results acquired for the run-up distances (L_{DDT}) in chapter 4 and correlated these values with the values of detonation cell size from Figure 5.1 and Table 5.3. These correlations are reported in Figures 5.2 and 5.3 for respectively the 75% and 90% blockage ratio configurations. The results show that the (L_{DDT}) distance was affected by the sensitivity of the mixtures. As the sensitivity decreases (larger λ size), the run-up distance L_{DDT} was larger. This observation agreed with previous studies, as they suggested that there is a relation between the run-up distance and mixture's sensitivity [40, 22].

From Figure 5.2, we can observe that for methane, propane, and ethane, in a 75% blockage ratio configuration, the (L_{DDT}/λ) was approximately 7.5. This result agreed well with the results obtained by Dorofeev et al. [13, 14, 16, 15], as they reported that distance

Table 5.3: Cell size and pressure correlations for methane, propane, ethane, ethylene, acetylene-argon as a function of λ [m] $= \alpha$ $[p_0[\text{kPa}]]^{-\beta}$

Mixture	α	β
Methane	0.8115	1.212
Propane	0.2489	1.347
Ethane	0.5172	1.594
Ethylene	0.1058	1.253
Acetylene-argon	0.1586	1.25

to be approximately 7λ. The results for ethane and acetylene-argon tests showed some deviation from the Dorofeev criteria, as we find (L_{DDT}/λ) approximately 26. In Figure 5.3 for 90% blockage ratio, L_{DDT}/λ for methane, propane, and ethane had however a higher value of 24, and approximately 45 for ethylene.

From Figure 5.2 and 5.3, we can see that the increase in the blockage ratio resulted in a higher (L_{DDT}/λ) criterion. Increasing the blockage ratio to 90%, resulted in a weaker transmitted shock. This led to lower post shock temperatures, and slower reaction rates [40]. This effect can be clearly seen in all the velocity profiles reported in chapter 4. For example, in Figure 4.33, the velocity of the transmitted shock after the obstacles, for a 75% blockage ratio in the acetylene test, was 1180 m/s. In Figure 4.35 the reported velocity of the transmitted shock was 900 m/s, corresponding to the test conducted for acetylene at 90% blockage ratio at the same conditions. Increasing the blockage ratio from 75% to 90% blockage ratio resulted in 23% velocity deficit, and hence, a weaker shock that lead to a higher (L_{DDT}/λ) criteria.

The figures also show that some mixtures clustered together depending on the value of their (L_{DDT}/λ). For example, methane, propane and ethane have the same value of 7.5, but that value was only valid for these three mixtures at 75% blockage ratio. Ethylene and

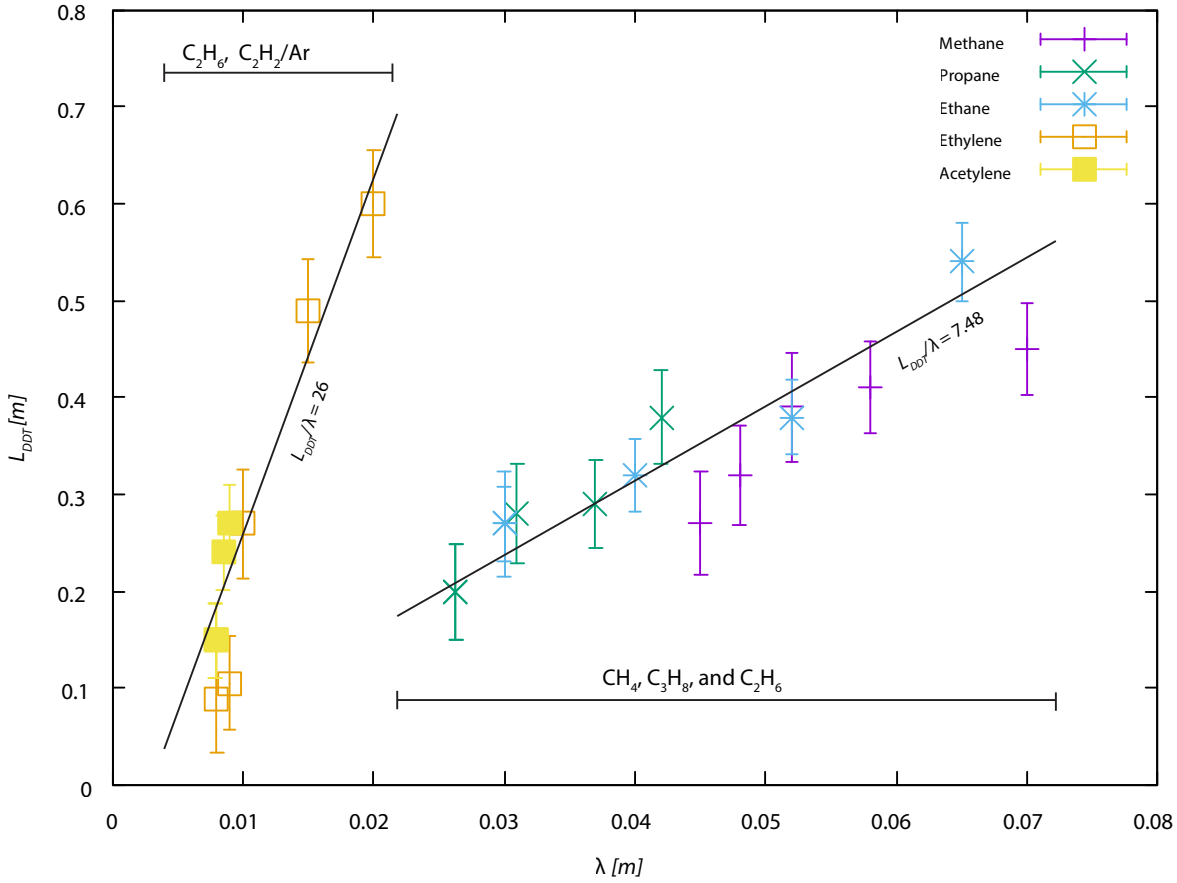


Figure 5.2: Correlation between the run-up distance to detonation L_{DDT} and detonation cell size λ, at 75%.

acetylene-argon have another value of (L_{DDT}/λ) equal to 26. The change in blockage ratio to 90% blockage ratio did not change that grouping pattern, as it is clearly observed from Figure 4.35 that methane, propane, and ethane clustered together with (L_{DDT}/λ) equal to 24. Ethylene deviated from these groups with a reported value of 45.

As discussed in Chapter 1, the χ parameter has been suggested to control the propensity for hot spot formation in the presence of temperature fluctuations. In our setup, the source of these fluctuations was caused by the non-uniform lead shock, resulting from the continuous Mach shock reflections generated by the organization of the front into fewer stronger modes. Figure 4.3, frames 8 and 9, show an example case of these shock reflections. We thus computed the χ parameter for all the mixtures investigated by the

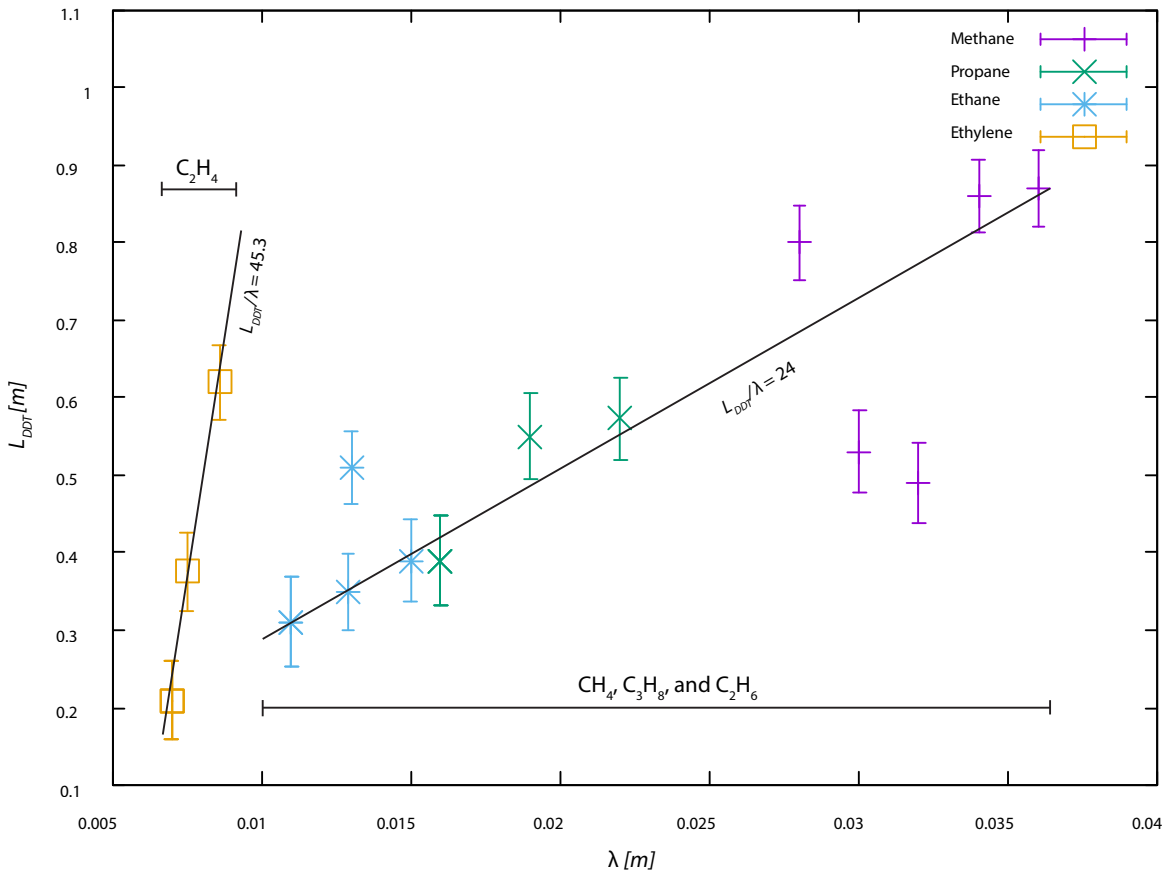


Figure 5.3: Correlation between the run-up distance to detonation L_{DDT} and detonation cell size λ, at 90% blockage ratio obstacles configurations.

method highlighted in section 2.3 in order to seek a correlation for the various mixtures. Figure 5.4 shows the correlation between the L_{DDT}/λ and χ. We can see that there is a correlation between that ratio and χ for fixed blockage ratio configurations. For example, the results for the 75% blockage ratio show that L_{DDT}/λ drops as χ grows. This observation suggests that the mixtures are more prone to DDT with increasing propensity for hot spot formation. The same result can be seen in the 90% blockage ratio configuration. However, the results for the two different blockage ratios indicates that a universal correlation cannot be drawn.

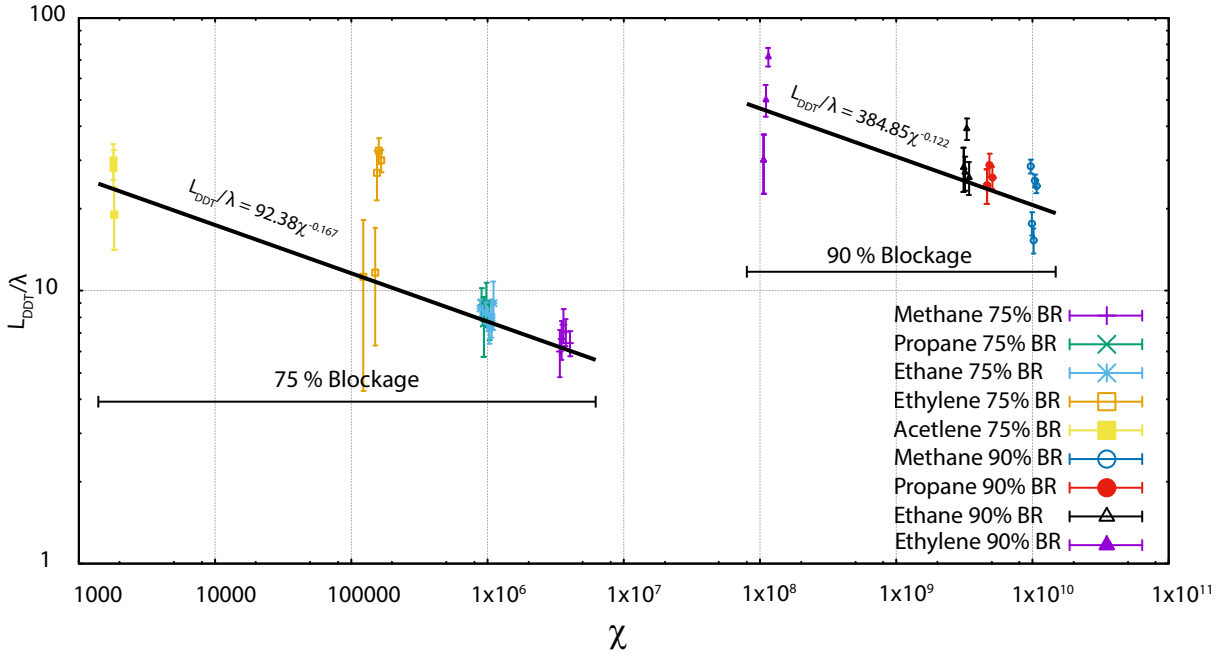


Figure 5.4: The correlation between (L_{DDT}/λ) and χ

5.2.2 Correlation with the Ignition Delay and 1D DDT Characteristic Length

In this section, we compared the DDT run-up distance L_{DDT} with another characteristic thermo-chemical length scale denoted as L_{1-D}. L_{1-D} is the distance that a 1D shock, traveling at the computed CJ deflagration speed would propagate before receiving pressure perturbations from the ignition events occuring at the flame. It provides a characteristic distance for DDT in 1D [42]. The definition of this length scale is illustrated in Figure 5.5. After being shocked, a fluid particle is convected at speed u and ignites after an ignition delay time (t_{ig}). After ignition, a forward facing compression wave caused by the expansion of that particle will propagate at a characteristic speed $u + c$ and will catch up with the front shock. We get:

$$L_{1-D} = ct_{ig}(\frac{u+c}{D_{deflagration}} - 1)^{-1} \tag{5.2}$$

Clearly, the ignition delay controls this characteristic length scale. Shorter ignition delay times will lead to shorter L_{1-D}. The state behind the shock was computed using the NASA CEA code[19], while the ignition delays were evaluated assuming negligible specific volume change using CANTERA [18] and the GRI-3.0 mechanism [44] for methane, sandiego2009 [52] for propane, and Wang-highT for ethane, ethylene and acetylene [32].

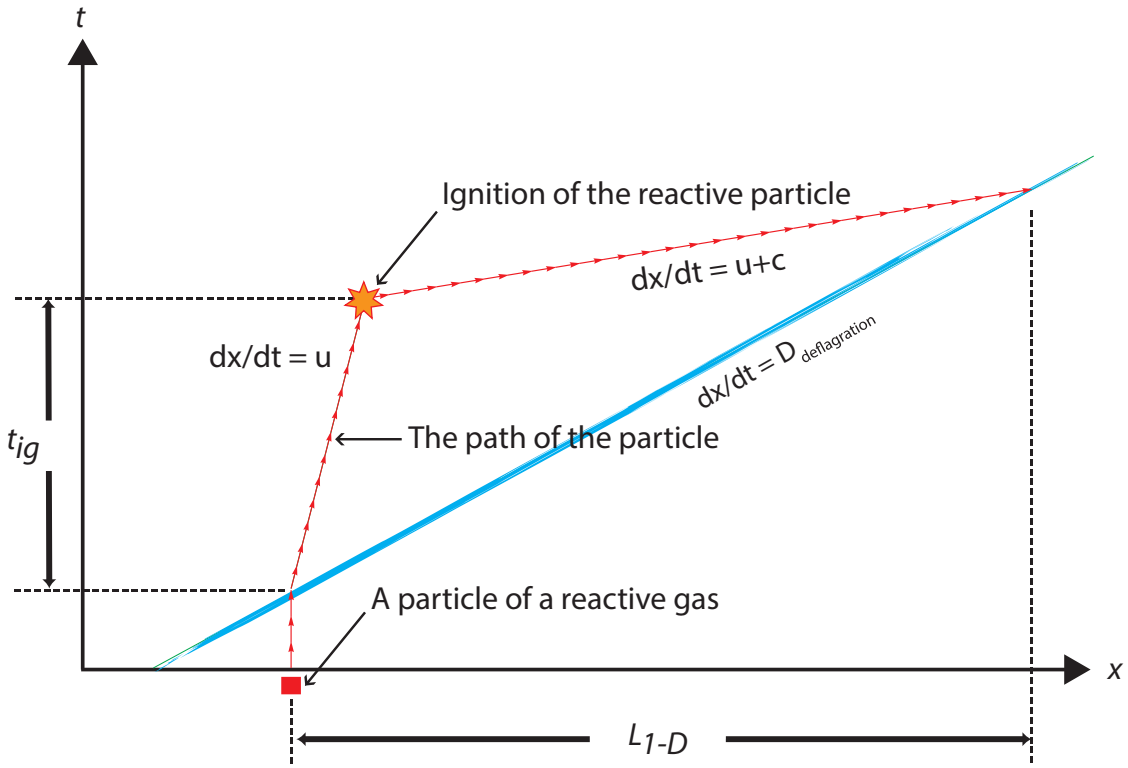


Figure 5.5: A space time diagram illustrating the L_{1-D} distance

Figure 5.6 shows the relation between the computed L_{1-D} characteristic length scale and the initial pressure of the mixtures for 75% and 90% blockage ratio. As seen in the figure, increasing the initial pressure resulted in decreasing the L_{1-D} distance, and this effect was mainly due to the shorter ignition delay times t_{ig}. We can also observe the effect of changing the blockage ratio on that distance. For each mixture, when we compare the results of the 75% and 90% blockage ratio, we can see that higher blockage ratio resulted in a higher L_{1-D}, and this was due to the weaker transmitted shock, leading to longer ignition delay times.

It can be seen that the shortest L_{1-D} distance was for acetylene-argon at 75% blockage ratio. This distance was 0.2 m. The longest L_{1-D} distance was for methane at 90% blockage ratio, with a value of 3.7x10^5 m. A summary of all the results from that graph are reported in Table 5.2.2.

Figure 5.7 shows the relation between L_{1-D} and L_{DDT}. The data from Figure 5.7 shows that L_{1-D} varies by seven orders of magnitude, because of the changes in the ignition delay times (t_{ig}) associated with the different thermo-chemical properties of the mixtures tested, while L_{DDT} varies only between 0.1 and 0.9 m, which is just the length of the channel. The dependence of L_{DDT} on L_{1-D} was fitted by a power law, yielding

$$L_{DDT} = 0.212{L_{1-D}}^{0.0676} \tag{5.3}$$

The smallness of the exponent thus suggests that no correlation can be drawn with this characteristic length scale. This is not surprising, since the role of fluctuations in the lead shock strength is not incorporated in the correlation.

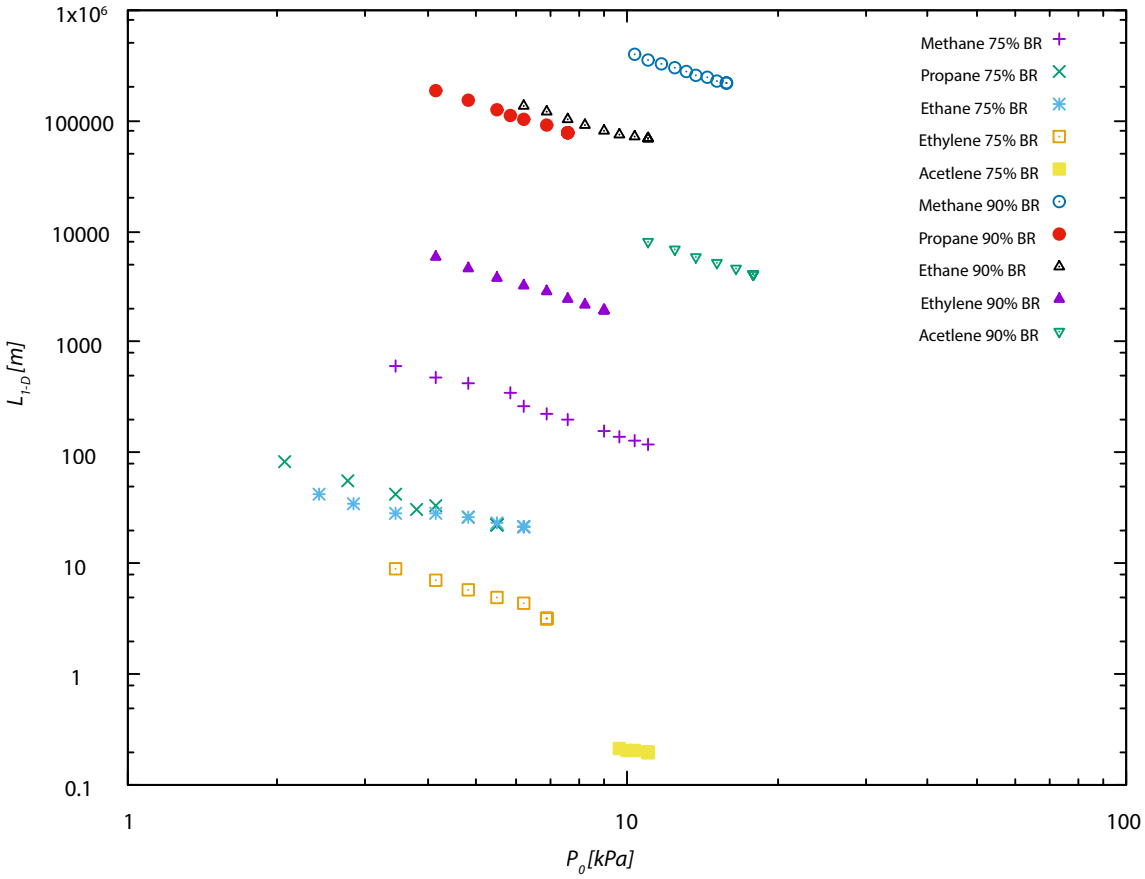


Figure 5.6: The correlation between the initial pressure p_0 and the characteristic length L_{1-D}.

Table 5.4: L_{1-D} and pressure correlations for methane, propane, ethane, ethylene, acetylene as a function of L_{1-D} [m] $= \theta$ $[p_0[\text{kPa}]]^{-\phi}$

	Mixture	θ	ϕ
75% Blockage Ratio			
	Methane	3915.3	1.459
	Propane	209.91	1.319
	Ethane	61.437	0.578
	Ethylene	59.57	1.495
	Acetylene	1.1658	0.745
90% Blockage Ratio			
	Methane	$9 * 10^6$	1.357
	Propane	$1 * 10^6$	1.453
	Ethane	$1 * 10^6$	1.192
	Ethylene	45258	1.445
	Acetylene	219525	1.379

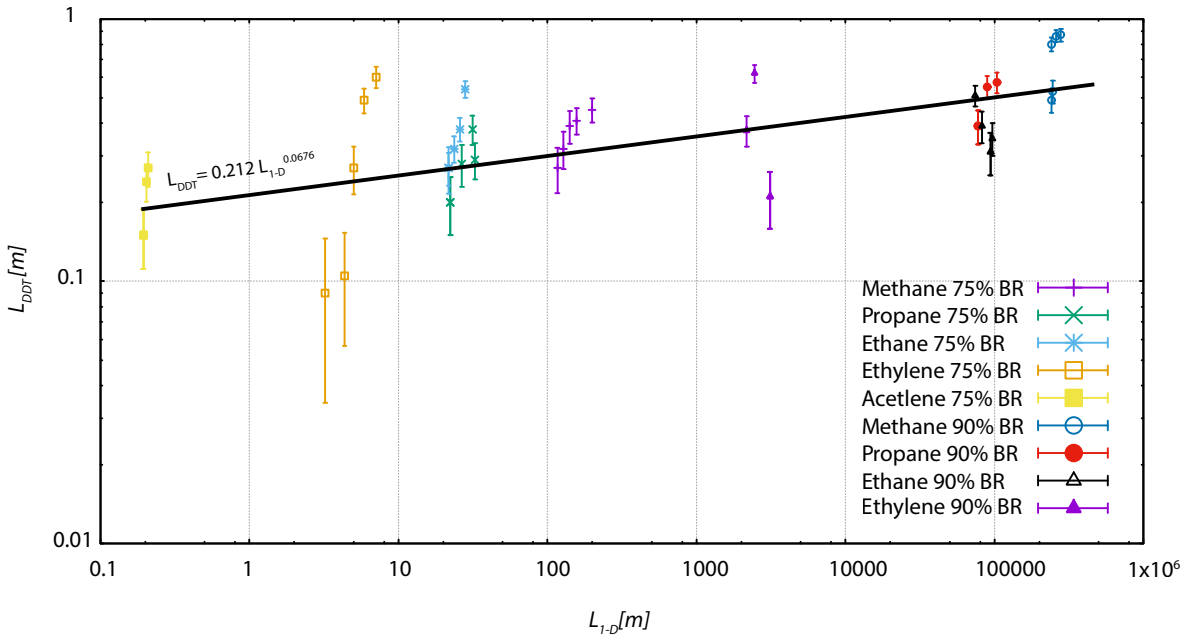


Figure 5.7: The correlation between the run up distance from deflagration to detonation (L_{DDT}) distance and L_{1-D}.

To reconcile the role of fluctuations, we investigated the influence of χ on a correlation with L_{1D}. Figure 5.8 shows the correlation between L_{DDT}/L_{1D} and χ. An excellent correlation is evident. A power-law fit, also shown in the figure yields

$$\frac{L_{DDT}}{L_{1-D}} = 1042.6\chi^{-0.861} \tag{5.4}$$

We can see that all the data fit the correlation well despite the changes in mixture's thermo-chemical properties, sensitivity, and change in blockage ratios. Higher values of χ resulted in shorter (L_{DDT}/L_{1-D}) ratios, highlighting the importance of the formation of hot spots in shortening this distance. This result also indicates that unstable mixtures with high χ values will detonate earlier than stable ones with lower values of χ. An unstable mixture's ability to generate hot spots is believed to be the main cause for their higher detonability. This resulted in a shorter L_{DDT}/L_{1-D}.

The results from Chapter 4, for methane and acetylene-argon, shows how fundamentally the structure of Mach reflections and the presence of hot spots away from the obstacles field can be linked to the correlation of (L_{DDT}/L_{1-D}) and χ. The ratio of (L_{DDT}/L_{1-D}) was almost unity for acetylene-argon at 75% blockage ratio, which corresponds to a lowest value of χ. The images obtained for acetylene-argon in Figures 4.32 and 4.34 of section 4.5 confirm these results, as there were no hotspots detected downstream.

On the contrary, the ratio (L_{DDT}/L_{1-D}) has been observed to be very small for methane at 75%, when compared to acetylene-argon, corresponding to a value of 0.003. The L_{DDT} distance was shorter than the theoretical L_{1-D}, and that was mainly because the formed hot spots, causing the flames to accelerate and detonate faster than was expected theoretically for flames assumed to receive no pressure perturbations. This conclusion can be supported by the high value of χ, as it reaches $400\text{x}10^6$. The images from section 4.1 support these findings, with hot spots seen downstream. In some other cases, these hotspot ignitions cause the flame-shock complex to re-initiate into detonation.

Changing the blockage ratio to 90% resulted in higher χ values. The high values of χ caused the mixtures to be unstable, and more sensitive to temperature fluctuations, and this resulted in hotspot generation that caused the (L_{DDT}/L_{1-D}) to be very short, as seen in methane with 90% with a value of (L_{DDT}/L_{1-D})=$250\text{x}10^{-6}$, and χ= $1\text{x}10^{10}$.

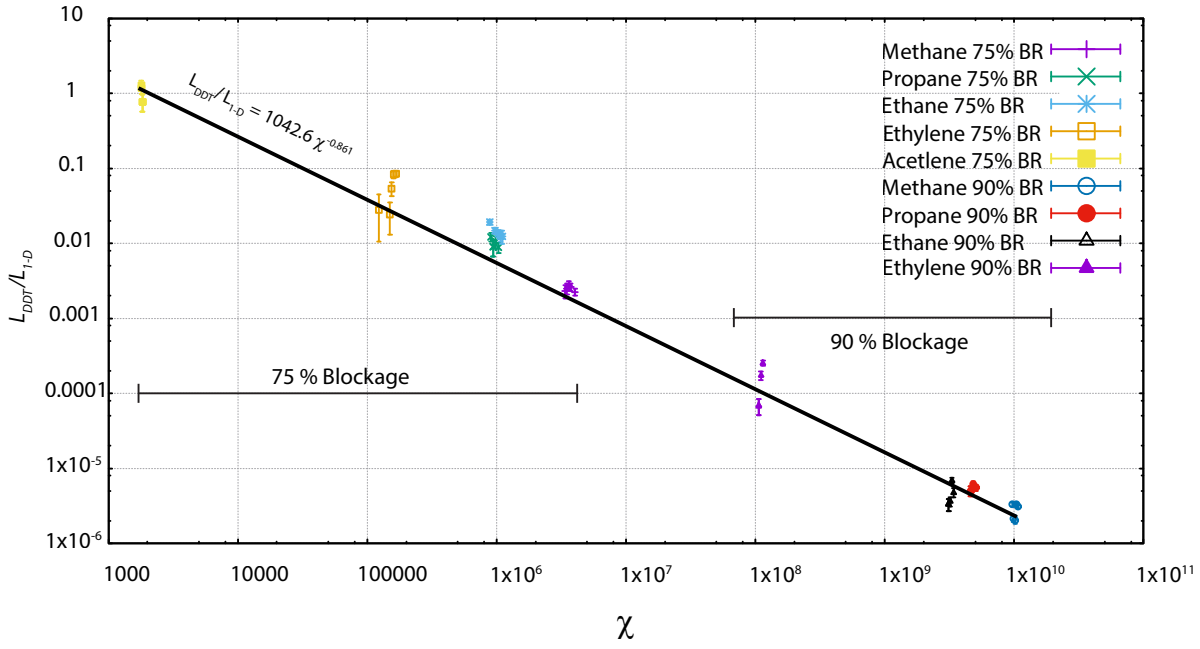


Figure 5.8: The correlation between (L_{DDT}/L_{1-D}) and χ

The correlation of Figure 5.8 indicates an approximate inverse relationship of the form:

$$\frac{L_{DDT}}{L_{1D}} \propto \chi^{-1} \tag{5.5}$$

From the definitions of L_{1D} and χ given by (5.2) and (1.1), we see that the ignition delay t_{ig} drops out from the correlation, which becomes:

$$L_{DDT} \backsimeq (\frac{L_{1D}}{\chi}) \backsimeq ct_r(\frac{E_a}{RT})^{-1} \tag{5.6}$$

The data have thus been re-plotted in Figure 5.9, which indeed shows that DDT length normalized by ct_r, which is the characteristic length of the reaction zone, remains nearly constant for sufficiently large χ, i.e., for sufficiently unstable mixtures. The correlation takes the form of

$$L_{DDT} \simeq 3000ct_r \tag{5.7}$$

The results of the last correlation indicate that the sole chemical kinetic timescale of importance in the DDT process of fast flames is the characteristic energy release time in a

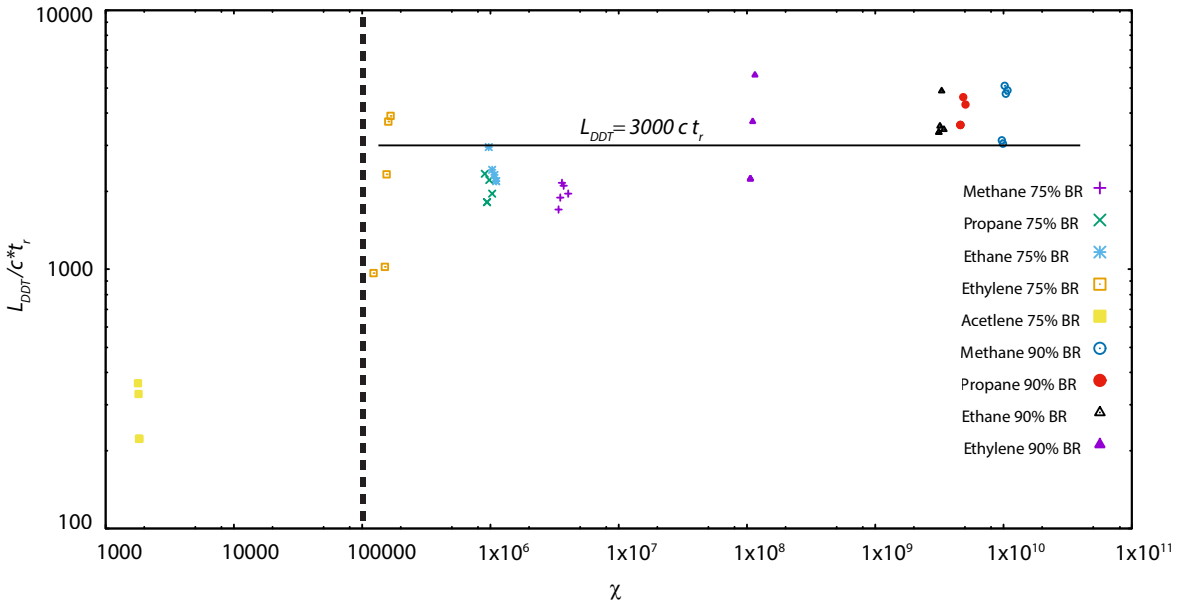


Figure 5.9: The variation of L_{DDT}/ct_r with χ

fluid particle t_r. This finding is compatible with Sharpe's treatment of DDT behind a lead shock in an individual hotspot[42], and substantiated by Tang and Radulescu's results [46], which showed that the acceleration of an individual hotspot front is controlled by the inverse of t_r, multiplied by the reduced activation energy $\frac{E_a}{RT}$. It is nevertheless quite remarkable that the same result appears to hold in a much more complicated scenario of a multi-hotspot ignition.

Chapter 6

Conclusion

6.1 Contributions to the State of Knowledge

The main contributions to the state of knowledge of the present thesis are as follows:

1. For most of the tests that resulted in DDT, the measured speed of the fast flame was found in very good agreement with the model introduced by Radulescu et al. [37], which assumed the reaction zone to be a Chapman-Jouguet deflagration. This confirms earlier observations that a sufficient condition for DDT is the acceleration of the flame to the Chapman-Jouguet critical deflagration velocity, as first suggested by Taylor and Tankin [47]. Some deviations from the model were observed in experiments conducted with 90% blockage ratio and were mainly due to the weaker transmitted shock that resulted in lower post shock temperatures and slower reaction rates.

2. In the present study, we attempted correlations of the DDT lengths obtained experimentally with different chemical kinetic length scales: the detonation cell size λ, and two characteristic lengths based on the ignition delay and reaction time.

   The correlations for L_{DDT}/λ were found to depend on the stability parameter χ for each blockage ratio investigated. The correlations showed a decreasing trend with χ, indicating that DDT is more likely in a more unstable mixture for the same cell

size. The results from the high speed camera confirmed this conclusion, as mixtures with high values of χ showed an organization of the flame-shock complex into fewer modes, favoring hot-spot ignition. Mixtures with low values of χ were found less likely to sustain fast flames, with hot spots not being observed in the far field.

The correlations also indicate that the 1D characteristic DDT length L_{1D}, based on the ignition delay evaluated for the average shock speed, is not an appropriate length scale to evaluate the propensity for DDT. This was suggested to be due to the wide variability in ignition delays in a medium with strong fluctuations. Instead, it was found that the main chemical kinetic timescale of importance in the DDT process is the characteristic energy release time in a fluid particle t_r. For sufficiently unstable mixtures with a high χ value in which hot-spot ignition was found to play an important role, a unique correlation was found between L_{DDT} and the reaction time t_r. This observation is in accord with the results obtained by Sharpe [42] and Tang and Radulescu [46], who showed that the acceleration of a fast flame from an individual hot spot is controlled by the inverse of the reaction time t_r.

6.2 Future Work

The present work showed that hot-spot ignition, which is favored in mixtures with sensitive kinetic rates to temperature fluctuations, favors DDT. Further quantification of this effect should rely on more detailed measurements linking the distribution of fluctuations at the front with the hot-spot distribution and their collective dynamics, in order to gain more insight into the empirical correlations proposed in the present study.

APPENDICES

Appendix A

75% Blockage Ratio Experiments

The full record of the shadow graphs experiments for the 75% blockage ratio configuration that has been discussed above.

A.1 Methane

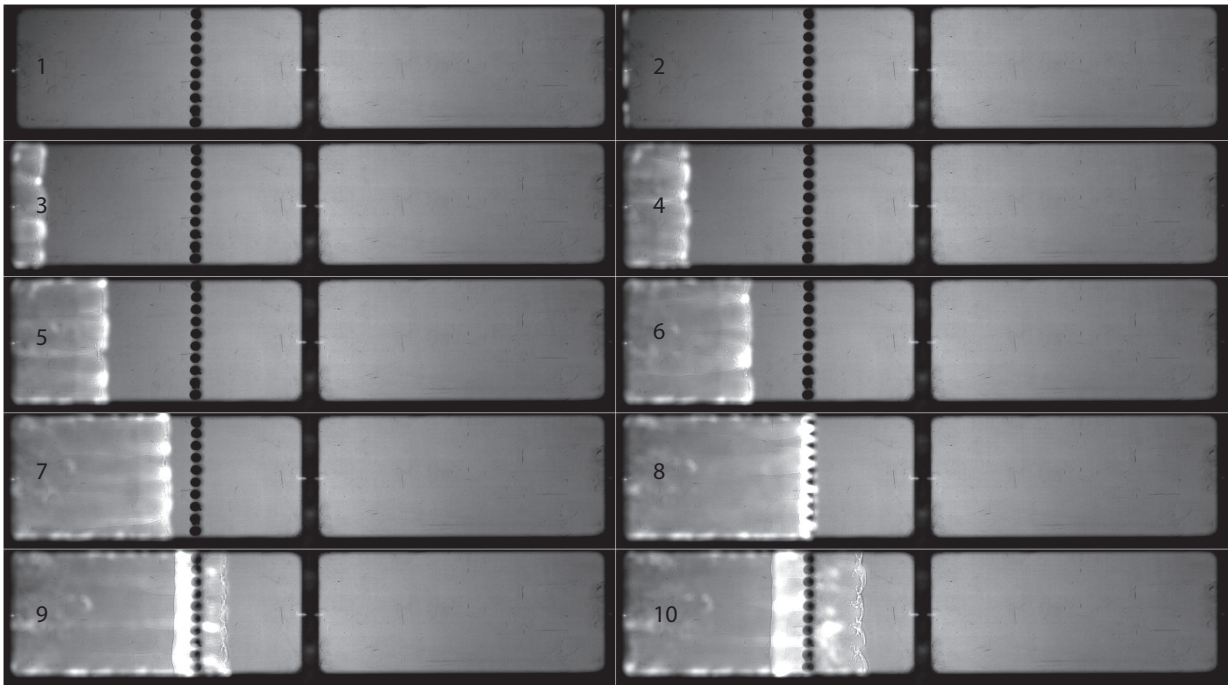


Figure A.1: The full record of the Shadowgraph images illustrating the re-initiation of detonation after interacting with obstacles in CH_4+$2O_2$, p_0=10.3 KPa. Recorded at 23.76 μs interframe, 1 μs exposure, 42049 fps

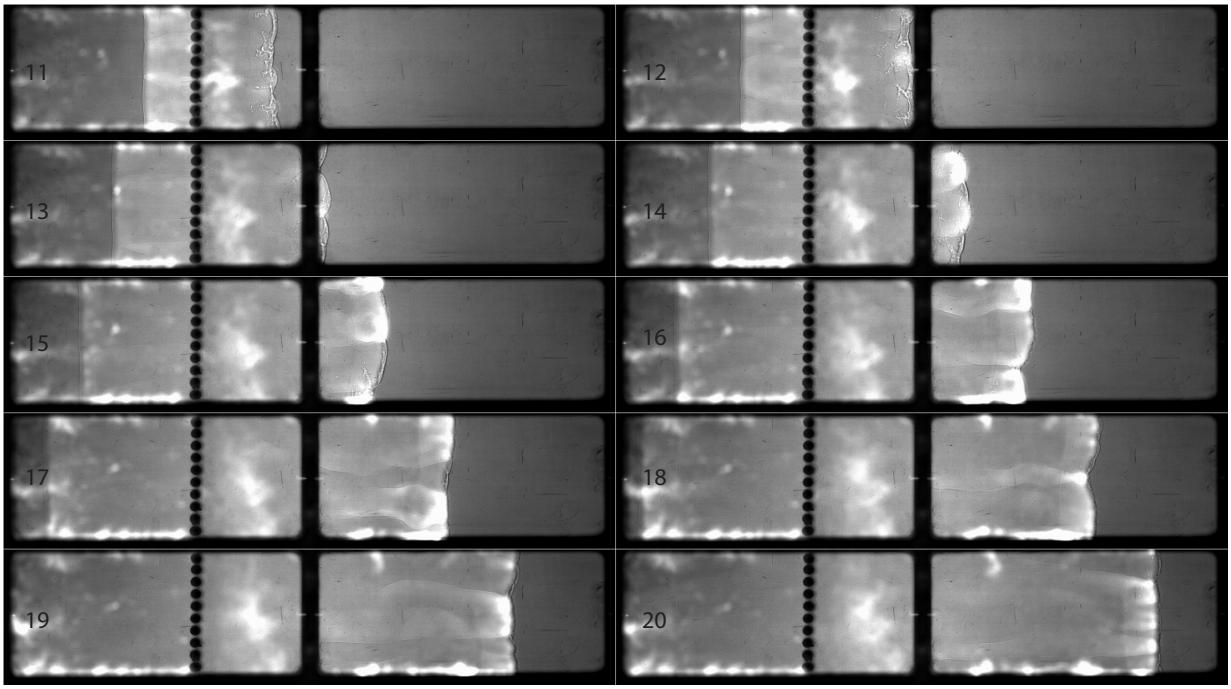


Figure A.2: The full record of the Shadowgraph images illustrating the re-initiation of detonation after interacting with obstacles in CH_4+$2O_2$, p_0=10.3 KPa. Recorded at 23.76 μs interframe, 1 μs exposure, 42049 fps

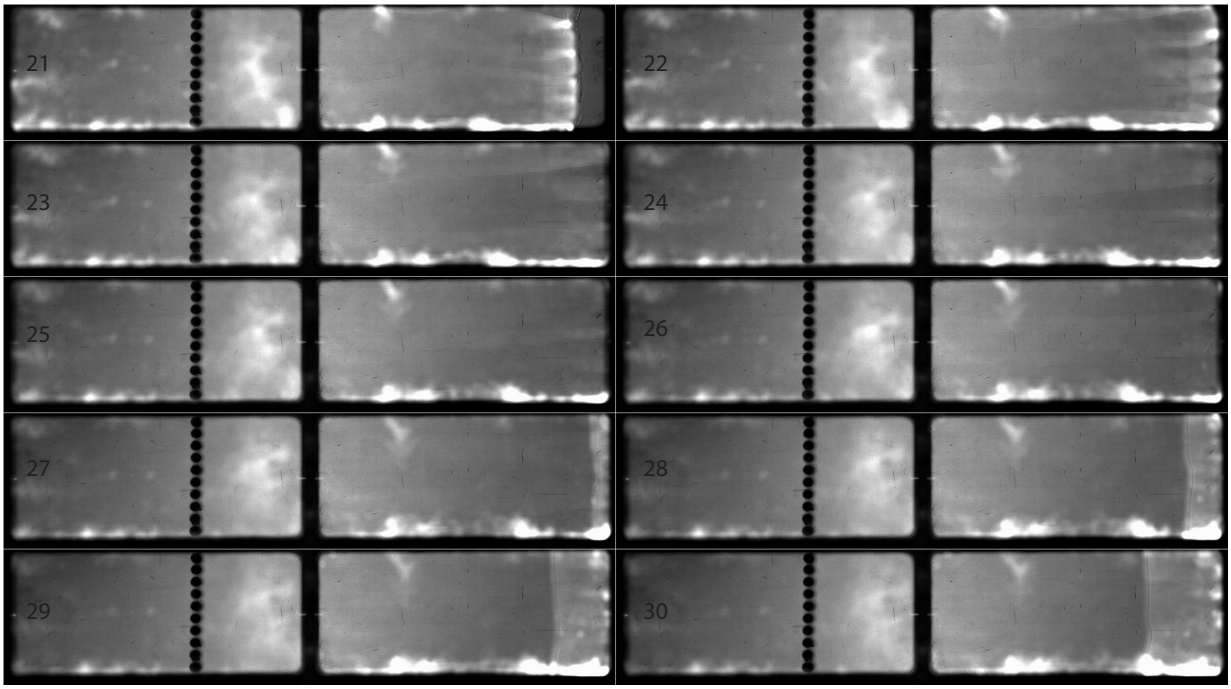


Figure A.3: The full record of the Shadowgraph images illustrating the re-initiation of detonation after interacting with obstacles in CH_4+$2O_2$, p_0=10.3 kPa (1.5 psi). Recorded at 23.76 μs interframe, 1 μs exposure, 42049 fps

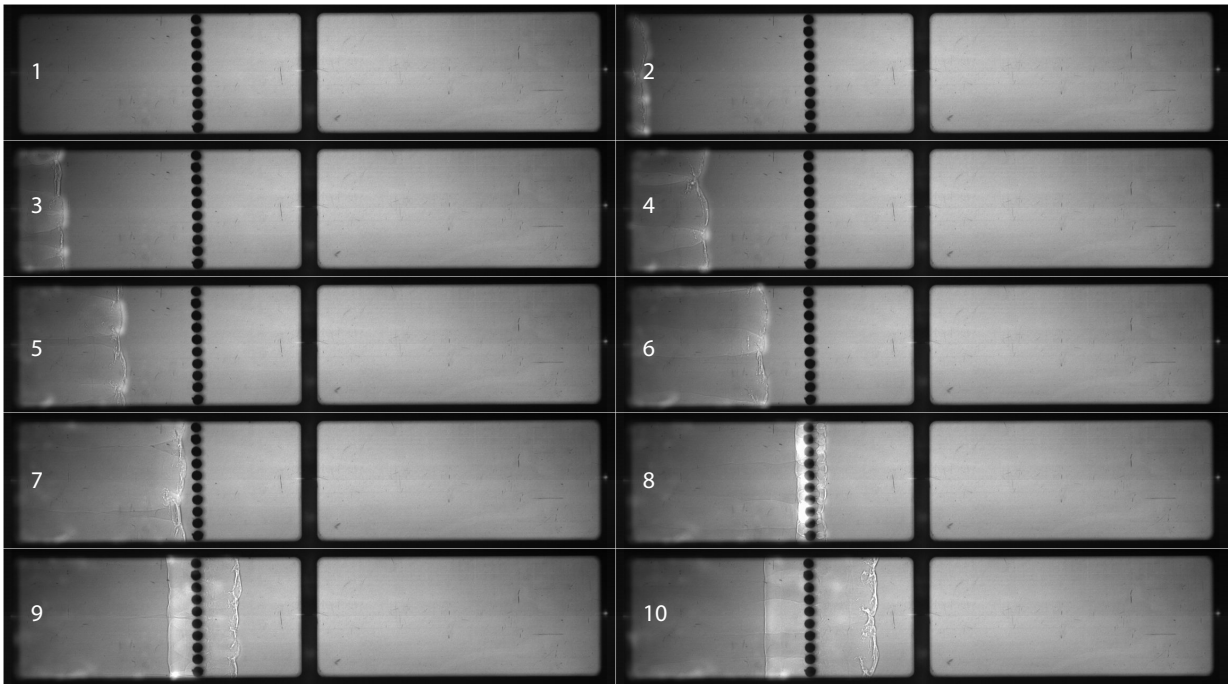


Figure A.4: The full record of the Shadowgraph images illustrating the re-initiation of detonation after interacting with obstacles in CH_4+$2O_2$, p_0=8.2 kPa (1.2 psi). Recorded at 23.76 μs interframe, 1 μs exposure, 42049 fps

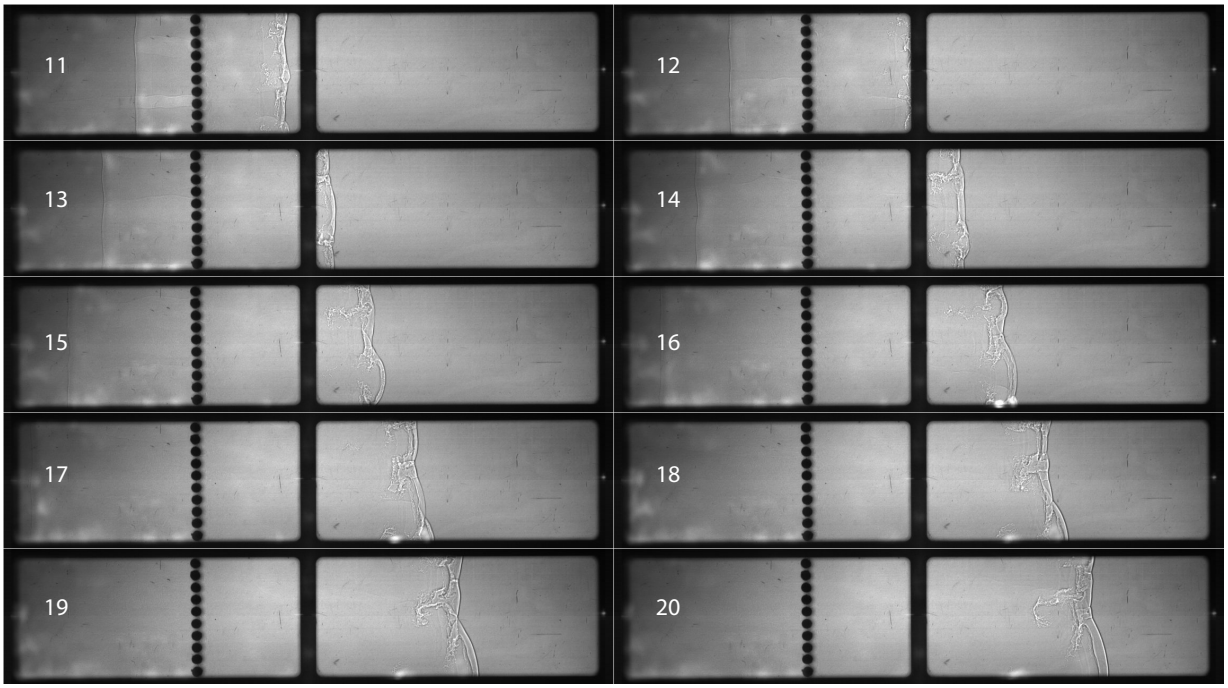


Figure A.5: The full record of the Shadowgraph images illustrating the re-initiation of detonation after interacting with obstacles in CH_4+$2O_2$, p_0=8.2 kPa (1.2 psi). Recorded at 23.76 μs interframe, 1 μs exposure, 42049 fps



Figure A.6: The full record of the Shadowgraph images illustrating the re-initiation of detonation after interacting with obstacles in CH_4+$2O_2$, p_0=8.2 kPa (1.2 psi). Recorded at 23.76 μs interframe, 1 μs exposure, 42049 fps

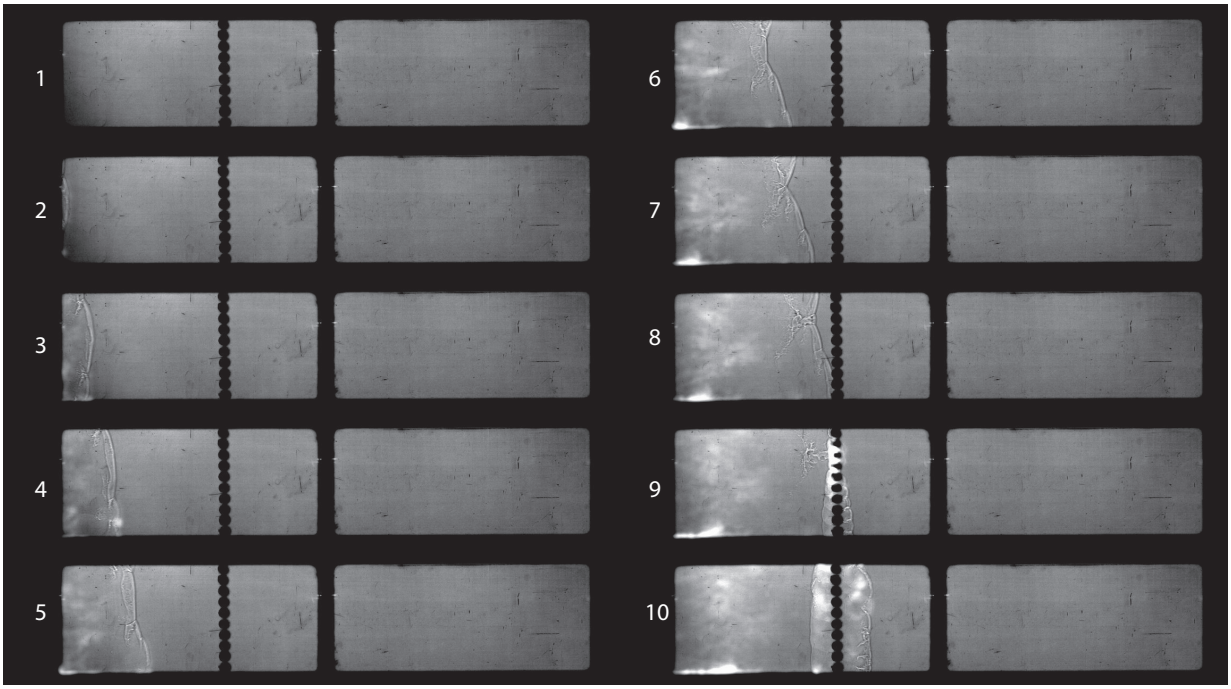


Figure A.7: The full record of the Shadowgraph images illustrating the re-initiation of detonation after interacting with obstacles in CH_4+$2O_2$, p_0=3.4 kPa (0.5 psi). Recorded at 23.76 μs interframe, 1 μs exposure, 42049 fps

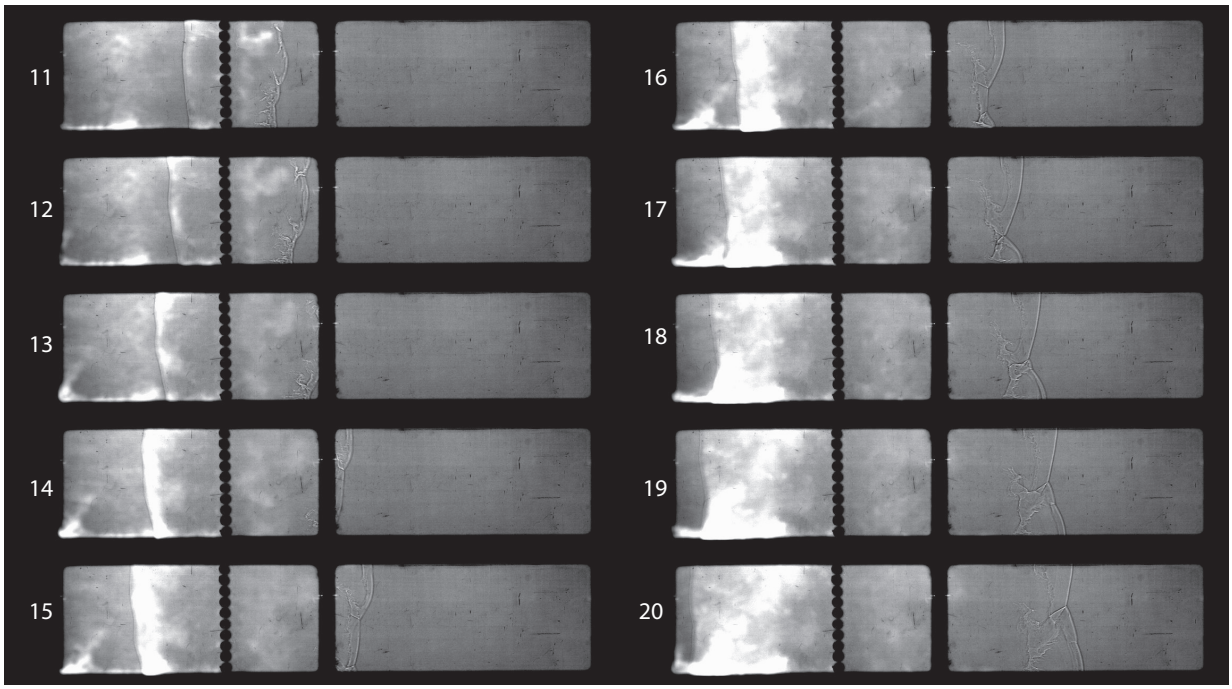


Figure A.8: The full record of the Shadowgraph images illustrating the re-initiation of detonation after interacting with obstacles in CH_4+2O_2, p_0=3.4 kPa (0.5 psi). Recorded at 23.76 μs interframe, 1 μs exposure, 42049 fps

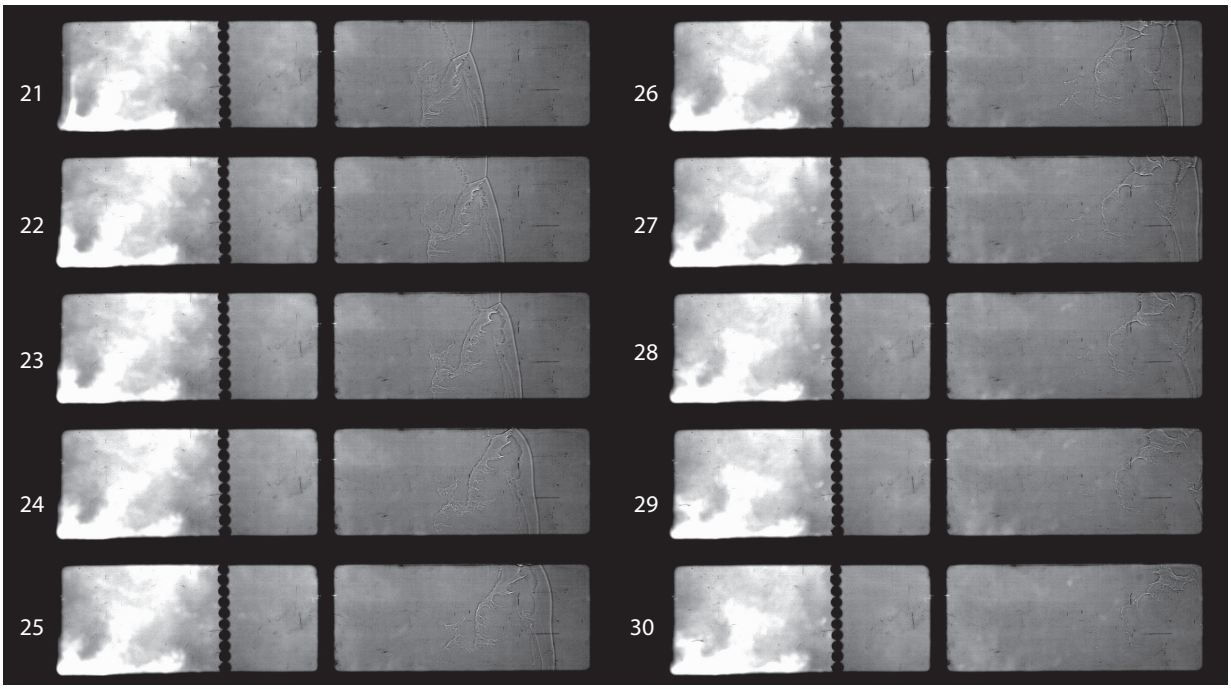


Figure A.9: The full record of the Shadowgraph images illustrating the re-initiation of detonation after interacting with obstacles in CH_4+2O_2, p_0=3.4 kPa (0.5 psi). Recorded at 23.76 μs interframe, 1 μs exposure, 42049 fps.

A.2 Ethane

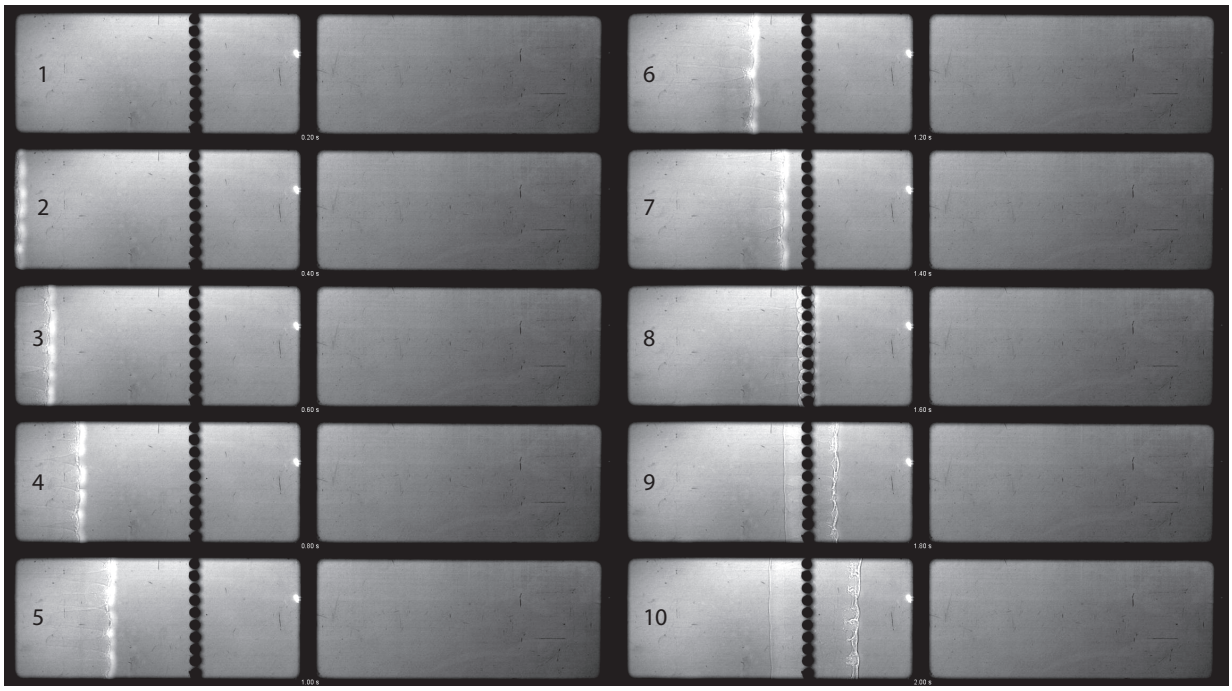


Figure A.10: The full record of the Shadowgraph images illustrating the re-initiation of detonation after interacting with obstacles in $2C_2H_6+7O_2$, p_0= 4.1 kPa(0.6 psi). Recorded at 23.53 μs interframe, 0.7 μs exposure, 42496 fps.

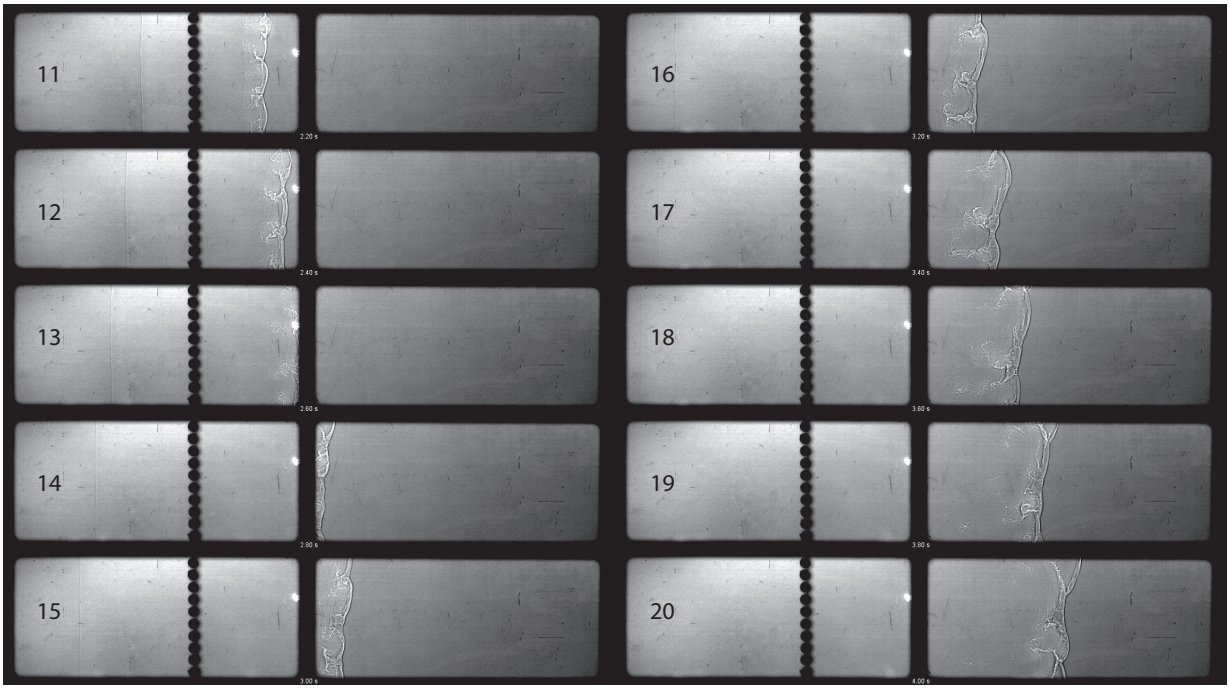


Figure A.11: The full record of the Shadowgraph images illustrating the re-initiation of detonation after interacting with obstacles in $2C_2H_6+7O_2$, p_0= 4.1 kPa(0.6 psi). Recorded at 23.53 μs interframe, 0.7 μs exposure, 42496 fps.

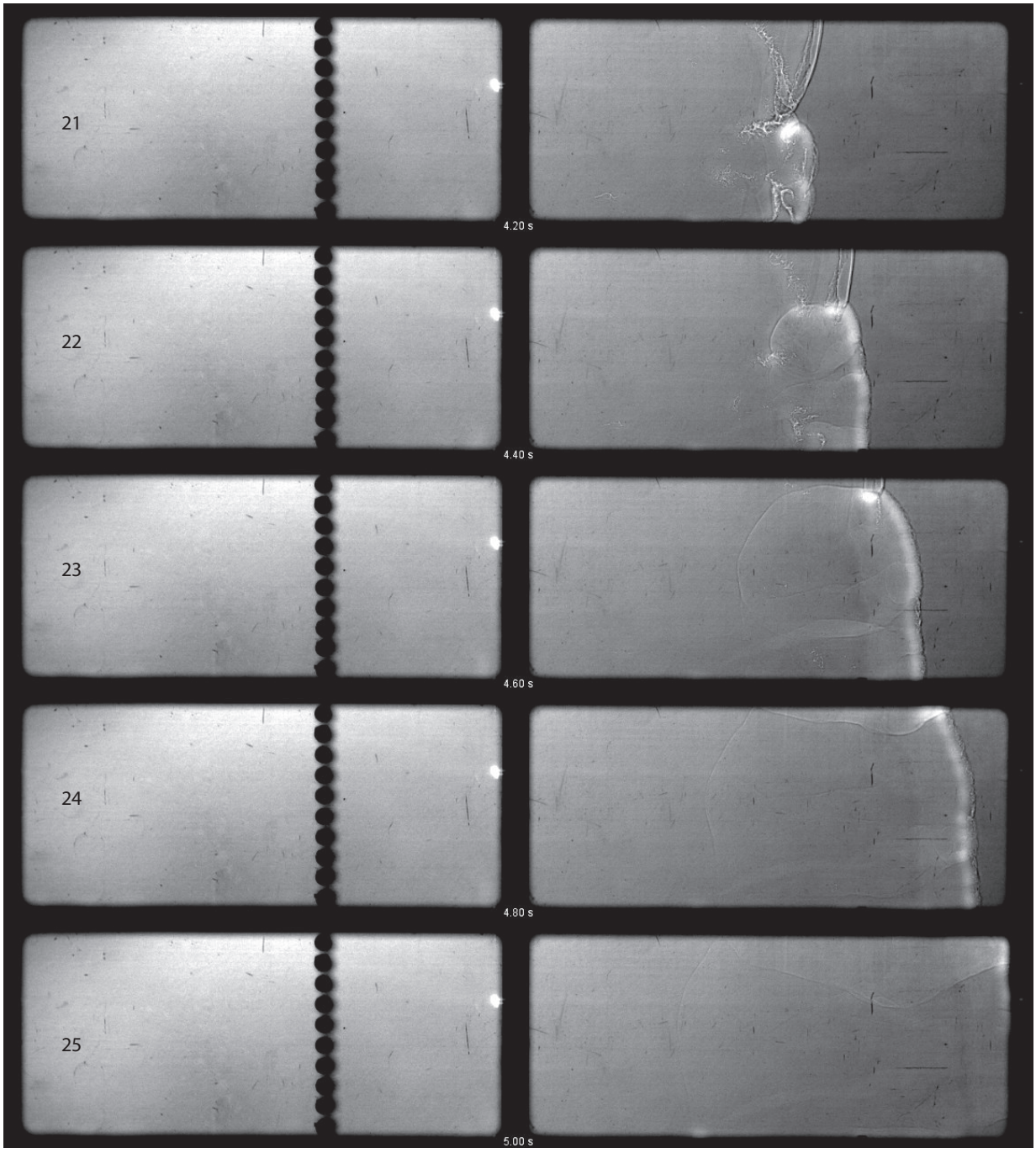


Figure A.12: The full record of the Shadowgraph images illustrating the re-initiation of detonation after interacting with obstacles in $2C_2H_6+7O_2$, p_0= 4.1 kPa(0.6 psi). Recorded at 23.53 μs interframe, 0.7 μs exposure, 42496 fps.

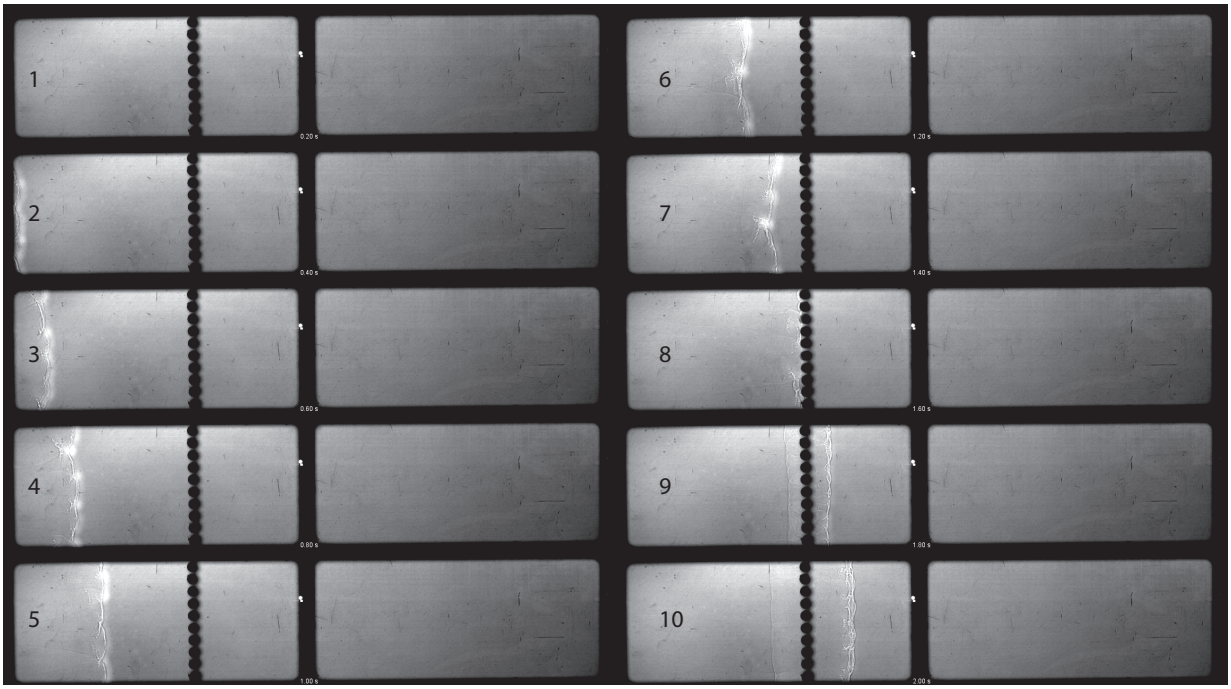


Figure A.13: The full record of the Shadowgraph images illustrating the failure of detonation after interacting with obstacles in $2C_2H_6+7O_2$, p_0=2.7 kPa(0.4 psi). Recorded at 23.53 μs interframe, 0.7 μs exposure, 42496 fps.

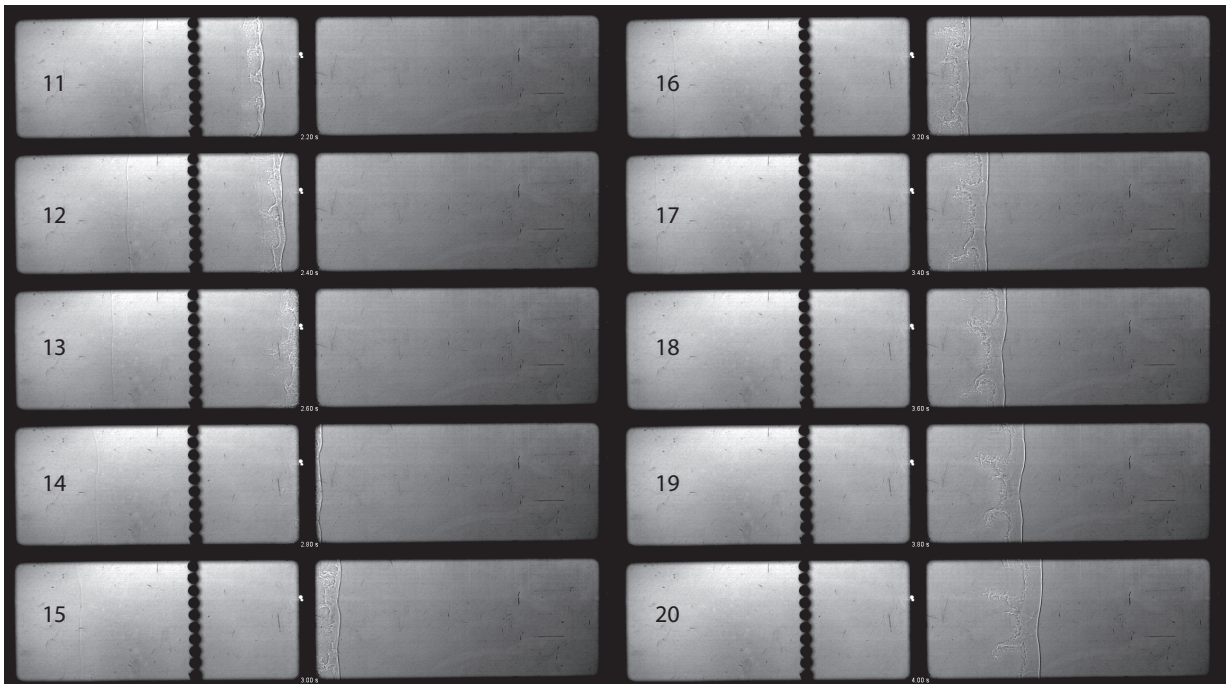


Figure A.14: The full record of the Shadowgraph images illustrating the failure of detonation after interacting with obstacles in $2C_2H_6+7O_2$, p_0=2.7 kPa(0.4 psi). Recorded at 23.53 μs interframe, 0.7 μs exposure, 42496 fps.

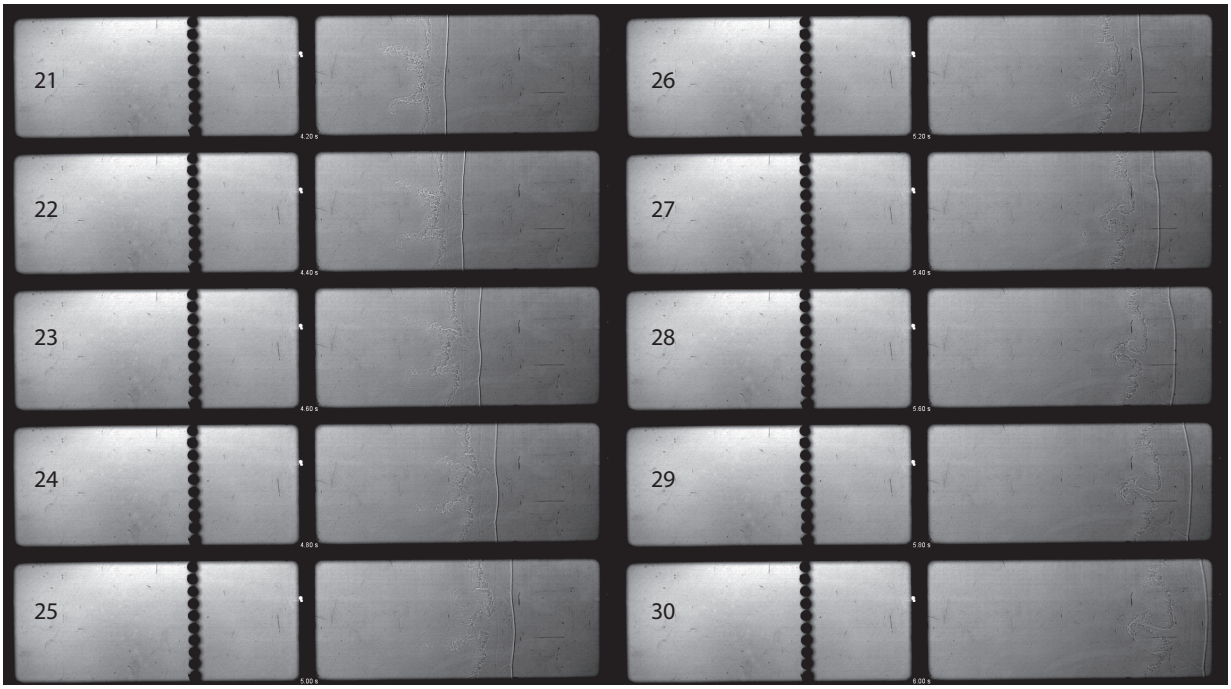


Figure A.15: The full record of the Shadowgraph images illustrating the failure of detonation after interacting with obstacles in $2C_2H_6+7O_2$, p_0=2.7 kPa(0.4 psi). Recorded at 23.53 μs interframe, 0.7 μs exposure, 42496 fps.

A.3 Ethylene

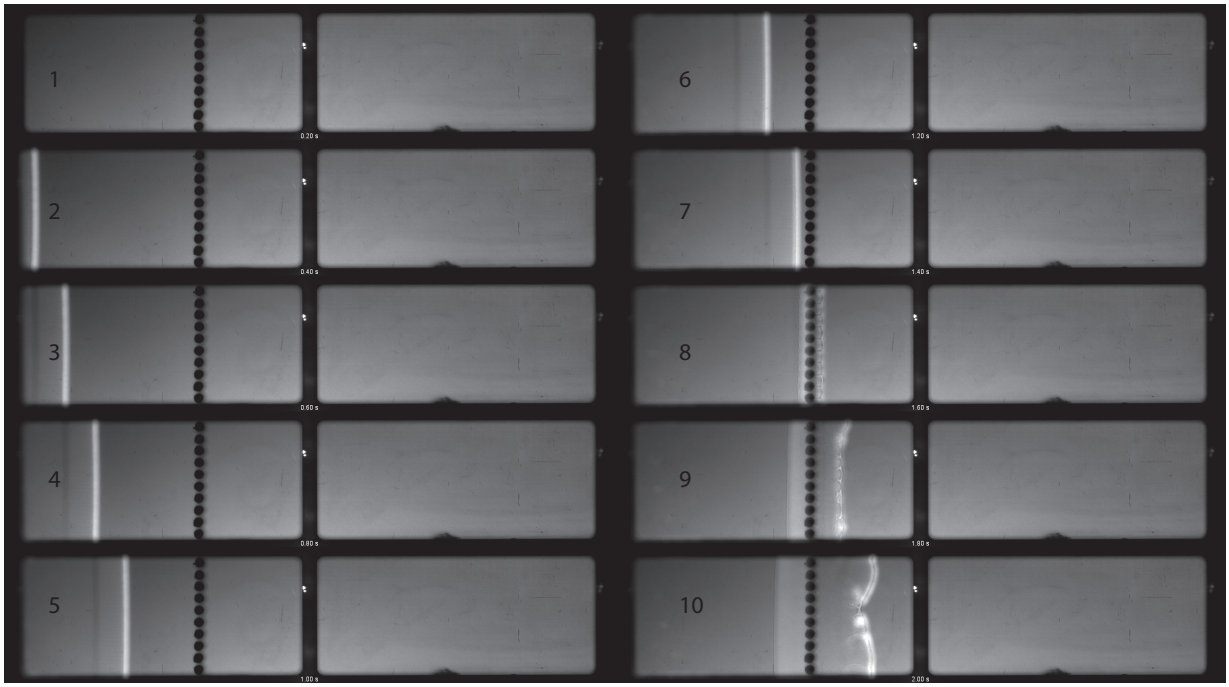


Figure A.16: The full record of the Shadowgraph images illustrating the re-initiation of detonation after interacting with obstacles in C_2H_4+$3O_2$, p_0=6.2 kPa (0.9 psi). Recorded at 23.53 μs interframe, 0.8 μs exposure, 42496 fps.

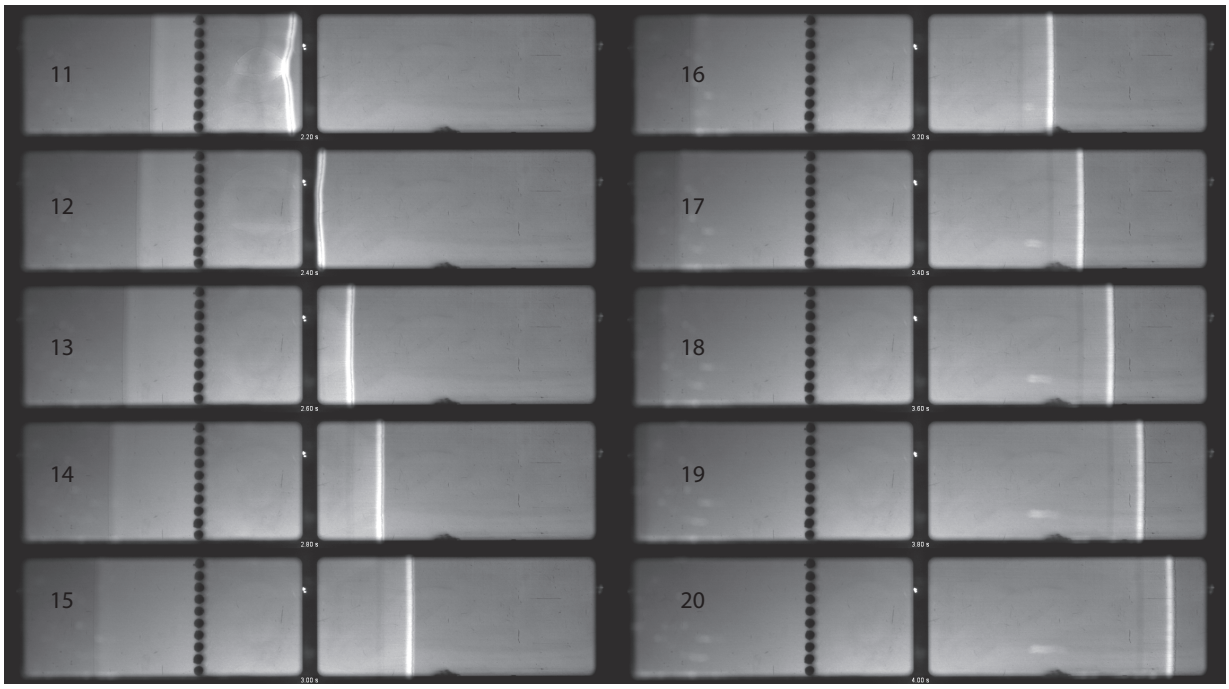


Figure A.17: The full record of the Shadowgraph images illustrating the re-initiation of detonation after interacting with obstacles in C_2H_4+$3O_2$, p_0=6.2 kPa (0.9 psi). Recorded at 23.53 μs interframe, 0.8 μs exposure, 42496 fps.

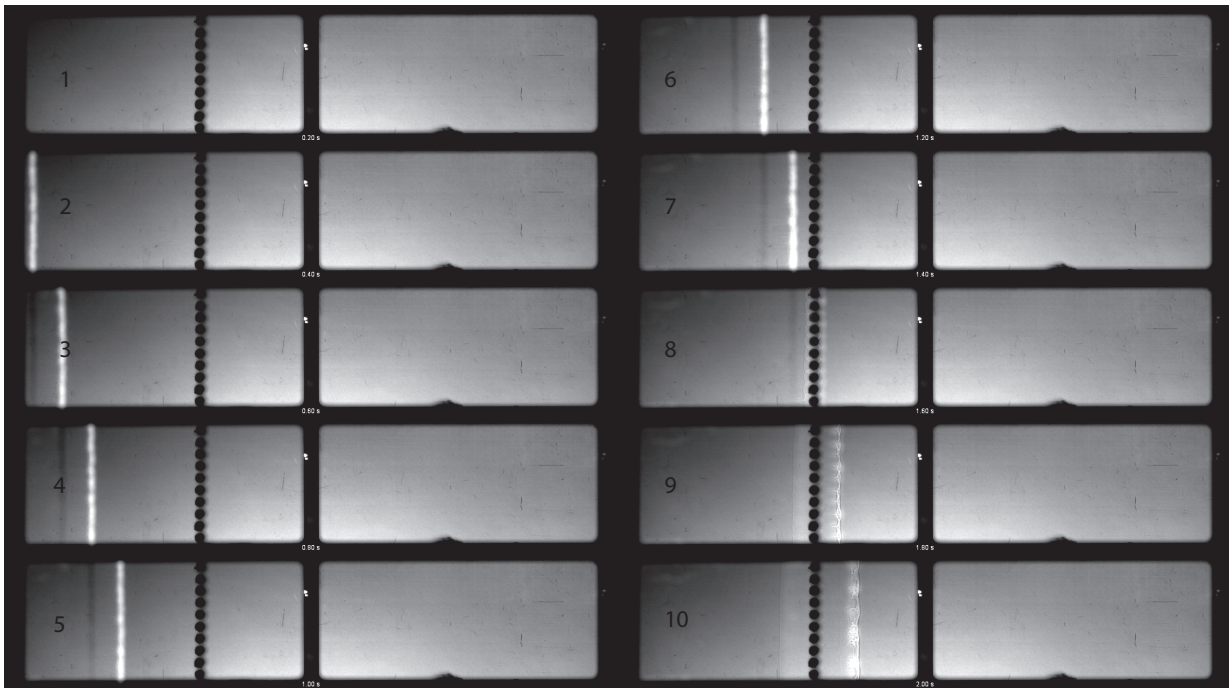


Figure A.18: The full record of the Shadowgraph images illustrating the failure of detonation after interacting with obstacles in C_2H_4+$3O_2$, p_0=3.4 kPa (0.5 psi). Recorded at 23.53 μs interframe, 0.8 μs exposure, 42496 fps.

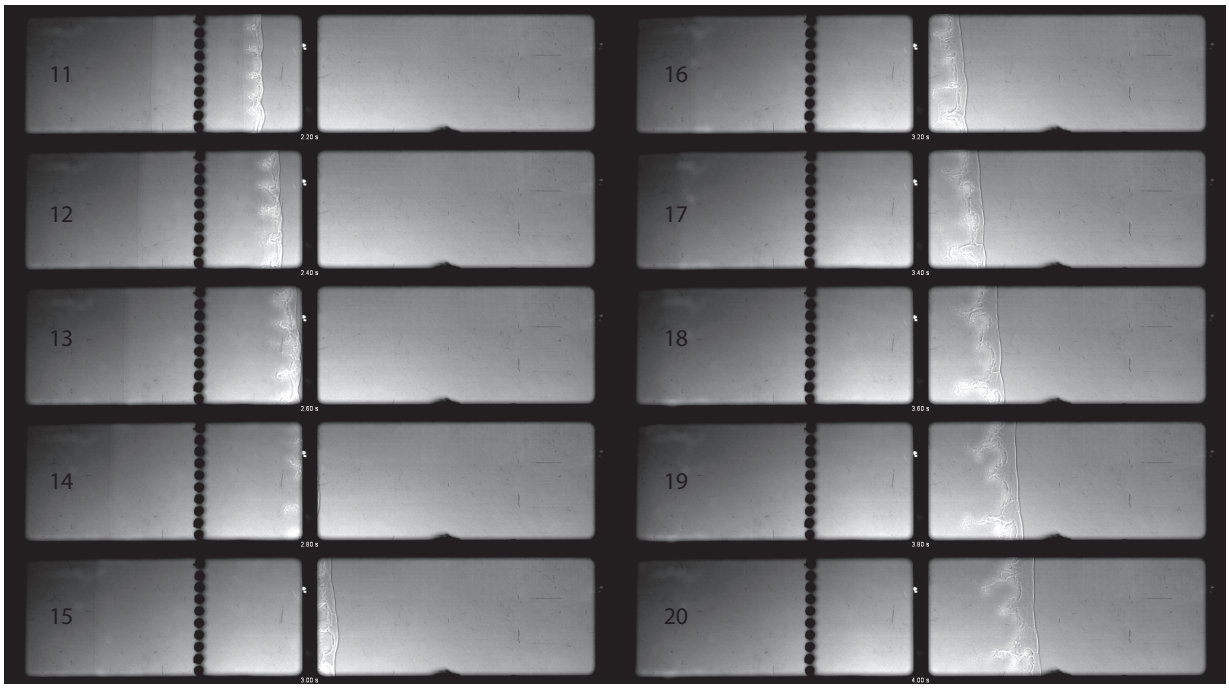


Figure A.19: The full record of the Shadowgraph images illustrating the failure of detonation after interacting with obstacles in C_2H_4+$3O_2$, p_0=3.4 kPa (0.5 psi). Recorded at 23.53 μs interframe, 0.8 μs exposure, 42496 fps.

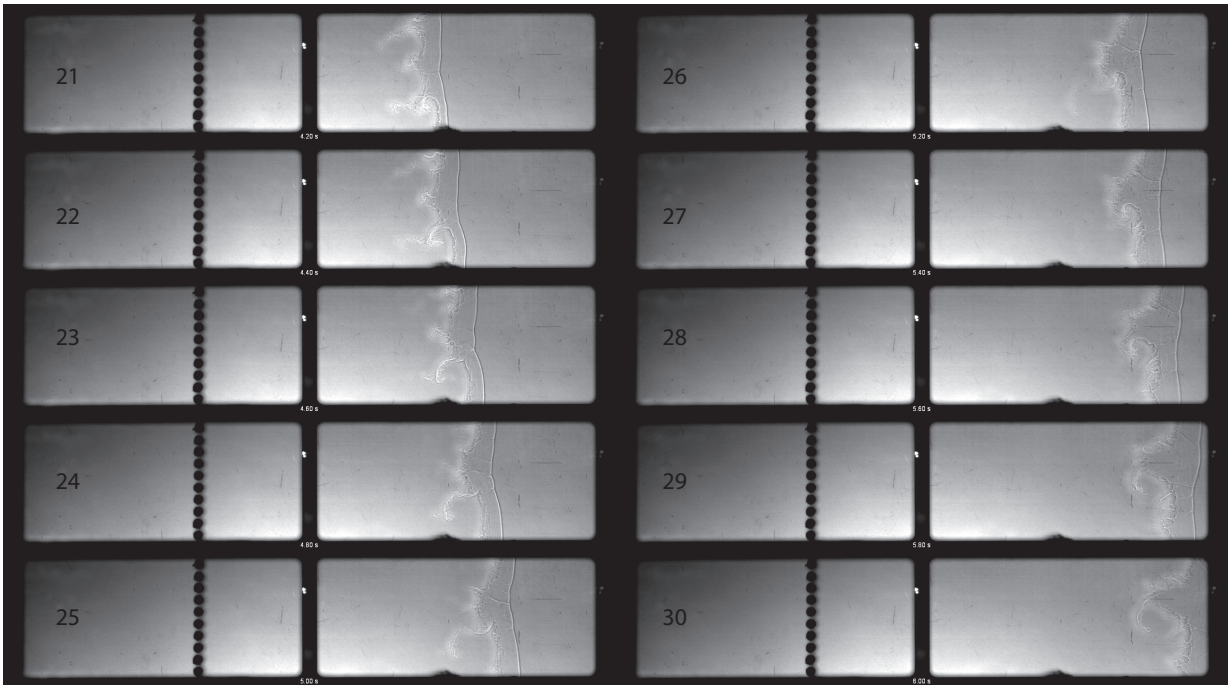


Figure A.20: The full record of the Shadowgraph images illustrating the failure of detonation after interacting with obstacles in C_2H_4+$3O_2$, p_0=3.4 kPa (0.5 psi). Recorded at 23.53 μs interframe, 0.8 μs exposure, 42496 fps.

A.4 Acetylene

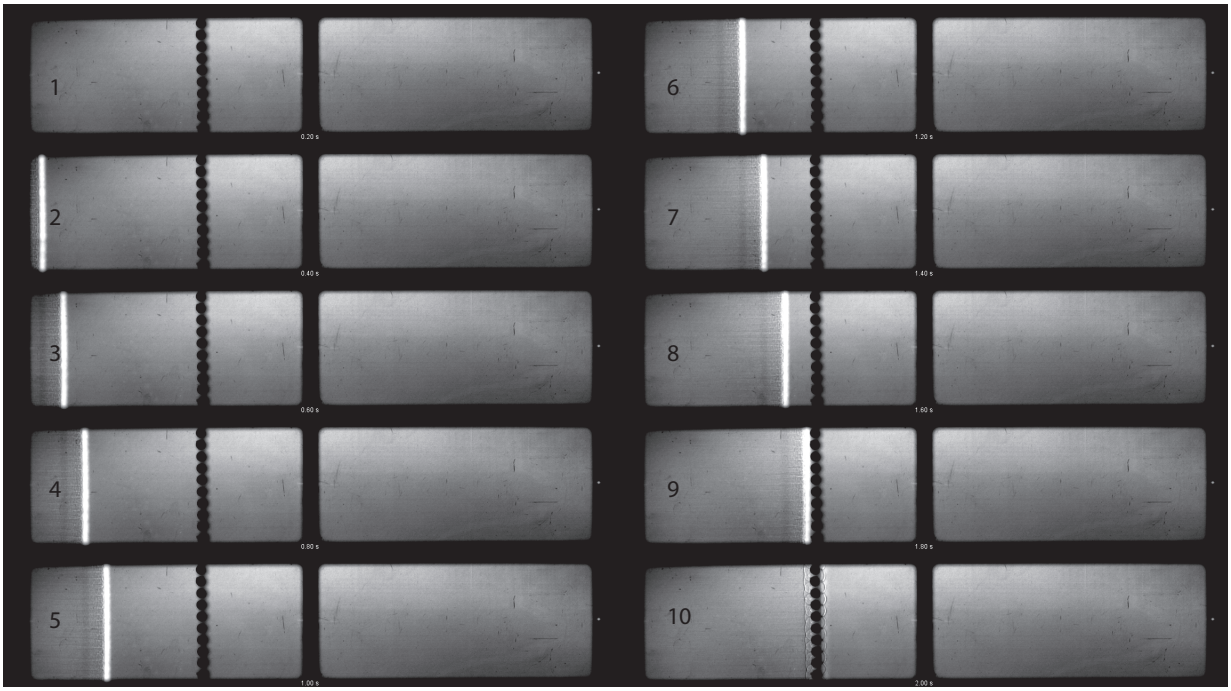


Figure A.21: The full record of the Shadowgraph images illustrating the re-initiation of detonation after interacting with obstacles in $2C_2H_2+5O_2+21Ar$, p_0=11.0 kPa (1.6 psi). Recorded at 23.53 μs interframe, 0.8 μs exposure, 42496 fps.

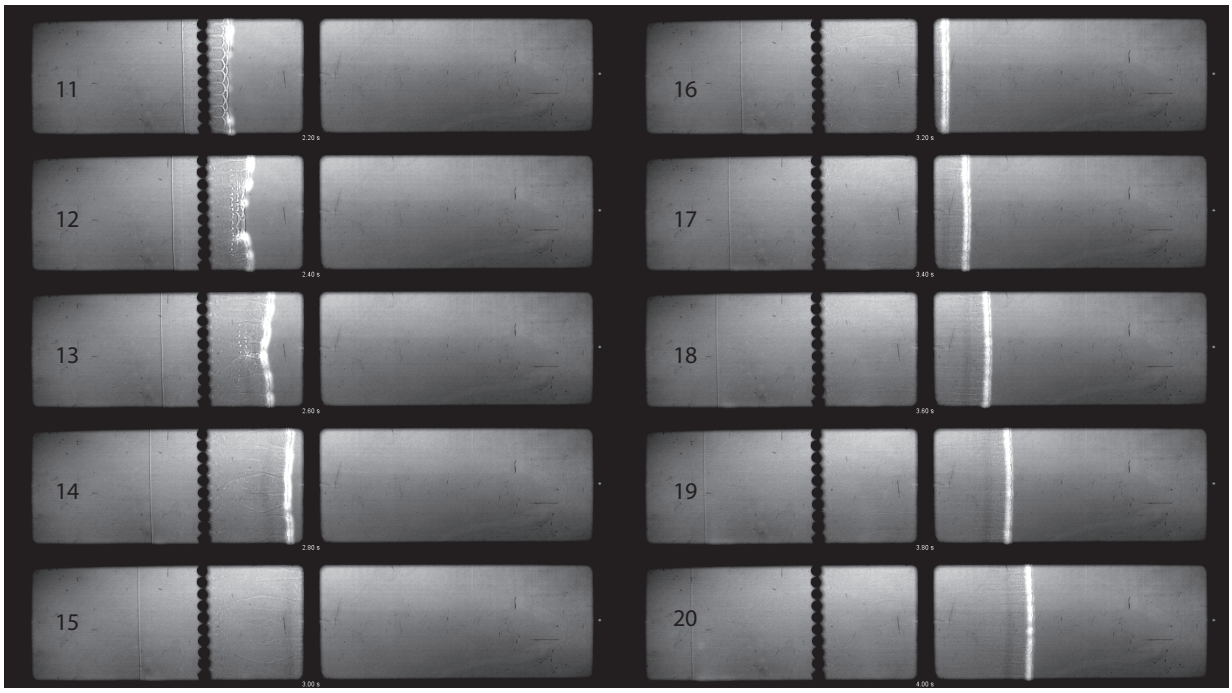


Figure A.22: The full record of the Shadowgraph images illustrating the re-initiation of detonation after interacting with obstacles in $2C_2H_2+5O_2+21Ar$, p_0=11.0 kPa (1.6 psi). Recorded at 23.53 μs interframe, 0.8 μs exposure, 42496 fps.

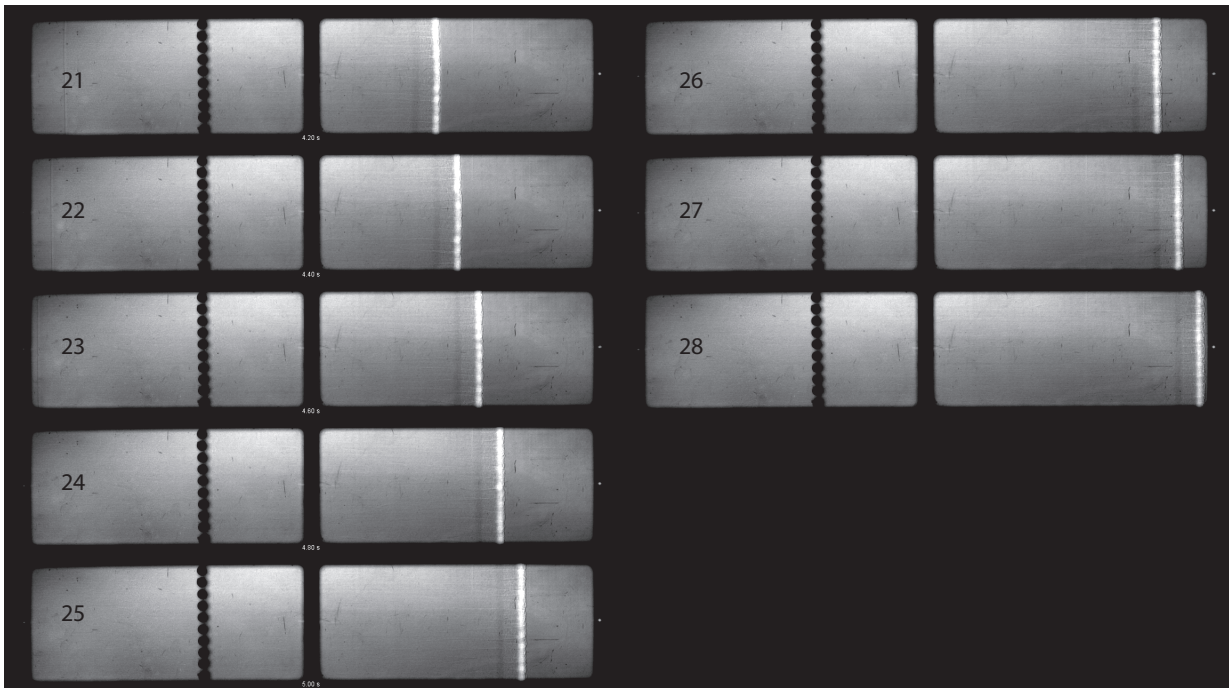


Figure A.23: The full record of the Shadowgraph images illustrating the re-initiation of detonation after interacting with obstacles in $2C_2H_2+5O_2+21Ar$, p_0=11.0 kPa (1.6 psi). Recorded at 23.53 μs interframe, 0.8 μs exposure, 42496 fps.

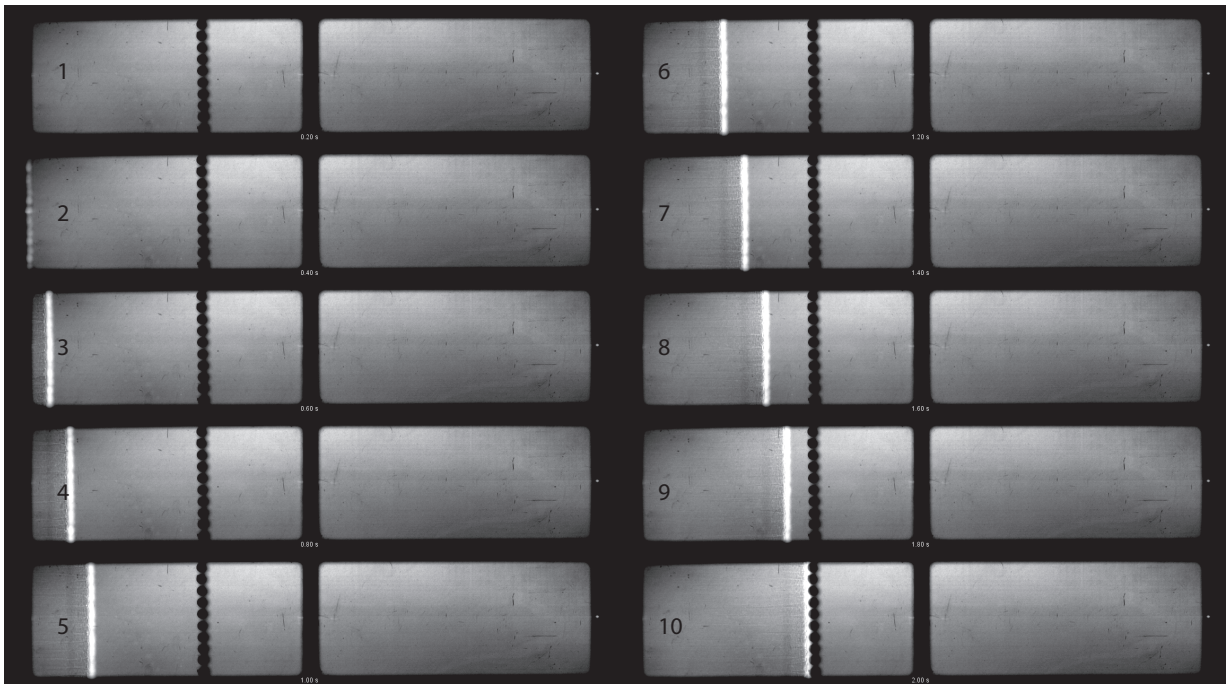


Figure A.24: Shadowgraph images illustrating the failure of detonation after interacting with obstacles in $2C_2H_2+5O_2+21Ar$, p_0=9.6 kPa (1.4 psi). Recorded at 23.53 μs inter-frame, 0.8 μs exposure, 42496 fps.

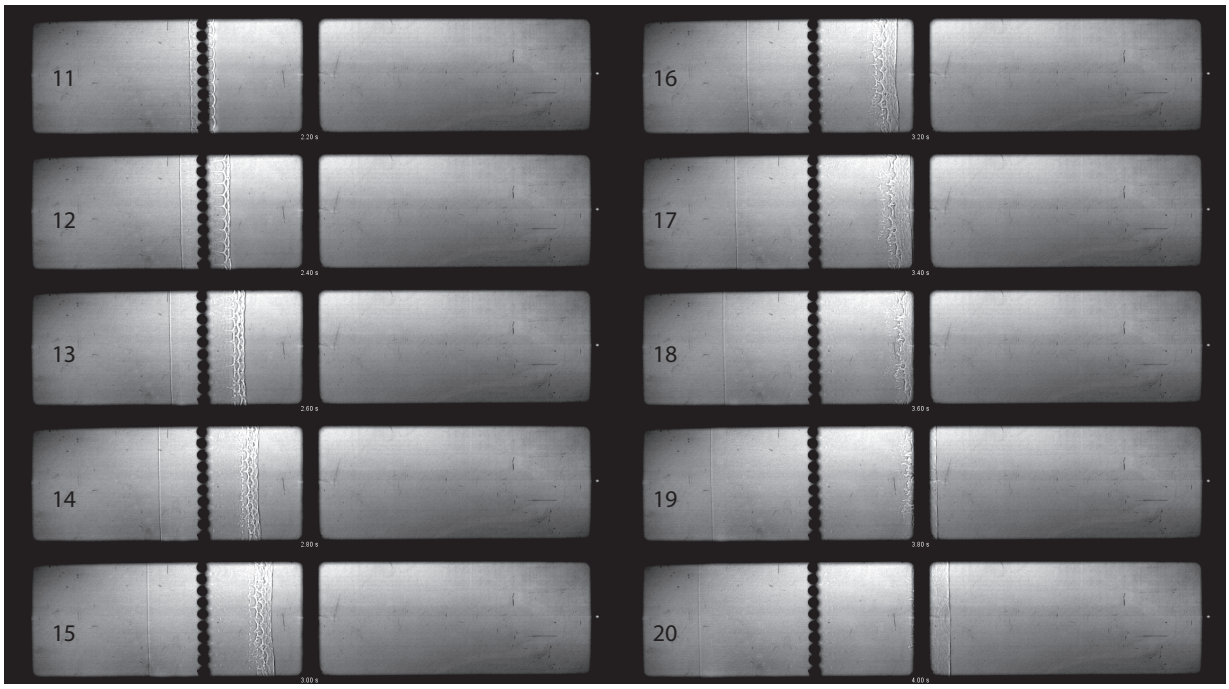


Figure A.25: Shadowgraph images illustrating the failure of detonation after interacting with obstacles in $2C_2H_2+5O_2+21Ar$, p_0=9.6 kPa (1.4 psi). Recorded at 23.53 μs inter-frame, 0.8 μs exposure, 42496 fps.

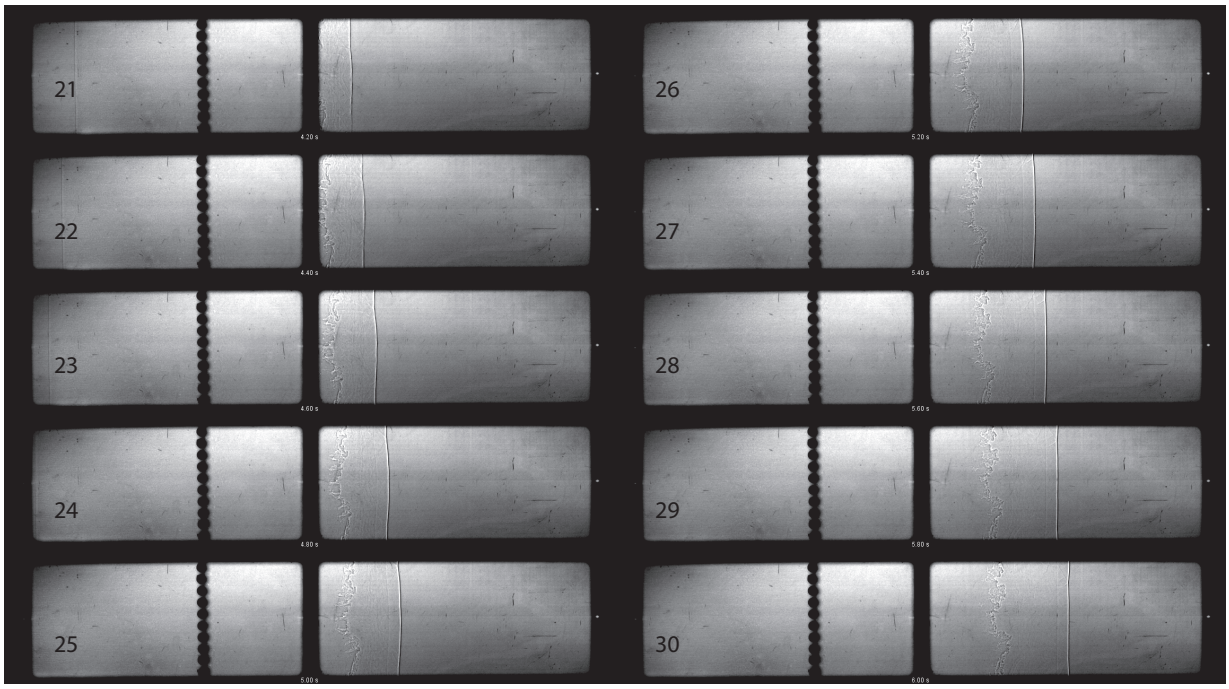


Figure A.26: Shadowgraph images illustrating the failure of detonation after interacting with obstacles in $2C_2H_2+5O_2+21Ar$, p_0=9.6 kPa (1.4 psi). Recorded at 23.53 μs inter-frame, 0.8 μs exposure, 42496 fps.

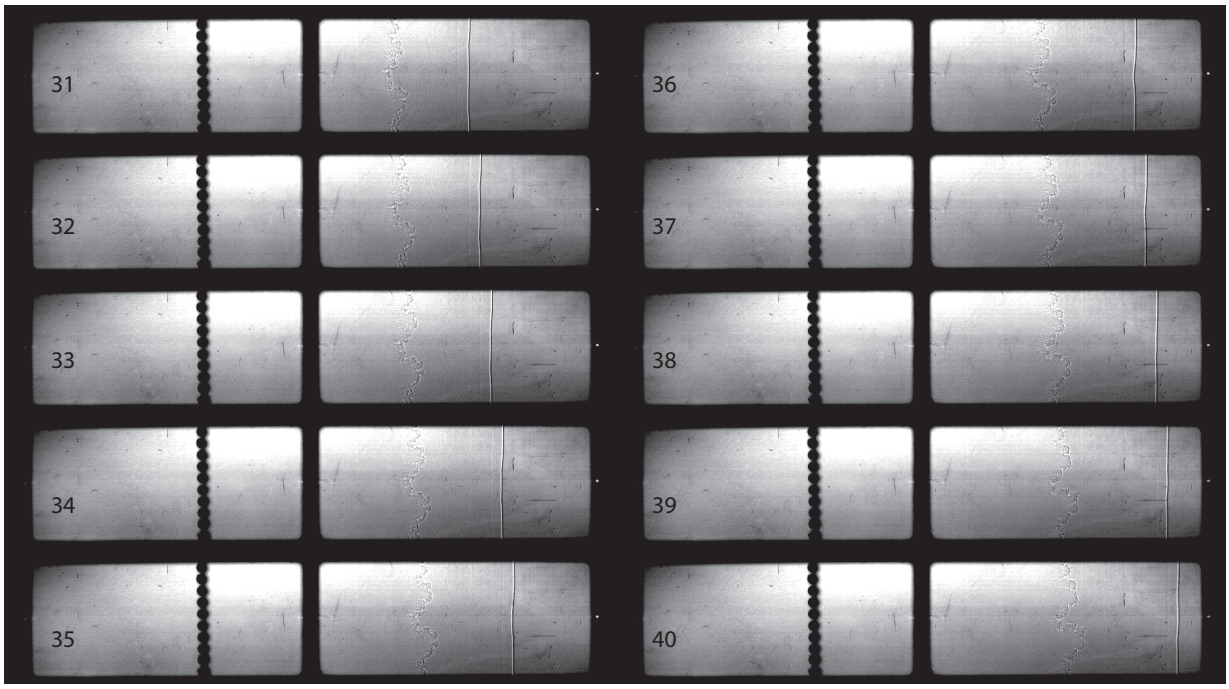


Figure A.27: Shadowgraph images illustrating the failure of detonation after interacting with obstacles in $2C_2H_2+5O_2+21Ar$, p_0=9.6 kPa (1.4 psi). Recorded at 23.53 μs inter-frame, 0.8 μs exposure, 42496 fps.

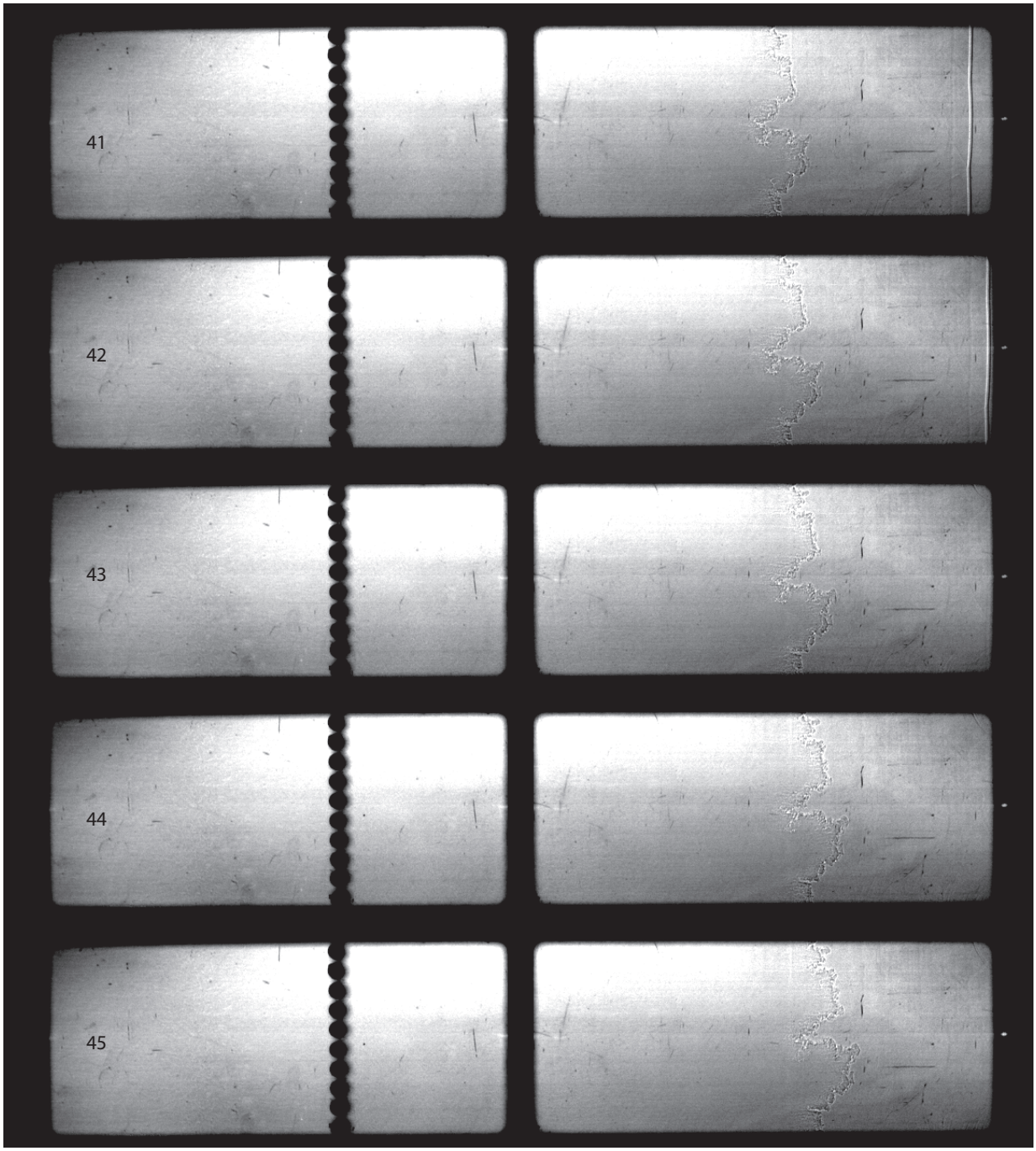


Figure A.28: Shadowgraph images illustrating the failure of detonation after interacting with obstacles in $2C_2H_2+5O_2+21Ar$, p_0=9.6 kPa (1.4 psi). Recorded at 23.53 μs inter-frame, 0.8 μs exposure, 42496 fps.

A.5 Propane

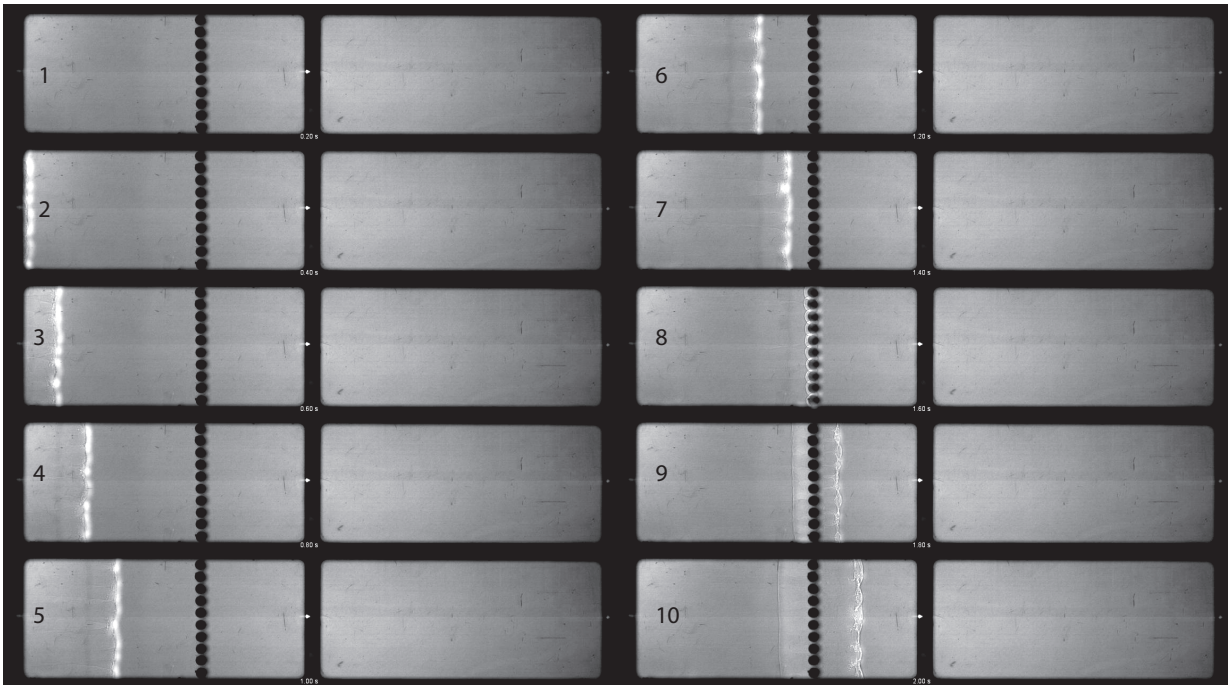


Figure A.29: The full record of the Shadowgraph images illustrating the re-initiation of detonation after interacting with obstacles in C_3H_8+$5O_2$, p_0=4.1 kPa(0.6 psi). Recorded at 23.53 μs interframe, 1.0 μs exposure, 42492 fps.

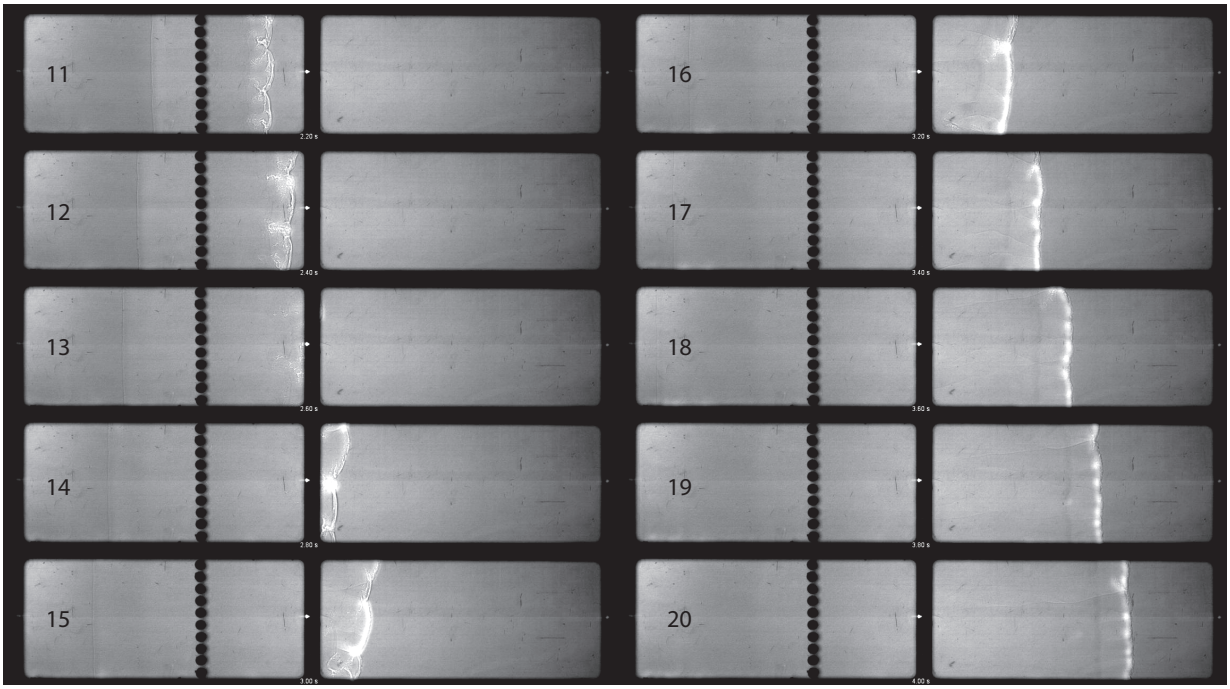


Figure A.30: The full record of the Shadowgraph images illustrating the re-initiation of detonation after interacting with obstacles in C_3H_8+$5O_2$, p_0=4.1 kPa(0.6 psi). Recorded at 23.53 μs interframe, 1.0 μs exposure, 42492 fps.

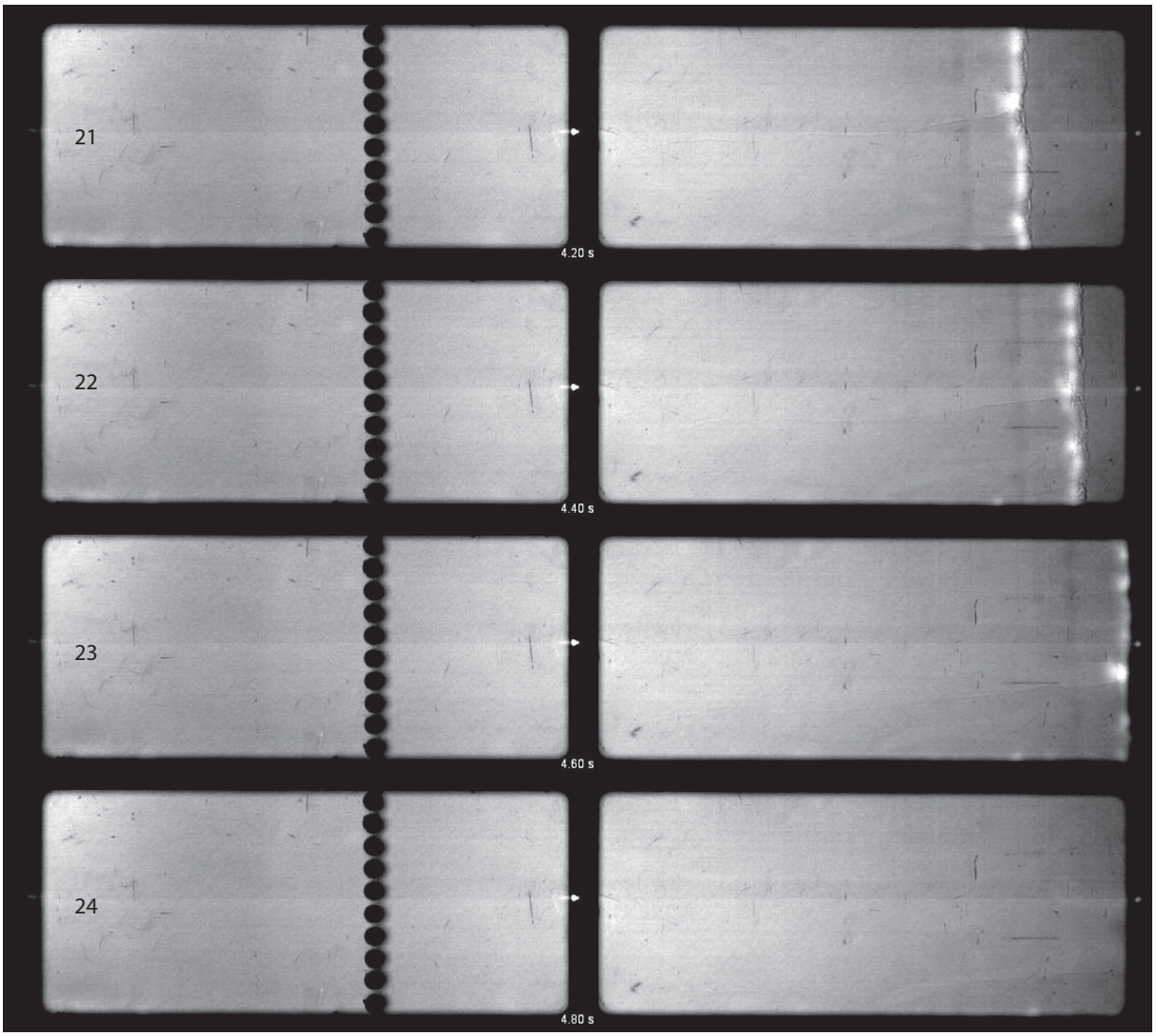


Figure A.31: The full record of the Shadowgraph images illustrating the re-initiation of detonation after interacting with obstacles in C_3H_8+$5O_2$, p_0=4.1 kPa(0.6 psi). Recorded at 23.53 μs interframe, 1.0 μs exposure, 42492 fps.

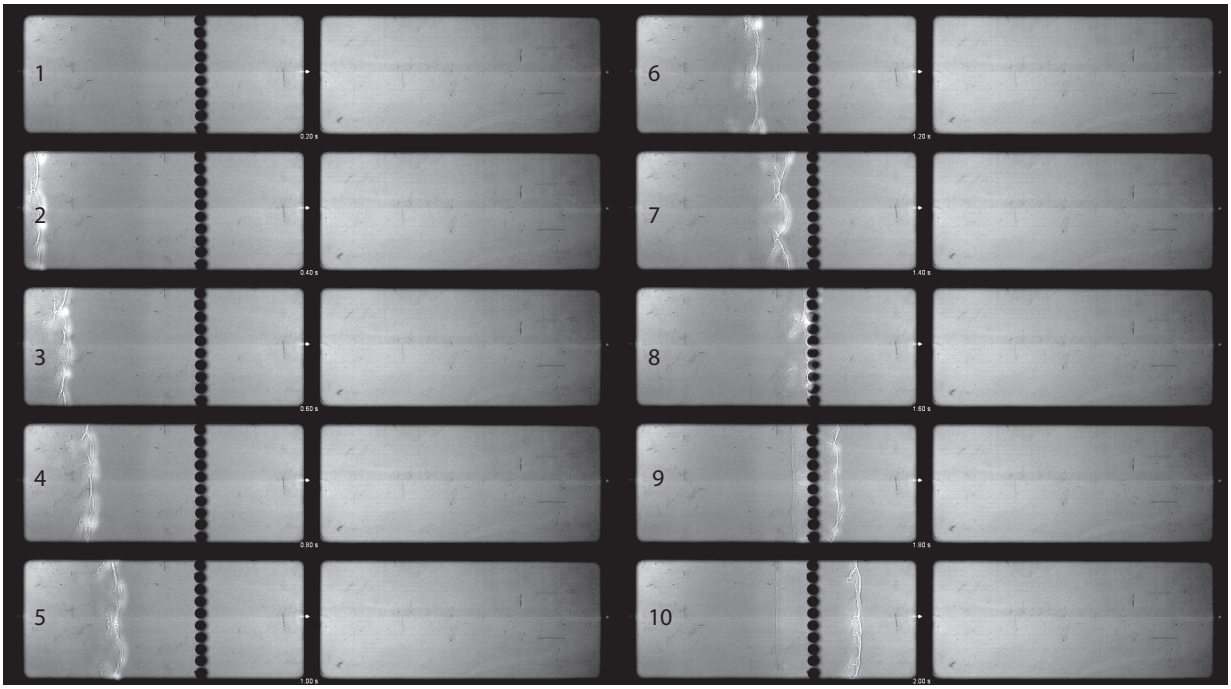


Figure A.32: The full record of the Shadowgraph images illustrating the propagation of fast flames after interacting with obstacles in C_3H_8+$5O_2$, p_0=2.0 kPa(0.3 psi). Recorded at 23.53 μs interframe, 1.0 μs exposure, 42492 fps.

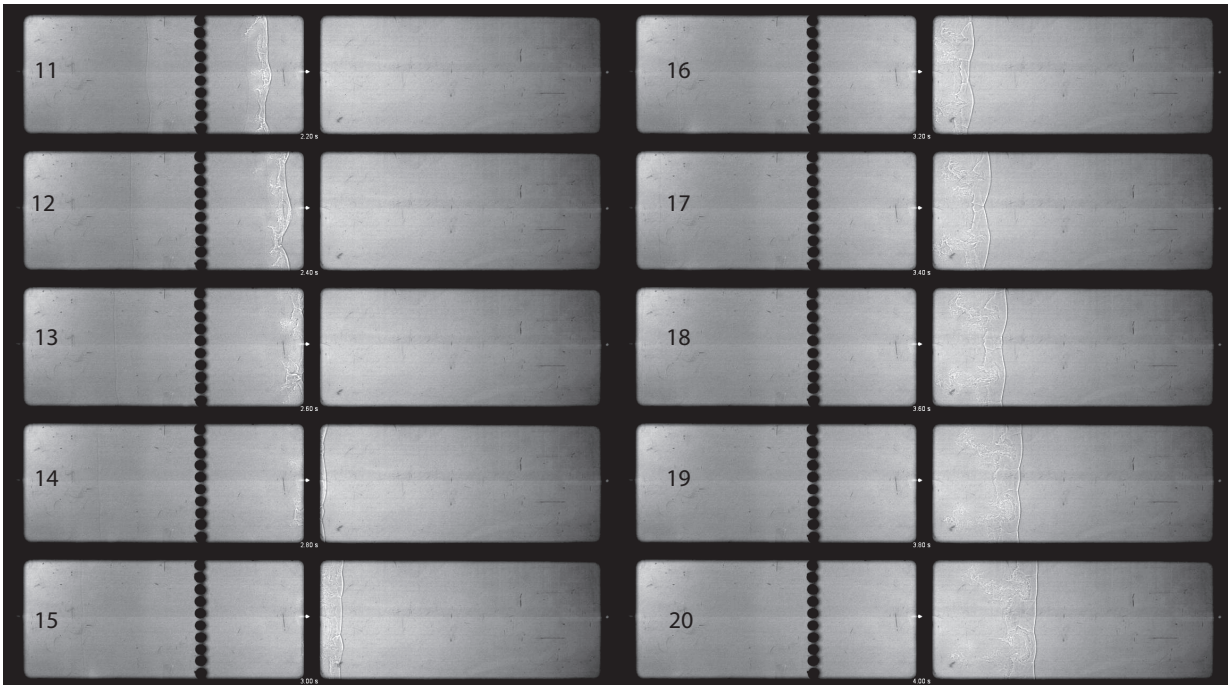


Figure A.33: The full record of the Shadowgraph images illustrating the propagation of fast flames after interacting with obstacles in C_3H_8+$5O_2$, p_0=2.0 kPa(0.3 psi). Recorded at 23.53 μs interframe, 1.0 μs exposure, 42492 fps.

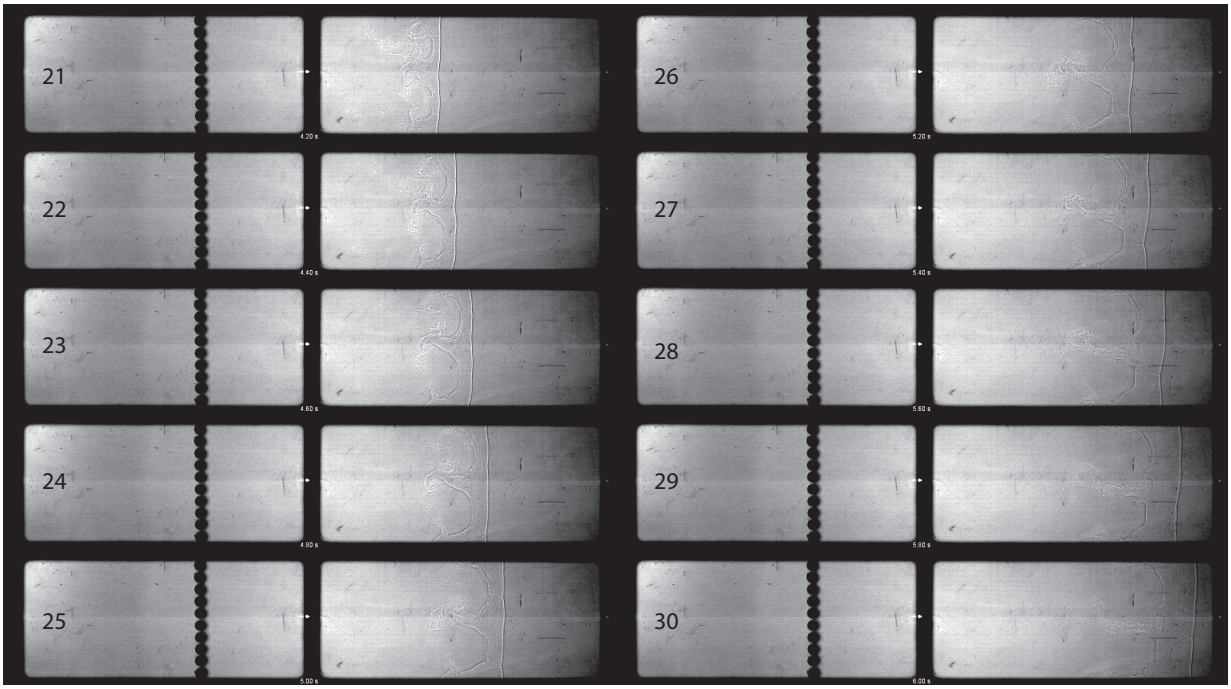


Figure A.34: The full record of the Shadowgraph images illustrating the propagation of fast flames after interacting with obstacles in C_3H_8+$5O_2$, p_0=2.0 kPa(0.3 psi). Recorded at 23.53 μs interframe, 1.0 μs exposure, 42492 fps.

Appendix B

90% Blockage Ratio Experiments

The full record of the shadow graphs experiments for the 90% blockage ratio configuration.

B.1 Methane

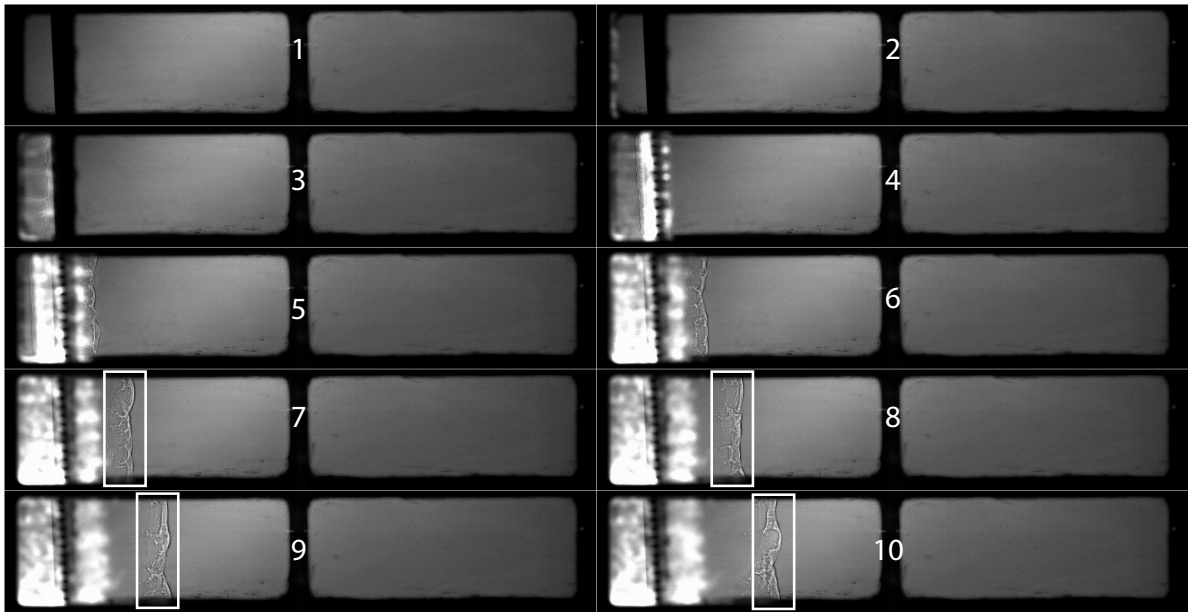


Figure B.1: The full record of the Shadowgraph images illustrating the re-initiation of detonation after interacting with obstacles in CH_4+$2O_2$, p_0=14.5 KPa. Recorded at 23.53 μs interframe, 0.7 μs exposure, 42496 fps

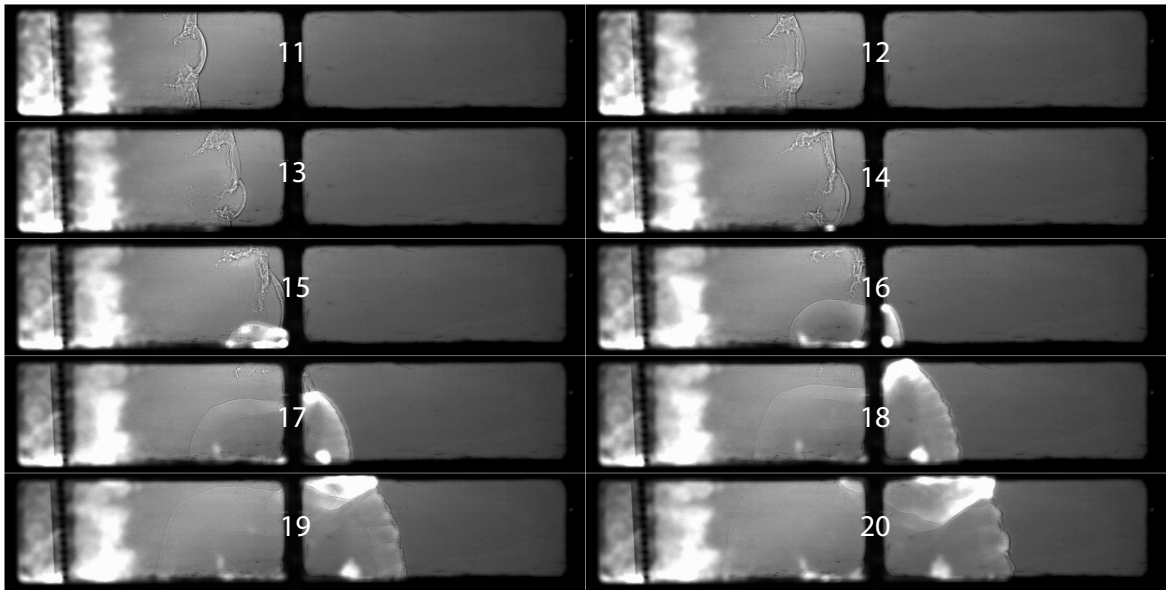


Figure B.2: The full record of the Shadowgraph images illustrating the re-initiation of detonation after interacting with obstacles in CH_4+$2O_2$, p_0=14.5 KPa. Recorded at 23.53 μs interframe, 0.7 μs exposure, 42496 fps

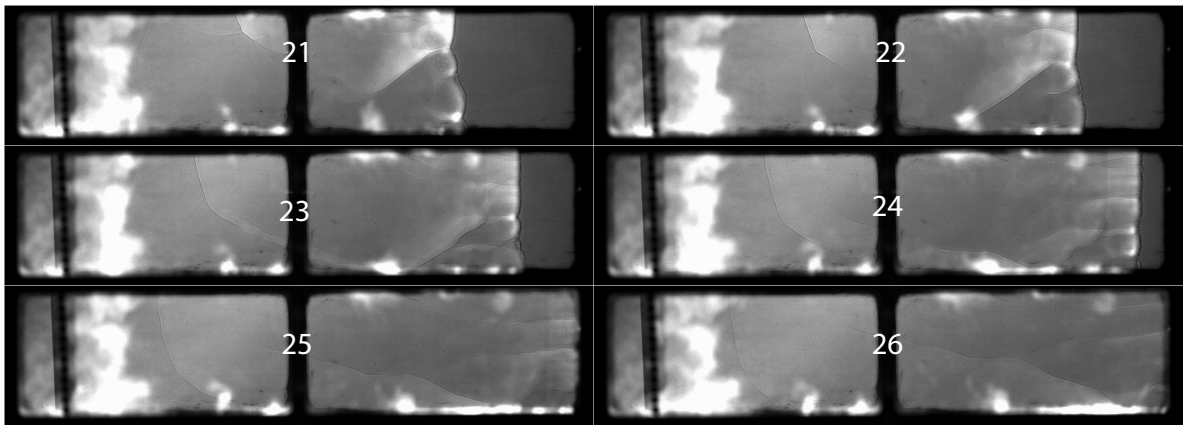


Figure B.3: The full record of the Shadowgraph images illustrating the re-initiation of detonation after interacting with obstacles in CH_4+$2O_2$, p_0=14.5 KPa. Recorded at 23.53 μs interframe, 0.7 μs exposure, 42496 fps

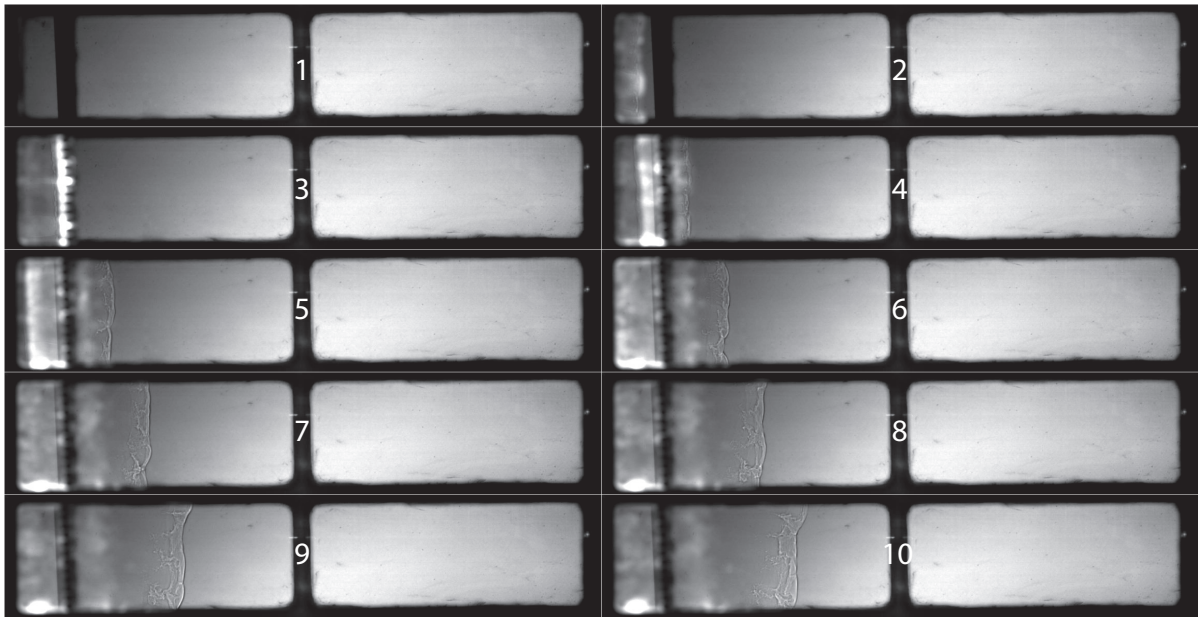


Figure B.4: The full record of the Shadowgraph images illustrating the failure of detonation after interacting with obstacles in CH_4+$2O_2$, p_0=12.4 KPa. Recorded at 23.53 μs interframe, 0.7 μs exposure, 42496 fps

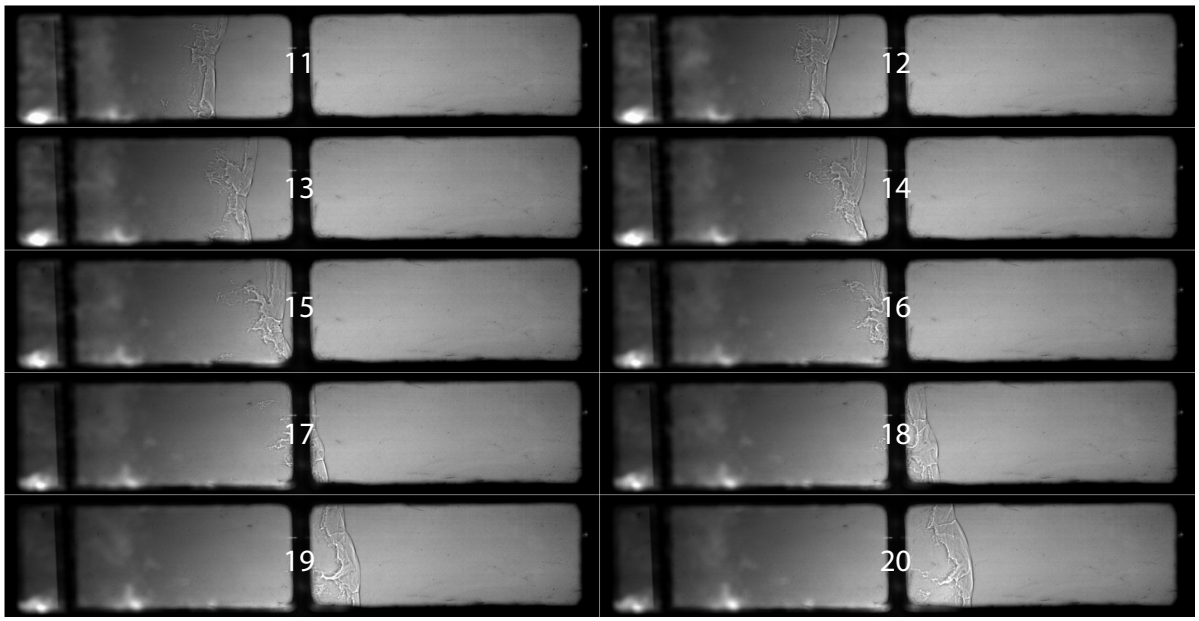


Figure B.5: The full record of the Shadowgraph images illustrating the failure of detonation after interacting with obstacles in CH_4+$2O_2$, p_0=12.4 KPa. Recorded at 23.53 μs interframe, 0.7 μs exposure, 42496 fps

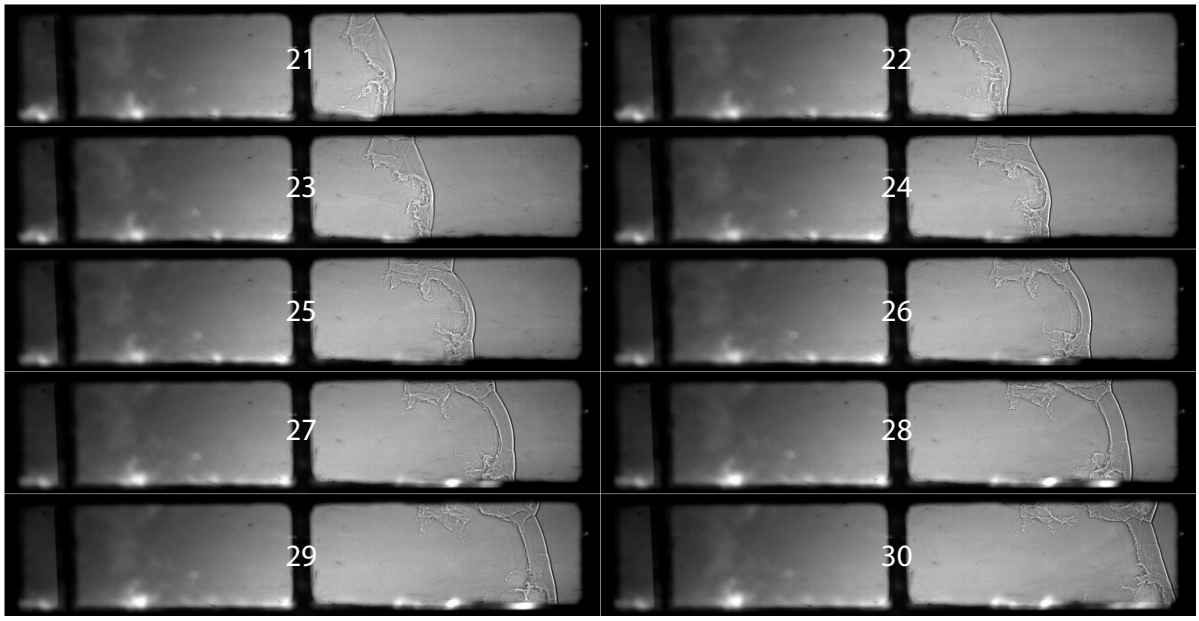


Figure B.6: The full record of the Shadowgraph images illustrating the failure of detonation after interacting with obstacles in CH_4+$2O_2$, p_0=12.4 KPa. Recorded at 23.53 μs interframee, 0.7 μs exposure, 42496 fps

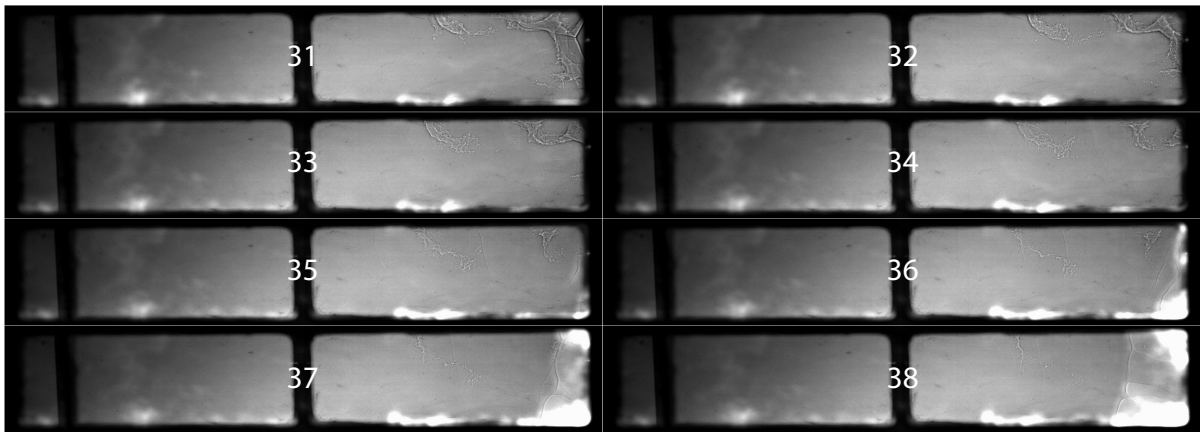


Figure B.7: The full record of the Shadowgraph images illustrating the failure of detonation after interacting with obstacles in CH_4+$2O_2$, p_0=12.4 KPa. Recorded at 23.53 μs interframe, 0.7 μs exposure, 42496 fps

B.2 Ethane

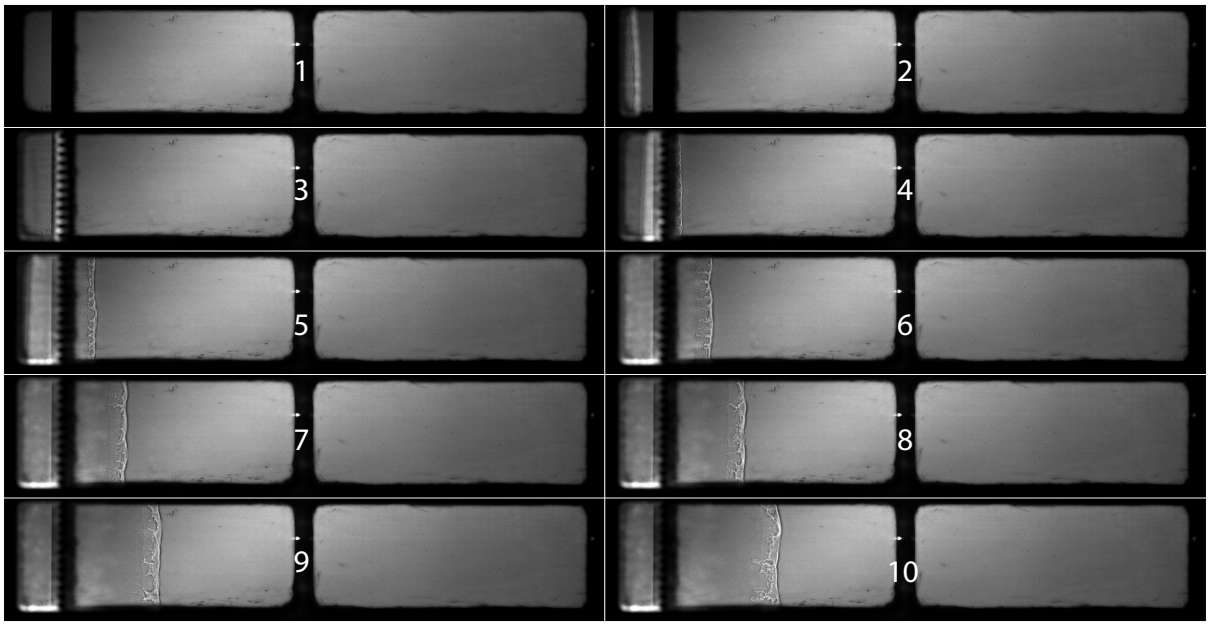


Figure B.8: The full record of the Shadowgraph images illustrating the re-initiation of detonation after interacting with obstacles in $2C_2H_6+7O_2$, p_0=9.6 KPa. Recorded at 23.53 μs interframe, 0.7 μs exposure, 42496 fps.

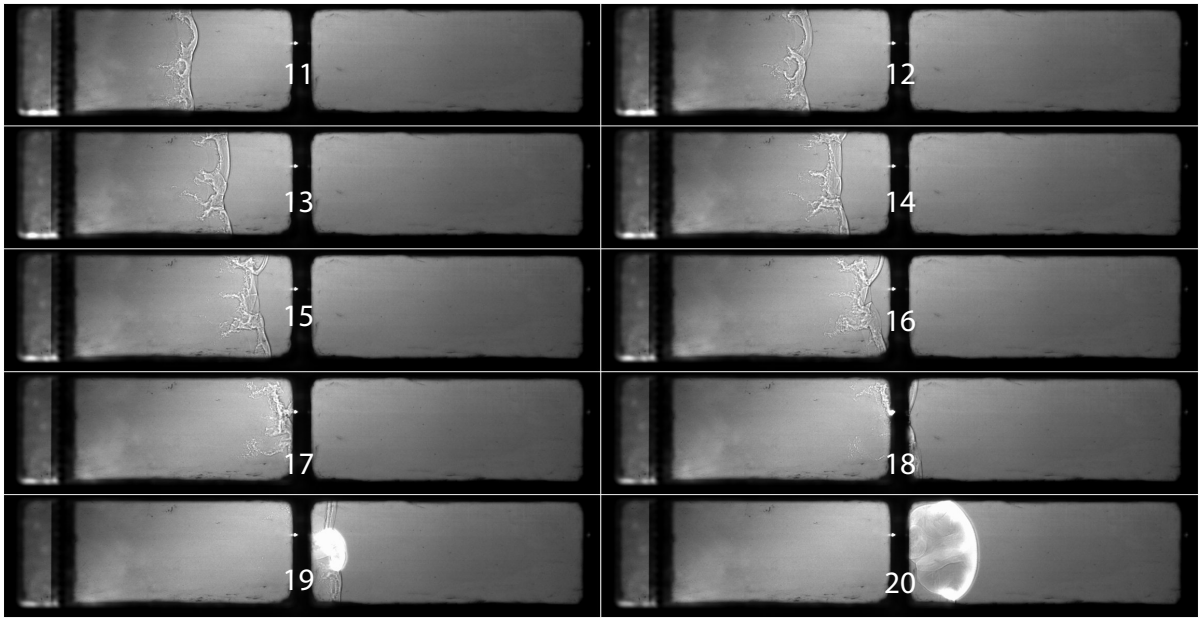


Figure B.9: The full record of the Shadowgraph images illustrating the re-initiation of detonation after interacting with obstacles in $2C_2H_6+7O_2$, p_0=9.6 KPa. Recorded at 23.53 μs interframe, 0.7 μs exposure, 42496 fps.

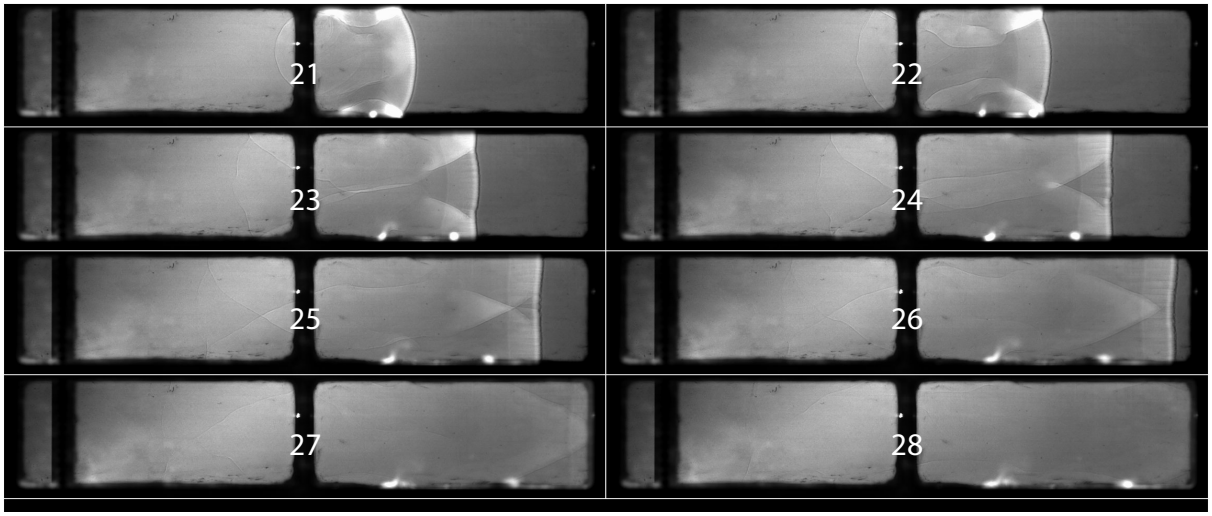


Figure B.10: The full record of the Shadowgraph images illustrating the re-initiation of detonation after interacting with obstacles in $2C_2H_6+7O_2$, p_0=9.6 KPa. Recorded at 23.53 μs interframe, 0.7 μs exposure, 42496 fps.

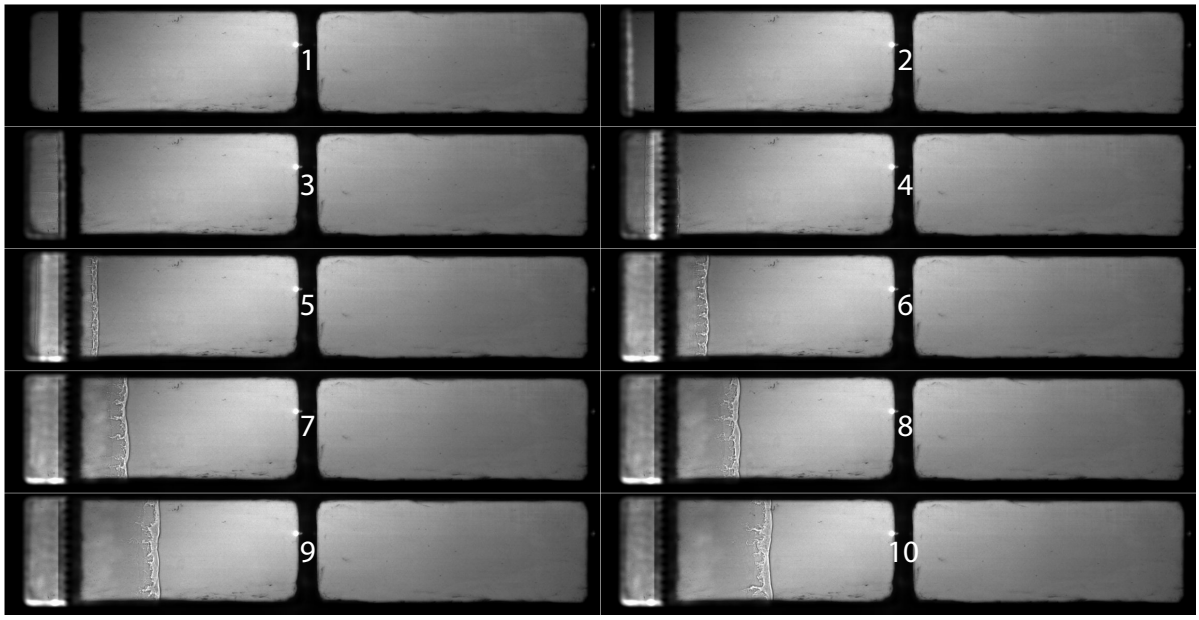


Figure B.11: The full record of the Shadowgraph images illustrating the failure of detonation after interacting with obstacles in $2C_2H_6+7O_2$, p_0=8.2 KPa. Recorded at 23.53 μs interframe, 0.7 μs exposure, 42496 fps.

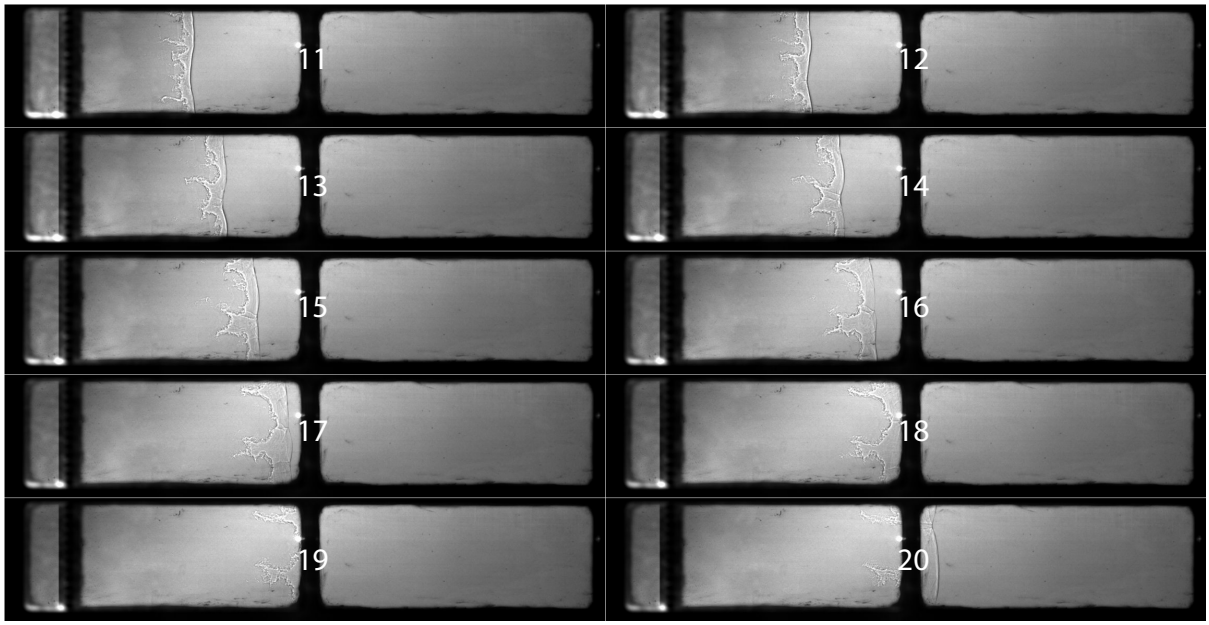


Figure B.12: The full record of the Shadowgraph images illustrating the failure of detonation after interacting with obstacles in $2C_2H_6+7O_2$, p_0=8.2 KPa. Recorded at 23.53 μs interframe, 0.7 μs exposure, 42496 fps.

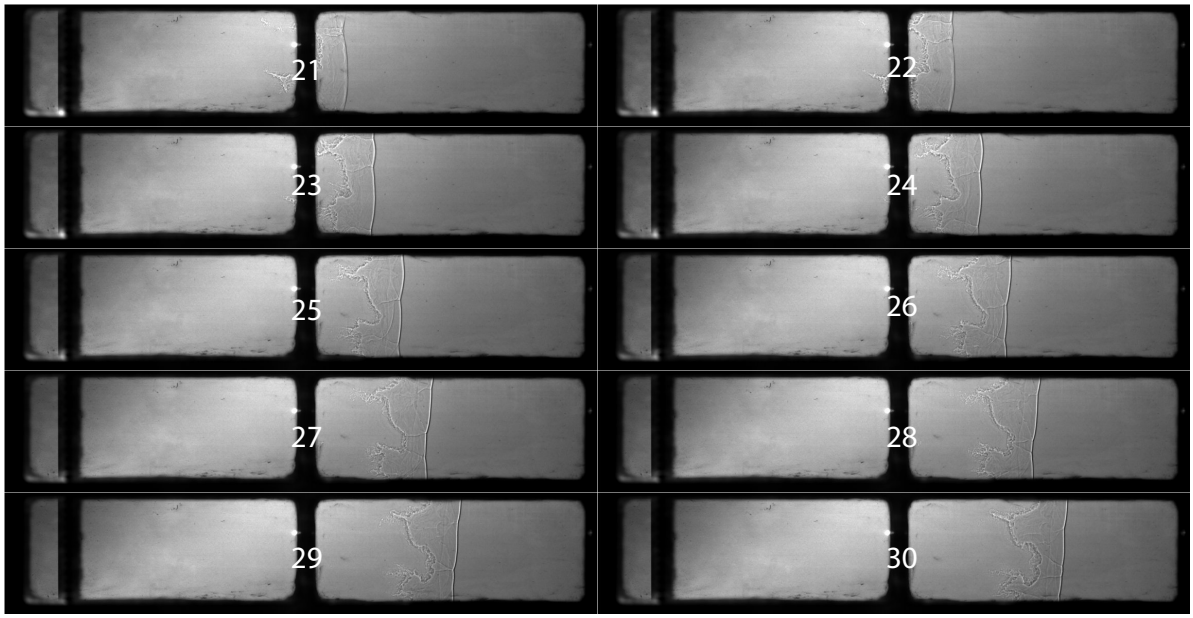


Figure B.13: The full record of the Shadowgraph images illustrating the failure of detonation after interacting with obstacles in $2C_2H_6+7O_2$, p_0=8.2 KPa. Recorded at 23.53 μs interframe, 0.7 μs exposure, 42496 fps.

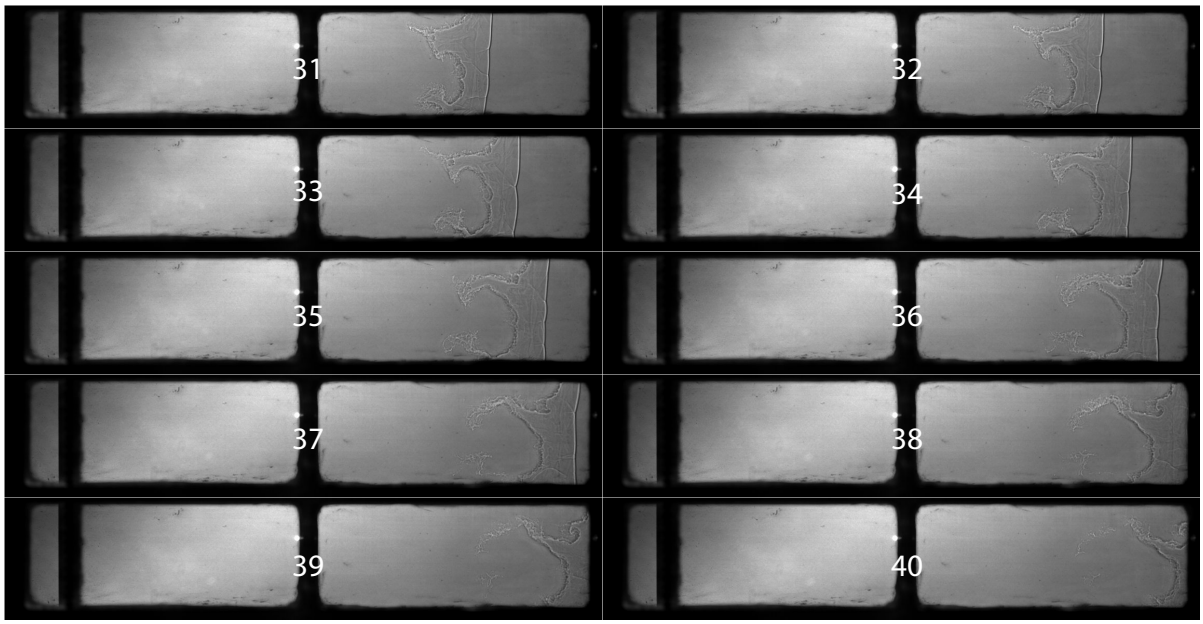


Figure B.14: The full record of the Shadowgraph images illustrating the failure of detonation after interacting with obstacles in $2C_2H_6+7O_2$, p_0=8.2 KPa. Recorded at 23.53 μs interframe, 0.7 μs exposure, 42496 fps.

B.3 Ethylene

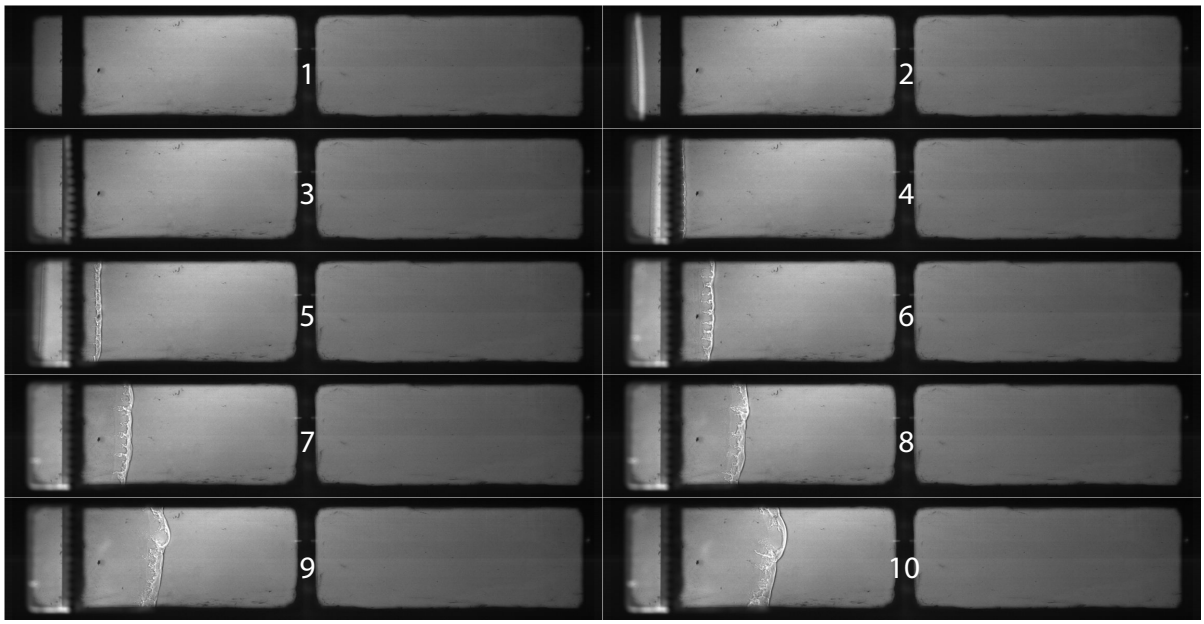


Figure B.15: The full record of the Shadowgraph images illustrating the re-initiation of detonation after interacting with obstacles in $C_2H_4+3O_2$, p_0=8.2 KPa. Recorded at 23.53 μs interframe, 0.8 μs exposure, 42496 fps.

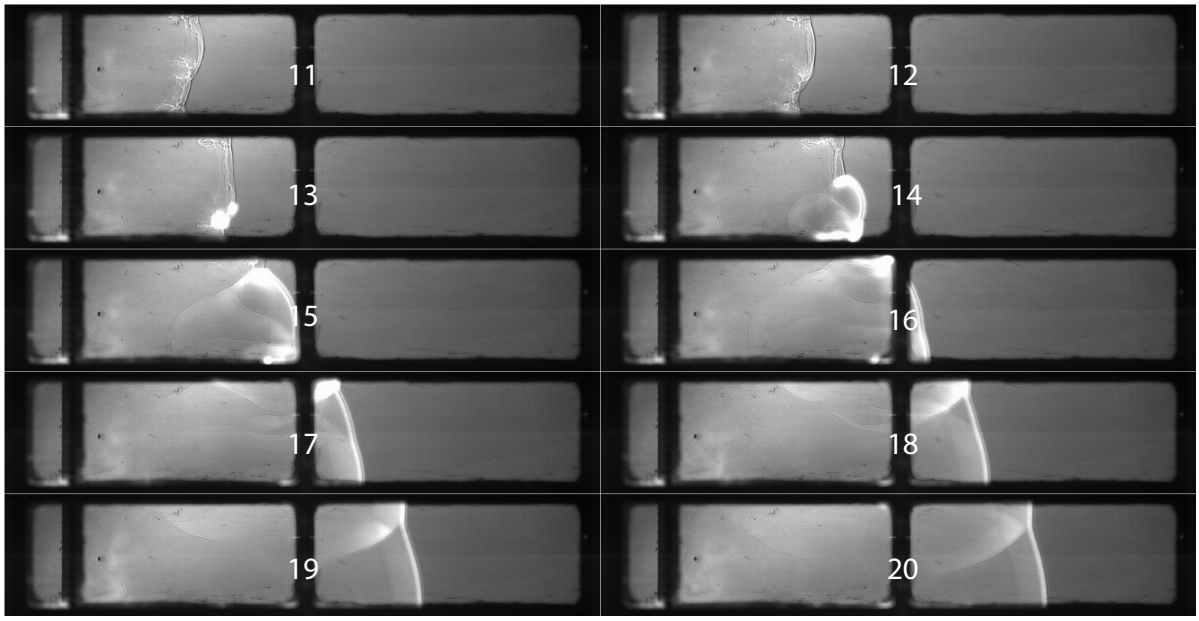


Figure B.16: The full record of the Shadowgraph images illustrating the re-initiation of detonation after interacting with obstacles in C_2H_4+$3O_2$, p_0=8.2 KPa. Recorded at 23.53 μs interframe, 0.8 μs exposure, 42496 fps.

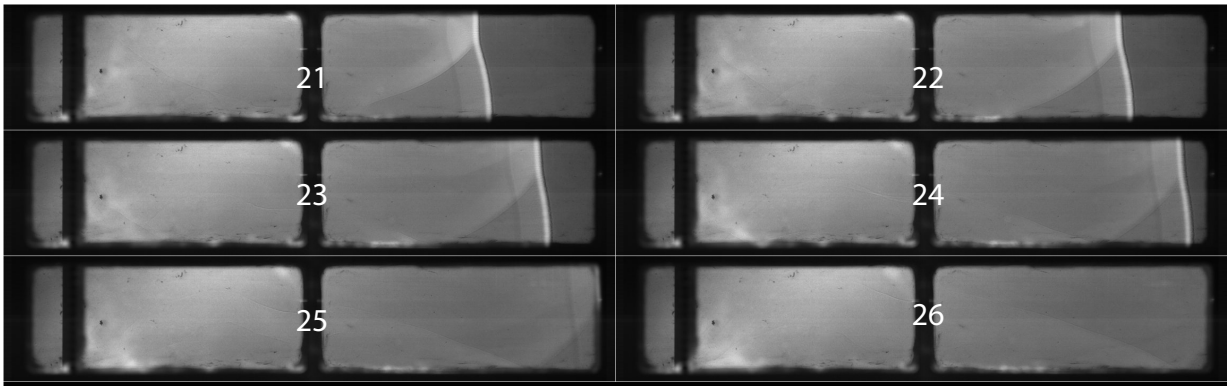


Figure B.17: The full record of the Shadowgraph images illustrating the re-initiation of detonation after interacting with obstacles in C_2H_4+$3O_2$, p_0=8.2 KPa. Recorded at 23.53 μs interframe, 0.8 μs exposure, 42496 fps.

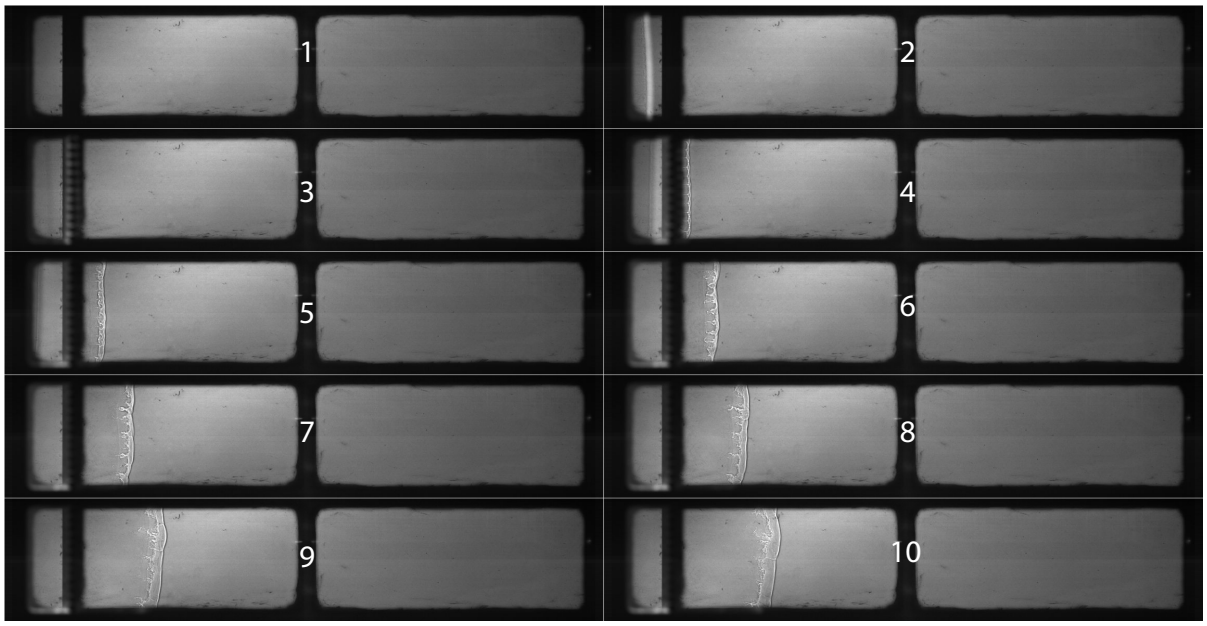


Figure B.18: The full record of the Shadowgraph images illustrating the failure of detonation after interacting with obstacles in C_2H_4+$3O_2$, p_0=6.2 KPa. Recorded at 23.53 μs interframe, 0.8 μs exposure, 42496 fps.

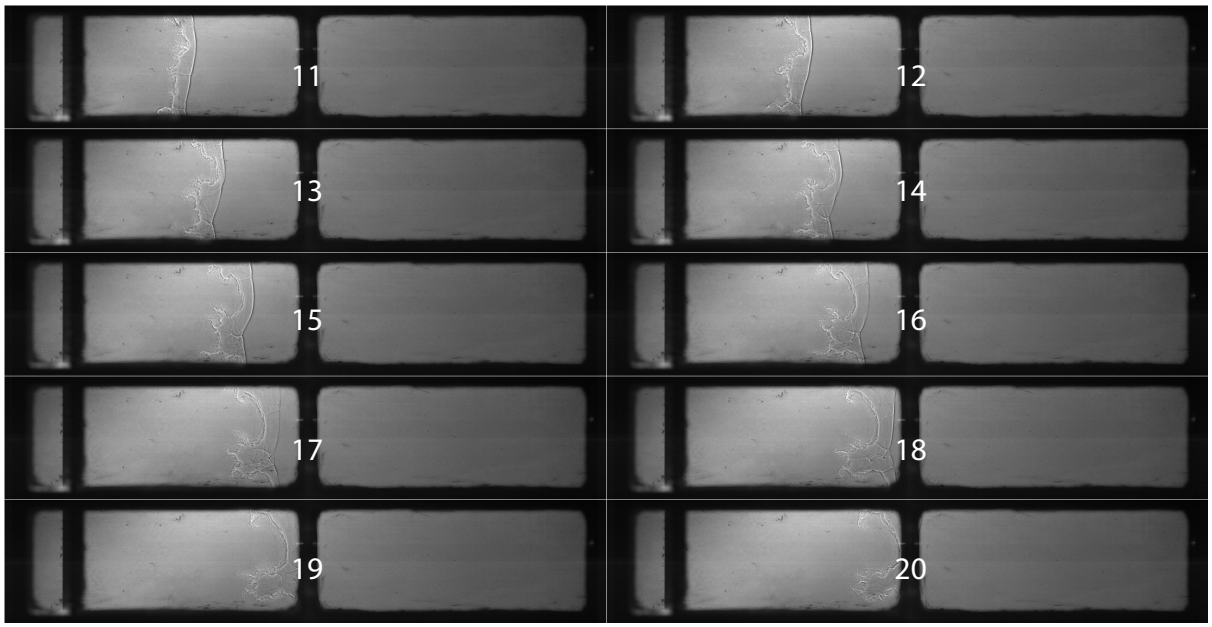


Figure B.19: The full record of the Shadowgraph images illustrating the failure of detonation after interacting with obstacles in C_2H_4+$3O_2$, p_0=6.2 KPa. Recorded at 23.53 μs interframe, 0.8 μs exposure, 42496 fps.

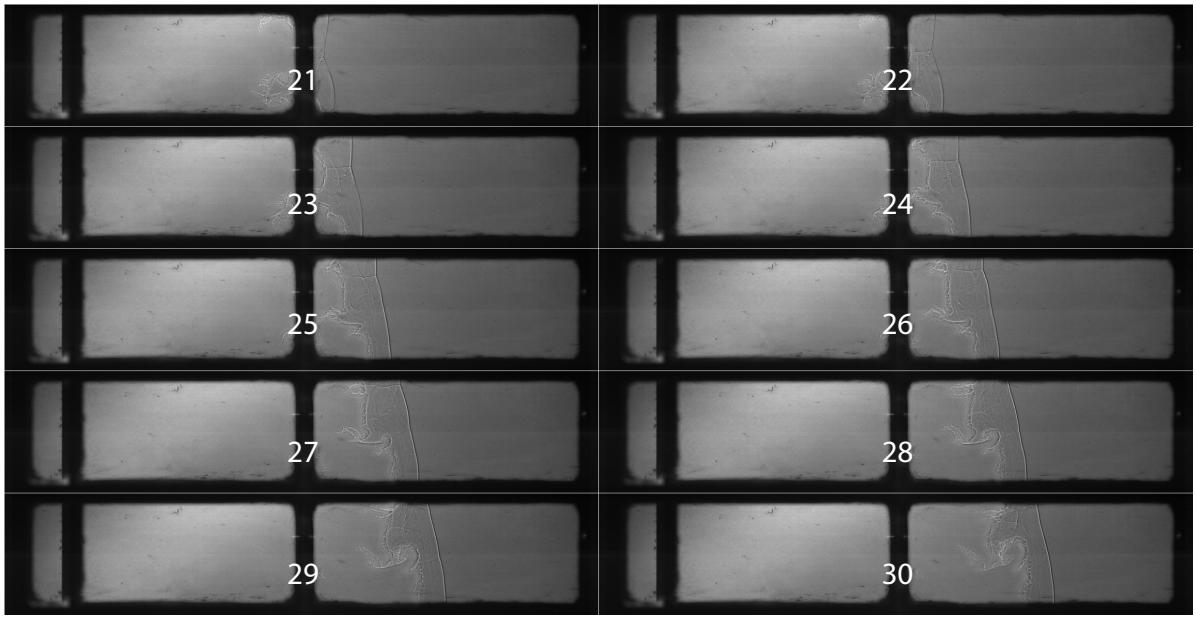


Figure B.20: The full record of the Shadowgraph images illustrating the failure of detonation after interacting with obstacles in C_2H_4+$3O_2$, p_0=6.2 KPa. Recorded at 23.53 μs interframe, 0.8 μs exposure, 42496 fps.

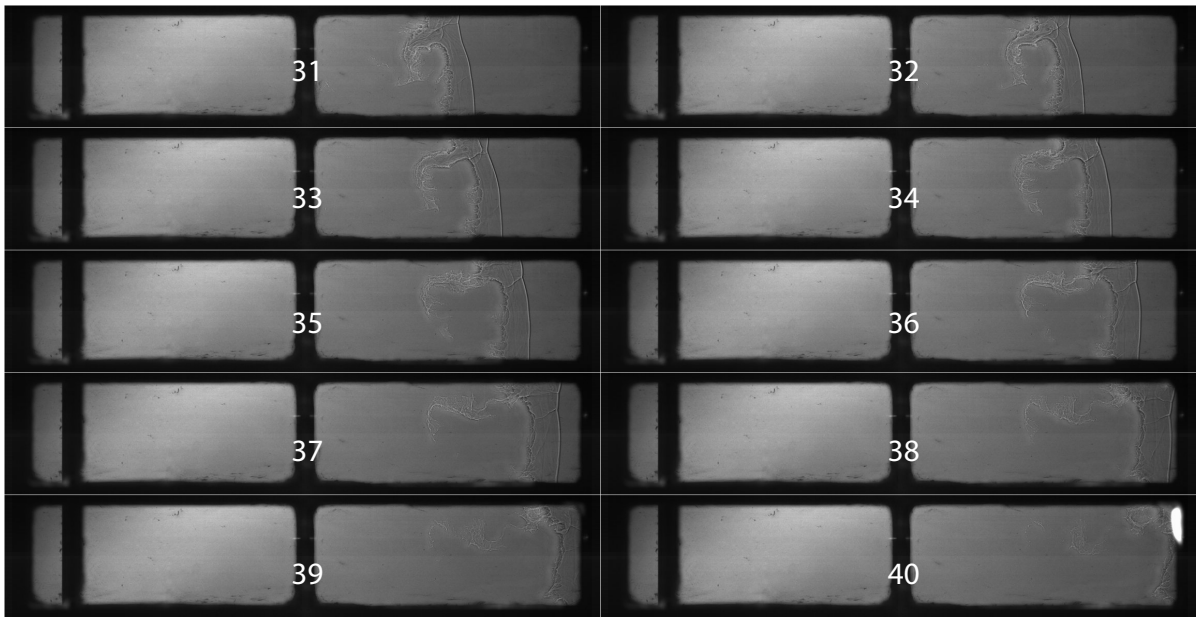


Figure B.21: The full record of the Shadowgraph images illustrating the failure of detonation after interacting with obstacles in C_2H_4+$3O_2$, p_0=6.2 KPa. Recorded at 23.53 μs interframe, 0.8 μs exposure, 42496 fps.

B.4 Acetylene

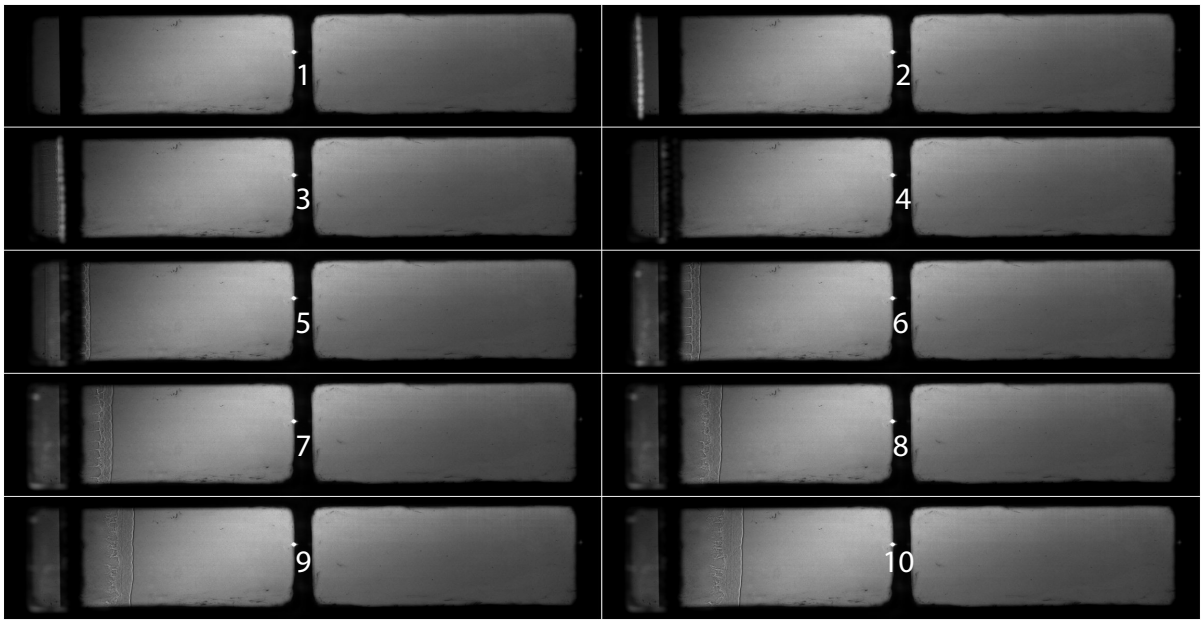


Figure B.22: The full record of the Shadowgraph images illustrating the failure of detonation after interacting with obstacles in $2C_2H_2+5O_2+21Ar$, p_0=11.0 KPa. Recorded at 23.53 μs interframe, 0.8 μs exposure, 42496 fps.

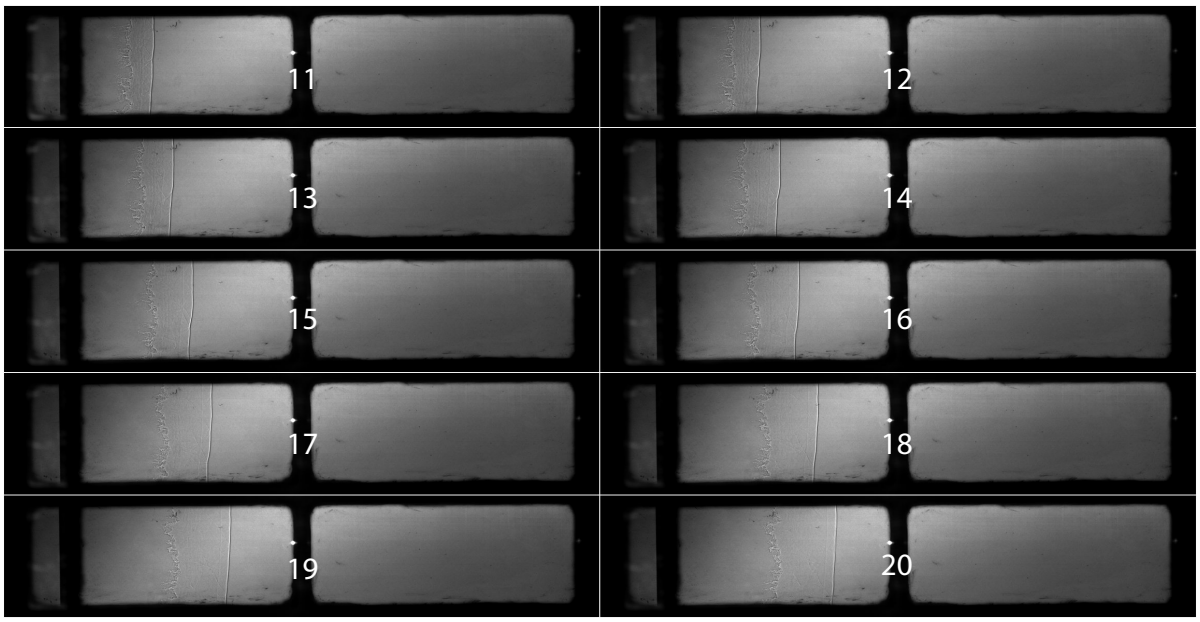


Figure B.23: The full record of the Shadowgraph images illustrating the failure of detonation after interacting with obstacles in $2C_2H_2+5O_2+21Ar$, p_0=11.0 KPa. Recorded at 23.53 μs interframe, 0.8 μs exposure, 42496 fps.

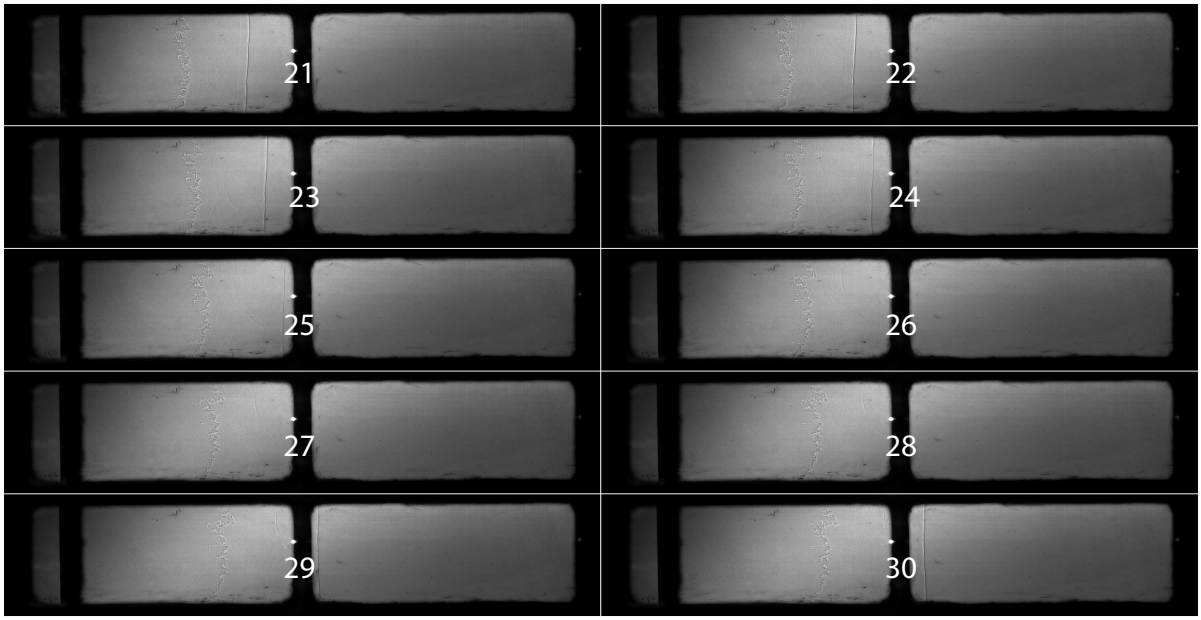


Figure B.24: The full record of the Shadowgraph images illustrating the failure of detonation after interacting with obstacles in $2C_2H_2+5O_2+21Ar$, p_0=11.0 KPa. Recorded at 23.53 μs interframe, 0.8 μs exposure, 42496 fps.

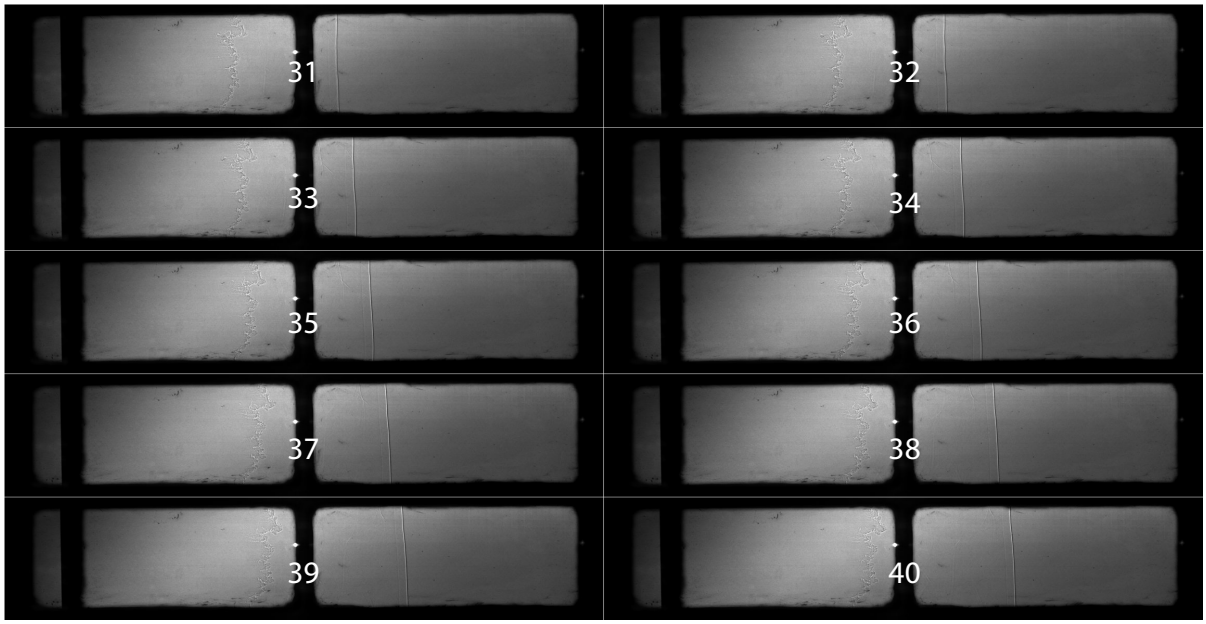


Figure B.25: The full record of the Shadowgraph images illustrating the failure of detonation after interacting with obstacles in $2C_2H_2+5O_2+21Ar$, p_0=11.0 KPa. Recorded at 23.53 μs interframe, 0.8 μs exposure, 42496 fps.

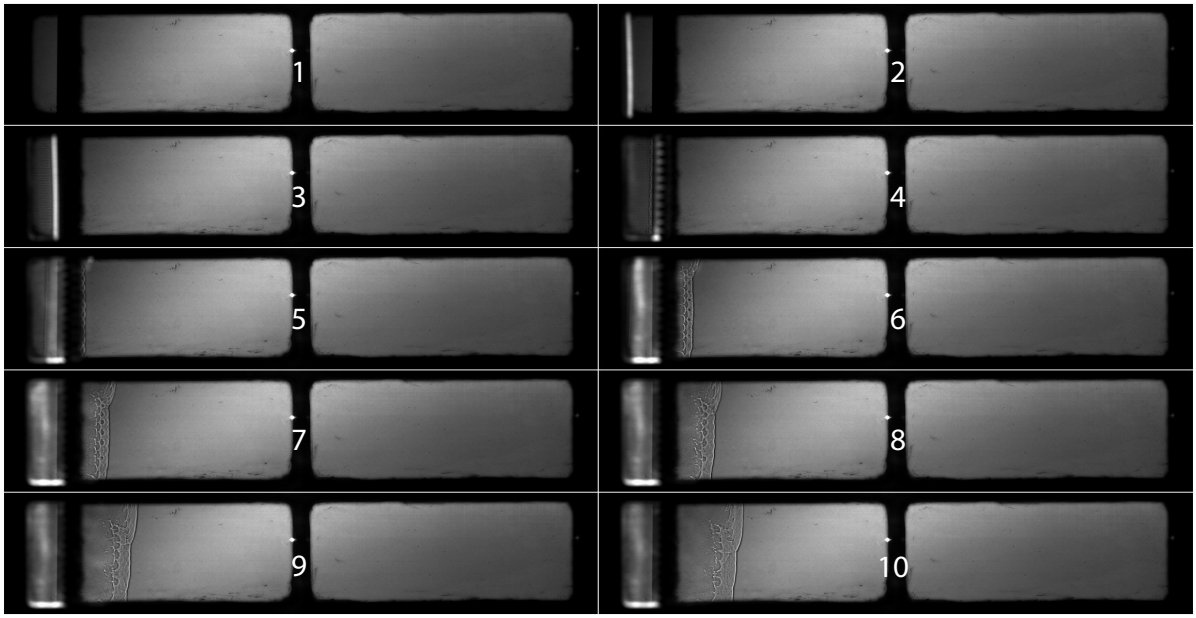


Figure B.26: The full record of the Shadowgraph images illustrating the failure of detonation after interacting with obstacles in $2C_2H_2+5O_2+21Ar$, p_0=17.9 KPa. Recorded at 23.53 μs interframe, 0.8 μs exposure, 42496 fps.

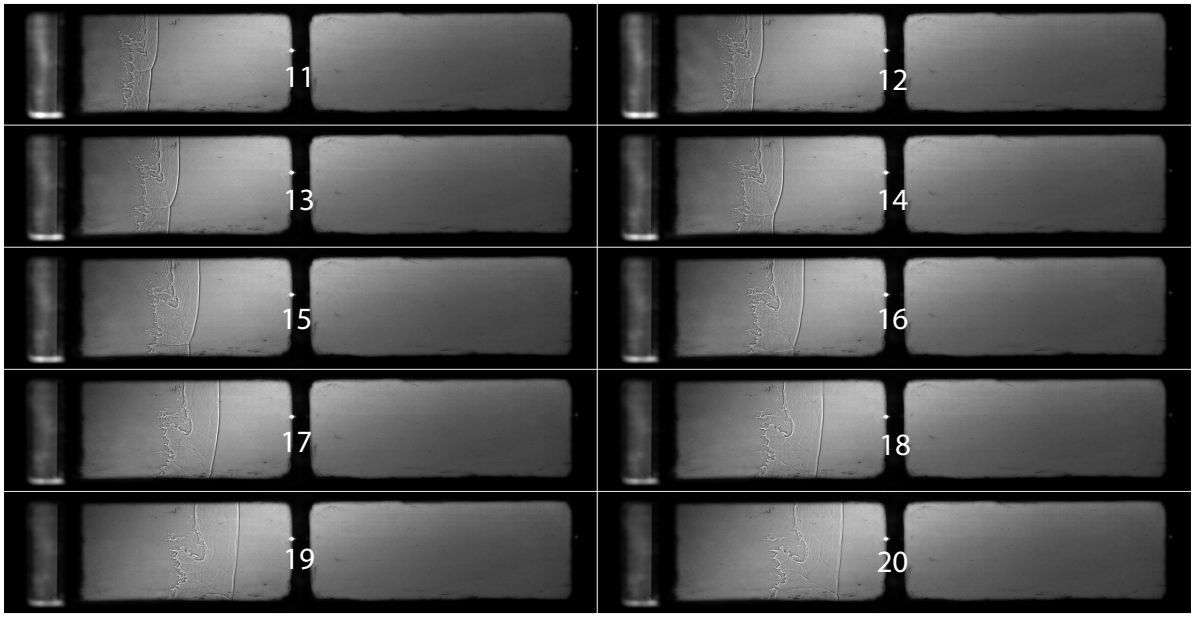


Figure B.27: The full record of the Shadowgraph images illustrating the failure of detonation after interacting with obstacles in $2C_2H_2+5O_2+21Ar$, p_0=17.9 KPa. Recorded at 23.53 μs interframe, 0.8 μs exposure, 42496 fps.

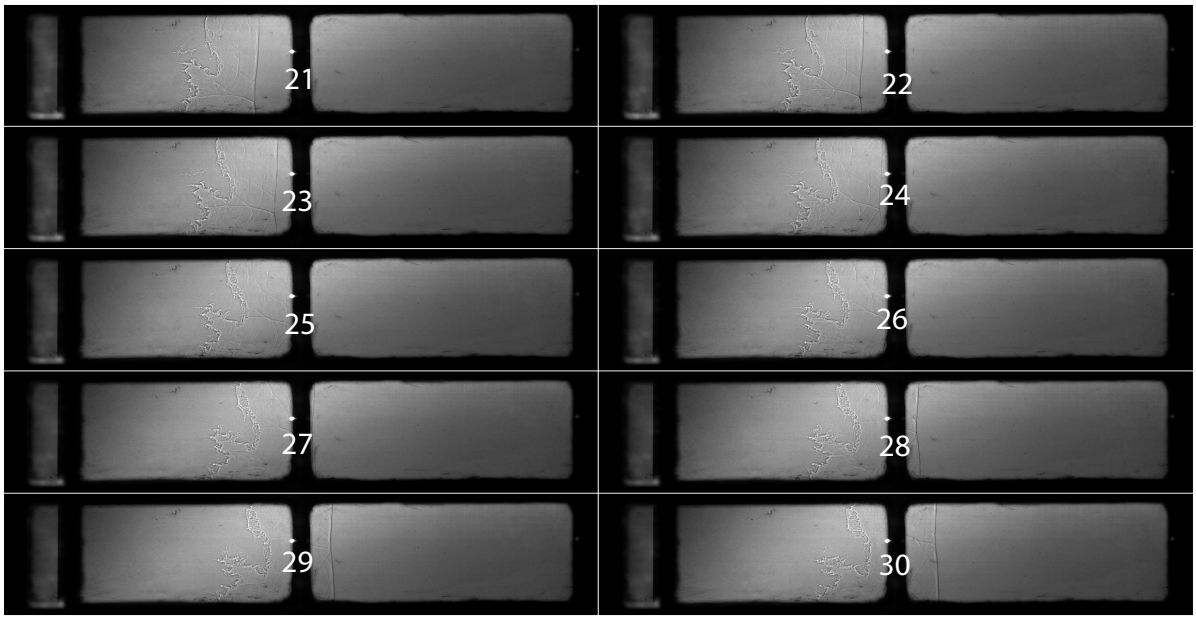


Figure B.28: The full record of the Shadowgraph images illustrating the failure of detonation after interacting with obstacles in $2C_2H_2+5O_2+21Ar$, p_0=17.9 KPa. Recorded at 23.53 μs interframe, 0.8 μs exposure, 42496 fps.

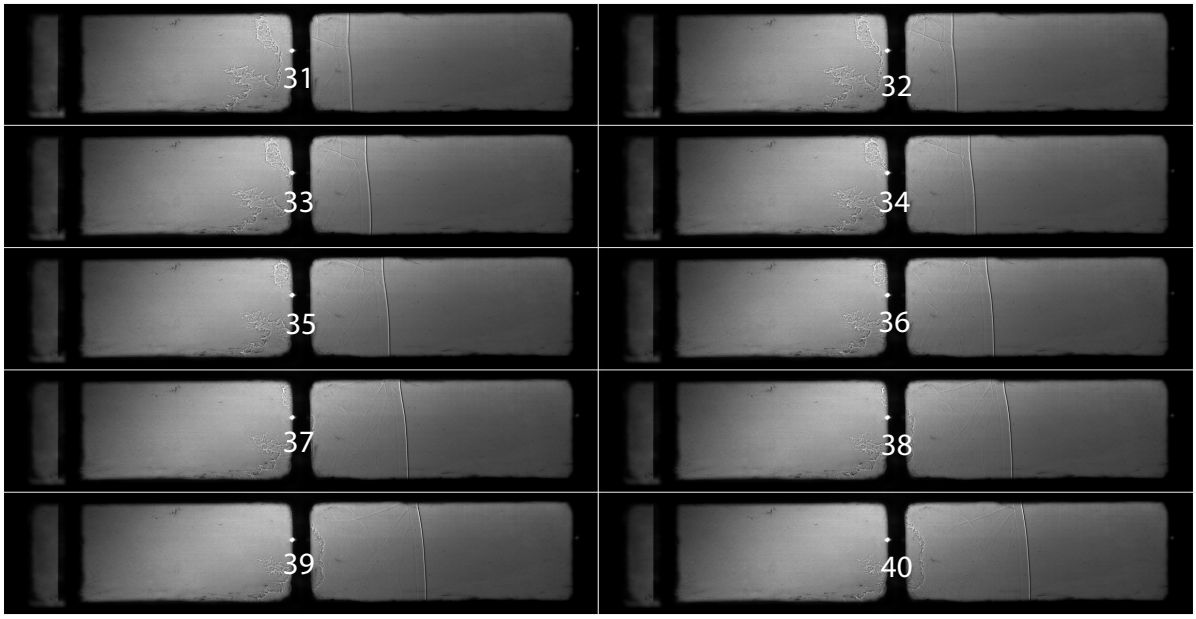


Figure B.29: The full record of the Shadowgraph images illustrating the failure of detonation after interacting with obstacles in $2C_2H_2+5O_2+21Ar$, p_0=17.9 KPa. Recorded at 23.53 μs interframe, 0.8 μs exposure, 42496 fps.

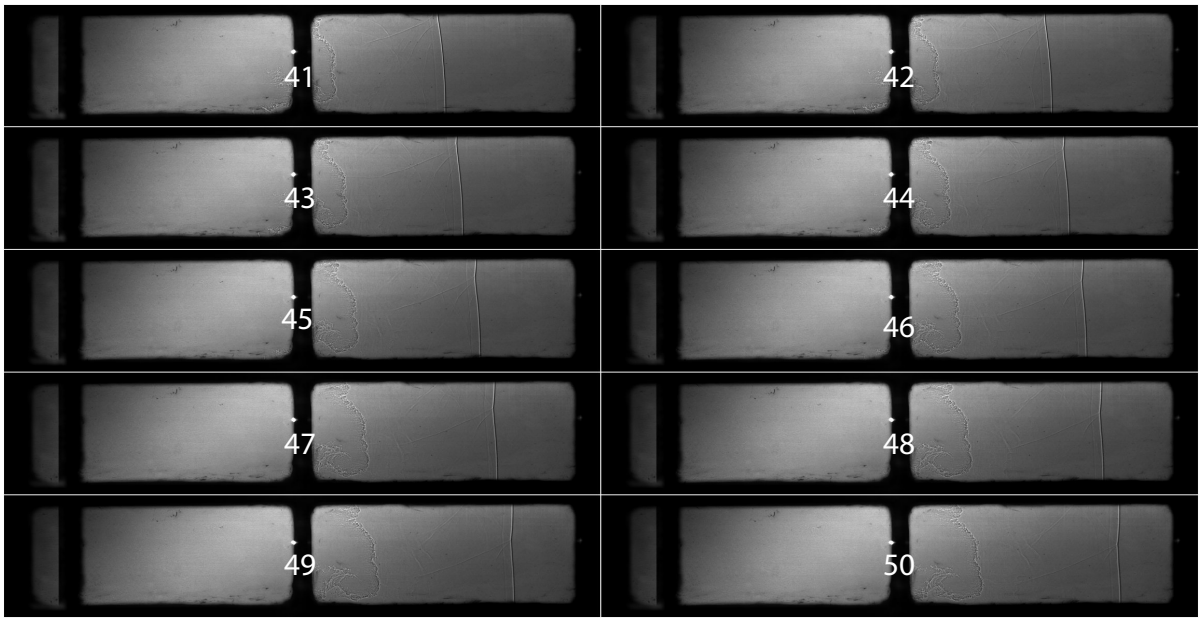


Figure B.30: The full record of the Shadowgraph images illustrating the failure of detonation after interacting with obstacles in $2C_2H_2+5O_2+21Ar$, p_0=17.9 KPa. Recorded at 23.53 μs interframe, 0.8 μs exposure, 42496 fps.

B.5 Propane

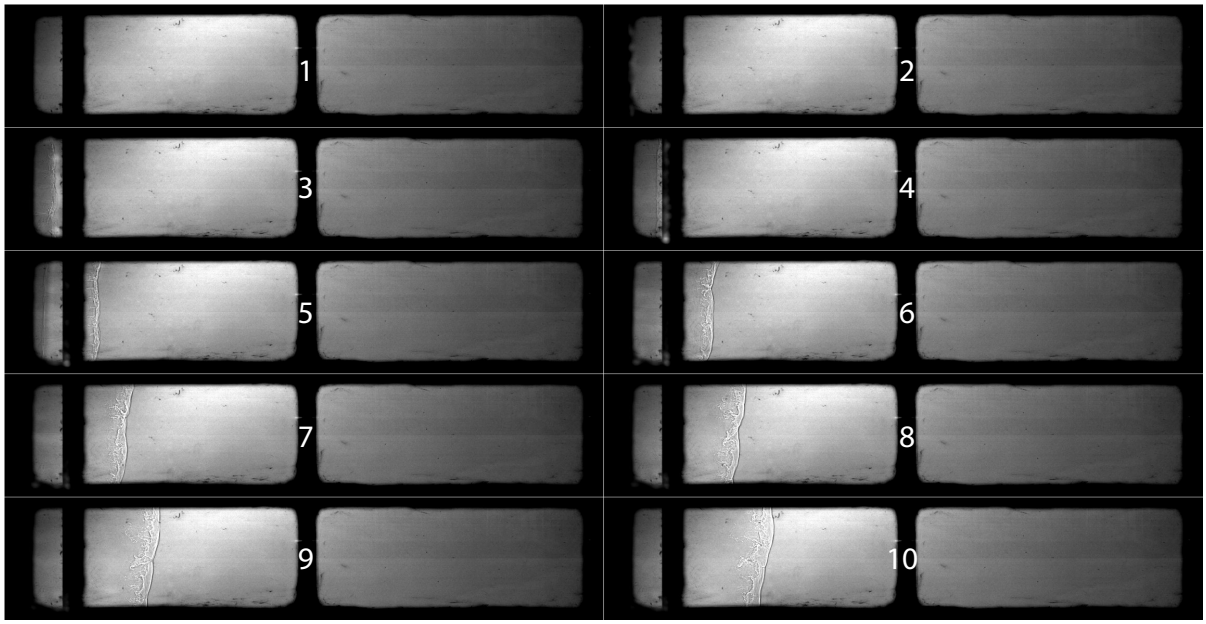


Figure B.31: The full record of the Shadowgraph images illustrating the failure of detonation after interacting with obstacles in $C_3H_8+5O_2$, p_0=4.1 KPa. Recorded at 23.53 μs interframe, 0.8 μs exposure, 42496 fps.

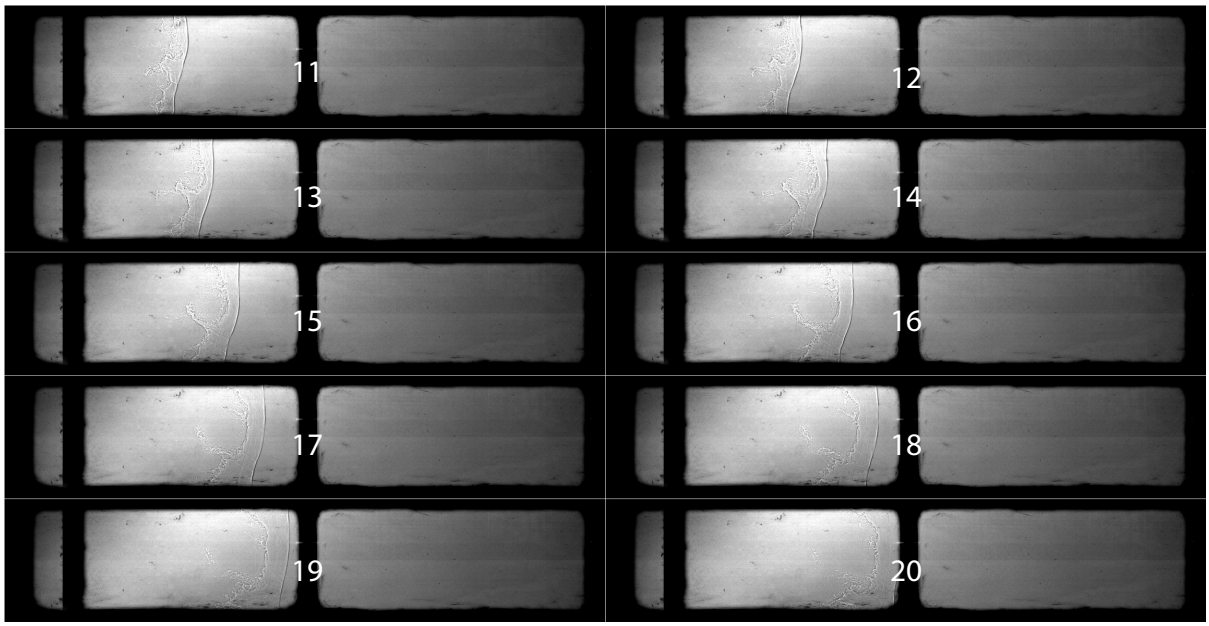


Figure B.32: The full record of the Shadowgraph images illustrating the failure of detonation after interacting with obstacles in C_3H_8+$5O_2$, p_0=4.1 KPa. Recorded at 23.53 μs interframe, 0.8 μs exposure, 42496 fps.

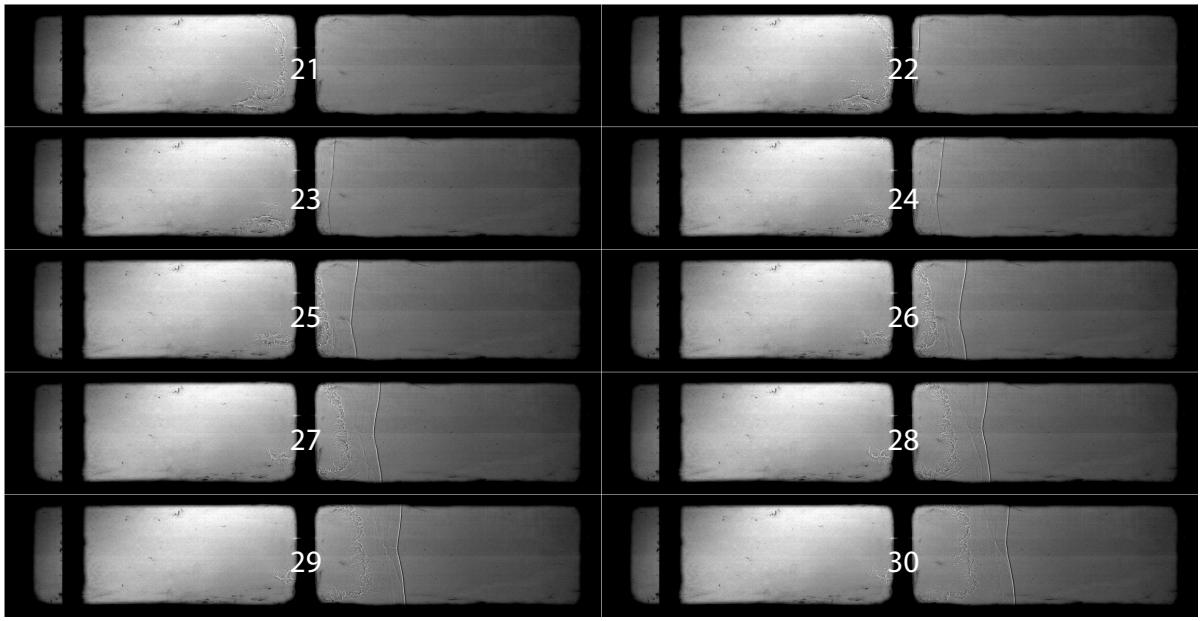


Figure B.33: The full record of the Shadowgraph images illustrating the failure of detonation after interacting with obstacles in C_3H_8+$5O_2$, p_0=4.1 KPa. Recorded at 23.53 μs interframe, 0.8 μs exposure, 42496 fps.

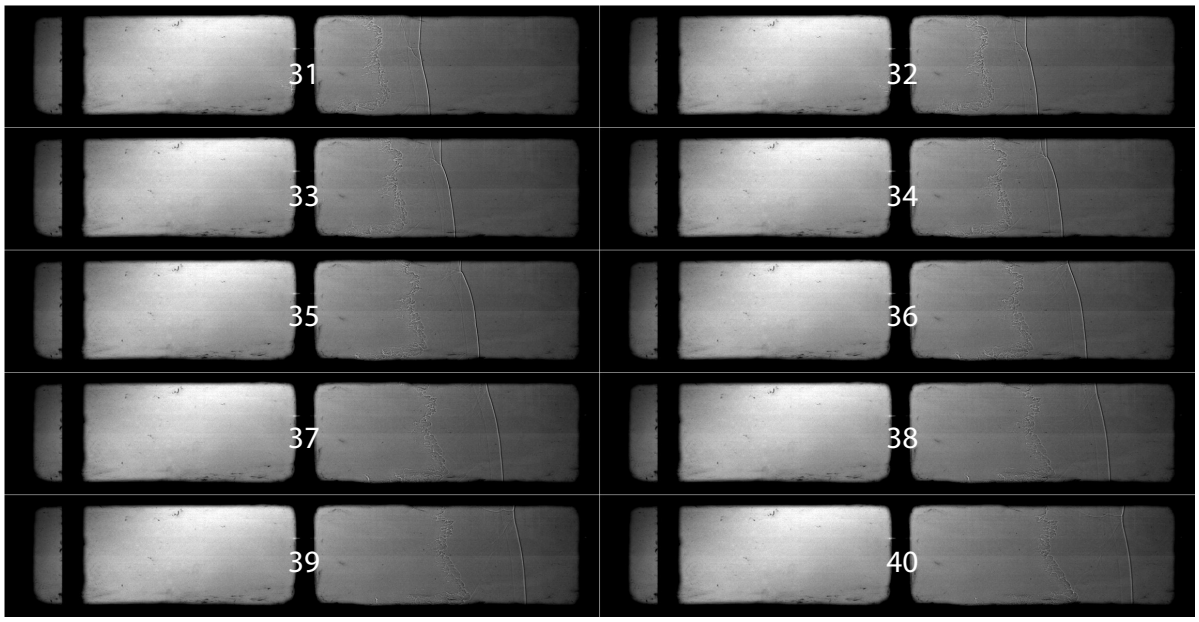


Figure B.34: The full record of the Shadowgraph images illustrating the failure of detonation after interacting with obstacles in C_3H_8+$5O_2$, p_0=4.1 KPa. Recorded at 23.53 μs interframe, 0.8 μs exposure, 42496 fps.

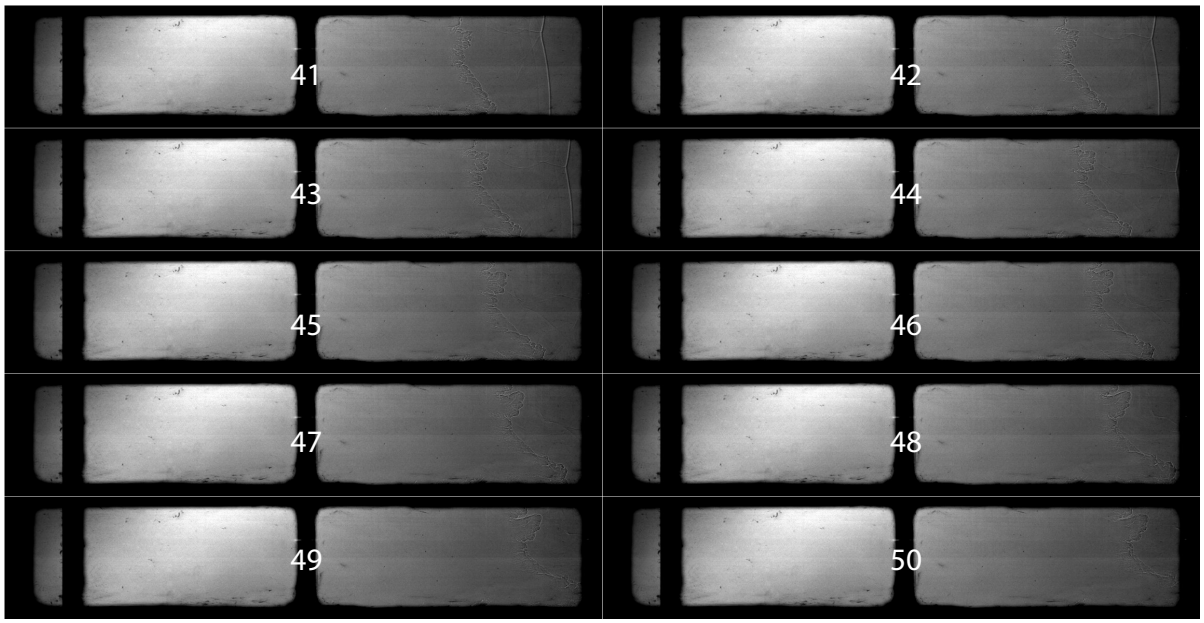


Figure B.35: The full record of the Shadowgraph images illustrating the failure of detonation after interacting with obstacles in C_3H_8+$5O_2$, p_0=4.1 KPa. Recorded at 23.53 μs interframe, 0.8 μs exposure, 42496 fps.

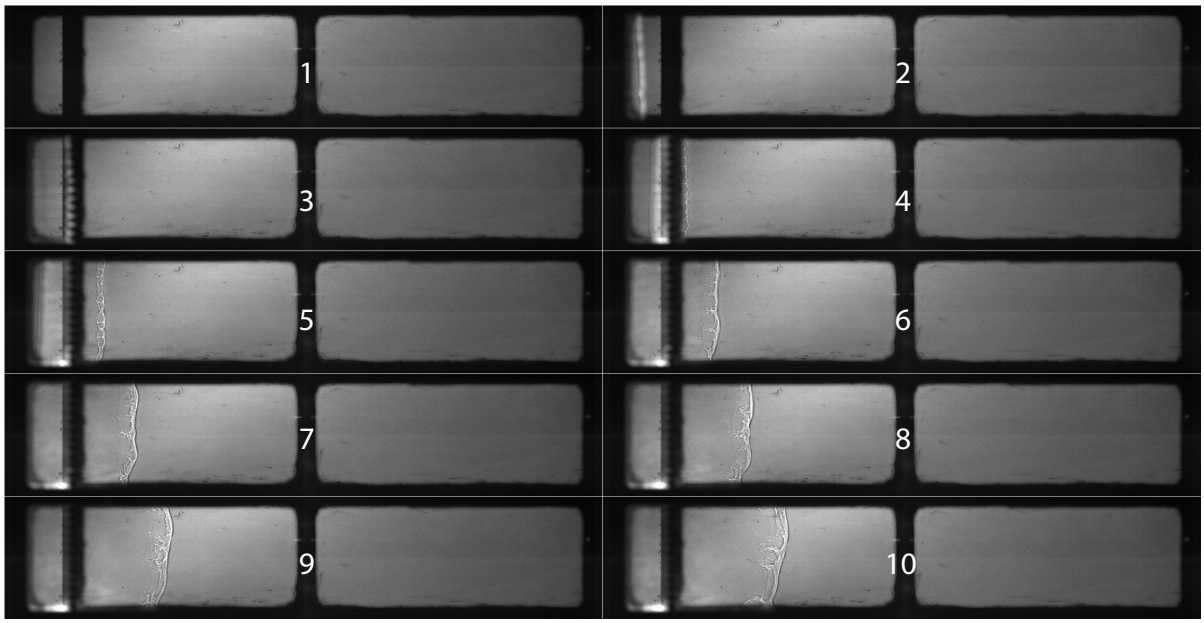


Figure B.36: The full record of the Shadowgraph images illustrating the re-initiation of detonation after interacting with obstacles in C_3H_8+$5O_2$, p_0=7.5 KPa. Recorded at 23.53 μs interframe, 0.8 μs exposure, 42496 fps.

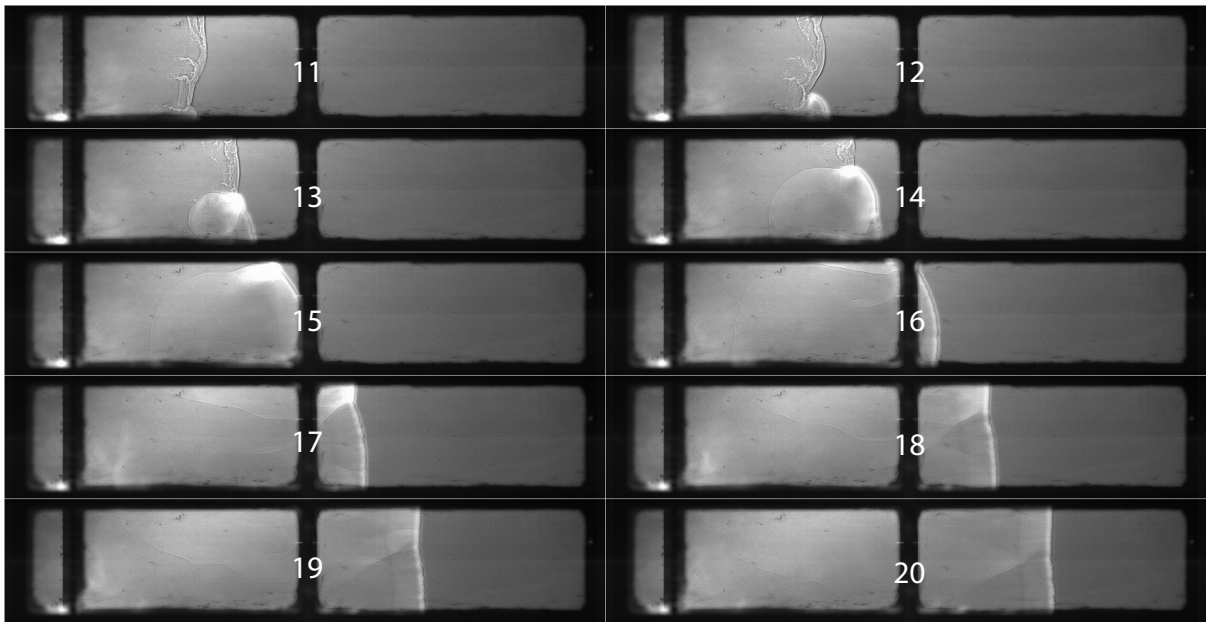


Figure B.37: The full record of the Shadowgraph images illustrating the re-initiation of detonation after interacting with obstacles in $C_3H_8+5O_2$, p_0=7.5 KPa. Recorded at 23.53 μs interframe, 0.8 μs exposure, 42496 fps.

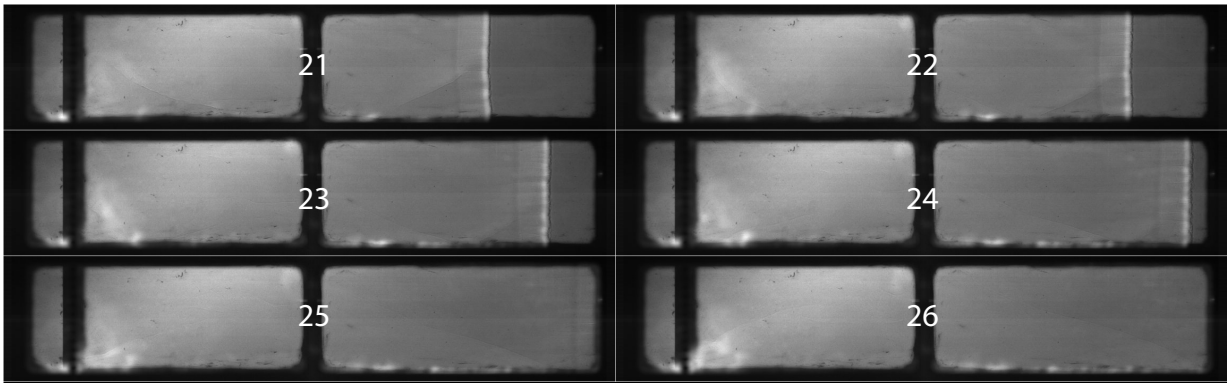


Figure B.38: The full record of the Shadowgraph images illustrating the re-initiation of detonation after interacting with obstacles in $C_3H_8+5O_2$, p_0=7.5 KPa. Recorded at 23.53 μs interframe, 0.8 μs exposure, 42496 fps.

Appendix C

Full List of Experiments

C.1 75 % Blockage ratio experiments

Table C.1: A full list of experiments conducted for the 75% blockage ratio experiments

Methane-Oxygen

Test#	Pressure [KPa] Driver—Driven	Date	Notes
Test 01	NA—3.4	2014-11-06	Fail to propagate as CJ detonation
Test 02	NA—4.1	2014-11-06	Fail to propagate as CJ detonation
Test 03	NA—4.8	2014-11-06	Fail to propagate as CJ detonation
Test 04	NA—6.2	2014-11-06	Fail to propagate as CJ detonation
Test 05	NA—5.5	2014-11-06	Fail to propagate as CJ detonation
Test 06	NA—6.8	2014-11-06	Fail to propagate as CJ detonation
Test 07	NA—8.9	2014-11-06	Re-Initiated
Test 08	NA—10.3	2014-11-06	Re-Initiated
Test 09	NA—7.5	2014-11-07	No Re-Initiation
Test 10	NA—7.2	2014-11-07	No Re-Initiation
Test 11	NA—6.9	2014-11-07	No Re-Initiation

Table C.2: Continuation of table C.1

Methane-Oxygen

Test#	Pressure [KPa] Driver—Driven	Date	Notes
Test 12	10.34—6.2	2014-11-11	Fail to propagate as CJ detonation. Driver(C2H4+3O2)
Test 13	10.34—6.2	2014-11-11	Fail to propagate as CJ detonation. Driver(CH4+2O2)
Test 14	NA—10.3	2014-11-11	No diaphragm.(C2H4+3O2) used as a mixture to test it
Test 15	13.1—6.2	2014-11-11	Fail to propagate as CJ detonation. Driver(C2H4+3O2)
Test 16	17.2—6.2	2014-11-11	Fail to propagate as CJ detonation. Driver(C2H4+3O2)
Test 17	17.2—6.2	2014-11-11	Re-Initiated, Driver(C2H4+3O2). Increased the HVI from 20 KV to 24 KV
Test 18	NA—7.5	2014-11-11	Re-Initiated. Driver(C2H4+3O2)
Test 19	17.9—5.8	2014-11-12	No Re-Initiation. Driver(C2H4+3O2)
Test 20	17.9—3.4	2014-11-12	No Re-Initiation. Driver(C2H4+3O2)
Test 21	17.9—4.1	2014-11-12	No Re-Initiation. Driver(C2H4+3O2)
Test 22	17.9—4.8	2014-11-12	No Re-Initiation. Driver(C2H4+3O2)
Test 23	17.9—6.8	2014-11-12	No Re-Initiation. Driver(C2H4+3O2)
Test 24	NA—6.8	2014-11-12	Re-Initiated
Test 25	NA—9.6	2014-11-12	Re-Initiated
Test 26	NA—11	2014-11-17	Re-Initiated
Test 27	17.92—3.4	2014-11-20	No Re-Initiation. Driver(C2H4+3O2)
Test 28	17.92—4.1	2014-11-20	No Re-Initiation. Driver(C2H4+3O2)
Test 29	NA—9.6	2014-12-18	Re-Initiate
Test 30	NA—8.2	2014-12-18	Re-Initiate
Test 31	17.9—4.8	2015-01-22	No Re-Initiation. Driver(2C2H6+7O2)

Table C.3: Continuation of table C.2

Propane-Oxygen

Test#	Pressure [KPa] Driver—Driven	Date	Notes
Test 01	NA—3.4	2014-12-17	Fail to propagate as CJ detonation
Test 02	NA—2.7	2014-12-17	Fail to propagate as CJ detonation
Test 03	NA—2.0	2014-12-17	Fail to propagate as CJ detonation
Test 04	NA—4.1	2014-12-17	Re-initiated
Test 05	NA—4.8	2014-12-17	Re-initiated
Test 06	NA—5.5	2014-12-17	Re-initiated
Test 07	NA—3.8	2014-12-17	Re-Initiated

Table C.4: Continuation of table C.3

Ethane-Oxygen

Test#	Pressure [KPa] Driver—Driven	Date	Notes
Test 01	NA—3.4	2015-01-15	Re-Initiated
Test 02	NA—2.7	2014-12-17	Fail to propagate as CJ detonation
Test 03	NA—3.1	2014-12-17	Fail to propagate as CJ detonation
Test 04	NA—4.1	2014-12-17	Re-initiated
Test 05	NA—4.8	2014-12-17	Re-initiated
Test 06	NA—5.5	2014-12-17	Re-initiated
Test 07	NA—6.2	2014-12-17	Re-Initiated
Test 07	NA—2.4	2014-12-17	Fail to propagate as CJ detonation

Table C.5: Continuation of table C.4

Ethylene-Oxygen

Test#	Pressure [KPa] Driver—Driven	Date	Notes
Test 01	NA—6.9	2014-11-27	Re-Initiated
Test 02	NA—3.4	2014-11-27	Fail to propagate as CJ detonation
Test 03	NA—4.1	2014-11-27	Re-initiated
Test 04	NA—4.8	2014-11-27	Re-initiated
Test 05	NA—5.5	2014-11-27	Re-initiated
Test 06	NA—6.2	2014-11-27	Re-initiated

Table C.6: Continuation of table C.5

Actylene-Oxygen-Argon

Test#	Pressure [KPa] Driver—Driven	Date	Notes
Test 01	NA—6.9	2014-12-19	Fail to propagate as CJ detonation
Test 02	NA—10.3	2014-12-19	Re-initiated
Test 03	NA—9.6	2014-12-19	Fail to propagate as CJ detonation
Test 04	NA—10.0	2014-12-19	Re-initiated
Test 05	NA—10.3	2014-12-19	Re-initiated. Re-test.
Test 06	NA—9.6	2014-12-19	Fail to propagate as CJ detonation. Re-test.
Test 07	NA—11.0	2014-12-19	Re-initiated

C.2 90 % Blockage ratio experiments

Table C.7: A full list of experiments conducted for the 90% blockage ratio experiments

Methane-Oxygen

Test#	Pressure [KPa] Driver—Driven	Date	Notes
Test 01	NA—10.3	2015-03-09	Fail to propagate as CJ detonation
Test 02	NA—11.0	2015-03-09	Fail to propagate as CJ detonation
Test 03	NA—11.7	2015-03-09	Fail to propagate as CJ detonation
Test 04	NA—12.4	2015-03-09	Fail to propagate as CJ detonation
Test 05	NA—13.1	2015-03-10	Re-Initiated
Test 06	NA—13.7	2015-03-10	Fail to propagate as CJ detonation
Test 07	NA—9.6	2015-03-10	Open-Shutter
Test 08	NA—14.4	2015-03-10	Re-Initiated
Test 09	NA—7.6	2015-03-10	Fail to propagate as CJ detonation
Test 10	NA—13.7	2015-03-13	Fail to propagate as CJ detonation
Test 11	NA—15.1	2015-03-13	Re-Initiated
Test 12	NA—15.8	2015-03-13	Re-Initiated
Test 13	NA—13.1	2015-03-13	Re-Initiated
Test 14	NA—14.4	2015-03-13	Fail to propagate as CJ detonation
Test 15	NA—14.4	2015-03-13	Re-Initiated
Test 16	NA—13.7	2015-03-17	Re-Initiated

Table C.8: Continuation of table C.7

Propane-Oxygen

Test#	Pressure [KPa] Driver—Driven	Date	Notes
Test 01	NA—5.5	2015-03-23	Re-initiated
Test 02	NA—4.8	2015-03-23	Re-initiated
Test 03	NA—5.5	2015-03-23	Fail to propagate as CJ detonation
Test 04	NA—4.8	2015-03-23	Fail to propagate as CJ detonation
Test 05	NA—6.2	2015-03-23	Re-initiated
Test 06	NA—6.9	2015-03-23	Re-initiated
Test 07	NA—4.1	2015-03-23	Fail to propagate as CJ detonation
Test 08	NA—7.6	2015-03-23	Re-initiated
Test 09	NA—5.8	2015-03-23	Fail to propagate as CJ detonation

Table C.9: Continuation of table C.8

Ethane-Oxygen

Test#	Pressure [KPa] Driver—Driven	Date	Notes
Test 01	NA—6.2	2015-03-13	Fail to propagate as CJ detonation
Test 02	NA—6.9	2015-03-13	Fail to propagate as CJ detonation
Test 03	NA—8.9	2015-03-13	Re-initiated
Test 04	NA—7.5	2015-03-13	Fail to propagate as CJ detonation
Test 05	NA—8.2	2015-03-17	Fail to propagate as CJ detonation
Test 06	NA—9.6	2015-03-17	Re-initiated
Test 07	NA—10.3	2015-03-17	Re-initiated
Test 08	NA—11.0	2015-03-17	Re-initiated
Test 09	NA—8.9	2015-03-17	Re-initiated
Test 10	NA—8.2	2015-03-17	Fail to propagate as CJ detonation

Table C.10: Continuation of table C.9

Ethylene-Oxygen

Test#	Pressure [KPa] Driver—Driven	Date	Notes
Test 01	NA—4.1	2015-03-23	Fail to propagate as CJ detonation
Test 02	NA—6.2	2015-03-23	Fail to propagate as CJ detonation
Test 03	NA—6.9	2015-03-23	Re-initiated
Test 04	NA—6.9	2015-03-23	Fail to propagate as CJ detonation
Test 05	NA—7.5	2015-03-23	Re-initiated
Test 06	NA—8.2	2015-03-23	Re-initiated
Test 07	NA—4.8	2015-03-23	Fail to propagate as CJ detonation
Test 08	NA—5.5	2015-03-23	Fail to propagate as CJ detonation
Test 09	NA—8.9	2015-03-23	Re-initiated

Table C.11: Continuation of table C.10

Acetylene-Oxygen-Argon

Test#	Pressure [KPa] Driver—Driven	Date	Notes
Test 01	NA—11.0	2015-03-23	Fail to propagate as CJ detonation
Test 02	NA—12.4	2015-03-23	Fail to propagate as CJ detonation
Test 03	NA—13.7	2015-03-23	Fail to propagate as CJ detonation
Test 04	NA—15.1	2015-03-23	Fail to propagate as CJ detonation
Test 05	NA—16.5	2015-03-23	Fail to propagate as CJ detonation
Test 06	NA—18.0	2015-03-23	Fail to propagate as CJ detonation

References

[1] Joanna Maria Karol Austin. "The role of instability in gaseous detonation". *Dissertation (Ph.D.), California Institute of Technology*, 2003.

[2] M. Berthelot and P. Vieille. "Sur la vitesse de propagation des phenomenes explosifs dans les gaz". *C. R. Acad. Sci. Paris*, 94(4):101–108, 1882.

[3] R. R. Bhattacharjee, S. S. M. Lau-Chapdelaine, G. Maines, L. Maley, and M. I. Radulescu. "Detonation re-initiation mechanism following the Mach reflection of a quenched detonation". *Proceedings of the Combustion Institute*, 34:1893–1901, 2012.

[4] Rohit Ranjan Bhattacharjee. "Experimental investigation of detonation re-initiation mechanisms following a Mach reflection of a quenched detonation". *M.A.Sc. Thesis, University of Ottawa*, 2013.

[5] D. Bradley and A. Mitcheson. "The venting of gaseous explosions in spherical vessels". *Combust Flame*, 32:221–55, 1978.

[6] J. Chao. "Critical deflagration waves that lead to the onset of detonation". *PhD Thesis, McGill University*, 2006.

[7] J. Chao, T. Otsuka, and J. H. S. Lee. "An experimental investigation of the onset of detonation". *Proceedings of the Combustion Institute*, 30:1889–1897, 2005.

[8] R. S. Chue, J. F. Clarke, and J. H. Lee. "Chapman-Jouguet Deflagrations". *Proceedings of Mathematical and Physical Sciences*, 441(1931):607–623, 8 June 1993.

[9] G. Ciccarelli and S. Dorofeev. "Flame acceleration and transition to detonation in ducts". *Progress in Energy and Combustion Science*, 34(4):499–550, 2008.

[10] R. Courant and K. O. Friedrichs. "Supersonic Flow and Shock Waves". *Wiley (1948)*, page 206, 2007.

[11] G. Darrieus. "Unpublished works presented at La Technique Moderne (1938) and at Congres de Mechanique Appliquee Paris". 1945.

[12] K. Dennis, L. Maley, Z. Liang, and M. I. Radulescu. "Implementation of large scale shadowgraphy in hydrogen explosion phenomena". *International Journal of Hydrogen Energy*, 39:11346–11353, July 15 2014.

[13] S. B. Dorofeev, A. S. Kochurko, and B. B. Chaivanov. "Detonation onset conditions in spatially nonuniform combustible mixtures". *Proceedings of the Sixth Symposium (International) on Loss Prevention and Safety Promotion in the Processes Industries. Norway, Oslo*, 4:1–19, 1989.

[14] S. B. Dorofeev, A. S. Kochurko, A. A. Efimenko, and B. B. Chaivanov. "Evaluation of the hydrogen explosion hazard". *Nuclear Engineering and Design*, 148:305–316, 1994.

[15] S. B. Dorofeev, V. P. Sidorov, M. S. Kuznetsov, I. D. Matsukov, and V. I. Alekseev. "Effect of scale on the onset of detonations". *Shock Waves*, 10:137–149, 2000.

[16] S. B. Dorofeev, Sidorov V.P., A.E. Dvoinishnikov, and W. Breitung. "Deflagration to detonation transition in large confined volume of lean hydrogen-air mixtures". *Combustion and Flame*, 104:95–110, 1996.

[17] G. Dupre, O. Peraldi, J. H. Lee, and R. Knystautas. "Propagation of detonation waves in an acoustic absorbing walled tube". *Proceedings of Astronaut Aeronaut*, 114:248–263, 1988.

[18] D. G. Goodwin, H. K. Moffat, and R. L. Speth. "Cantera: An object-oriented software toolkit for chemical kinetics". *thermodynamics, and transport processes,*, http://www.cantera.org, 2015, Version 2.2.0.

[19] S. Gordon and B. McBride. "Computer program for calculation of complex chemical equilibrium compositions and applications". *Tech. rep., NASA Reference Publication*, 1311, 1994.

[20] J. S. Grondin and J. H. S. Lee. "Experimental observation of the onset of detonation downstream of a perforated plate". *Shock Waves*, 20(5):381–386, 2010.

[21] M. J. Hargather and G. S. Settles. "Retrorerflective shadowgraph technique for large-scale flow visualization". *Applied Optics*, 48(22):4449–4457, 2009.

[22] M. S. Kuznetsov, V. I. Alekseev, and S. B. Dorofeev. "Comparison of critical conditions for DDT in regular and irregular cellular detonation systems". *Shock Waves*, 10(3):217–223, 2000.

[23] L. D. Landau. "Theory of slow combustion". *Zh Exp Teor Fiz*, 12:14–240, 1944.

[24] Sebastien She-Ming Lau-Chapdelaine. "Numerical simulations of detonation re-initiation behind an obstacle". *M.A.Sc. Thesis, University of Ottawa*, 2013.

[25] J. H. S. Lee. *"The Detonation Phenomenon"*. Cambridge University Press.

[26] J. H. S. Lee. "Dynamic Parameters of Gaseous Detonations". *Annual Review of Fluid Mechanics*, 16:311–336, 1984.

[27] J. H. S. Lee and I. O. Moen. "The mechanism of transition from deflagration to detonation in vapor cloud explosions". *Progress in Energy and Combustion Science*, 6(4):359–389, 1980.

[28] P. Mach and M.I. Radulescu. "Mach reflection bifurcations as a mechanism of cell multiplication in gaseous detonations". *Proceedings of the Combustion Institute*, 33(2):2279–2285, January 2011.

[29] L. Maley, R. Bhattacharjee, S. M. Lau-Chapdelaine, and M.I. Radulescu. "Influence of hydrodynamic instabilities on the propagation mechanism of fast flames". *Proceedings of the Combustion Institute*, 35(21):17–26, 2015.

[30] Logan Maley. "On Shock Reflections in Fast Flames". *M.A.Sc. Thesis, University of Ottawa*, 2015.

[31] Brian McNeilly Maxwell. "Turbulent Combustion Modelling of Fast-Flames and Detonations Using Compressible LEM-LES". *PhD Thesis, University of Ottawa*, 2016.

[32] Wang Mechanism. "http://shepherd.caltech.edu/wang.html". 2005.

[33] E. S. Oran and V. N. Gamezo. "Origins of the deflagration to detonation transition in gas phase combustion". *Combustion and Flame,*, 148:447, Jan, 2007.

[34] Norbert Peters. *"Turbulent combustion"*. Cambridge University Press, 2000.

[35] M. I. Radulescu, G. J. Sharpe, C. K. Law, and J. H. S. Lee. "The hydrodynamic structure of unstable cellular detonations". *Journal of Fluid Mechanics*, 580:31–81, 2007.

[36] M. I. Radulescu, G. J. Sharpe, J. H. S. Lee, C. B. Kiyanda, A. J. Higgins, and R. K. Hanson. "The ignition mechanism in irregular structure gaseous detonations". *Proceedings of the Combustion Institute*, 30:1859–1867, 2005.

[37] M. I. Radulescu, W. Wang, M. Saif, L. Maley, M. Levin, and A. Pekalski. "On Chapman-Jouguet deflagrations". *Proceedings of the 25th International Colloquium on the Dynamics of Explosions and Reactive Systems, Leeds, UK.*, 2015.

[38] Matei I Radulescu. "The propagation and failure mechanism of gaseous detonations: experiments in porous-walled tubes". *PhD Thesis, McGill University*, 2003.

[39] M.I. Radulescu, G. Sharpe, and D. Bradley. "A universal parameter quantifying explosion hazards, detonability and hot spot formation, the χ number". *in Proceedings of the Seventh International Seminar on Fire and Explosion Hazards, (D. Bradley, G. Makhviladze, V. Molkov, P. Sunderland, and F. Tamanini, eds.)*, pages 617–626, 2013.

[40] M. P. Romano, M. I. Radulescu, A. J. Higgins, and J. H. S. Lee. "Sensitization of pentane-oxygen mixtures to DDT via cool flame oxidation". *Combustion and flame*, 132(3):387–394, 2003.

[41] G. D. Roy, S. M. Frolov, A. A. Borisov, and D. W. Netzer. "Pulse detonation propulsion: challenges, current status, and future perspective". *Prog Energy Combust Sci*, 30(6):545–672, 2004.

[42] G. J. Sharpe. "Shock-induced ignition for a two-step chain-branching kinetics model". *Physics of Fluids*, 14(12):4372–4388, 2002.

[43] M. Shepherd and J. Kaneshige. "Detonation database", July 1997.

[44] G. Smith, D. M. Golden, M. Frenklach, N. Moriarty, B. Eiteneer, M. Goldenberg, C. Bowman, R. Hanson, S. Song, G. W.C.Jr., V. Lissianski, and Z. Qin. "GRI MECH 3.0". *Technical Report*, http://www.me.berkeley.edu/gri-mech.

[45] R. Sorin, R. Zitoun, and D. Desbordes. "Optimization of the deflagration to detonation transition: reduction of length and time of transition". *Shock Waves*, 15(2):137–145, 2006.

[46] J. Tang and M. I. Radulescu. "Dynamics of shock induced ignition in Fickett's model: Influence of χ". *Proceedings of the Combustion Institute*, 34:2035–2041, 2013.

[47] G. I. Taylor and R. S. Tankin. "Fundamentals of Gasdynamics (Ed. EMMONS, H. W.)". pages 622–686, Princeton University Press(1958).

[48] G. Thomas, R. Bambrey, and C. Brown. "Experimental observations of flame acceleration and transition to detonation following shock-flame interaction". *Combustion Theory and Modelling*, 5(4):573–594, 2001.

[49] P. A. Urtiew and A. K. Oppenheim. "Experimental observations of the transition to detonation in an explosive gas". *Proc. R. Soc. Lond.*, A295:13–28, 1965.

[50] P. A. Urtiew and A. K. Oppenheim. "Onset of Detonation". *Combustion and Flame,*, 9:405–407, 1965.

[51] A. Veseri, W. Breitung, and S.B. Dorofeev. "Run-up distances to supersonic flames in obstacle-laden tubes". *Journal de Physique IV*, 12:333–340, 2002.

[52] F. Williams. "San Diego Mechanism,". *Technical Report, University of California San Diego*, http://web.eng.ucsd.edu/ mae/ groups/ combustion/ mechanism.html.